NATIONAL AERONAUTICS AND SPACE ADMINISTRATION

The Deep Space Network
Progress Report 42-33

March and April 1976

JET PROPULSION LABORATORY
CALIFORNIA INSTITUTE OF TECHNOLOGY
PASADENA, CALIFORNIA

June 15, 1976

NATIONAL AERONAUTICS AND SPACE ADMINISTRATION

The Deep Space Network
Progress Report 42-33

March and April 1976

JET PROPULSION LABORATORY
CALIFORNIA INSTITUTE OF TECHNOLOGY
PASADENA, CALIFORNIA

June 15, 1976

Prepared Under Contract No. NAS 7-100
National Aeronautics and Space Administration

Put on your desk

TECHNICAL REPORT STANDARD TITLE PAGE

1. Report No. 42-33	2. Government Accession No.	3. Recipient's Catalog No.
4. Title and Subtitle THE DEEP SPACE NETWORK PROGRESS REPORT MARCH AND APRIL 1976		5. Report Date June 15, 1976 6. Performing Organization Code
7. Author(s) JPL Staff		8. Performing Organization Report No.
9. Performing Organization Name and Address JET PROPULSION LABORATORY California Institute of Technology 4800 Oak Grove Drive Pasadena, California 91103		10. Work Unit No. 11. Contract or Grant No. NAS 7-100 13. Type of Report and Period Covered Progress Report
12. Sponsoring Agency Name and Address NATIONAL AERONAUTICS AND SPACE ADMINISTRATION Washington, D.C. 20546		14. Sponsoring Agency Code

15. Supplementary Notes

16. Abstract

This report describes work performed for the JPL/NASA Deep Space Network (DSN). Progress is presented on DSN supporting research and technology, advanced development and engineering, and implementation, and DSN operations which pertain to mission-independent or multiple-mission development as well as to support of flight projects. Each issue contains a description of the functions and facilities of the DSN.

17. Key Words (Selected by Author(s))	18. Distribution Statement
Ground Support Systems Spacecraft Communications Communications Mathematical and Computer Sciences	Unclassified -- Unlimited

19. Security Classif. (of this report)	20. Security Classif. (of this page)	21. No. of Pages	22. Price
Unclassified	Unclassified	211	

HOW TO FILL OUT THE TECHNICAL REPORT STANDARD TITLE PAGE

Make items 1, 4, 5, 9, 12, and 13 agree with the corresponding information on the report cover. Use all capital letters for title (item 4). Leave items 2, 6, and 14 blank. Complete the remaining items as follows:

3. Recipient's Catalog No. Reserved for use by report recipients.

7. Author(s). Include corresponding information from the report cover. In addition, list the affiliation of an author if it differs from that of the performing organization.

8. Performing Organization Report No. Insert if performing organization wishes to assign this number.

10. Work Unit No. Use the agency-wide code (for example, 923-50-10-06-72), which uniquely identifies the work unit under which the work was authorized. Non-NASA performing organizations will leave this blank.

11. Insert the number of the contract or grant under which the report was prepared.

15. Supplementary Notes. Enter information not included elsewhere but useful, such as: Prepared in cooperation with... Translation of (or by)... Presented at conference of... To be published in...

16. Abstract. Include a brief (not to exceed 200 words) factual summary of the most significant information contained in the report. If possible, the abstract of a classified report should be unclassified. If the report contains a significant bibliography or literature survey, mention it here.

17. Key Words. Insert terms or short phrases selected by the author that identify the principal subjects covered in the report, and that are sufficiently specific and precise to be used for cataloging.

18. Distribution Statement. Enter one of the authorized statements used to denote releasability to the public or a limitation on dissemination for reasons other than security of defense information. Authorized statements are "Unclassified—Unlimited," "U. S. Government and Contractors only," "U. S. Government Agencies only," and "NASA and NASA Contractors only."

19. Security Classification (of report). NOTE: Reports carrying a security classification will require additional markings giving security and downgrading information as specified by the Security Requirements Checklist and the DoD Industrial Security Manual (DoD 5220.22-M).

20. Security Classification (of this page). NOTE: Because this page may be used in preparing announcements, bibliographies, and data banks, it should be unclassified if possible. If a classification is required, indicate separately the classification of the title and the abstract by following these items with either "(U)" for unclassified, or "(C)" or "(S)" as applicable for classified items.

21. No. of Pages. Insert the number of pages.

22. Price. Insert the price set by the Clearinghouse for Federal Scientific and Technical Information or the Government Printing Office, if known.

Preface

Beginning with Volume XX, the Deep Space Network Progress Report changed from the Technical Report 32- series to the Progress Report 42- series. The volume number continues the sequence of the preceding issues. Thus, Progress Report 42-20 is the twentieth volume of the Deep Space Network series, and is an uninterrupted follow-on to Technical Report 32-1526, Volume XIX.

This report presents DSN progress in flight project support, tracking and data acquisition (TDA) research and technology, network engineering, hardware and software implementation, and operations. Each issue presents material in some, but not all, of the following categories in the order indicated.

Description of the DSN

Mission Support
- Ongoing Planetary/Interplanetary Flight Projects
- Advanced Flight Projects

Radio Science

Special Projects

Supporting Research and Technology
- Tracking and Ground-Based Navigation
- Communications—Spacecraft/Ground
- Station Control and Operations Technology
- Network Control and Data Processing

Network and Facility Engineering and Implementation
- Network
- Network Operations Control Center
- Ground Communications
- Deep Space Stations

Operations
- Network Operations
- Network Operations Control Center
- Ground Communications
- Deep Space Stations

Program Planning
- TDA Planning
- Quality Assurance

In each issue, the part entitled "Description of the DSN" describes the functions and facilities of the DSN and may report the current configuration of one of the five DSN systems (Tracking, Telemetry, Command, Monitor & Control, and Test & Training).

The work described in this report series is either performed or managed by the Tracking and Data Acquisition organization of JPL for NASA.

Contents

Network Control and Data Processing

NETWORK AND FACILITY ENGINEERING AND IMPLEMENTATION

Network

Deep Space Stations

OPERATIONS

Network Operations

Deep Space Stations

Network Functions and Facilities

N. A. Renzetti
Office of Tracking and Data Acquisition

The objectives, functions, and organization of the Deep Space Network are summarized; deep space station, ground communication, and network operations control capabilities are described.

The Deep Space Network (DSN), established by the National Aeronautics and Space Administration (NASA) Office of Tracking and Data Acquisition under the system management and technical direction of the Jet Propulsion Laboratory (JPL), is designed for two-way communications with unmanned spacecraft traveling approximately 16,000 km (10,000 miles) from Earth to the farthest planets of our solar system. It has provided tracking and data acquisition support for the following NASA deep space exploration projects: Ranger, Surveyor, Mariner Venus 1962, Mariner Mars 1964, Mariner Venus 1967, Mariner Mars 1969, Mariner Mars 1971, and Mariner Venus Mercury 1973, for which JPL has been responsible for the project management, the development of the spacecraft, and the conduct of mission operations; Lunar Orbiter, for which the Langley Research Center carried out the project management, spacecraft development, and conduct of mission operations; Pioneer, for which Ames Research Center carried out the project management, spacecraft development, and conduct of mission operations; and Apollo, for which the Lyndon B. Johnson Space Center was the project center and the Deep Space Network supplemented the Manned Space Flight Network (MSFN), which was managed by the Goddard Space Flight Center (GSFC). It is providing tracking and data acquisition support for Helios, a joint U.S./West German project; and Viking, for which Langley Research Center provides the project management, the Lander spacecraft, and conducts mission operations, and for which JPL also provides the Orbiter spacecraft.

The Deep Space Network is one of two NASA networks. The other, the Spaceflight Tracking and Data Network, is under the system management and technical direction of the Goddard Space Flight Center. Its function is to support manned and unmanned Earth-orbiting satellites. The Deep Space Network supports lunar, planetary, and interplanetary flight projects.

From its inception, NASA has had the objective of conducting scientific investigations throughout the solar system. It was recognized that in order to meet this objective, significant supporting research and advanced technology development must be conducted in order to provide deep space telecommunications for science data return in a cost effective manner. Therefore, the Network is continually evolved to keep pace with the state of the art of telecommunications and data handling. It was also recognized early that close coordination would be needed

between the requirements of the flight projects for data return and the capabilities needed in the Network. This close collaboration was effected by the appointment of a Tracking and Data Systems Manager as part of the flight project team from the initiation of the project to the end of the mission. By this process, requirements were identified early enough to provide funding and implementation in time for use by the flight project in its flight phase.

As of July 1972, NASA undertook a change in the interface between the Network and the flight projects. Prior to that time, since 1 January 1964, in addition to consisting of the Deep Space Stations and the Ground Communications Facility, the Network had also included the mission control and computing facilities and provided the equipment in the mission support areas for the conduct of mission operations. The latter facilities were housed in a building at JPL known as the Space Flight Operations Facility (SFOF). The interface change was to accommodate a hardware interface between the support of the network operations control functions and those of the mission control and computing functions. This resulted in the flight projects assuming the cognizance of the large general-purpose digital computers which were used for both network processing and mission data processing. They also assumed cognizance of all of the equipment in the flight operations facility for display and communications necessary for the conduct of mission operations. The Network then undertook the development of hardware and computer software necessary to do its network operations control and monitor functions in separate computers. This activity has been known as the Network Control System Implementation Project. A characteristic of the new interface is that the Network provides direct data flow to and from the stations; namely, metric data, science and engineering telemetry, and such network monitor data as are useful to the flight project. This is done via appropriate ground communication equipment to mission operations centers, wherever they may be.

The principal deliverables to the users of the Network are carried out by data system configurations as follows:

- The DSN Tracking System generates radio metric data; i.e., angles, one- and two-way doppler and range, and transmits raw data to Mission Control.
- The DSN Telemetry System receives, decodes, records, and retransmits engineering and scientific data generated in the spacecraft to Mission Control.
- The DSN Command System accepts coded signals from Mission Control via the Ground Communications Facility and transmits them to the spacecraft in order to initiate spacecraft functions in flight.

The data system configurations supporting testing, training, and network operations control functions are as follows:

- The DSN Monitor and Control System instruments, transmits, records, and displays those parameters of the DSN necessary to verify configuration and validate the Network. It provides operational direction and configuration control of the Network, and provides primary interface with flight project Mission Control personnel.
- The DSN Test and Training System generates and controls simulated data to support development, test, training and fault isolation within the DSN. It participates in mission simulation with flight projects.

The capabilities needed to carry out the above functions have evolved in three technical areas:

(1) The Deep Space Stations, which are distributed around Earth and which, prior to 1964, formed part of the Deep Space Instrumentation Facility. The technology involved in equipping these stations is strongly related to the state of the art of telecommunications and flight-ground design considerations, and is almost completely multimission in character.

(2) Ground communications technology supports the Earth-based, point-to-point voice and data communications from the stations to the Network Operations Control Center at JPL, Pasadena, and to the mission operations centers, wherever they may be. It is based largely on the capabilities of the common carriers throughout the world, which are engineered into an integrated system by the Goddard Space Flight Center for support of all NASA programs. We use the term "Ground Communications Facility" for the sets of hardware and software needed to carry out the above functions.

(3) The Network Operations Control Center is the functional entity for centralized operational control of the Network and interfaces with the users. It has two separable functional elements; namely, Network Operations Control and Network Data Processing. The functions of the Network Operations Control are:

- Control and coordination of Network support to meet commitments to Network users.

- Utilization of the Network data processing computing capability to generate all standards and limits required for Network operations.
- Utilization of Network data processing computing capability to analyze and validate the performance of all Network systems.

The personnel who carry out the above functions are located in the Space Flight Operations Facility, where mission operations functions are carried out by certain flight projects. Network personnel are directed by an Operations Control Chief.

The functions of the Network Data Processing are:

- Processing of data used by Network Operations Control for control and analysis of the Network.
- Display in the Network Operations Control Area of data processed in the Network Data Processing Area.
- Interface with communications circuits for input to and output from the Network Data Processing Area.
- Data logging and production of the intermediate data records.

The personnel who carry out these functions are located approximately 200 meters from the Space Flight Operations Facility. The equipment consists of minicomputers for real-time data system monitoring, two XDS Sigma 5s, display, magnetic tape recorders, and appropriate interface equipment with the ground data communications.

DSN Telemetry System Data Records

E. C. Gatz
DSN Systems Engineering Office

The DSN Telemetry System now includes the capability to provide a complete magnetic tape record, within 24 hours of reception, of all telemetry data received from a spacecraft. This record, the Intermediate Data Record, is processed and generated almost entirely automatically, and provides a detailed accounting of any missing data.

I. Introduction

The current configuration of the DSN Telemetry System is identified as the DSN Telemetry System, Mark III-75. This system is described, and a block diagram is presented in Ref. 1. A key feature of the system is the generation of Telemetry Intermediate Data Records (IDRs). These, and other data records, are discussed in Ref. 2. This article describes in detail the capability that has been implemented in the Deep Space Network to generate the Telemetry IDRs.

II. Definitions

A. Original Data Record (ODR)

Telemetry ODRs are those records made by digital recorders at the Deep Space Station at the time of reception of data from a spacecraft. For telemetry, these records are made subsequent to bit or symbol synchronization and, where applicable, decoding. Two types of Telemetry ODRs are made:

(1) Data Decoder Assembly (DDA) ODRs are made at 64-m stations only, and normally contain high-rate data, i.e., data at rates of 2 kbps and higher.

(2) Telemetry and Command Processor (TCP) ODRs are made at all stations and contain medium- or low-rate data, i.e., data at rates of 2 kbps and lower.

Both records contain telemetry data formatted as high-speed or wideband data blocks, identical to those transmitted from the station in real time.

B. Intermediate Data Record

IDRs are digital tape records made at the Network Operations Control Center (NOCC). For telemetry data, an IDR contains all the data, time ordered by earth-received time, of a given data stream, spacecraft, and Deep Space Station (DSS). Data from different stations (during station overlaps, for example) are therefore on different IDRs. A data stream is defined as these data received on one subcarrier and one carrier from a specified spacecraft. During a pass, the bit rate may change, or the station may change the stream from one

processor to another, but all such data will be on one IDR. For missions which produce multiple streams, multiple IDRs would be generated on a pass.

This record contains, as a minimum, the same data as the ODR for the same time period. The data on the IDR are in the same format as the ODR; additional records are added to provide label and summary information. The IDR is the interface for non-real-time telemetry data delivery to the flight projects. Each completed telemetry IDR and a printed summary listing are deliverable to a flight project within 24 hours after end-of-pass.

III. Functional Operation

The general configuration of data flow and data record generation are shown in Fig. 1. A more detailed description of the NOCC portion is contained in Ref. 3. The step-by-step process in generating the IDR is described in the following paragraphs.

A. Real-Time Data

In real time, all telemetry data are transmitted from the Deep Space Station to the flight project via Ground Communications Facility (GCF) high-speed and wideband data circuits. These same data are recorded at the NOCC on the Network Data Log (NDL). Experience has shown that these real-time streams have gaps caused by GCF problems and outages, by equipment malfunctions, or by loss of lock at the DSS. The subsequent steps in the IDR process are to detect these gaps and recover the data where possible.

B. Gap Lists

The telemetry equipment in the NOCC monitors each active telemetry stream and generates a list of data gaps. A gap in a stream is defined as any discontinuity in data block serial number, or any anomaly in the regular time sequence of data blocks.

Each gap consists of a pair of data block definitions: the last good block before a gap and the first good block after a gap. This block definition includes:

(1) Data type code

(2) Spacecraft number

(3) Block serial number

(4) Time tag

(5) DSS lock status code

(6) DSS configuration code

(7) Received signal strength

(8) Signal-to-noise ratio (SNR)

(9) Gap reason code

  (a) Discontinuity in block serial number

  (b) Time tag increment discontinuity

  (c) Out-of-lock condition

  (d) Change of configuration

(10) Estimate of equivalent number of data blocks in the gap

These gap lists are maintained in a computer file for use in recalling the missing data.

C. Gap List Editing

Any gap list, or selected portions thereof, can be reviewed by an analyst. Both printed outputs and cathode ray tube (CRT) displays are available. With the CRT display, the analyst can scan the list and mark any or all gaps for recall. This edited gap list is used by the recall processor to recall missing data from DSS ODRs after each pass.

D. Recall Process

The edited gap list is used to recall data automatically from the DSS ODRs. The NOCC Data Record Processor reads the gap list file, and generates the appropriate recall requests for the DSS. At the DSS, the responses are generated from the Automatic Total Recall Program (ATRS). This process is described in Ref. 4.

E. Merge Process

The final step in the IDR generation is the merging of the recalled data with the recorded (NDL) real-time data. This process is performed in the NOCC on the Data Records Processor, in an off-line non-real-time process. All inputs are via magnetic tape. The merge process generates a single IDR tape, with both real-time and recalled data arranged in proper time sequence and duplicates removed. In addition, the IDR tape contains a label record and summary records. The IDR format is shown in Fig. 2.

During the merge process, any gaps which are completely filled are deleted from the list; any unfilled gaps remain and are included in the summary record.

The IDR File Label Record contains:

(1) DSS number

(2) Pass number

(3) IDR start and stop times (approximate)

(4) Data types

(5) Spacecraft number

The IDR File Summary Record contains:

(1) DSS, pass, spacecraft number

(2) Data types

(3) IDR start and stop times (exact)

(4) Number of data blocks expected

(5) Number of data blocks written

(6) Number of data blocks missing

(7) List of all remaining data gaps

Included with each gap is a recall status code indicating either no recall tried, recall tried but not recoverable (e.g., an ODR failure), recall tried but data still defective, or a null gap with no missing data but included for information (e.g., for a bit rate change). The summary data are also listed on a printed output which accompanies each IDR tape.

IV. Performance

The Telemetry IDR function is now operational and has been used in support of the Viking Project, starting in April 1976. In routine operation, the IDRs are delivered to the project within 24 hours of the completion of each pass.

Content of the IDR consistently runs in excess of 99.9% of the expected data. This process therefore provides a timely record of the best data available on the ground for deep space missions.

References

1. Gatz, E. C., "DSN Telemetry System, 1973-76," in *The Deep Space Network Progress Report 42-23*, pp. 5–9, Jet Propulsion Laboratory, Pasadena, California, October 15, 1974.

2. Gatz, E. C., "DSN Data Record Generation," in *The Deep Space Network Progress Report 42-20*, pp. 178–181, Jet Propulsion Laboratory, Pasadena, California, April 15, 1974.

3. Friesema, S. E., et al., "Network Control System Project Block III Software," in *The Deep Space Network Progress Report 42-28*, pp. 122–134, Jet Propulsion Laboratory, Pasadena, California, August 15, 1975.

4. Hlavaty, F. M., "Automatic Total Recall Program for Replay of DSN 7-Track DODR's," in *The Deep Space Network Progress Report 42-25*, pp. 137–141, Jet Propulsion Laboratory, Pasadena, California, February 15, 1975.

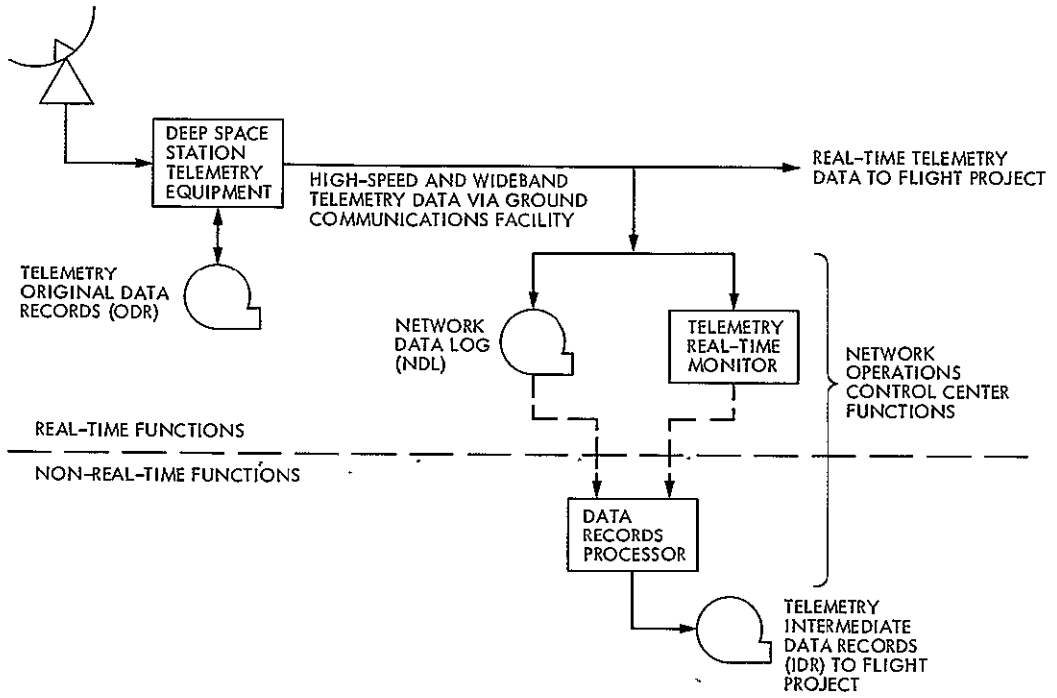

Fig. 1. DSN Telemetry System data record configuration

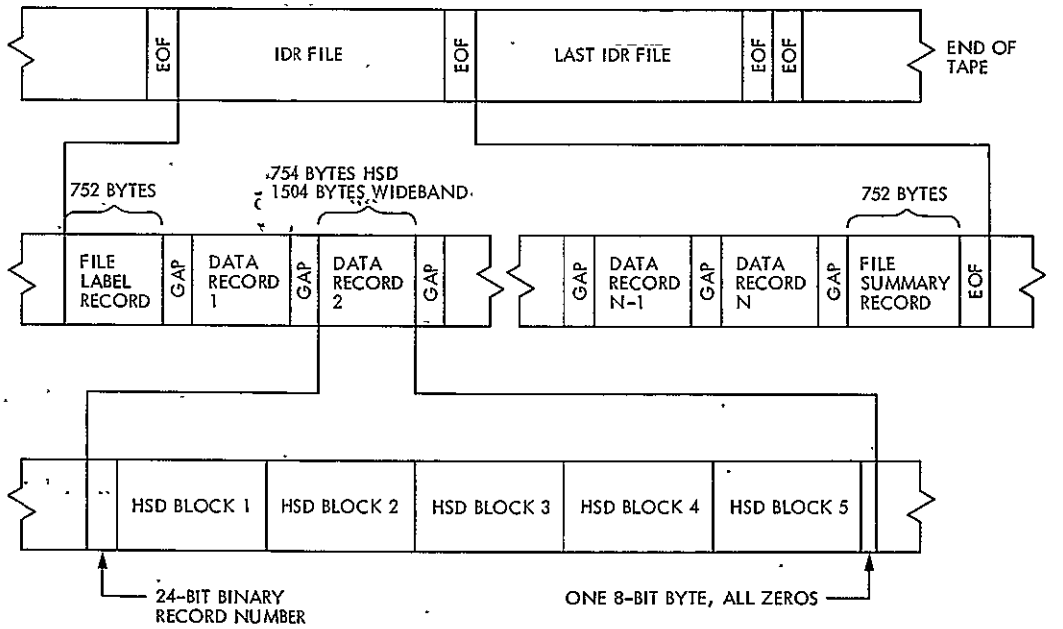

Fig. 2. Telemetry IDR format

Viking Mission Support

D. J. Mudgway
DSN Systems Engineering Section

D. W. Johnston
DSN Operations Section

On April 26, 1976, the Network Operations Control Center was declared available for planetary operations in support of the Viking Project. This final capability in the Network configuration for Viking had been delayed since February with hardware and software problems both in the Control Center and at the Deep Space Stations. The effect of these problems, particularly insofar as they affected production of intermediate data records, the resolution of the problems, and the current status of the Network Operations Control Center in the Viking environment, is given in this article.

Also discussed are the Operational Verification Tests performed to check out the new capabilities and associated procedures. The Viking Project tests supported by the DSN and finally the DSN support of Viking cruise operations, along with some statistics on performance, are included.

I. Implementation

By January 1976, DSN implementation of the planetary configuration for Viking had progressed to the point where thirteen key items remained outstanding. These items were as follows:

(1) FR 2000 recorder to provide high-rate analog playback at all 64-m deep space stations.

(2) Occultation recorders to add two dedicated FR 1400 recorders to DSS 14 at Goldstone and DSS 43 in Australia to allow recording of Viking telemetry data simultaneously with occultation data.

(3) Replace A.B. Dick printers with G.E. Terminettes for higher speed and better reliability.

(4) Command backup printer to provide a second hard copy of all commands transmitted in case of printer failure.

(5) Auto Conscan to provide more accurate pointing of antenna for reception of X-band signals.

(6) Auto Track detectors and recorders to more accurately align RF boresight and verify antenna pointing.

(7) Provide ±1 MHz doppler bias in place of existing 5-MHz bias for better doppler resolution and offset of high doppler frequencies.

(8) Phase II version of Monitor software to accommodate both Block II and Block III receivers.

(9) Original Data Record (ODR) recall software to provide Network Operations Control Center with capability for recall of digital original data records directly from the deep space stations.

(10) Provide the Network Operations Control Center with an operational capability to generate intermediate data records from a Network Data Log and a gap list in conjunction with the original data record recall software.

(11) Permit the Network Control System tracking subsystem to accommodate the ±1 MHz doppler bias change.

(12) Increase the Mars radar X-band transmitter power to 400 kW.

(13) Provide additional technical staff, in lieu of the Station Monitor and Control Consoles (SMC IIA), at DSS 43 in Australia and DSS 63 in Spain to handle Viking planetary operations.

A schedule was developed that showed completion of all items except the FR 2000 and station staffing at DSS 63 by the end of February 1976. These two latter items were to be completed by March 15, 1976. All milestones were met with the exception of the Auto Conscan software at DSS 44 in Australia, the original data record recall, and intermediate data record production. The Auto Conscan problem having to do with an erroneous time change from one day to the next day over midnight was corrected by April 1, but the other two items continued to present new problems.

Early in March, the Network Operations Control Center began delivering intermediate data records to the Project during Viking demonstration test DT-4. During this period, the Network Operations Control Center operations crews were supported heavily by engineering development personnel.

The Network Operations Control Center was then turned over to the operations staff for more routine operational production of intermediate data records. Troubles immediately became apparent both at the stations and in the Network Operations Control Center. As a consequence, the DSN was not ready to support routine operations with the intermediate data records on April 1 as previously committed, and a special task team was established on March 29 to identify and correct the problems. A deadline for accomplishment of this task was set by the Viking Project for April 26.

Turning first to the station end of the system, four areas of improvement were identified as follows:

(1) Use of highest quality certified tape on 9-track high-density digital tape machines.

(2) More rigorous attention to tape recorder alignment and calibration.

(3) Record and playback on the same machines to minimize skew problems.

(4) Use of the new version of the intermediate data record recall software which provided, among other things, the ability to continue the operating in the "search" mode in the presence of a large number of tape read errors.

With these measures in effect at the stations, an immediate improvement in intermediate data record quality was noted, although reliability in the Network Operations Control Center hardware and software continued to remain poor.

Some statistics of intermediate data record production in the first two weeks following this work is given in Table 1.

At this point, the attention of the Task Team turned to the Network Operations Control Center itself, particularly the Network Data Processing Terminal (NDPT) and the Network Data Processing Area (NDPA) shown in Fig. 1. Specific issues considered essential to completion of an operational capability by April 26 were:

(1) Correct the intermediate data record summary statement of the number of data blocks expected and missed in real-time.

(2) Correct the signal level and signal-to-noise ratio statements on the intermediate data record summary.

(3) Provide a correct statement of the recall codes which give the reasons for blocks missed and the type of recall procedures initiated.

(4) Correct several errors in the gap detection logic that gave erroneous number of gaps or garbled messages when particular numbers of gaps were accumulated.

In addition to this work on the software running in the Data Records Processor, it was decided to provide an extra computer and magnetic tape unit in the Network Data Processing Terminal to perform the function of merging the recalled data with the real-time data. This additional "merge" capability permitted recall and merge activity to be carried out simultaneously, a capability considered necessary to meet the operational requirement of intermediate data record delivery within 24 hours of the end of each pass.

The software and hardware additions described above involved two weeks of intensive implementation and testing. Daily status meetings were held to resolve problems and reallocate priorities and resources. By April 21, all the work was completed and had passed through acceptance testing.

On April 22, the DSN Operations organization was briefed on the capabilities then available in the Network Operations Control Center. It was these capabilities, enhanced to some limited extent as time permitted, that the Network Operations Control Team will use to support Viking planetary operations.

With this capability delivered for operational support, the implementation task for Viking may be considered complete.

A number of known problems remain and some as yet unknown problems must be expected as the DSN configuration for Viking matures with operational use.

Improvements will always be desired or become necessary as the operations teams accumulate experience in the mission environment. These facts were recognized in committing the DSN to operational support. To the extent that the exigencies of the Viking mission permit, these issues will be resolved as they arise during the progress of the mission.

II. Testing and Training

A. Operational and Verification Tests

The basic objectives and scope of operational verification tests (OVTs) DSN-Viking Mission Control and Computing Center (VMCCC) system Integration tests (SITs) and ground data system (GDS) Tests are detailed in previous articles in this series (Refs. 1-4).

The OVTs in the period covered here were modified to operationally test the following previously untested items.

(1) 26 m–64 m joint failure mode configurations

(2) Automatic total recall system (ATRS)

(3) Intermediate data records (IDRs)

(4) Modified Viking command procedures

(5) New wide-band data lines (WBDL)

(6) New 64 m Configuration (Code 61) with dual high-speed data lines (HSDLs) to provide 100% redundancy for Viking Lander 1 (VL1) operations.

B. 26 m—64 m Joint Failure Mode Configurations

Four OVTs were scheduled for DSSs 11-14, 42-43, and 61-63, starting in December 1975 and completed in January 1976. The purpose of these tests was to exercise failure mode configurations documented in the Network Operations Plan which minimize data outage in the event of a hardware failure at the 64-m station during operations with three spacecraft. A summary of test results follows:

(1) *DSS 42 and 43 planetary failure mode OVT.* The final OVT was completed and was 100% successful.

(2) *DSS 61 and 63 planetary failure mode OVTs.* The last two OVTs were completed successfully. Success rating was 95% on OVT 3 and 100% on OVT 4.

(3) *DSS 14 planetary OVT.* Another objective of this test was to verify that the wideband data line was performing to specification. Secondary objective was to check performance of newly implemented, but not fully acceptance tested, automatic recall program. Test was completed successfully.

C. ATRS, IDR and Command Procedure OVTs

As described in detail in Sect. I, the ATRS-IDR capability was scheduled to be available for limited procedure generation and check out on Jan. 5, 1976, constituting the initial operator training on the system. Due to numerous hardware and software problems in this very complex system, the training actually started about mid-February.

During the month of March 1976 an OVT was scheduled for each of the nine DSSs along with the Network Operations Control Center (NOCC), using a sequence designed to exercise the recall functions by use of planned data outages, thus exercising all the functions necessary for the production of IDRs. These tests exercised the new telemetry recall program (DOI-5082-OP) and also the new 16-kb/s analog recall capability at the 64 m DSSs utilizing the FR 2000 analog recorders. The tests were

very successful from a training viewpoint, although the number of 100% complete IDRs produced fell short of expectations and could be regarded as approximately 40% overall successful.

During March, IDRs were also produced from selected Viking Orbiter 1 (VO1) and VO2 spacecraft instrument calibration passes. This activity was supported by the personnel "in training," who were assisted and advised by the engineering personnel responsible for the development of the system. These passes resulted in a total of 80 IDRs being produced, 55 of which proved to be faulty.

As detailed in Sect. I, during this period a task team was formed to concentrate on the isolation and rectification of problems in the system, and the April 1, 1976 "fully operational" date for the system was moved to April 26, 1976 to enable the hardware, software, and procedural changes to be implemented. These changes have been extensively tested, and at the time of writing it appears that the system will successfully support the Viking planetary operations.

D. Modified Viking Command Procedures

The original DSN command system capabilities agreed to by the Viking project had a limitation where, in the event of a 360 computer or HSDL failure, the DSS could only manually send commands to the Viking Orbiter spacecraft in blocks of six commands. Further, if the failure occurred when the command system was in the idle 1 mode, the station could not effectively transmit any commands successfully from the preloaded stack. In this instance the DSS had to select "Cal-2" mode to set the "ACTIVE" flag which interrupted the idle sequence, and, as soon as the system went to "idle 2" the commands would immediately be promoted from the active stack and be radiated without the prerequisite idle sequence and therefore be aborted by the spacecraft.

This situation was known just prior to launch and a procedural work around was generated that corrected the situation without requiring any software changes. However, it was agreed not to introduce any changes at that time as the new procedures (both project and DSN) would invalidate the training just then completed. These new procedures were exercised successfully by every shift at every station, and after station on-site training had been completed, are now fully operational. This gives the capability for a DSS to manually recover successfully from an idle 1 situation and also to manually transmit 16 contiguous commands to the Viking Orbiter (VO) spacecraft.

These new command procedures were included in the sequence used for the nine OVTs discussed in Subsection B. The command procedures part of these tests were 100% successful at all stations.

E. New Wide-Band Data Lines (WBDLs)

To meet the Viking dual-station wideband planetary test and flight support requirements from DSSs 43 and 63, NASA Communications (NASCOM) activated a new wideband data channel JPL-Goddard Space Flight Center (GSFC) in early February 1976 via the new RCA domestic satellite routing. This new wideband (WB) service operates at 56 kb/s and provides dual (27.6 kb/s) wideband channels utilizing time division multiplexing (TDM) mode of operation. When first activated in support of the DSN OVTs, difficulties were experienced by NASCOM and the commercial carriers in getting this new facility to meet NASCOM transmission standards; however, the problems were resolved by mid-February 1976 and allowed the DSN and Viking project to meet the required dual-station wideband testing.

F. New DSS Configuration

Requests were received from the Viking Mission Control Team personnel for the DSN to examine the possibility of providing a full back up configuration to and from the overseas 64-m stations for the initial Viking Lander (VL) acquisition and subsequent 20 passes.

A reevaluation of the station configurations resulted in a new configuration (Fig. 1) which allows for processing of Orbiter engineering and science, while simultaneously processing the Lander engineering and science on four separate streams. The Lander data are first priority data during this period with engineering processed on two different streams, one routed via prime high-speed data line (HSDL) and the other via "back-up" high-speed data line. The lander science is also processed on two separate streams routed via high-speed data line and wide-band data line.

The two HSDLs terminate at JPL on two separate computers so that not only is there 100% redundancy on the VL telemetry data streams, but also the JPL-DSS command stream is duplicated from JPL through the station computers to the Command Modulation Assembly (CMA) exciter switch. This means that a failure anywhere from the JPL 360 computer, through the GCF, NASCOM and DSS can immediately be rectified by reselecting one switch at the DSS.

Three OVTs were scheduled to precede Demonstration Test No. 4 (DT-4) from Feb. 21, to Feb. 23, 1976, one for each 64-m station. The objective of these OVTs was to insure that station equipment was operational for DT-4 and operating personnel were exercised by following a realistic time-line simulating the Mars orbit insertion (MOI) and VL initial acquisition of the mission using Code 61 configuration. These tests were completely successful.

III. DSN Support of Additional Viking Testing

In addition to the OVTs discussed above, the DSN supported System Integration Tests (SITs), Ground Data System (GDS) Tests, and Demonstration Test Number Four (DT-4). See Ref. 4. The various tests are described in the following subsections.

A. System Integration Tests

DSS 14 completed SIT testing in November 1975. This report will cover tests for DSS 43 and 63 only. This testing did not occur earlier because planetary implementation was not completed at the overseas 64-m station until early January. A test summary follows:

1. **DSS 43 test.** All test items attempted were accomplished. Due to a number of delays encountered throughout the test, a retest was required.

2. **DSS 43 retest.** The following items were tested: DIS monitor software, Dual S- and X-Band doppler, Telemetry Data Rates not tested on previous SIT test, and the command procedures not exercised on previous SIT test. The SIT retest was successful. All test objectives were met.

3. **DSS 63 SIT test.** All SOE items were exercised, except DODR recall and dual S-band doppler. All items tested met test objectives. The test was considered successful and no retest was required.

SIT testing that could not be accomplished to date will be tested along with delinquent GDS items, in GDS 11.0 test, scheduled for the second week in May '76.

B. Ground Data System Tests

1. **DSS 11 and 14, GDS 5.31 retest.** The prime purpose for the retest was to test failure mode configurations that were not tested on first GDS test. Test objectives were not met and test was considered unsuccessful with a retest required.

2. **DSS 11 and 14, second 5.31 GDS retest.** 90% of test objectives were met. The test was considered successful with no retest required.

3. **DSS 43, GDS 5.32 test.** 95% of test objectives met. The test was considered successful with no retest required.

4. **DSS 63, GDS 5.32 test.** Major test objectives were met. The test was considered successful with no retest required.

5. **DSS 14, 43 and 63, GDS 6.0 test.** This was a 36-hour planetary GDS test designed to test the Ground Data System prior to beginning flight team testing. Only 80% of test objectives were met. Retest was required.

6. **DSS 63, GDS 6.0 retest.** This test did not require full resources originally used. DSS 63 was used for this test because of ease in scheduling time for test, not because items to be tested had failed at DSS 63 on first GDS test. Remaining objectives to be tested were successfully completed with this retest. GDS 6.0 was to be the final GDS test, but due to late implementation of several software programs and additional hardware, additional testing will be required. GDS 11.0, designed for this purpose, is a catchall GDS test and will be completed the second week of May 1976.

C. Demonstration Test Number Four (DT-4)

This was the first major project test exercising planetary configurations and procedures to simulate that part of the mission beginning 52 hours prior to lander touchdown and continued through lander pass No. 9. The total duration of this test was eleven days, but the DSN was required to participate for only three days, beginning at lander touchdown minus 37 hours and continuing through lander initial acquisition pass No. 1.

DSSs 11, 14, 43, and 63 were the participating stations for Demonstration Test Number Four (DT-4). The test was considered 100% successful.

The additional DSN testing and extra effort in preparing for DT-4 paid excellent dividends. The DSN support for DT-4 was rated as excellent by the test conductor. The test was also very productive as numerous items surfaced during the test that will require further refinements, and adequate time is available to accomplish these goals prior to orbital operations.

With the successful completion of DT-4, the DSN and the Viking Project have met an important milestone in the overall readiness of the DSN to support Viking Planetary Operations.

IV. DSN Support of Cruise Operations

Viking spacecraft activities during the cruise to Mars have required a very high level of support from the DSN. The level of activity and complexity of this support have approached that anticipated during planetary operations and have generally exceeded that of the planetary test exercises as well. A summary of the major cruise support activities is provided in the following subsections.

A. Significant Mission Events

Table 1 lists the significant Viking cruise activities that have been supported by the DSN thus far in Calendar Year 1976. Many of the spacecraft activities required the transmission of large numbers of commands and/or processing of multiple telemetry streams, including the highest Viking data rate (16.2 kbits/s) by the stations. These activities also imposed a workload on the Network Operations Control Center (NOCC) and Ground Communications Facility (GCF) far beyond that which would be expected in a normal "quiet cruise."

B. DSS Support

While Table 1 illustrates the magnitude and complexity of the Viking mission events supported by the DSN, Table 2 depicts the extent of support provided by the Deep Space Stations in terms of the total number of passes, tracking hours, and commands transmitted. The only major outage to occur at a DSS since January 1 was an antenna servopump motor failure at DSS 44 that required scheduling adjustments for the period March 9 through 12 to avoid large gaps in Viking coverage. The schedule was adjusted to meet the Viking Project requirement of no gaps to exceed 3 hours, and the impact on operations was minimal.

C. Network Operations Control Center (NOCC) Operations

Implementation of the NOCC continued throughout this reporting period under the Network Control System (NCS) Project. A number of unexpected problems caused delays in subsystem delivery schedules and will result in an incomplete transfer of the NOCC to operations on July 1 as planned. A major effort was concentrated on meeting the DSN commitment to the Viking Project for Intermediate Data Record production, which required the completion of an operable NOCC telemetry subsystem. This requirement was met and IDR production was accomplished in support of Viking operations after March 1. Training of operations personnel to perform the functions involved in the routine generation of IDR products during the prime mission planetary operations was conducted throughout this reporting period and is now 80% complete. Final operations procedures and system problems workarounds were addressed by an IDR investigation team formed by DSN operations and will be completed by May 1.

D. DSN Discrepancy Report Status

Table 3 summarizes failures and anomalies in Viking committed Network resources as documented by the Discrepancy Report (DR) System. The chart covers the first quarter of the calendar year. The station dependent number is unusually high due to continued development of new capabilities being demonstrated for the first time in support of the Viking Project.

The remaining open DR's are under active investigation and are of no immediate impact to operations.

References

1. Mudgway, D. J., and Johnston, D. W., "Viking Mission Support," in *The Deep Space Network Progress Report 42-26*, pp. 8–16, Jet Propulsion Laboratory, Pasadena, Calif., April 15, 1975.

2. Mudgway, D. J., et al., "Viking Mission Support," in *The Deep Space Network Progress Report 42-27*, pp. 10–27, Jet Propulsion Laboratory, Pasadena, Calif., June 15, 1975.

3. Mudgway, D. J., and Johnston, D. W., "Viking Mission Support," in *The Deep Space Network Progress Report 42-30*, pp. 57–60, Jet Propulsion Laboratory, Pasadena, Calif., Dec. 15, 1975.

4. Mudgway, D. J., et al., "Viking Mission Support," in *The Deep Space Network Progress Report 42-29*, pp. 10–14, Jet Propulsion Laboratory, Pasadena, Calif., Oct. 15, 1975.

Table 1. Intermediate data record statistics

Date	Pass	DSS	Rate, bits/s	Blocks received in real-time	Blocks missed in real-time	Blocks missing after recall	Percent delivered
4/8/76	DT-7	43	8K/2K	23393	Not available	3	99.9
			8K	16160		9	99.9
	DT-7	43	250	1118		0	100
			250	529		0	100
4/11/76	DT-7	43	2K/8K	23010		6	99.9
			2K/8K	6923		0	100
			250	274		0	100
4/12/76	237	63	2K	10628		47	99.6
			8K	23650		109	99.6
			8K	5278		9994	
			2K	3628		2	
4/11/76	236	63	2K	22184		82	99.6
4/14/76	219	63	2K	9981	101	0	100
4/15/76	220	63	2K	8716	10	0	100
			2K	4798	7	0	100
			8K	23755	30	1	99.99
			2K	13941	1	0	100
4/16/76	221	63	1/2K	6714	34	34	99.496
			8K	73343	850	92	99.875
4/17/76	241	14	8K	80895	2	2	99.998
	252	63	8K	38092	2034	13	99.96
			1/2K	8132	30	30	99.63
4/20/76	DT-4R	63	16K	19021	91	21	99.89
4/21/76	DT-4R	14	8K	47775	3250	13	99.98

Blocks Received in Real-Time means the number of wideband blocks received on the Network data log in real-time as the data are delivered to the Mission Control and Computing Center.

Blocks Missing After Recall means the number of blocks which were not available after one recall operation from the digital original data record at the station.

Blocks Recalled means the number of blocks recalled from the station digital original data record by the Network Operations Control Center recall process or working in conjunction with the ATRS recall software at the station.

Percent Delivered means the percentage of total blocks on the digital original data record that were delivered on the intermediate data record.

Table 2. Viking significant events supported by the DSN

Date	Spacecraft	Activity
Jan. 5	Orbiter 1	Mars atmospheric water detector (MAWD) calibration
Jan. 5	Lander 2	Tape recorder maintenance
Jan. 6	Orbiter 1	High-gain antenna (HGA) calibration utilizing DSS 14 X-Band capability
Jan. 7	Lander 1	Tape recorder maintenance
Jan. 7	Orbiter 1	MAWD calibration
Jan. 8	Lander 1	Gas chromatograph mass spectrometer (GCMS) bakeout number 2
Jan. 13	Lander 2	GCMS oven characteristics sequence
Jan. 14	Lander 1	GCMS bakeout number 2
Jan. 14	Orbiter 2	X-band telemetry experiment
Jan. 15	Lander 2	Tape recorder maintenance
Jan. 16	Lander 1	Tape recorder maintenance
Jan 16 & 17		X-Band telemetry experiment
Jan. 20	Lander 2	GCMS oven characteristics sequence
Jan. 28	Lander 1	GCMS oven characteristics sequence
Jan. 31	Lander 2	GCMS bakeout
Feb. 2	Lander 1	GCMS oven characteristics sequence
Feb. 3	Lander 2	Tape recorder maintenance
Feb. 4	Lander 1	MAWD calibration
Feb. 6	Lander 2	GCMS vents
Feb. 7	Lander 1	GCMS bakeout
Feb. 9	Lander 1	Infrared thermal mapper calibration
Feb. 9	Orbiter 1	Visual imaging subsystem (VIS) scan calibration
Feb. 10	Lander 2	Power conditioning sequence (battery charge/discharge)
Feb. 11	Orbiter 2	MAWD calibration
Feb. 11	Lander 2	Tape recorder maintenance
Feb. 12 & 13	Lander 1	GCMS bakeout
Feb. 13	Orbiter 2	Infrared thermal mapper calibration and VIS scan calibration
Feb. 15	Orbiter 2	VIS scan calibration playback
Feb. 17	Lander 1	GCMS vents 4 and 5 close and atmospheric analysis
Feb. 18	Orbiter 1	Tape recorder maintenance and HGA calibration
Feb. 19	Lander 1	Power conditioning sequence
Mar. 8	Orbiter 1	MAWD calibration
Mar. 8	Orbiter 2	Tape recorder maintenance
Mar. 10	Lander 1	Tape recorder maintenance
Mar. 10	Orbiter 1	HGA calibration
Mar. 11	Orbiter 2	MAWD calibration
Mar. 11	Lander 2	Tape recorder maintenance
Mar. 15	Orbiter 2	Accelerometer and gyro calibration
Mar. 16	Orbiter 2	Photo calibration
Mar. 16	Orbiter 1	Tape recorder maintenance
Mar. 18	Orbiter 1	Accelerometer and gyro calibration
Mar. 22	Lander 1	Inertial reference unit (IRU) number 2 calibration
Mar. 23	Orbiter 1	Photo calibration
Mar. 22 - 24	Orbiter 1 & 2	Playback of photo calibration data
Mar. 26	Lander 2	IRU number 2 calibration
Mar. 27	Orbiter 1	HGA calibration
Apr. 11	Orbiter 1	Onboard computer software update
Apr. 12	Orbiter 1	Scan calibration
Apr. 14	Orbiter 2	Onboard computer software update
Apr. 15	Orbiter 2	Scan calibration
Apr. 16	Orbiter 2	VIS picture playback
Apr. 16	Lander 2	Tape recorder maintenance
Apr. 17	Orbiter 1	VIS playback
Apr. 17	Lander 1	Battery charge and tape recorder maintenance
Apr. 18	Orbiter 2	Very long baseline interferometer (VLBI) with quasar source

Table 3. DSS support of Viking cruise operations

Month	DSS	No. of passes	Hours tracked	Commands transmitted
January	11	10	71:30	100
	12	25	211:26	245
	14	15	112:29	324
	42	8	35:55	0
	43	24	150.09	21
	44	27	183.36	20
	61	14	107:55	191
	62	36	309:29	345
	63	12	117:55	0
Monthly total:		171	1300:24	1246
February	11	2	04:54	0
	12	32	278:52	564
	14	11	99:38	15
	42	31	139:33	21
	43	17	124:05	59
	44	11	48:25	13
	61	4	37:51	0
	62	32	290:13	624
	63	24	219:47	556
Monthly total:		164	1243:18	1852
March	11	15	71:16	17
	12	24	171:31	302
	14	17	124:23	0
	42	17	62:33	0
	43	20	101:23	0
	44	26	131:04	197
	61	7	67:03	0
	62	31	276.30	259
	63	32	299:21	338
Monthly total:		189	1305:04	1113
Report total:		524	3848:46	4211

Table 4. Viking Discrepancy Reports, Jan. 1 to Mar. 31, 1976

Resolution	DSS 11	DSS 12	DSS 14	DSS 42	DSS 43	DSS 44	DSS 61	DSS 62	DSS 63	MIL 71	Network	Communications	NDPA	NOCA	Total
Facility dependent	21	24	106	29	64	19	24	24	53	16	5	24	20	28	457
Facility independent	4	5	8	7	3	0	0	3	3	1	2	6	5	12	59
Other or unavoidable	2	2	2	0	1	0	0	1	0	1	9	4	1	2	25
Total DRs closed	27	31	116	36	68	19	24	28	56	18	16	34	26	42	541
Total DRs generated	29	33	128	38	75	19	26	29	81	18	17	34	41	46	614
DRs open as of Mar. 31, 1976	2	2	12	2	7	0	2	1	25	0	1	0	15	4	73

NDPA = Network Data Processing Area
NOCA = Network Operations Control Area

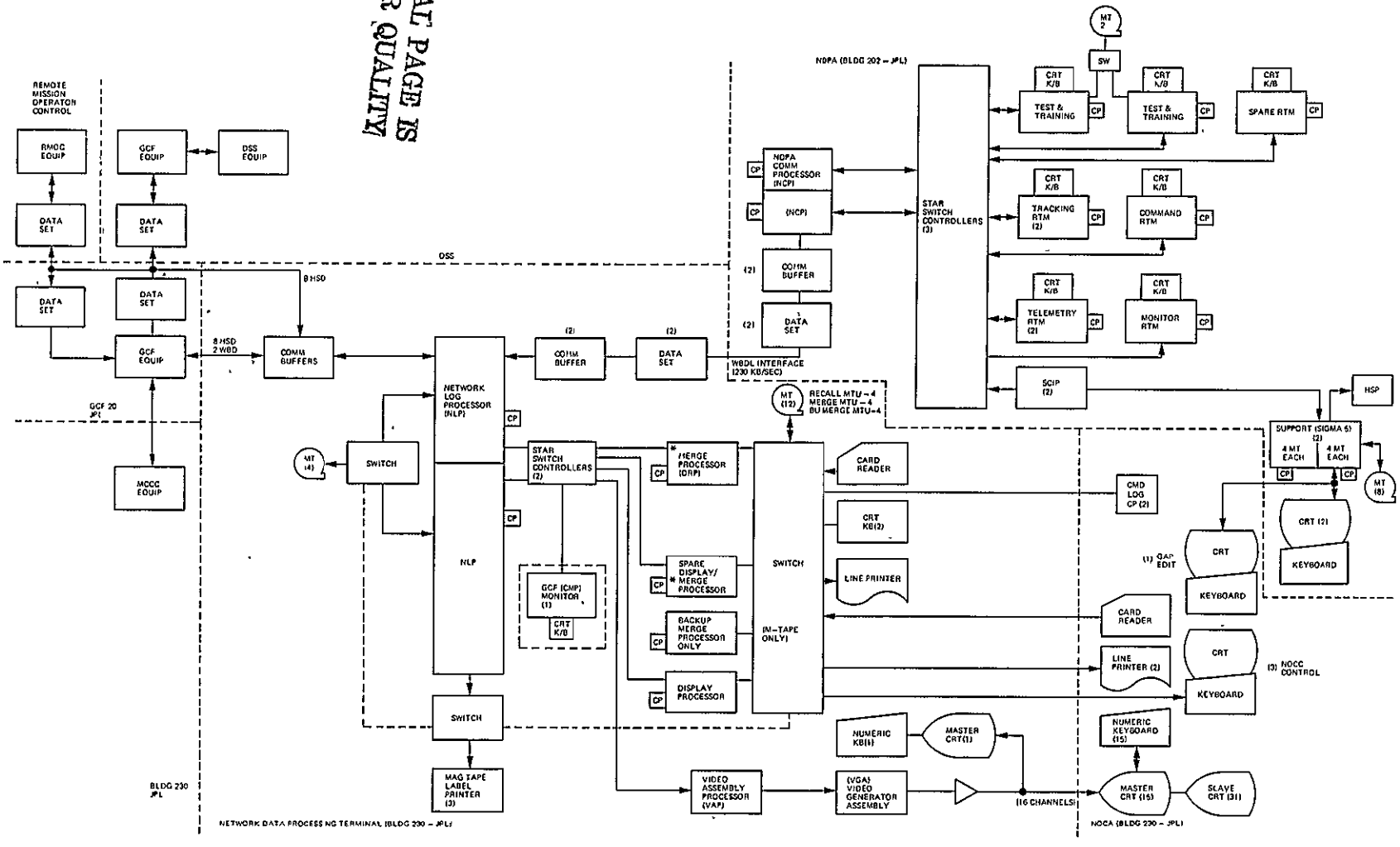

Fig. 1. Network Operations Control Center block diagram, 1976 to 1977

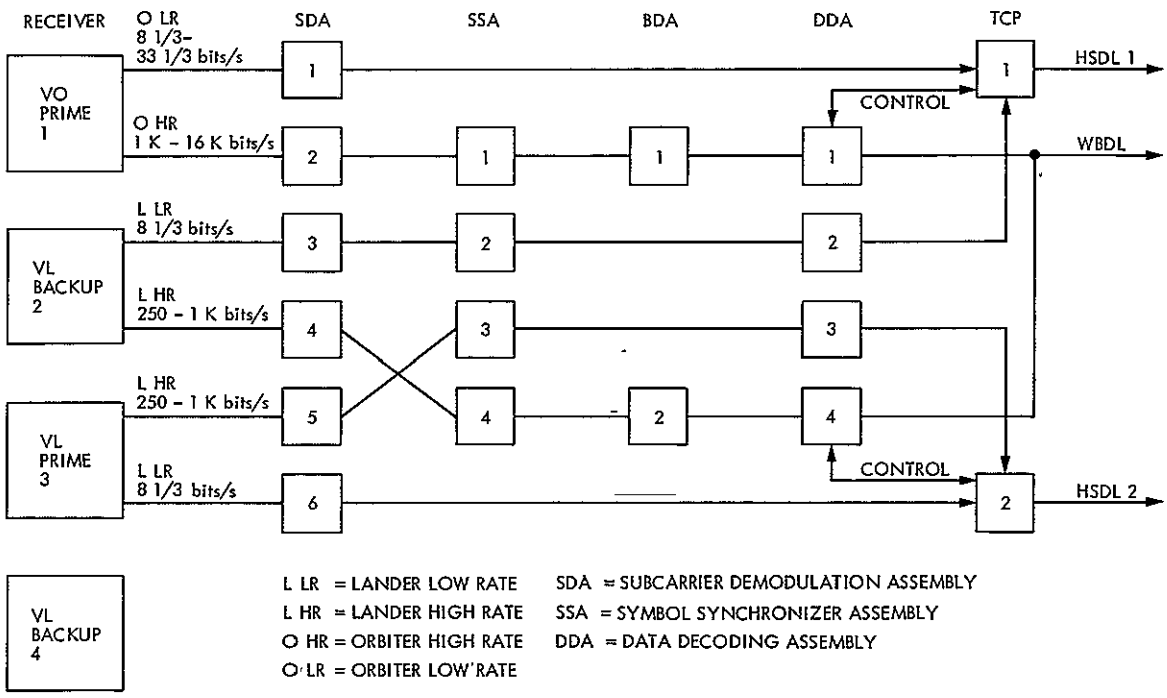

Fig. 2. Station configuration for four data streams

Pioneer 10 and 11 Mission Support

R. B. Miller
DSN Systems Engineering Office

Possible improvements in the Deep Space Network and their potential effect on the telecommunications limit of Pioneer 10 and on Pioneer 11 Saturn encounter are discussed.

I. Introduction

The Pioneer 10 spacecraft is continuing to return data on new regions of the solar system never before explored by a man-made object. Project estimates are predicting a spacecraft useful life out to 1983. With existing DSN configuration at a 64-m station, the telecommunications limit at minimum bit rate will be reached in mid-1980 at a range of about 22 Astronomical Units (AU) which is 2 AU beyond the orbit of Uranus. It is therefore interesting to explore how potential improvements in performance at DSN 64-m stations might enable extending the telecommunications limit closer to the projected end of useful spacecraft life.

Performance improvements are also of vital interest to Pioneer 11 Saturn encounter where the highest data rate possible is desired to return full imaging, but with a telecommunications link designed for Jovian distances. The problem is compounded by the nearness of the Saturn encounter to solar superior conjunction.

Performance improvement at 26-m stations is of interest for Pioneer 11 coverage improvement between now and the Saturn encounter.

Figure 1 shows the predicted telecommunications performance for both 26- and 64-m Deep Space Stations. Solar conjunction, elevation, and spacecraft antenna-pointing can cause reduction in performance from the values on the chart.

As Pioneer 10 approaches the limit of telecommunications, the two Helios spacecraft may still be alive and Pioneer Venus still orbiting Venus while both Mariner Jupiter Saturn (MJS) 1977 spacecraft are between Jupiter and Saturn. The fact that the Deep Space Network will most likely still be oversubscribed in 1979 through 1981 is important to keep in mind when considering some of the possible ways of extending the telecommunications limit.

II. Projected Spacecraft Life

Pioneer 10 is projected to have sufficient attitude-control propellant (used for antenna-pointing) out to 1989. The 1983 useful end of life is determined from the projected Radio-Isotope Thermoelectric Generator (RTG) degradation to the minimum point for the operation of the science instruments.

There are also some practical problems to be solved in maintaining control of the spacecraft with the large round-trip light times in the latter part of the mission.

Pioneer 11 RTG prediction is to reach the minimum power for science operation in 1984.

III. Potential Performance Improvements at the 64-m Deep Space Stations

The practical (existing technology) prospects for improving the 64-m performance are listed in Table 1.

The potential improvement is the difference the listed item would make in the telecommunications limit compared to the existing 64-m configuration (12-Hz loop, 22 K diplex cone) expressed in dB. The range ratio is the performance improvement translated to a factor which can be used to multiply the geocentric range. It is convenient to express the improvement in range as a ratio because some of the items are multiplicative. For example, if we used items (a) and (c), the range ratio would be $1.12 \times 1.09 = 1.22$, which would extend the range to 1.22×22 AU $= 26.8$ AU. Items (b), (c), and (d) are all different possible improvements in system temperature and do not add, while items (a), (e), and (f) are multiplicative along with any one of the items from (b) through (d).

Item (a) is available now in the operational configuration, and it is planned to use it. The 1.0 dB improvement extending the range to 24.6 AU is only an estimate which it is planned to refine by some testing on Pioneer 10 in the near future.

Item (b) is a special "listen-only" (no uplink transmission to the spacecraft) configuration currently available, but adds serious operational constraints when the total DSN loading is taken into account. First, a second station (26-m) would have to simultaneously view the spacecraft in order to provide commanding. Second, getting into this configuration requires extra station time before and after each pass.

Items (c) and (d) involve implementing known possible improvements to the operational receiver front ends, where (c) would be the usual operation configuration of transmitting to the spacecraft while receiving (diplex mode) which would have no operational constraints, where (d) would be the new equivalent of item (b) with the same operational constraints as item (b).

The improved cone is currently in the DSN program for completion prior to 1979; however, it is subject to being dropped from DSN plans because of tightening resource constraints and the need to give priority to implementations required for prime mission events.

Items (e) and (f) are possible structural improvements to the 64-m antennas which might be reasonable from an engineering standpoint for a 1980 implementation if they could be accommodated within the total NASA program; however, mission support requirements of MJS might preclude allowing the extended station downtime required for the first station until late 1981-early 1982. These improvements are, however, not in the current DSN plans until post-1985.

IV. Summary of Potential 64-m Performance Improvement Benefit to Pioneer 10

With the current 64-m operational configuration, Pioneer 10 should reach its telecommunications limit at about 22 AU (geocentric) some time in the first half of 1980. Use of the available 3 Hz loop in the Block IV receiver should extend this to about 24.6 AU reached in early 1981. Use of a planned improved receiver front end in the usual diplex mode would extend the potential range to 26.8 AU reached at the end of 1981 or early 1982. Shaped hyperbola and extension to 70 meters (not currently in the DSN plan early enough to benefit Pioneer 10) would further increase the potential range to 31.3 AU, which (extrapolating the attached curve a bit too far) would probably be early 1983, coincident with the projected useful spacecraft life. The listen-only modes, items (b) and (d), would not be recommended because of operational impact.

V. Effect on Pioneer 11 Saturn Encounter of 64-m Performance Improvement

Pioneer 11 will be 8 degrees from the Sun at Saturn encounter, and the desired bit rate is 1024 bits/s. It can be seen from the attached curve that even with the planned improvement of item (c)—an 18.5K diplex cone—it will probably not be possible to achieve 1024 bits/s. With the listen-only (14.5K) mode of item (d), the 1024 bit rate might become marginally useful. The operational constraints of requiring a 26-m simultaneously for uplink would probably be practical for on the order of one week of the 60-day Saturn encounter period.

VI. 26-m Performance Improvements and Their Effect on Pioneer 11

An experimental lower noise cone has been implemented on one of the Goldstone 26-m antennas which has provided an 0.7-dB improvement as well as a 3-Hz loop in the receiver which provided an additional 1.5 dB improvement. Using the left side of the attached figure, you can see this should extend the coverage from the single 26-m station for Pioneer 10 at 16 b/s for one year to the end of this year. However, Pioneer 10 drops off rather quickly and no further 26-m improvement appears practical in a time scale to benefit Pioneer 10. A very small performance improvement would enable 26-m coverage of Pioneer 11 at 16 b/s out to Saturn encounter in September 1979. For this reason, an activity has been initiated to install two other 3-Hz loops that were available at an Australian and a Spanish 26-m station for a 1.5-dB improvement. There are no additional 26-m experimental lower noise cones available, and it is doubtful the DSN program will be able to accommodate building any more in the Pioneer 11 time scale.

Table 1. 64-m Improvements

Item	Potential improvement	Range ratio
(a) 3 Hz loop in receiver	1.0 dB	1.12
(b) Current listen-only (18 K)	0.8 dB	1.11
(c) Improved cone: Diplex (18.5 K)	0.7 dB	1.09
(d) Improved cone: Listen-only (14.5 K)	1.8 dB	1.23
(e) Shaping hyperbola	0.5 dB	1.06
(f) Enlarge to 70-meter	0.8 dB	1.10

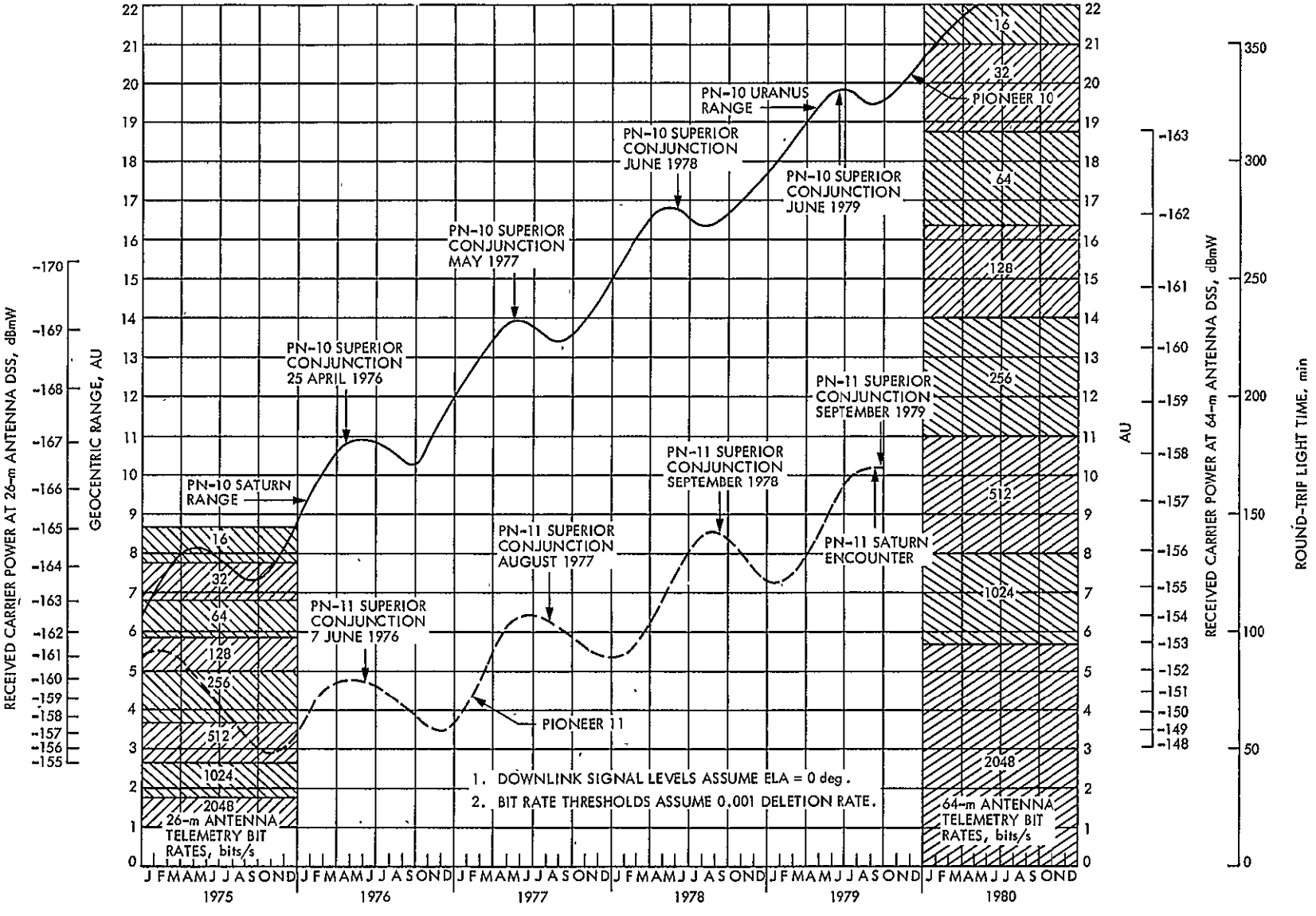

Fig. 1. Downlink performance estimates for Pioneers 10 and 11

Helios Mission Support

P. S. Goodwin
DSN Systems Engineering Office
W. G. Meeks
R. E. Morris
Network Operations Office

With Helios-1 completing its third perihelion and Helios-2 passing its first perihelion, much valuable scientific data were obtained about the inter-Earth-Sun regions. The first solar occultation of Helios-2 is anxiously awaited as the next important mission phase. Preparations are underway for Helios-2 first entry into solar occultation in mid-May 1976. This article reports on the activities around Helios-1 and -2 perihelions.

I. Introduction

This is the ninth article in a series that discusses Helios-1 and Helios-2 mission support. The previous article (Ref. 1) reported on Helios-2 prelaunch and launch activities, spacecraft maneuvers, Helios-1 and Helios-2 cruise operations, and DSN-STDN cross-support status. This article covers Helios-1 third perihelion, Helios-2 first perihelion, spacecraft TWT and ranging anomalies, Helios DSN-STDN cross-support, and DSN performance.

II. Mission Operations and Status

A. Helios-1 Operations

As reported in the last Helios Progress Report (Ref. 1), the Helios-1 spacecraft ranging system failed to respond on 28 January 1976. Ranging became possible again on 17 March 1976 due to higher spacecraft temperature. The problem was, as suspected, associated with the spacecraft ranging transponder temperatures, and corrected itself as the spacecraft approached the Sun. (This problem is explained more fully in this article, Subsection IV-B.)

On day-of-year (DOY) 82 (22 March 1976), seven days before the third perihelion, a spacecraft anomaly occurred. At approximately 0726 GMT, during a station gap, Experiment 1 switched OFF. Both high voltages for Sensor A and Sensor B of Experiment 10 dropped to zero, and the read-in mode (DM4, FM3—which should have covered the gap) stopped. The cause of this anomaly is undetermined at this writing.

A similar incident occurred on DOY 82 in 1975 (23 March 1975) with Experiment 10 (high-voltage breakdown). The conclusion then was that an internal spike into

or out of Experiment 10 was the cause of the problem. Both Experiments 1 and 10 were reconfigured, and the memory checked. All are presently performing correctly.

On Monday, 29 March 1976 at 1600 GMT (Launch +475 days), Helios-1 successfully passed its third perihelion with a minimum distance from the Sun of 0.31 AU, and at a distance from the Earth of 0.933 AU. The temperatures experienced by the spacecraft were slightly higher than those during the second perihelion. The spacecraft system's performance was excellent, and the Helios Project Office expressed confidence in obtaining a fourth perihelion without problems.

The switch to the high-power mode was successfully performed on DOY 97 (6 March 1976) at 0805 GMT. The spacecraft is presently using its high-gain antenna, and is spinning at 60.235 rev/min.

B. Helios-2 Operations

In early February 1976, while Helios-2 was in its cruise phase, the spacecraft team detected a slight decrease in the solar aspect angle. To keep the spin axis of the spacecraft within one degree around the nominal position, two attitude correction maneuvers were performed on DOY 51 (20 February 1976) and DOY 55 (24 February 1976). The solar aspect angle was changed from 89.0 degrees to 89.5 degrees.

Helios-2 was transmitting from traveling wave tube (TWT)-1 on high power when, on DOY 99 (8 April 1976), the hard limit for the helix (tube element) current was reached. When the limit was reached, TWT-1 was switched to the medium power mode. All TWT-1 parameters for medium power mode were normal, but after careful analysis of the situation the transmitter was commanded to TWT-2, medium power. It was also decided by the Spacecraft Operations Team that Helios-2 would remain in medium power mode until the end of the primary mission. TWT-2 has subsequently (20 April) been commanded to the high-power mode and experienced the "out of limits" helix current condition also. (The TWT was allowed to remain in high power for only 45 minutes.) Presently, the Helios-2 spacecraft is transmitting from TWT-2, medium power. It is unclear at this time if the higher temperatures now being felt by the spacecraft have any relation to the helix current increase.

Helios-2 passed its first perihelion on Saturday, 18 April 1976, at 0229 GMT (Launch +92 days) with a minimum distance from the Sun of 0.29 AU. The spacecraft was operating in the medium power mode, high-gain antenna. The Helios-2 spacecraft came nearly 3-million kilometers (2-million miles) closer to the Sun than its predecessor, Helios-1, and experienced approximately 10% more heat. All spacecraft subsystems and experiments performed well during the perihelion, and continue as the spacecraft approaches its first solar superior conjunction. Data returned by the two Helios spacecraft will be correlated with data from Pioneers 10 and 11 (in the outer reaches of the solar system).

C. Spaceflight Tracking and Data Network (STDN) Cross-Support

Meetings were held on 18 and 19 March 1976 at Goddard Space Flight Center (GSFC) with GSFC and JPL personnel in attendance. The purpose of these meetings was to discuss the DSN-STDN cross-support for the Helios Project and to finalize the DSN-STDN Interface Agreement. Also, some operational problem areas that required attention were discussed. A better understanding of each network's problems, capabilities, and limitations was an important aspect of these meetings.

THE DSN-STDN Interface Agreement for Cross-Support for Project Helios was distributed on 15 April 1976. The purpose of this document is to establish the necessary interfaces and operational plans to provide tracking of the Helios-1 and Helios-2 spacecraft by the STDN and analog recording of Helios telemetry data.

The STDN-Madrid station has been providing telemetry recording cross-support for the Helios-1 spacecraft since 15 January 1976. On 9 April, the downlink signal level reached recording threshold and the Madrid support was suspended until the link margin comes above threshold again (approximately September/October 1976).

The Goldstone STDN station, previously down for a major reconfiguration, became operational on 6 April, after an engineering test was conducted. The results at the time of the test were inconclusive because the analog magnetic tape recordings could not be properly evaluated in real-time. Results of STDN (MIL-71)[1] reduction/comparisons of the Goldstone STDN and Echo (DSS 12) analog magnetic tape recordings are not yet complete. Helios passes since the test have been supported from the Goldstone STDN station. The DSN will continue to request cross-support from this STDN station until recording threshold is reached (estimated for mid-May 1976).

[1] DSN equipment located at S/C Compatibility Test Station at MILA, Cape Canaveral.

An engineering evaluation of sending in real-time a STDN receiver baseband output (i.e., the data modulated 32-kHz Helios telemetry subcarrier) to a DSN station via intersite microwave is now in progress. The purpose of this test is to determine if the losses we presently experience in the " STDN/record/STDN(MIL-71) reduction " mode can be minimized, therefore increasing the data quantity and quality to be derived from the STDN cross-support. This evaluation is expected to be completed during May 1976.

D. Actual Tracking Coverage Versus Scheduled Coverage

This report covers tracking activities for a 65-day period for the Helios-1 and Helios-2 spacecraft, from 6 February through 11 April 1976. Operations during this period include cruise, inferior conjunctions of both spacecraft, and Helios-1 third perihelion.

Helios-1, sharing equal priority with Pioneers 10 and 11, was tracked 125 times for a total of 704 hours. The Helios-1 allocation was approximately one-third of the total Pioneer/Helios-1 allotment. This represents a 9 percent increase in the number of passes, and 70 percent increase in hours tracked. The average pass duration continues to linger around 5.6 hours. Overlapping view periods and heavy demands on the Network, causing split-pass coverage, is responsible for this figure. (This type of tracking coverage for extended mission spacecraft is likely to continue.) Owing to critical phases of the Helios-1 mission (inferior conjunction and third perihelion), the 64-meter subnetwork accounted for 381 hours, or approximately 54 percent of the total of 704 hours. This represents an increase of 232 hours or 150 percent increase in 64-meter coverage.

In addition to the DSN tracking coverage, the Spaceflight Tracking and Data Network, controlled from the Goddard Space Flight Center (GSFC), also tracked the Helios-1 spacecraft 18 times for a total of 79 hours. Analog tape recordings of the spacecraft telemetry data are processed at STDN (MIL-71) and sent to JPL via High-Speed Data Line (HSDL) to be incorporated in the Master Data Record (MDR), which is sent to the Helios Project for use in the production of Experimenter Data Records.

Helios-2, enjoying equal priority with the two Viking spacecraft, is presently in prime mission phase approaching its first solar encounter (perihelion). The total tracking coverage shared between the two Viking and Helios-2 spacecraft was 574 passes, equaling 5248 hours. The Helios-2 portion was approximately 45 percent of the total, or 246 passes and 2149 hours of tracking coverage. This represents 100% of required DSN coverage for the Helios-2 spacecraft.

The Spaceflight Tracking and Data Network tracked Helios-2 only once during this period for 4 hours. This track was in parallel with DSN coverage and was part of an engineering evaluation of the Goldstone STDN station performance.

After the prime mission phase of Helios-2 (approximately mid-May 1976), tracking priority will equal that of Helios-1 and Pioneers 10 and 11. DSN tracking coverage is expected to decrease during the next reporting period due to this priority change and increased Viking planetary activities.

III. Special Helios Tests

The Helios-1 spacecraft ranging system failed on 28 January 1976 (Ref. 1). In an attempt to find the cause, a special Helios-1 ranging channel test was performed on 5 March 1976 at DSS 14. For this experiment, the ranging uplink channel was modulated continuously with a coherent 250-kHz sine wave instead of the normal pseudo-random code ("square wave"). The Precision Signal Power Measurement (PSPM) equipment was then used to look for any sidebands at the fundamental (S-band frequency minus 250 kHz) first and second harmonics (see Fig. 1). The visual interpretation of the CRT-displayed power spectrum showed no ranging sidebands. The solution to the Helios-1 spacecraft ranging problem had to wait until 17 March (see Subsection IV-B, this report).

On behalf of Helios passive experiments 11 and 12 (Celestial Mechanics and Faraday Rotation, respectively) the Helios Project requested that the Mu-2 ranging system be used at the Goldstone Mars Station (DSS 14) instead of the Planetary Ranging Assembly (PRA) during perihelion and occultation phases of Helios-1 and Helios-2. At very small Sun-Earth-Probe (SEP) angles, the Mu-2 system has greater accuracy than the PRA. An implementation schedule was formulated (see Fig. 2) and set in motion. All milestones were successfully met and the Mu-2 became the prime ranging equipment for Helios and Viking at DSS 14, and will continue to be prime until January 1977.

IV. DSN System Performance for Helios

A. Command System

Helios command activity has continued to rise during this report period. With Helios-2 still in prime mission and Helios-1 experiencing its third perihelion, this

increase came as no surprise. An 83% increase, or 11,085 commands, were sent to the two Helios spacecraft during the months of February and March. This boosts the cumulative command totals to 31,376 for Helios-1 and 9,059 for Helios-2. Two Command System aborts occurred during February—none in March. The first abort was caused by a procedural error. Command modulation was turned off 10 minutes early. It occurred on 8 February with the Helios-1 spacecraft.

The second Command System abort, on 27 February at DSS 61 with Helios-2, was due to a loose pin in the configuration register card file. The Command System was inoperative for 31 minutes while the repair was made.

The Command System downtime due to equipment problems was 24.7 hours for the two-month period. Four outages exceeded one hour, the longest being 7 hours and 50 minutes. The Command Modulator Assembly (CMA) failed early in the pass and could not be restored. This downtime is significantly higher (approximately 400%) than the last report period. However, because of Network loading, redundant stations and/or equipment strings not being available in some cases, longer than normal Command System downtimes resulted.

B. Tracking System

Solutions to two significant ranging anomalies, reported in the last Helios Progress Report (Ref. 1) were discovered during this report period. It had been noted earlier (first observed on 12 December 1975 while ranging over the Weemala Station at Tidbinbilla, Australia (DSS 42) on Helios-1) that sometimes the pseudo digital range versus integrated doppler (DRVID) values for a series of range acquisitions during a single pass would differ from each other by a multiple of 1024 range units (the half-period of the clock component). With analysis, it was decided that this could be caused by the station transmitting a ranging code inverted from what it should be. This theory was confirmed by observing the failure in real time and confirming that the station had inadvertently instructed the Planetary Ranging Assembly (PRA) to send an inverted code. The Block III and Block IV systems are inverted in respect to each other, as are the Helios and Viking ranging codes. This understandably results in a confusing operational situation, complicated by "Load and Go" countdowns.

The second ranging problem was the Helios-1 spacecraft loss of ranging capabilities observed on 28 January 1976 (Ref. 1). This was the second time that Helios-1 spacecraft ranging system had ceased to respond. The Spacecraft Analysis Team theorized that the failure was associated with spacecraft temperature. On DOY 77 (17 March 1976), it was possible again to perform ranging on Helios-1. In analyzing the history of the Helios-1 ranging performance, the spacecraft team stated that the ranging transponder does not function when the Very Stable Oscillator (VSO) temperature is between 5°C and 18°C. The performance is good above and below this temperature region.

Two reports on the "Effect of the Sun on Doppler Noise" were distributed in February by the DSN Operations Analysis Tracking Subgroup. The first describes the analysis performed on the data collected during the second Helios-1 superior conjunction. The second report presents the somewhat surprising hypothesis that the solar contribution to doppler noise is proportional to the total electron content along the station-spacecraft line-of-sight. The results of this latter study are found elsewhere in this DSN Progress Report, entitled, "Doppler Noise Considered as a Function of the Signal Path Integration of Electron Density" (Ref. 2).

C. Telemetry System

The DSN has considerable data on 64-meter station performance when tracking spacecraft in angular proximity of the Sun, but little was known of 26-meter performance in this region. The Helios-1 and Helios-2 inferior conjunctions (March 14 and March 24, respectively) presented an excellent opportunity to gather this kind of data. These data will be added to other data base information to formulate a telemetry performance model under high solar noise conditions. The objective is to increase reliability of telemetry predictions during low Sun-Earth-Probe angles. A plan was devised by the DSN Telemetry Analysis Subgroup to select, gather, and analyze the required parameters. Two special data types were selected as inputs. The first consisted of special system noise temperature stripchart recordings. The second data type was the gathering of short periods of one-per-second doppler data and unfiltered automatic gain control (AGC). These data were gathered during times when the SEP angle was less than 15 degrees. The data were shipped to JPL and analyzed by the DSN Telemetry Analysis Subgroup.

Quick-look reports were distributed on each inferior conjunction finding. Preliminary conclusions were (1) the signal level (SL) degradation and the signal-to-noise ratio (SNR) degradation are due to decreased receiver loop SNR margin causing increased phase jitter, and (2) the experienced System Noise Temperature (SNT) correlates very closely with the predicted values.

The "Load and Go" station countdowns are still suspected to be a factor in the number of out-of-limits SL and SNR residuals. Not only Helios, but all projects are experiencing these difficulties.

IV. Conclusions

As the two Helios spacecraft speed past the Sun, the subsystems and experiments are performing well, sending to Earth valuable data about our solar system. Although each spacecraft has experienced some anomalies with TWTs, mission objectives and performance have not been degraded. The Helios-1 spacecraft ranging subsystem is functioning again and the Helios Project is looking forward to its fourth perihelion.

Agreements were published and interfaces established regarding DSN-STDN cross-support. A meeting at GSFC did much to smooth out engineering and operational difficulties. On-going efforts are continuing in the evaluation of the DSN-STDN cross-support data.

The Mu-2 ranging equipment will be prime at DSS 14. This equipment promises to give better resolution at very small Sun-Earth-Probe (SEP) angles, needed for Helios spacecraft Experiments 11 and 12.

The Helios-1 and Helios-2 inferior conjunctions provided an opportunity to gather data pertaining to 26-meter station performance during small SEP angles. Specific data were collected and will aid in the formulation of a performance model for better 26-meter performance predictions.

With the end of prime mission of Helios-2 (May 1976), the DSN tracking priority of both Helios spacecraft will equal that of Pioneers 10 and 11. This, coupled with Helios spacecraft distance from Earth being greater than 1 AU, will likely lead to a decrease in DSN tracking coverage. The telemetry recording threshold is almost reached using STDN stations, and little support can be expected from this source until September/October. However, the news that the German Government plans to modify the Weilheim Telecommand Station for receiving capability was very happily received by the Helios Project.

Acknowledgments

The authors wish to thank the following members of the Network Operations Analysis Group for their contribution of periodic Network Performance Reports:

Command: R. Gillette, R. B. Frampton, W. L. Tucker

Telemetry: R. Allis, J. W. Hendricks, C. Lunde

Tracking: A. L. Berman, L. Bright, R. S. Schlaifer, G. L. Spradlin

References

1. Goodwin, P. S., Meeks, W. G., and Morris, R. E., "Helios Mission Support" in *The Deep Space Progress Report 42-32*, pp. 31–37, Jet Propulsion Laboratory, Pasadena, California, April 15, 1976.
2. Berman, A. L., "Doppler Noise Considered as a Function of the Signal Path Integration of Electron Density" in *The Deep Space Progress Report 42-33*. Jet Propulsion Laboratory, Pasadena, California (published in the present volume).

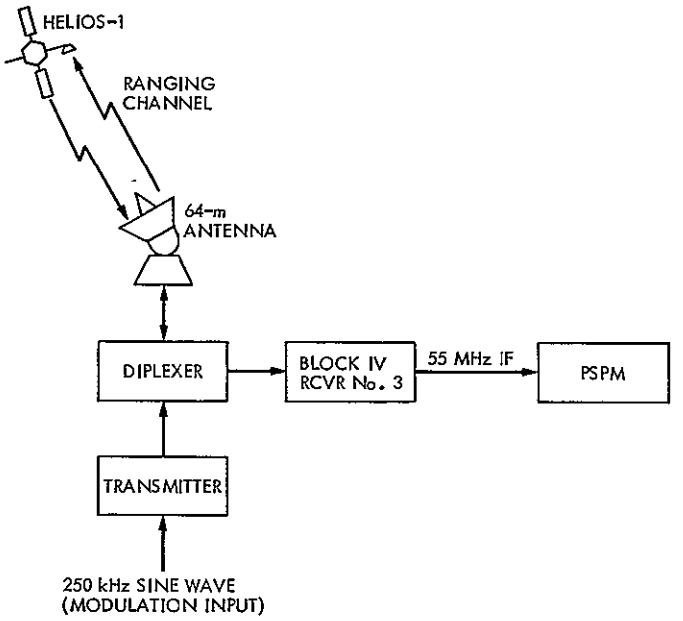

Fig. 1. Helios 1 ranging investigation (DSS 14), simplified system block diagram

	IMPLEMENTED AND TESTED BY
• INSTALLATION (INCLUDING TESTING) OF Mu-2 RANGING AT DSS 14	9 APRIL 1976
• END-TO-END DATA SYSTEM TEST	12 AND 13 APRIL 1976
• DEMONSTRATION PASS (HELIOS OR VIKING)	14 APRIL 1976
• OPERATIONAL SUPPORT WITH Mu-2 RANGING	15 APRIL 1976

Fig. 2. Implementation schedule for Mu-2 ranging support

A Distributed Data Base Management Capability for the Deep Space Network

A. I. Bryan
DSN Systems Engineering Office

This article reports on the Configuration Control and Audit Assembly (CCA), which has been designed to provide a distributed data base management capability for the DSN. The CCA utilizes capabilities provided by the DSN standard minicomputer and the DSN standard nonreal-time high-level management-oriented programming language, MBASIC. The characteristics of the CCA for the first phase of implementation are described.

I. Introduction

A significant cost item in providing operations support services for the DSN is the availability of management and operations information to support the planning, scheduling, and performance of these services. In order to reduce the costs associated with the acquisition, maintenance, and distribution of the management and operations information, the DSN has designed and is planning to implement a distributed data base management capability, identified as the Configuration Control and Audit Assembly (CCA). By direction from the NASA Office of Tracking and Data Acquisition (OTDA), the CCA implementation will proceed on a two-phase basis. The first phase of implementation will culminate with a 6-month demonstration (2 January, 1977–2 July, 1977) of the basic hardware, software, and data base design of the CCA. The primary objectives of the demonstration will be to establish economic feasibility and technical design. The second phase will provide a full implementation of CCAs and data base for the DSN, but will be contingent upon a successful CCA demonstration and approval by OTDA.

II. Criteria and Justification for a Data Base Management Capability

The provision of a data base management capability for the DSN is based on the following criteria:

(1) Provide an easily accessible source of valid information to support DSN management activities.

(2) Provide a more cost-effective method of acquiring, maintaining, and retrieving management information.

The DSN has determined that a distributed data base design, utilizing standard DSN minicomputers, will meet

the above criteria. This design was selected as an optimum approach for the following reasons:

(1) The provision of a master data base and user terminals at each DSN operations center (Jet Propulsion Laboratory, Goldstone Deep Space Communications Complex (DSCC), Australia DSCC, and Spain DSCC) reduces data entry costs, and minimizes the errors and loss of data in transit to the DSN data base.

(2) The DSN is able to utilize identical peripherals and basic computers for both control of the DSN deep space communication equipment and performance of the data base management task. This reduces overall DSN costs by the cross-utilization of spares, maintenance equipment, and personnel.

(3) The distributed system approach enables the utilization of relatively low-cost equipment, while at the same time increasing data throughput by the performance of independent real-time data handling functions in parallel.

(4) The distributed system approach insulates the DSN from a major disruption due to a single computer failure. A computer malfunction would result in the loss of only a portion of the total DSN data base handling capability.

III. Functional Design

The major functions to be performed by each CCA are:

(1) Acquisition of data and maintenance of a current data base .

(2) Provision of communications between CCAs

(3) Provision for access to the data base and retrieval of data

The following is a brief description of the functional design of the DSN distributed data base and the data base management functions performed by each CCA.

A. The DSN Distributed Data Base

The distributed data base concept to be implemented for the DSN is based upon the separation of the total collection of DSN data into parts, and each part being maintained and utilized at a DSN operations center. Portions of the DSN data base will be maintained and utilized at JPL, Australia DSCC, Spain DSCC, and Goldstone DSCC. The portion of the DSN data base at a complex is a "master data base" for that complex. The structure of each master data base is identical and under configuration control by the DSN.

The data base being implemented for the DSN is a hierarchical (inverted tree) information structure, divided into seven top-level categories with various subcategories and files within each subcategory. Each major category is a collection of files in a data base organized to support a particular activity.

References to data within one major category are performed by starting with the name of the category and successively narrowing the specification to the file, file record, or file record element of interest.

Cross-reference between categories (or any two files in the data base) is effected by the use of cross-reference keys. The major cross-reference keys for the DSN data base are a specified small set of common elements such that any record in the data base is accessible starting from at least one of the major cross-reference keys.

A detailed discussion of the DSN data base design will be the subject of another DSN Progress Report.

B. Acquisition of Data and Maintenance of a Current Data Base

The CCA provides a means by which the data base is updated by a transaction input process. A transaction is defined to be any data which would add to, delete from, or alter the contents of the data base.

Transactions are accommodated and controlled via standard DSN software to ensure that the integrity of the data base is maintained. The transaction software provides an interactive interface to the user, and allows the user to input data according to a standard format at an on-line terminal. The CCA will also accommodate the entry of transactions via a batch input process. For entry of transaction data, the user is assisted via prompting, and each transaction is checked for correct syntax and displayed for validation before being recorded (stored) by the CCA.

Recording of transactions is performed immediately upon validation, but the data base is not updated by the transaction data at this time. Instead, the transactions are placed on temporary disk storage until a scheduled periodic data base update is performed. Data base updates are performed on a periodic basis at intervals not to exceed 1 week. The actual update interval will be determined by the number of transactions being handled at a location. Data base updates will be performed by a

designated operator, utilizing standard DSN-supplied software. This software will provide for (1) eliminating old data base files, (2) establishing new data base files, (3) deletion of obsolete file records, (4) insertion of new file records, (5) sorting and merging of file records, and (6) editing of file records.

C. Data Communications Between JPL And The DSCC CCAs

As shown in Fig. 1, the implementation of the data communications function is based upon local reporting of exceptions to files containing plans data. Plans files (e.g., the "As Designed" configurations of DSN equipment at DSS 11, DSS 12, DSS 14) are maintained at both a DSCC and the JPL CCAs. The current master files at a DSCC (e.g., the "As Built" configurations of DSN equipment at DSS 11, DSS 12, DSS 14), which represent the actual state of a DSCC after being updated by transactions, are compared to the plans data, and a file of exception data is generated. The exception file is updated each time the data base is updated. The exception file is made available to local DSCC management for local reporting and is also transmitted via high-speed data (HSD) lines to JPL on a periodic basis (at least once per week) to enable Network status to be determined from the JPL copy of the plans file and the exception data. Data communications between JPL and the DSCC CCAs utilizes the Ground Communications Facility High-Speed Data System. Undetected errors in data communications are specified at less than or equal to 1 block error in 10^9 blocks (1200 bits per HSD block).

D. Access To The DSN Data Base And Retrieval of Data

Access to and retrieval of data from the DSN data base are provided by the DSN standard programming language MBASIC. (Ref. 1). MBASIC (Management-oriented BASIC) is a high-level interactive programming language (an advanced version of the BASIC language developed at Dartmouth College) which contains language elements that are designed to place emphasis on management information processing applications support.

Information retrieval from the data base is accomplished by user applications programs written in MBASIC. MBASIC provides the means whereby the authorized user, operating from a remote terminal device, may access any DSN file to any sub-level, read the data into the user's working storage, extract and operate on data, format the data for a report, and output a hard-copy report from the selected data base contents. For very generalized reporting, normally all that is required is an MBASIC "COPY" statement to display selected DSN data base contents in a human-readable format at the user's terminal.

IV. Phase I Implementation of CCAs

Phase I implementation of the CCAs will culminate with a demonstration study to establish economic feasibility and the technical design of the distributed data base management capability.

To perform the demonstration study, one complete CCA will be installed at the Goldstone DSCC (DSS 12, Bldg. G26-101), and supplemental hardware will be added to an existing Telemetry Processor Assembly of the DSS Telemetry Subsystem located at JPL (Compatibility Test Area 21, Bldg. 125-B17) to make up a CCA. The configuration of CCAs for the demonstration is shown in Fig. 2.

A. CCA Demonstration Hardware

The hardware portion of each CCA will consist of a Modcomp (Model II-25) minicomputer with 65 536 words (16 bits per word) of core memory, two magnetic tape transports, a moving head disk unit, an operator's keyboard-printer device, a high-speed printer, and user terminal devices.

B. CCA Demonstration Software

The software provided with the Phase I implementation of the CCA will operate within the confines of the standard Modcomp operating system (Max III), allowing multiperipheral communication under a real-time operating system. The user will communicate with the CCA through the MBASIC processor and an established collection of service routines. The following is a general description of the software elements comprising the distributed data base management capability for the first phase of implementation.

(1) *System monitor.* The system monitor software acts as an executive between the operating system and the user. It allows remote application users to access the MBASIC processor.

(2) *HSD communications interface.* The HSD communications system software module provides the capability to transmit data between the DSCC CCAs and the central (JPL) CCA. This is a nonresident software module, which is loaded into core and activated on a scheduled basis by the CCA operator.

(3) *Checkpoint and recovery.* The checkpoint and recovery functions provided by the CCA system software will detect and report computer failures due to power failure on memory parity error. Upon restart after such computer failures, a message will be output to each on-line user, stating that the CCA system has been restarted and the approximate time of the computer failure.

(4) *Self-test and maintenance.* Self-test and maintenance routines are included as part of the CCA system software. These routines will check the integrity of the assembly hardware and will aid in localizing a hardware malfunction.

(5) *Transactions.* On-line transactions will be accommodated by the CCA software. The user will be provided with prompting to achieve error-free and efficient entry of data.

(6) *Updates.* A service routine to provide updating of the master data base will be included. Its design will accommodate the periodic updating of the master data base files by transaction data.

(7) *Compare.* A service routine to provide exception data will be included. Its design will provide the capability to produce an exception report from a comparison of the master data base and the plan base files.

(8) *Maintenance utilities.* Utility programs provided by the Modcomp system will give the user the capabilities to prepare and debug programs.

(9) *Record access routines.* A collection of record access routines will be provided to establish access into the data base by key parameter.

C. CCA Demonstration Data Base

The data base to be utilized for the data base management capability demonstration study will consist of edited files taken from the existing operational Configuration Audit Data Base for Deep Space Station 12. The demonstration data base will include the As Designed Equipment Configuration files, the As Built Equipment Configuration files, and the Master Property Index of Equipment files. Throughout the demonstration period, the demonstration data base will be maintained and periodically updated by transactions. The demonstration data base is an integral portion (a major category, "Physical Plant and Tagged Equipment Data") of the total DSN data base and as such, can be directly transferred to operations if Phase II of the CCA implementation is effected.

V. Conclusion

The distributed data base management capability will improve the overall operating efficiency of the DSN and will reduce operations costs by providing valid operations support data at each DSN Deep Space Communications Complex. Data errors will be reduced by the provision of a data base near the source of data inputs, and data base integrity will be achieved by the utilization of standard DSN software for the data management task.

The distributed system design is now technically and economically feasible as a result of

(1) The availability of a minicomputer with data handling capabilities approaching those found only on much more expensive computers a few years ago.

(2) Cross-utilization of a low-cost standard DSN minicomputer.

(3) The availability of reliable and almost error-free communications links between CCAs.

The implementation of the distributed data base management capability will be effected in two phases. Following the completion of the first phase, a six-month (January 1977–July 1977) demonstration study will be done in order to establish the economic feasibility and the technical design of the distributed data base management capability. Based on the results of the demonstration study and approval by OTDA, the second phase of implementation will provide the total distributed data base management capability at each DSN operations center.

Reference

1. *Fundamentals of MBASIC, Vol. I and II,* Jet Propulsion Laboratory, Pasadena, California, March and October 1973 (JPL internal document).

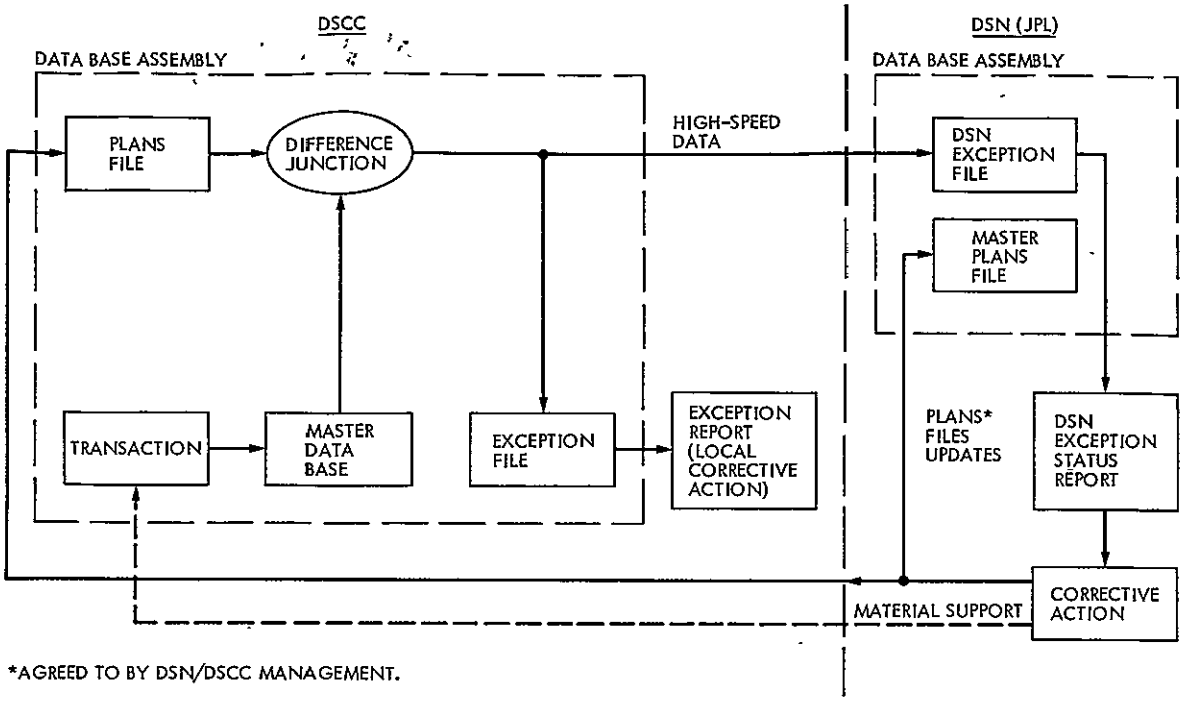

Fig. 1. Communications between JPL and the DSCC CCAs; generation and utilization of exception data

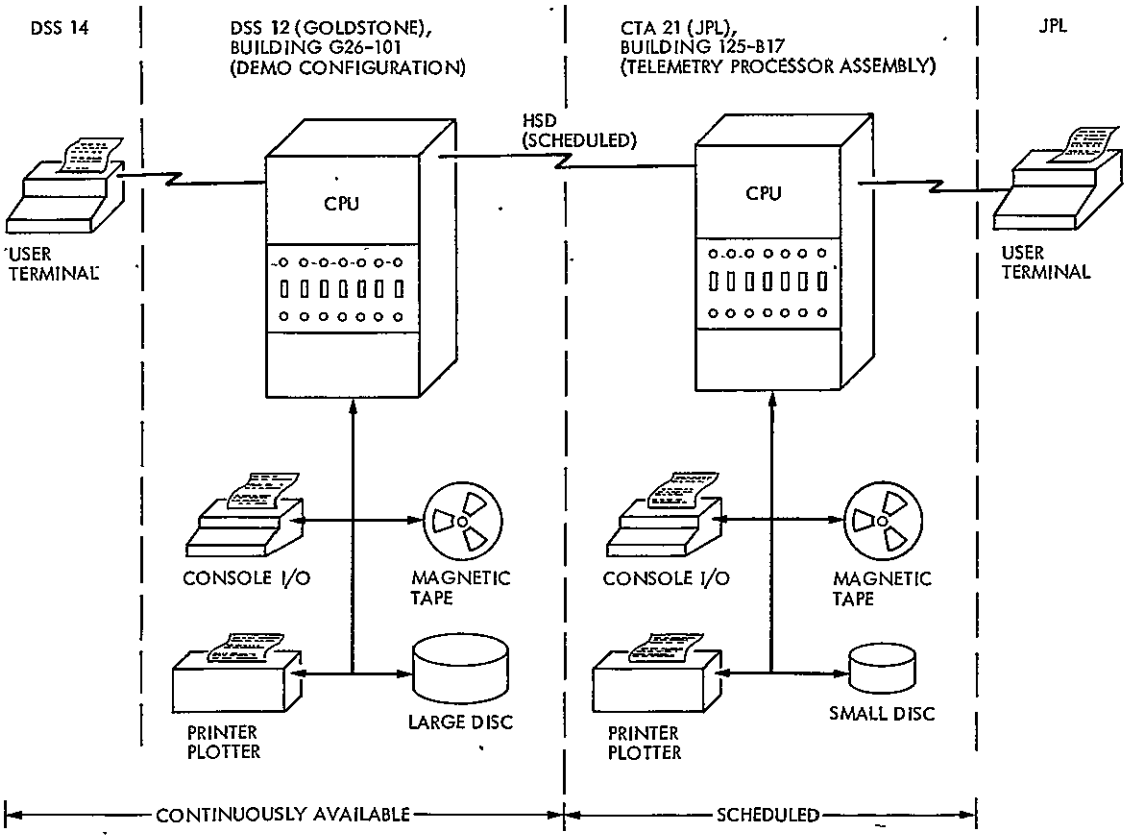

Fig. 2. General configuration of the CCA demonstration equipment

ALSEP–Quasar Differential VLBI

M. A. Slade, R. A. Preston, A. W. Harris, L. J. Skjerve, and D. J. Spitzmesser
Tracking Systems and Applications Section

A program of Apollo Lunar Surface Experiments Package (ALSEP)–Quasar Very Long Baseline Interferometry (VLBI) is being carried out at the Jet Propulsion Laboratory. These observations primarily employ a "4-antenna" technique, whereby simultaneous observations with two antennas at each end of an intercontinental baseline are used to derive the differential interferometric phase between a compact extragalactic radio source (usually a quasar) and a number of ALSEP transmitters on the lunar surface. A continuous ALSEP–quasar differential phase history over a few-hour period can lead to extremely high angular accuracy ($\lesssim 10^{-3}$ arcsecond) in measuring the lunar position against the quasar reference frame. Development of this application of the "4-antenna" technique has been underway at JPL for more than a year and is now producing high-quality data utilizing Deep Space Network (DSN) stations in Australia, Spain, and Goldstone, California, as well as the Spaceflight Tracking and Data Network (STDN) "Apollo" station at Goldstone. These high accuracy observations are of value to tie the lunar ephemeris to a nearly inertial extragalactic reference frame, to test gravitational theories, and to measure the Earth–moon tidal friction interaction.

I. Introduction

The development of a high-precision, nearly inertial, celestial reference frame defined by the positions of extragalactic radio sources (principally quasars) will offer many unique opportunities to perform both astronomical and geophysical studies at previously unrealizable levels of accuracy. These positions will be derived from analysis of extremely accurate VLBI observations. The internal consistency of the new reference frame should be two orders of magnitude better than that of the present "optical star" celestial reference frame (~0.1 arcsecond). In addition, the great distances associated with the extragalactic sources will eliminate the optical star catalog problems arising from stellar proper motions. As part of a program of making accurate measurements of universal time and polar motion, a group at JPL is engaged in an extensive effort to build such a quasar reference frame (Preston *et al.*, 1975). A similar effort is also being undertaken by a group at the Massachusetts Institute of Technology (MIT) and the Goddard Space Flight Center, again primarily for geophysical studies (see Robertson, 1975; Counselman, 1976).

The ALSEP–quasar VLBI program represents the first systematic use of the new quasar reference frame for performing high accuracy solar system studies.[1] Essentially, the ALSEP transmitters on the lunar surface are being tracked against the quasar background as one might follow a planet's motion across an optical star field. These angular observations, in combination with range observations obtained by laser pulse time-of-flight (Bender *et al.*, 1973), will be used for refining the parameters of the Earth–moon system and for extremely precise tests of gravitational theories. When more radio beacons are placed in orbit about or landed on other planets, such observational programs are certain to become more numerous.[2]

The authors are presently conducting an intensive survey of the ecliptic region of the sky to identify extragalactic sources which are suitable for the quasar reference frame. The principal requirement that must be satisfied for intercontinental baselines is that the source have compact components on a size scale of no more than a few thousandths of an arcsecond in angular extent. The structure of the source should be simple, preferably a point source. Figure 1 shows the results of this survey. To this point, 43 sources with sufficient strength for ALSEP–quasar observations (>0.5 jansky) have been found within 10 degrees of the ecliptic. To truly form a high-precision reference frame, the relative positions of these objects should be accurately determined. Although accurate source positions are not yet available, it is important to note that the finite lifetime of the ALSEP transmitters demands that the ALSEP–quasar data be obtained now. Interpretation of observations after the reference frame is developed is no less valuable. Some scientific goals also can be achieved by tracking the moon's motion as it makes successive passes of the same quasars without precise absolute positions being known.

The VLBI technique involves the passive reception of radio signals from celestial radio sources at two widely spaced antennas, each with extremely precise but independent clocks and frequency systems. The radio signals may be from a natural source (quasars, radio galaxies) or a man-made source such as the ALSEP transmitters. By digitally recording the received signals on magnetic tape at both antennas, the tapes can be brought to a common location for cross-correlation to produce the VLBI observable, fringe phase. Differential VLBI (ΔVLBI) refers to the application of this technique to simultaneous observations of objects located close together in the sky. If the fringe phase data from two closely spaced sources are differenced, common error sources tend to cancel, and the resultant differential fringe phase data provide a precise measure of the angular separation of the two sources. Specifically, significant reductions occur in the sensitivity to antenna site location, UT1, polar motion, troposphere, ionosphere, and certain instrumental effects such as clock offset errors and frequency drifts (see Counselman *et al.*, 1972, and Preston, 1974). Differential VLBI has been intensively used for ALSEP–ALSEP observations by a group at MIT (King, 1975).

The ALSEP–quasar observations employ a "4-antenna" technique in which the differential phase is obtained with no integer cycle ambiguities by continuous observations of both the extragalactic source and a number of ALSEP transmitters on the lunar surface. A continuous ALSEP–quasar differential phase history over a few-hour period can lead to extremely high angular accuracy ($\lesssim 10^{-3}$ arcsecond) in measuring the lunar position relative to the quasar reference frame if systematic error sources can be sufficiently reduced. These error sources include: (1) source structure effects, (2) propagation media effects, and (3) instrumental phase effects. Careful selection of sources and various calibration techniques promise to allow the observations to be utilized at nearly their potential accuracy.

II. Technique Development

After some feasibility studies for ALSEP–quasar VLBI (Slade *et al.*, 1972), the ΔVLBI technique was first tried in a January, 1972, "2-antenna" experiment involving Mariner 9 and several quasars (Slade *et al.*, 1974). The "2-antenna" approach to ΔVLBI requires that single antennas at each end of the baseline move back and forth in unison between the two celestial sources. Hence the resultant phase history on each of the sources is not continuous, and unambiguous "phase connection" must be performed during the periods off source (i.e., no integer cycle mistakes). The results were not of high accuracy ($\sim$0.1 arcsecond) due to the small amount of data and the inability to connect phase, but seemed promising enough to perform a trial "2-antenna" ALSEP–quasar experiment on October 20, 1973, with DSN antennas in Spain and South Africa moving between ALSEP 14 and quasar

[1] In 1972, an attempt was made to use the Mariner 9 spacecraft in Mars orbit to make a single tie of the planet's orbit to the quasar reference frame. See text.

[2] Such experiments are planned during the Viking Mission to Mars with I. I. Shapiro, MIT, as principal investigator (Michael *et al.*, 1972).

OJ287. The observations were made using a narrow-bandwidth (24-kilohertz) recording system, which had a relatively low signal-to-noise performance. This recording system demanded observing the relatively strong quasar OJ287 (~2 jansky), even though this choice of natural source was not ideal because the separation between the moon and quasar was fairly large (~7 degrees). The phase history for both sources in this experiment is shown in Fig. 2a. Least-square fitting of linear and quadratic terms to the differential phase, after correcting a cycle error at 06:00 hours, produced the residual differential phase shown in Fig. 2b. The rms fluctuation in phase about the mean is 0.175 cycles. Fitting the differential phase with a constant and diurnal sine and cosine amplitudes gave the corrections to differential right ascension and declination. The former errors on these quantities when the data are weighted to give a χ^2 of 1 are 3.0×10^{-3} and 4.5×10^{-3} arcsecond, respectively. Systematic errors will degrade these estimates by about a factor of 2.

Despite the moderate success of the above ALSEP–quasar experiment, the "2-antenna" switching approach to differential VLBI has several inherent difficulties. Most importantly, the probability of mistakenly moving at wrong times to the wrong position is quite high. Because antenna moving at high drive rates is not programmed, a fallible human operator must command the operations. Also severe propagation media or frequency system fluctuations may make phase connection difficult through the "planned" gaps even if the antenna pointing is done flawlessly at both ends. Finally, the accuracy of the differential phase data obtained with the "2-antenna" technique is degraded due to the non-simultaneity of the fringe phase determinations on the two sources. These reasons motivated the investigation of the continuous tracking of both signals by "4-antenna" experiments, a technique first employed with natural sources for relativity experiments (Counselman *et al.*, 1974). (The "2-antenna" experiments would, of course, still be performed if the special antennas required as described below were not available for a particular time-critical experiment.)

In ALSEP–quasar "4-antenna ΔVLBI," a large antenna (26-meter) at each end of the VLBI baseline observes an extragalactic source, while smaller "acquisition aid" antennas that are attached to the large dishes are observing the stronger ALSEP transmissions. Even though the principal axes of the smaller antennas and their associated parent dishes are aligned, the wider beamwidth of the smaller antennas allows them to view the moon at the same time the narrow-beamwidth larger dishes are pointed at an extragalactic source a few degrees from the moon (see Figs. 3 and 4). The ALSEP signals are so strong that, even with the small acquisition aid antennas, the signal-to-noise ratio (SNR) for the ALSEP signals is much greater than the SNR obtained with the 26-meter antennas on a strong natural source (~2–3 jansky).

The ALSEP–quasar observations mainly utilize Deep Space Network 26-meter antennas in Australia, Spain, and California, where the associated acquisition aid antennas have 3-decibel beamwidths of 16 degrees. In addition, the 26-meter STDN "Apollo" antenna at Goldstone, California with an acquisition aid beamwidth of 8 degrees is also occasionally used.

A schematic diagram of the instrumental configuration for ALSEP–quasar ΔVLBI is shown in Fig. 5. An important feature of this configuration is that the local oscillator signals that are used in the downward frequency conversion of the S-band ALSEP and quasar signals are all derived from a common rubidium frequency standard, thereby allowing any frequency drifts of the frequency standard to cancel when the ΔVLBI observable is formed. Data are recorded by a Mark II VLBI recording system (Clark, 1973) developed by the National Radio Astronomy Observatory (NRAO). The Mark II system records a 2-megahertz bandwidth of data by placing (two-level) digital samples on a video tape at a rate of 4 megabits per second. ALSEP and quasar signals are recorded on alternate seconds and thus are practically (but not truly) continuous. The 2-megahertz bandwidth allows signals from up to three ALSEPs to be simultaneously recorded. In order to maximize the signal-to-noise ratio for the ALSEP signals, which are each only a few kilohertz wide, a specifically designed series of bandpass filters is inserted into the 2-megahertz baseband to filter out much of the noise when ALSEP signals are being recorded. The phase characteristics of these filters were carefully designed to introduce no additional instrumental phase effects.

From January to August 1974, this particular "4-antenna" technique was debugged through engineering tests of the acquisition aid antennas, deployment and testing in Australia of a Mark II recording terminal, and software development in connection with use of the NRAO correlator. An acquisition aid antenna was installed on Deep Space Station (DSS) 62 near Madrid, Spain. The installation of an acquisition aid antenna was requested for DSS 11 at Goldstone.

Until the acquisition aid at DSS 11 was installed, the use of the acquisition aid-equipped Apollo station at Goldstone was arranged with the cooperation of the

STDN. On September 18, 1974, a "4-antenna" experiment between the Apollo Station and DSS 42 in Australia was conducted. The continuous phase track for ALSEP 15 during part of this experiment is shown in Fig. 6. The quasar OP-192 tracked during this experiment was somewhat weaker than expected. On a subsequent experiment between Apollo and Australia on January 1, 1975, the quasar observed (3C446) also appeared weaker than anticipated. Engineering tests during subsequent months revealed instrumental difficulties with the ALSEP filter box in Australia.

By June 1975, the Goldstone DSN acquisition aid became operational at DSS 11 and a Mark II terminal had been deployed to Spain. On June 19, 1975 a "4-antenna" experiment with Australia was performed. On July 31, 1975, an experiment was performed between the Apollo STDN station and Spain. Further experiments were performed between DSS 11 and DSS 62 on November 23, 1975, and between DSS 11 and DSS 42 on December 27, 1975. Experiments using DSS 11 have yielded amplitudes on the natural source as anticipated from theoretical signal-to-noise calculations.

III. Data Processing Techniques

The cross-correlation of the data tapes from these experiments has been done at NRAO in Charlottesville, Virginia on a special hardware–software correlator. (A similar correlator is now being built by JPL and Caltech and should be ready for use by mid-1976.)

The computer software at the NRAO correlator was designed for the processing of natural source data. The rapid motion of the moon requires special provisions to account for the different time variation of the interferometric phase for the various ALSEP transmitters. The so-called "fringe phase" from the NRAO correlator (Clark *et al.*, 1972) for wide-band noise sources can be represented by

$$\phi_{corr} = \phi_B - \phi_A + \phi_I + \phi_V$$

where ϕ_B results from offsetting in delay and multiplying together of the two bit-streams

$$\phi_B = (\omega_2 - \omega_1)t + \omega_2\tilde{\tau}_M + \omega_0(\tau - \tilde{\tau}_M)$$

and ϕ_A results from the modeled phase stopping of the lobe rotator

$$\phi_A = (\omega_2' - \omega_1')t + \omega_2'\tau_M - \Delta\omega_{LO}\,t$$

In these expressions

t = time from midnight on day of experiment from Station 1 recorder, UTC.

τ = actual group delay including propagation media and instrumental effects

τ_M = model-group delay

$\tilde{\tau}_M$ = model group delay (bit-quantized)

ω_i = total effective mixing frequency at station i

ω_i' = estimate of ω_i used in processing

ω_0 = effective bandpass center

$\Delta\omega_{LO}$ = analytic offset (to avoid zero frequency)

ϕ_I = instrumental phase shift

ϕ_V = visibility phase due to source angular structure

For an ALSEP transmitter, ω_0 becomes ω_a, the center frequency of the ALSEP line.

The model delay τ_M to be quantized and used in cross-correlation is computed by a simple model:

$$\tau_M = A + B\cos(\omega_E[t - t_0]) + T$$

where A, B, t_0 are functions of the baseline, its orientation in space, and the source position, ω_E is the sidereal rotation rate of Earth, and T is an adjustable clock offset to allow for the different clock initialization at different stations.

The model delay for the ALSEP transmitters cannot be adequately modeled by this simple formula for any significant length of time. The approach we have followed to obtain stopped fringe phase is to match $(\omega_2'\,\tau_M - \Delta\omega_{LO}\,t)$ to a good model $\omega_2'\,\tau_{ALSEP}$ and its first three time derivatives at a given time t by adjusting the parameters A, B, t_0, and $\Delta\omega_{LO}$ every 10 minutes.

The phase as a function of time is recovered from the correlation functions $\rho\,(\tau_i, t_n)$ measured at $i = 1 \rightarrow N$ delays at times t_n. The correlation functions are complex:

$$\rho\,(\tau_i, t_n) = \rho_c\,(\tau_i, t_n) + j\rho_s(\tau_i, t_n)$$

where ρ_c is the output of the so-called "cosine" channel and ρ_s is the sine channel output of the hardware correlator.

The estimates of the cross-power spectrum $S_{12}(\omega_k, t_n)$ at frequency ω_k time t_n (equispaced at Δt) are computed from the cross-correlation function by a discrete Fourier transform in the lag domain (see Moran, 1974):

$$S_{12}(\omega_k, t_n) = \sum_i [\rho(\tau_i, t_n)]\, W(\tau_i) \exp[j\omega_k(\tau_i + \Delta\tau_n)]$$

where

$$\omega_k = 2\pi\,(k-1)\,B_0/N'$$

$$\Delta\tau_n = \tau_M(t_n) - \widetilde{\tau}_M(t_n)$$

The frequency range of the spectrum from 0 to B_0 is governed by the bandpass filter of the Mark II recorders and is 1.8×10^6 hertz in our application. The spectral weighting function is $W(\tau_i)$. N' can be larger than N for interpolation purposes. The term $\Delta\tau_n$ is necessary to correct for the discrete delay tracking of the correlator.

The phase of an individual ALSEP is then extracted from $S_A(t_n) = S_{12}(\omega_A, t_n)$ of ω_k closest to the ALSEP center frequency. $S_A(t_n)$ is fitted by a function $A_K \exp j\left[\phi_0^K + \dot{\phi}^K t_n + \frac{1}{2}\ddot{\phi}^K t_n^2\right]$ for t_n ($n = n_0$ to n_f) over a specified time interval of length L, where $L = (n_f - n_0)\Delta t$. The epoch of the estimated amplitude A_K, phase ϕ_0^K, fringe rate $\dot{\phi}^K$, and, if necessary, rate of fringe rate $\ddot{\phi}^K$ for interval K is $t_{n_0} + L/2$ because the center of the interval yields the smallest correlation between the estimated parameters and the smallest phase uncertainty (rigorously for a 3-parameter fit).

IV. Expected Performance

The "4-antenna" technique allows the differential interferometric fringe phase to be observed for each source without 2π ambiguity for the length of the experiment, with the differential phase between the two sources providing a precise measure of their angular separation. The inherent angular precision available from the ΔVLBI observable can be represented as being a small fraction of the interferometer fringe spacing in the sky (neglecting geometric effects for simplicity at the moment):

$$\sigma_{\Delta\theta} = \left(\frac{\sigma_{\Delta\phi}}{2\pi}\right)\left(\frac{\lambda}{D}\right)$$

where

$\sigma_{\Delta\theta}$ = uncertainty in angular separation, $\Delta\theta$ (radians)

$\sigma_{\Delta\phi}$ = uncertainty in measuring differential phase, $\Delta\phi$ (radians)

λ = the S-band wavelength (0.13 meters)

D = the baseline length (meters)

and

λ/D = the interferometer fringe spacing.

For our experiments, $\sigma_{\Delta\phi} \approx 30$ degrees of phase and $D \gtrsim 8 \times 10^3$ kilometers, which yields

$$\sigma_{\Delta\theta} \approx 1.4 \times 10^{-9} \text{ radians or } 2.8 \times 10^{-4} \text{ arcseconds}$$

However, this inherent precision is degraded by factors due to the position in the sky of the two objects, the baseline orientation, the limited mutual visibility of the two objects from both ends of the baseline, and systematic errors.

In order to show the effects of the corrupting geometric factors, computer error analyses were performed. The results of this study are presented in Fig. 7 for a typical lunar–quasar geometry: a source separation of 2 degrees and a mean source declination of 15 degrees. This study assumed that a differential fringe phase data point was obtained every 5 minutes and that the rms noise associated with each data point was 0.1 S-band cycles. The solve-for parameters were the differential right ascension, differential declination, and a constant offset in phase between sources. Notice that geometric degradation factors play an important role for about 2 hours into an experiment, at which point the resultant angular precision tends to level out at a magnitude approximately equivalent to the previously calculated value for the inherent precision of a single observation. As the experiment length and number of observations increases, the expected angular precision continues to slowly improve. On a Goldstone–Australia baseline, mutual visibility limits an experiment to about 4 hours for any source position. On a Goldstone–Spain baseline, mutual visibility ranges from 0 to 6 hours, depending on the declination of the sources.

The expected angular precision of these observations may not translate directly into angular accuracy due to the corrupting effects of systematic error sources. Three

systematic error sources could be important: (1) differential instrumental phase drifts, (2) differential propagation media effects, and (3) differential phase variations due to small-scale structure in the extragalactic radio sources. These error sources will be discussed in some detail below.

The primary origin for the first of these possible errors is due to the separate receiver chains (maser amplifiers, mixers, etc.) used at each station for the signals from the main antenna and the acquisition aid antenna. Initial testing indicates that the differential phase variations due to the receiver chains, excluding masers, do not exceed 0.1 S-band cycles. Additional tests, including masers, are planned. In order to calibrate out slow differential phase drifts during actual experiments, the receiver phases are calibrated in one or both of the following ways:

(1) The signal paths are interchanged periodically (~30-minute intervals) by means of a waveguide switch preceding the masers.

(2) Periodically, the main antennas are briefly pointed at the moon to allow the phase drift between receivers to be measured directly.

Another possible source of instrumental phase variation arises due to the motion of the moon in the beam pattern of the acquisition aid antennas as the main antenna tracks the extragalactic radio source. This variation is quite small for the angular separation in our experiments, however, and can be completely removed by calibration of the phase as a function of angle off-axis.

Another source of instrumental phase variation deserves brief mention. The crystal oscillators controlling the transmitted frequency of the ALSEPs are subject to drift due to environmental effects, especially when the lunar terminator passes the ALSEP. This variation requires monitoring of the received frequency of the ALSEP signals, and calculating the geometric doppler effect to derive the transmitter frequency as a function of time. The parameters of this calculation are known well enough to derive the frequency to the required accuracy (see King, 1975). In order to simplify the procedure to obtain this frequency, separate observations of ALSEP doppler have often been made with the cooperation of the STDN by MIT ΔVLBI experimenters. Of course, the Mark II video tapes of the experiments contain this information, but the procedures to obtain doppler signals from these tapes (e.g., autocorrelation) to the required accuracy of ~5 hertz are not simple.

Significant systematic effects will exist in the differential phase due to propagation media (i.e., troposphere, ionosphere, space plasma). These effects can be calibrated (at some level) and/or modeled with solve-for parameters in the data analysis. We have estimated the magnitude of these systematic effects (also see King, 1975) by some simple models.

The systematic part of the tropospheric contribution to the differential phase $\Delta\phi_{trop}$ is estimated for the case of 30-degree elevation at one station and high elevation at the other, for a 3-degree separation in elevation at the former station, i.e., a worst-case geometry. If we take a typical value for the zenith contribution of 2 meters, we obtain at 30-degree elevation that $\Delta\phi_{trop} \simeq 1000$ degrees of phase. If surface conditions are measured, a calibration for the dry part of the troposphere to 2% (20 degrees or 0.05 cycle) of differential phase appears completely realistic (Berman, 1970; Chao, 1974). The wet part of the troposphere is highly variable, especially at some times of the year. The use of microwave radiometry sensing techniques (Schaper *et al.*, 1970, Moran and Rosen, 1975, Resch, 1975) appears to be able to calibrate the path-length variations due to water vapor content to the equivalent of 1–2 centimeters (0.08–0.15 S-band cycles). A radiometer is available at Goldstone, and will be used unless other higher priority experiments using the radiometer conflict. Radiometers at the overseas stations do not yet exist, but may be deployed on an experimental basis within a year.

For a night-time ionosphere with integrated total electron content of 10^{17} electrons/meter^2, and the geometry as in the tropospheric case above, we calculate that for elevations at the first station between 5 and 35 degrees, $\Delta\phi_{ion} \simeq 210$ degrees of phase. Therefore, a calibration of 10% appears adequate, which can be achieved with present calibration schemes. However, daytime ionospheric electron content is an order of magnitude greater than night. Better calibration of the ionosphere will soon be available, since all DSN complexes are now being equipped with automated 24-hour/day meteorological monitoring assemblies which include a new polarization tracking receiver. These receivers will monitor the ionospheric electron content between the DSN site and a synchronous satellite by measuring the Faraday rotation of a linearly polarized signal transmitted by the satellite. The accuracy of the measurements should be better than a 0.9-centimeter equivalent path length at S-band (Burnell *et al.*, 1975). Mapping errors from line-of-sight of the synchronous satellite to the experiment observation path will degrade this accuracy. However, for experiments with

Australia, the line-of-sight to ATS-5 from Australia will be at an elevation of ~15 degrees in the quadrant of the sky towards California. For experiments with Spain, observations of satellites over the Atlantic Ocean also may be able to reduce mapping errors. The satellite which initially will be observed is a West German "Symphonie" satellite station-keeping at 11°W longitude. Total accuracy of the actual *average* path length of 1–2 centimeters at S-band seems quite possible at this time.

Several other calibration schemes also are being pursued. Simultaneous observations of the extragalactic radio sources at X-band several times during an experiment is possible in principle. The Venus antenna at Goldstone, the Aries antenna, and all 64-meter stations will soon have X-band receivers, and thus S–X calibration for the ionosphere could be possible occasionally. When the UT1–polar motion wide-band switching equipment is available, we will obtain data on the extragalactic source at a 40-megahertz synthesized bandwidth to derive group delay measurements. A DRVID scheme (MacDoran, 1970) comparing phase and group delay effects from the ionosphere also may contribute significant ionospheric information. Modeling these effects in the data analysis with solve-for parameters is also a possibility.

Apart from the systematic effect discussed above, random variations in electron content about the mean also will occur. These variations in the experiment path length will not be related to the fluctuation along the line-of-sight of the Faraday rotation data. We can estimate the size of these variations by examining the scatter in a short baseline S-band VLBI experiment using very stable (hydrogen maser) frequency systems in which the lines-of-sight to the same source penetrate the ionosphere with angular separation equivalent to our differential angular separation between ALSEPs and natural source. The relevant baseline length is ~20 kilometers. In a 16-kilometer baseline experiment using hydrogen masers at each end, Thomas *et al.* (1976) found no variations within that experimental accuracy of 7 centimeters (~0.5 cycle). A theoretical estimate of the expected random variations can be made knowing the measured width of the spatial autocorrelation function of the ionosphere. An accepted average value for this width is ~400 kilometers (Mathur *et al.*, 1970, Dickinson *et al.*, 1970). Using this, one expects to find the random variations about the average differential path contribution to be well under 0.1 cycle, although direct experimental evidence for this may be several years away.

The interstellar medium through which the quasar signals travel also contributes a difference in differential path length. However, over the course of an experiment, the variation in this contribution will be negligible. The large constant part simply contributes to the overall constant in phase between extragalactic radio source phase and ALSEP signal phase.

The systematic errors introduced by source structure appear manageable, but are difficult to accurately assess at this time. Extensive observations exist for only a relatively small collection of sources (~10) which are selectively chosen for rapid variability. A realistic worst-case phase change over an ALSEP–quasar experiment seems likely to be ~0.5 cycles. Simple models of the structure could remove much of this variation for most sources, but may require a modest monitoring program to obtain the model parameters.

In summary, considering the expected angular precision of the measurements as well as the possible systematic error sources, the "4-antenna" observations should allow determinations of the angular separations of sources with an accuracy of better than 10^{-3} arcseconds.[3]

V. Scientific Goals

The direct goal of the ALSEP–quasar observations is to accurately tie the lunar orbit to the nearly inertial quasar reference frame. Currently NASA is planning to intercompare a number of techniques which might be used for future high-accuracy geodetic measurements. Two of these techniques are VLBI and Lunar Laser Ranging. A tie of the lunar orbit to the VLBI quasar reference frame could prove a valuable tool in any intercomparison of these two techniques.

By monitoring the angular motion of the moon with respect to this extragalactic radio source reference frame, several other valuable scientific results can be achieved. The effects to be observed can be divided naturally into two categories by the motions which give the principal sensitivity to the effects:

(1) Motion in the plane of the lunar orbit.

(2) Motion of the orbit plane.

[3]It should be noted that an MIT group has found repeatability of $\sim 10^{-3}$ arcsecond in measuring the differential separation of a pair of extragalactic sources (Wittels, 1975). These sources had a 1/2-degree separation, and the observations were made at a wavelength of 3.8 centimeters where the ionosphere is an order of magnitude less important than at S-band (13 centimeters).

The first category contains effects which cause the moon's mean longitude to depart quadratically with time from the predictions of Newtonian or general relativistic gravitational theory. These effects are a time variation of the gravitational constant ($\dot{G}$) and tidal friction. The tidal interaction has major implications for the origin and evolution of the Earth–moon system (see, e.g., Kaula and Harris, 1975): The lunar orbit has changed greatly over time under the influence of tidal dissipation. Knowing the magnitude of this effect would enable the time scale for the orbital changes to be determined. Time variation of the gravitational constant is a crucial prediction of many non-Einsteinian cosmologies (e.g., Hoyle, 1973, Brans and Dicke, 1961; Dirac, 1938).

These quadratic effects in mean longitude L are commonly characterized by the magnitude of the time derivative of the mean motion n, which itself is the time derivative of L. Empirical estimates of the total anomalous part of $\dot{n}$ range from the classical value of -22.44 ± 0.5 arcseconds/century^2 (Jones, 1939) to recent estimates of -65 ± 10 arcseconds/century^2 (Van Flandern, 1975) and -37 ± 6 arcseconds/century^2 (Muller and Stephenson, 1975). A nominal value for $\dot{n}_{total}$ of $\sim$30 arcseconds/century^2 leads to a discrepancy in longitude ΔL over 3 years of

$$\Delta L = -14 \times 10^{-1} \text{ arcseconds}$$

The sensitivity of ALSEP–quasar VLBI to $\dot{n}_{total}$ can be greatly increased by combination with lunar laser ranging data. This added sensitivity occurs because the long time base and comparable accuracy of the laser ranging observations strongly constrain the 3 parameters necessary for a quadratic fit to the longitude discrepancy.

The effect on the lunar mean longitude of a slow time variation of G can easily be computed from its effect on the mean motion:

$$\frac{\dot{n}}{n} = \frac{2\dot{G}}{G}$$

If $\dot{G}/G$ had a value of 5×10^{-11} year^{-1}, then over three years the resultant longitude discrepancy would be

$$\Delta L \simeq 8 \times 10^{-4} \text{ arcseconds}$$

assuming L_0 and n are well known. Tidal friction also affects the mean longitude, with separability coming from large solar terms which also give sensitivity to $n_\oplus$, the mean motion of the Earth about the sun. $n_\oplus$ is only affected by $\dot{G}$, and thus the contribution from $\dot{G}$ alone can be separated, albeit slowly. The best present experimental limit of the present value of $\dot{G}$ comes from analysis of radar observations of the inner planets (Reasenberg and Shapiro, 1975):

$$\left(\left|\frac{\dot{G}}{G}\right|\right)_{present} < 1 \times 10^{-10} \text{ year}^{-1}$$

Combination of the above data types (laser ranging, VLBI, and planetary radar) in a joint solution would extract the optimum information concerning tidal friction and $\dot{G}$.

The second category above contains effects causing motion of the orbit plane, i.e., the longitude rate of the lunar node and perigee. The most important of these is a general relativistic precession of the lunar orbital angular momentum, first discussed by de Sitter (1916), but not yet detected with significant accuracy (see Weinberg, 1972, and Slade, 1971). This precession causes an advance of the longitude of the lunar node and perigee of $\sim 20 \times 10^{-3}$ arcseconds/year.

The detection of these effects can most effectively utilize the accuracy of ΔVLBI by many repeated observations of the same quasars. Source position uncertainty then becomes unimportant. The observation of several ALSEP transmitters during each experiment allows solution for the position of the center of mass of the moon, removing in large part any libration uncertainties. The libration ephemeris has been greatly improved using the laser ranging data (Williams *et al.*, 1973), and the uncertainties presently are no worse than 3×10^{-3} arcseconds geocentric. Analysis of observations of the differential ALSEP phases by the MIT group (Counselman *et al.*, 1972, 1973; King, 1975) give the relative ALSEP positions and greatly alleviate any remaining difficulty with the physical librations.

VI. Summary

JPL is presently developing a high-precision, nearly inertial, celestial reference frame composed of compact extragalactic sources (principally quasars) for use in both astronomical and geophysical studies. The ALSEP–quasar VLBI program will utilize this new quasar reference frame to perform dynamical investigations of the lunar orbit by monitoring the moon's motion relative to angularly nearby quasars. These high-accuracy measurements are of value to tie the lunar ephemeris to the quasar frame, to test gravitational theories, and to measure the Earth–moon tidal friction interaction.

Acknowledgments

We are indebted to B. Johnson, K. Fox, E. Cohen, W. Ross, and personnel of the Deep Space Network stations and scheduling office. The personnel of the Apollo STDN station, especially J. Renfrew and W. O. Wood, has been very cooperative in our experiments. Helpful discussions by P. L. Bender, J. B. Thomas, M. Reid, J. Romney, J. Moran, A. Niell, W. Sjogren, J. Williams, K. W. Yip, H. N. Royden, and many staff members of the National Radio Astronomy Observatory (NRAO) are deeply appreciated. Coordinated experiments and other support by R. W. King, W. Snow, and C. C. Counselman, III, have greatly aided the development of this program.

References

Bender, P. L., *et al.*, "The Lunar Laser Ranging Experiment," *Science*, Vol. 182, pp. 229–238, 1973.

Berman, A. L., "A New Tropospheric Range Refraction Model," in *The Deep Space Network*, Space Programs Summary 37-65, Vol. II, pp. 140–163, Jet Propulsion Laboratory, Pasadena, Calif., Sept. 30, 1970.

Brans, C., and Dicke, R. H., "Mach's Principle and a Relativistic Theory of Gravitation," *Phys. Rev.*, Vol. 124, pp. 925–935, 1961.

Burnell, H., Phillips, H., and Zanteson, R., "Meteorological Monitoring Assembly," in *The Deep Space Network Progress Report 42-29*, Jet Propulsion Laboratory, Pasadena, Calif., 1975.

Chao, C. C., *The Tropospheric Calibration Model for Mariner Mars 1971*, Technical Report 32-1587, Jet Propulsion Laboratory, Pasadena, Calif., March 1, 1974.

Clark, B. G., Weimer, R., and Weinreb, S., *The Mark II VLB System*, NRAO Electronics Division Internal Report 118, 1972.

Clark, B. G., "The NRAO Tape-Recorder Interferometer System," *Proceedings of the IEEE*, Vol. 61, No. 9, pp. 1242–1248, Sept. 1973.

Counselman, C. C., III, Hinteregger, H. F., and Shapiro, I. I., "Astronomical Applications of Differential Interferometry," *Science*, Vol. 178, pp. 607–608, 1972.

Counselman, C. C., III, *et al.*, "Lunar Baselines and Libration from Differential VLBI Observations of ALSEPS," *The Moon*, Vol. 8, pp. 484–489, 1973.

Counselman, C. C., III, "Solar Gravitational Deflection of Radio Waves Measured by Very-Long-Baseline Interferometry," *Phys. Rev. Letters*, Vol. 33, pp. 1621–1623, 1974.

Counselman, C. C., III, "Radio Astronomy," *Annual Review of Astronomy and Astrophysics*, Vol. 14, 1976.

de Sitter, W., "Planetary Motion and the Motion of the Moon According to Einstein's Theory," *Mon. Not. Roy. Astron. Soc.*, Vol. 76, 1916.

Dicke, R. H., "The Secular Acceleration of the Earth's Rotation and Cosmology," in *The Earth-Moon System*, eds. B. G. Marsden and A. G. W. Cameron, pp. 98–164, Plenus, New York, 1966.

Dickinson, D. F., Grossi, M. D., and Pearlman, M. R., "Refractive Corrections in High-Accuracy Radio Interferometry," *Journal of Geophysical Research*, Vol. 75, pp. 1619–1621, 1970.

Dirac, P. A. M., *Proc. Roy. Soc. A.*, Vol. 165, p. 199, 1938.

Hoyle, F., *Quart. J. Rev. Astron. Soc.*, Vol. 13, pp. 328–329, 1972.

Jones, H. S., "The Rotation of the Earth and the Secular Acceleration of the Sun, Moon and Planets," *Mon. Not. Roy. Astron. Soc.*, Vol. 99, pp. 541–558, 1939.

Kaula, W. M., and Harris, A. W., "Dynamics of Lunar Origin and Orbital Evolution," *Reviews of Geophysics and Space Physics*, Vol. 13, pp. 363–371, 1975.

King, R. W., *Precision Selenodesy via Differential Very-Long Baseline Interferometry*, Ph.D. Thesis, Massachusetts Institute of Technology, Cambridge, Mass., 1975.

MacDoran, P. F., "A First-Principles Derivation of the Differenced Range Versus Integrated Doppler (DRVID) Charged-Particle Calibration Method," in *The Deep Space Network*, Space Programs Summary 37-62, Vol. II, Jet Propulsion Laboratory, Pasadena, Calif., February 1970.

Mathur, N. C., Grossi, M. D., and Pearlman, M. R., "Atmospheric effects in very long baseline interferometry," *Radio Science*, Vol. 5, pp. 1253–1261, 1970.

Michael, W. H., Jr., "Radio Science Experiments: The Viking Mars Orbiter and Lander," *Icarus*, Vol. 16, pp. 57–73, 1972.

Moran, J. M., "Very Long-Baseline Interferometric Observations and Data Reduction," Center for Astrophysics, Harvard College Observatory and Smithsonian Astrophysical Observatory, Preprint Series No. 108, May 1974.

Moran, J. M., and Rosen, B. R., "The Estimation of Tropospheric Propagation Path Length from Ground-Based Microwave Measurements," presented at the Annual Meeting of the U. S. National Comm. International Union of Radio Science, Boulder, Colorado, 1975.

Muller, P. M., and Stephenson, F. R., "The Acceleration of the Earth and Moon from Early Astronomical Observations," in *Growth Rhythms and History of the Earth's Rotation*, edited by E. D. Rosenberg and S. K. Runcorn, John Wiley, New York, 1975.

Preston, R. A., "Dual-Spacecraft Radio Metric Tracking," in *The Deep Space Network Progress Report 42-22*, Jet Propulsion Laboratory, Pasadena, Calif., 1974.

Preston, R. A., *et al.*, "JPL Catalog of VLBI Radio Sources," *Bull. AAS* (in press, 1975).

Resch, G. M., "Comparison of Microwave Radiometric and In-Situ Measurements of Tropospheric Water Vapor," presented at the Annual Meeting of the U. S. National Comm. International Union of Radio Science, Boulder, Colorado, 1975.

Reasenberg, R. D., and Shapiro, I. I., "Bound on the Secular Variation of the Gravitational Interaction," in *Proceedings of the 5th Conference on Atomic Masses and Fundamental Constants*, Paris (in press, 1975).

Robertson, D. S., *Geodetic and Astrometric Measurements with Very-Long-Baseline Interferometry*, Ph.D. Thesis, Massachusetts Institute of Technology, Cambridge, Mass., 1975.

Schaper, L. W., Staelin, D. H., and Waters, J. W., "The Estimation of Tropospheric Electrical Path Length by Microwave Radiometry," *Proc. Inst. Elec. Electron. Eng.*, Vol. 58, pp. 272–273, 1970.

Slade, M. A., *The Orbit of the Moon*, Ph.D. Thesis, Massachusetts Institute of Technology, Cambridge, Mass., 1971.

Slade, M. A., MacDoran, P. F., and Thomas, J. B., "Very Long Baseline Interferometry (VLBI) Possibilities for Lunar Study," in *The Deep Space Network*, Technical Report 32-1526, Vol. XII, pp. 35–39, Jet Propulsion Laboratory, Pasadena, Calif., 1972.

Slade, M. A., *et al.*, "The Mariner 9 Quasar Experiment: Part I," in *The Deep Space Network*, Technical Report 32-1526, Vol. XIX, pp. 31–35, Jet Propulsion Laboratory, Pasadena, Calif., 1974.

Thomas, J. B., *et al.*, "Radio Interferometry Measurements of a 16-km Baseline with 4-cm Precision," in *The Deep Space Network*, Technical Report 32-1526, Vol. XVIII, Jet Propulsion Laboratory, Pasadena, Calif., Dec. 1973.

Van Flandern, T. C., "A Determination of the Rate of Change of G," *Mon. Not. Roy. Astron. Soc.*, Vol. 170, No. 2, pp. 333–342, Feb. 1975.

Weinberg, S., *Gravitation and Cosmology*, John Wiley, New York, 1972.

Williams, J. G., *et al.*, "Lunar Physical Libration and Laser Ranging," *The Moon*, Vol. 8, pp. 469–483, 1973.

Wittels, J. J., *Positions and Kinematics of Quasars and Related Radio Objects Inferred from VLBI Observations*, Ph.D. thesis, Massachusetts Institute of Technology, Cambridge, Mass., 1975.

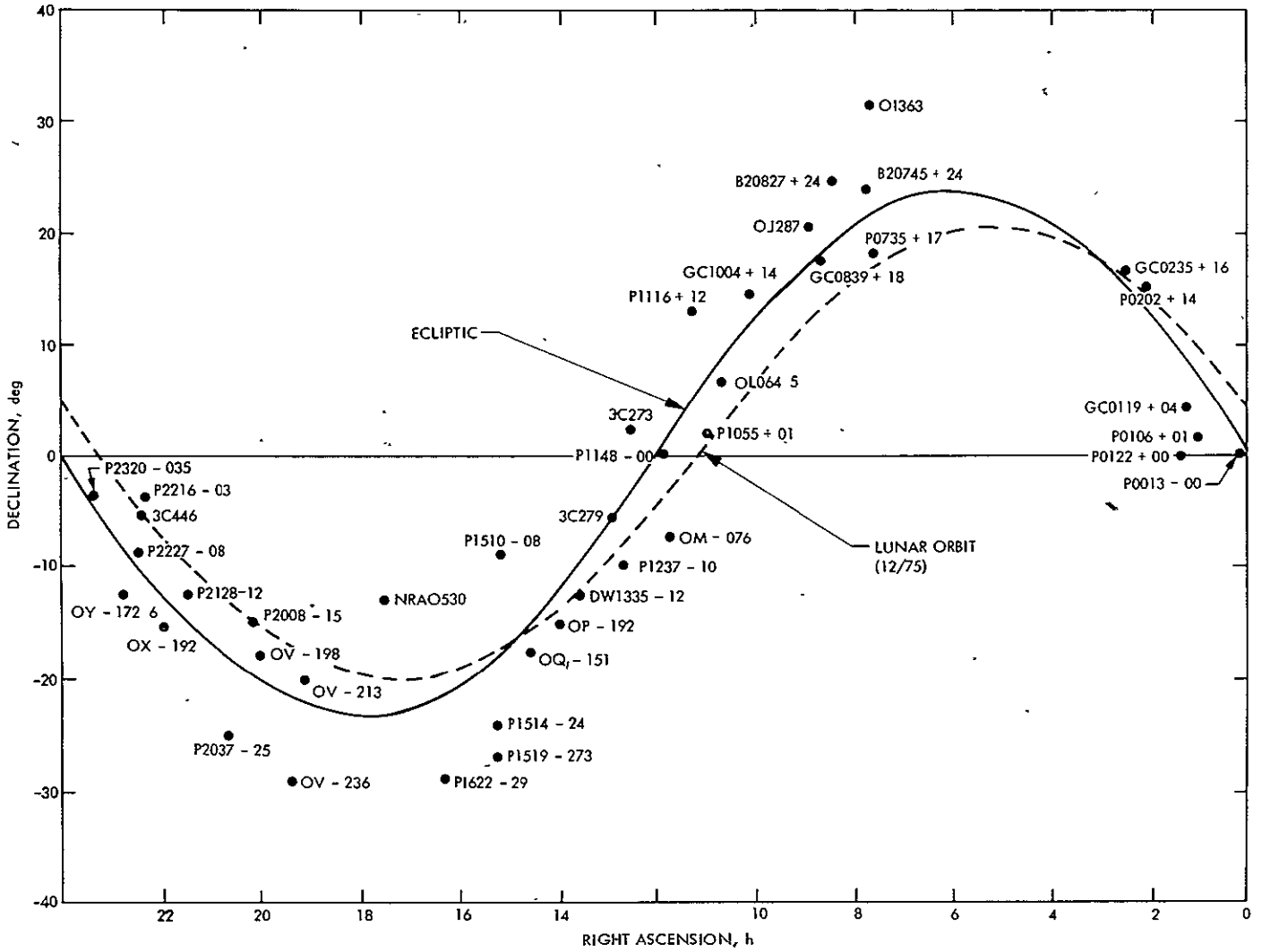

Fig. 1. Extragalactic VLBI sources within 10 deg of ecliptic (>0.5 jansky)

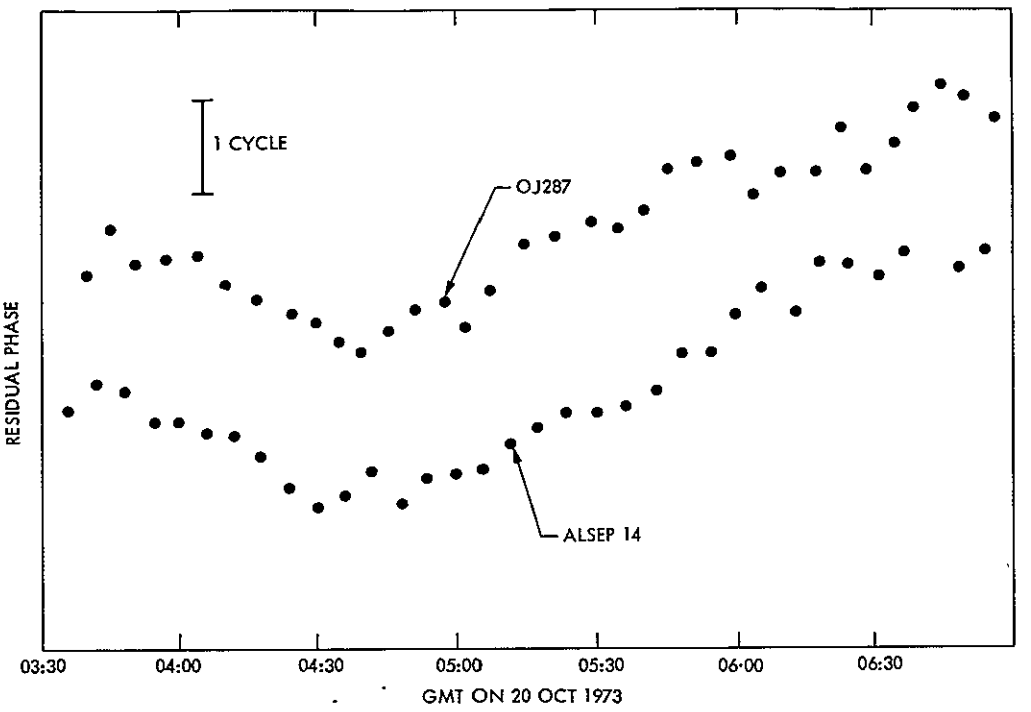

Fig. 2a. VLBI phase residuals on Oct. 20, 1973 "2-antenna" experiment. The points represent the mean values of data segments. The fluctuation about these means is typically 0.04 cycles for ALSEP 14 and 0.11 cycles for OJ287.

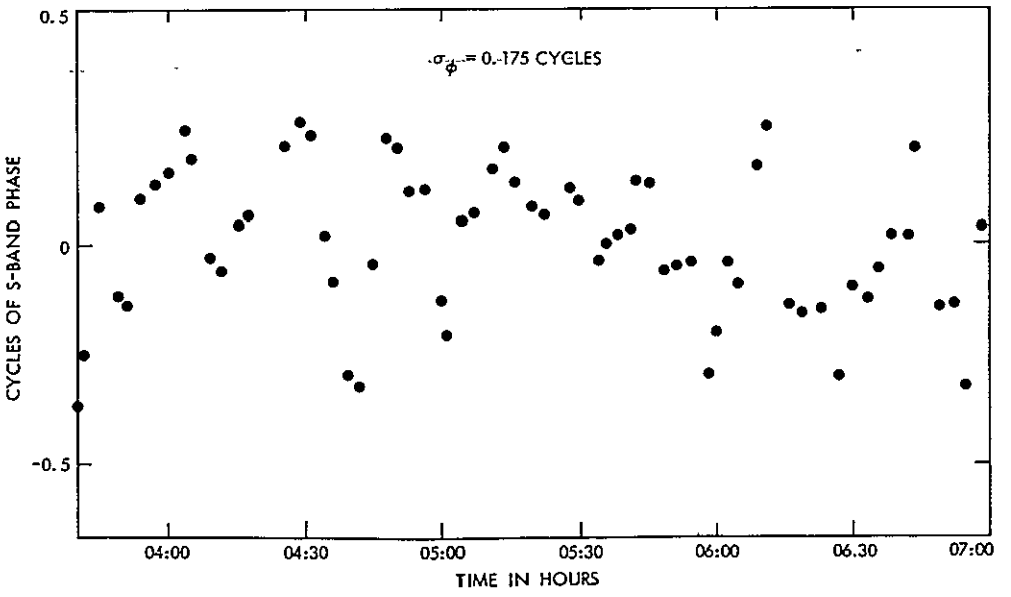

Fig. 2b. Differential phase of Fig. 2a. Fitted by quadratic polynomial in time. Note expanded scale on abscissa.

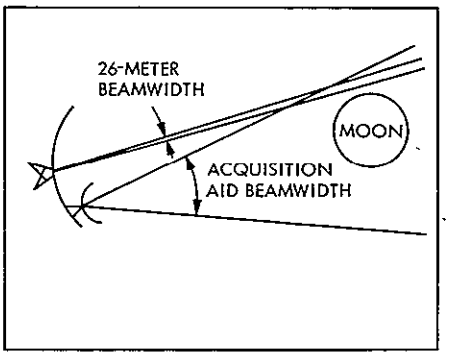

Fig. 3. Conceptual diagram of 26-m/acquisition aid antenna beam patterns

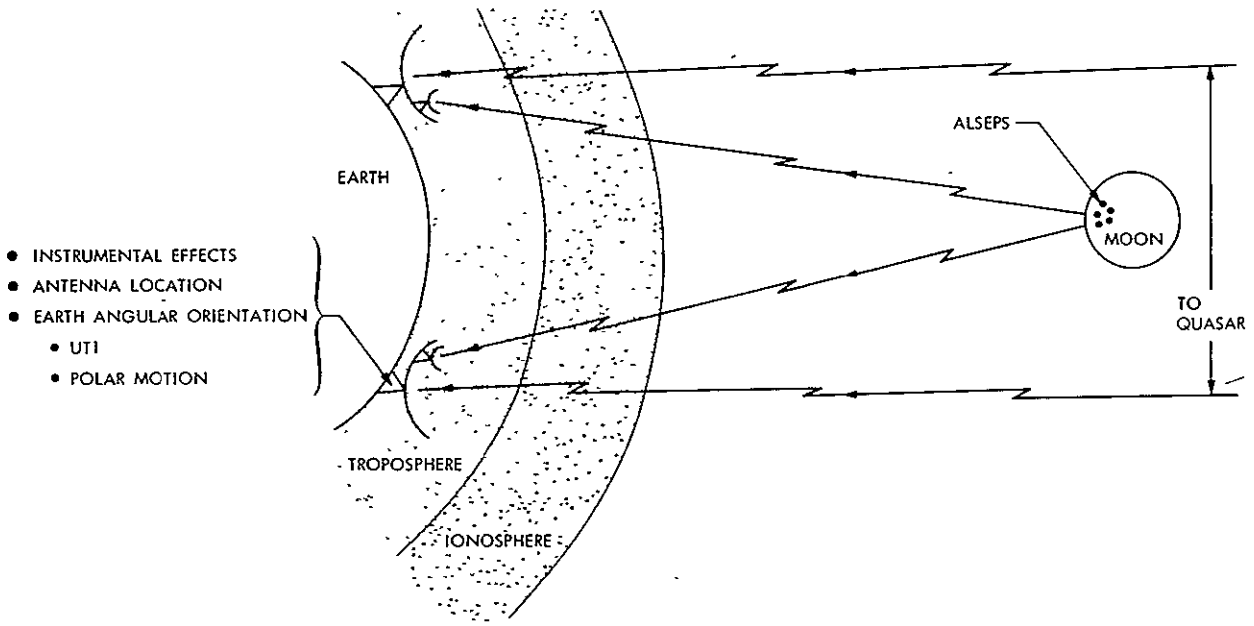

Fig. 4. Cancellation of common error sources with "4-antenna" ΔVLBI

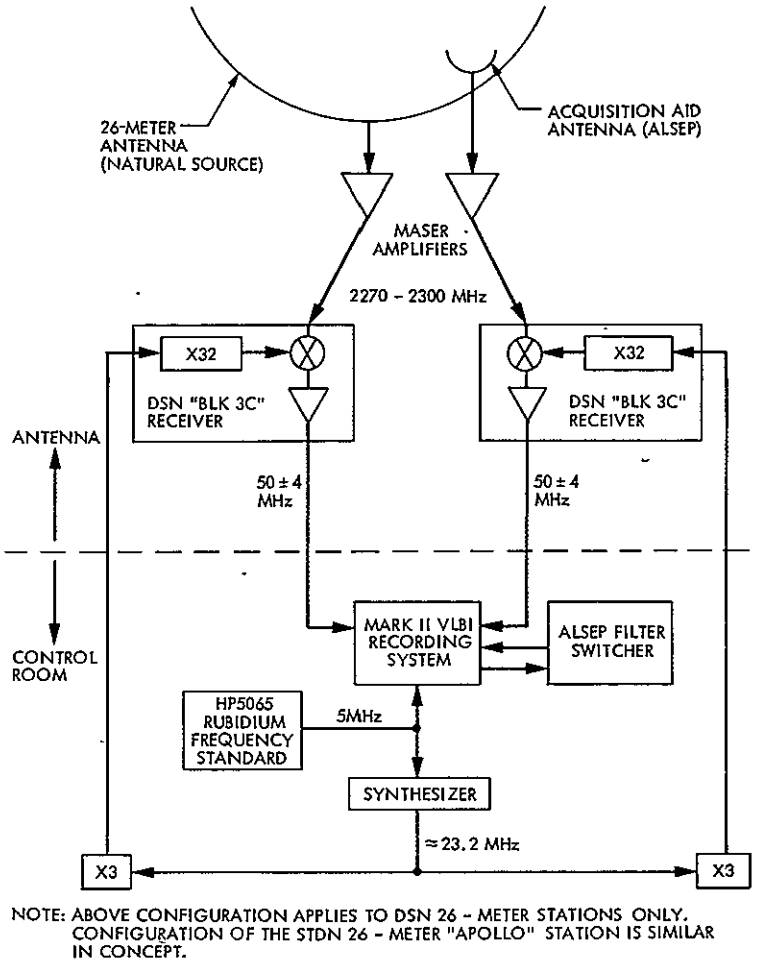

NOTE: ABOVE CONFIGURATION APPLIES TO DSN 26 – METER STATIONS ONLY. CONFIGURATION OF THE STDN 26 – METER "APOLLO" STATION IS SIMILAR IN CONCEPT.

Fig. 5. ALSEP–quasar VLBI instrumental configuration

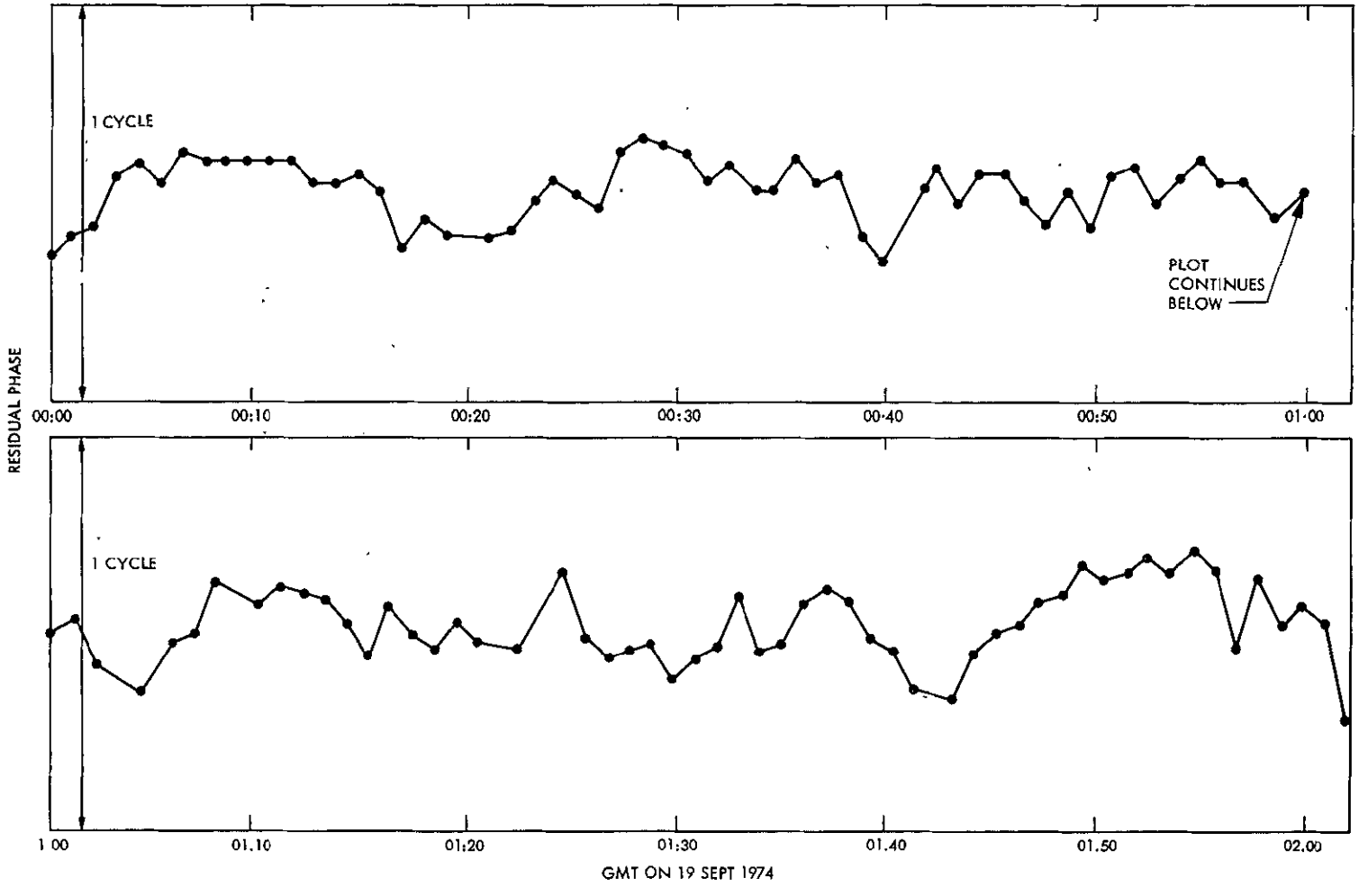

Fig. 6. VLBI phase residuals for ALSEP 15 on Sept. 19, 1974 "4-antenna" experiment. The lines joining points have no physical meaning. The instrumental noise is typically 0.03 cycles.

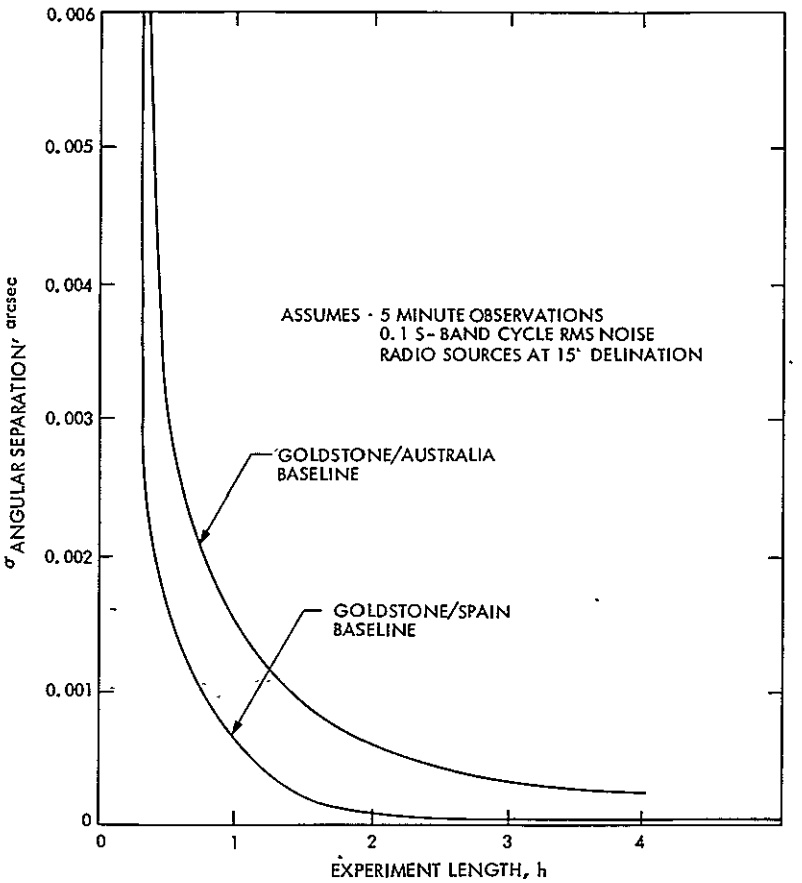

Fig. 7. ΔVLBI precision as function of experiment length

Conceptual Studies for New Low-Cost 64-m Antennas

R. Levy
DSN Engineering Section

Recent software developments expedite design investigations of proposed new 64-m antenna structures. The software consists of programs to generate structure model data and a design program that chooses preferential cross-sectional sizes of the structural members. Numerous new designs are summarized that can represent weight savings of from 25% to 50% with respect to the tipping weight of the existing Mars antenna. These designs provide a more favorable symmetrical support for the reflector backup and tend to provide superior surface accuracy for gravity, although not necessarily wind, loading on the antenna.

I. Introduction

The objective of the present study program is to examine cost reductions that may have become possible in the design of new 64-m antenna structures. The basis of comparison is the existing Mars (DSS 14) 64-m antenna, which is retained as a standard of reference for proposed new designs. The present article considers only the economies in the fabrication of the antenna-reflector backup and support structures. These are measured in terms of reduction of weight of the "tipping" structure, which consists of all the components that can rotate about the elevation axis. Any economies achieved through weight reduction of the tipping structure will perpetuate approximately proportionate economies in other components such as the alidade, pedestal, foundation, drives and bearings. Additional concurrent studies in progress consider cost reductions for these additional components through weight reduction of the tipping structure and also through new approaches to their individual configurations. Furthermore, since the present discussion considers only an exploratory examination of the backup structure weight reduction, examinations are continuing for promising additional improvements.

The original 64-m antenna structure was designed over 10 years ago, and at that time only limited software was available to analyze the expected performance using highly idealized analytical models. Since that time, the NASTRAN (Ref. 1) and the JPL-IDEAS (Ref. 2) computer programs have been developed with much greater problem size analysis capability so that less drastic

analytical idealizations are necessary, which improves the accuracy of analyses. Furthermore, the IDEAS program has design capability to establish preferential member sizes (areas of rods or thicknesses of plates) in accordance with a performance objective for the design. Although the design process requires an iterative set of analysis-redesign cycles, these cycles are executed rapidly so that the present computer cost of design is comparable to former costs for computer analysis only. The historical process of analyzing a particular design, examining the results, subjective estimation of parameter changes that might produce design improvements, modifying the computer data, returning to the computer analysis program for verification, and then possible additional recycling of the process just described, was not only expensive in computer and manpower effort, it was also lengthy with respect to calendar time. The same process is now automated and can be performed within a time span measured by hours or days rather than weeks, permitting much greater depth of study for new designs and variation thereof.

A further extension of the opportunities to produce better designs occurs in newer methods of data preparation. Formerly, it was necessary to devote hundreds of manhours to fill out keypunch coding forms for the thousands of data cards needed to describe the structure and its loading. Today, the process is almost entirely automated, so that except for occasional special requirements, all of the necessary data cards are produced within a few minutes by special-purpose data generator programs. Consequently, the exploratory range for new designs can conveniently cover a much wider scope than heretofore.

II. Background

Two major conceptual innovations in the field of antenna structure design have occured since the completion of the successful Mars antenna structure in the middle 1960s. The first of these was the clarification of the conceptual idea of "homologous" deformation by Von Hoerner (Ref. 3), and the second was the antenna support configuration devised to emphasize homologous deformations that was adopted within the Bonn antenna (Ref. 4).

It has been well known for many years that the absolute magnitude of surface deformations is unimportant from a microwave efficiency standpoint in comparison to the deformations from any alternative paraboloid that best-fits the distorted surface. Specifically, Ruze (Ref. 5) gave a simplified equation from which the antenna surface efficiency and gain could be computed from the knowledge of the root mean square (rms) half-pathlength deviations of the reflecting surface from a best-fitting paraboloid. Utku and Barondess (Ref. 6) gave the equations from which the properties of the best-fitting paraboloid and rms pathlength deviation could be determined from the deflections of the structure. Von Hoerner's innovation was to propose that the properties of the structural members that supported the reflector surface could be chosen to promote the occurrence of relatively small rms deflections from the best-fit paraboloid, although the magnitudes of the absolute deflections could be relatively large. In principle, the concept of homologous deformation, whereby all of the deformations of the surface fall exactly upon a paraboloid, is conceivable in the case of gravity loading on antenna structures. That is, if we are concerned only with the deformations caused by the change in orientation of the gravity loading vector with respect to the antenna surface, the properties of the individual members of the structure can be chosen so that the deformed surface at every antenna elevation angle exactly fits an alternative paraboloid. In application, however, the homologous design is not achieved because of constraints upon the choices of member sizes for stress and buckling requirements, practical manufacturing considerations, and stiffness requirements for acceptable vibratory performance. Furthermore, when antennas are subjected to substantial wind loading, it is impossible to conceive of a design that can approach homology simultaneously for gravity loading and the host of variable distributions of wind loadings that can occur. Consequently, practical designs tend to be a compromise between homology for gravity loading and the maintaining of some minimum measure of absolute stiffness for vibratory and wind loading. The JPL-IDEAS design program can be used to provide compromise designs with respect to homology and the foregoing practical considerations.

The innovation in the Bonn antenna was to depart from the heretofore customary support of the antenna backup structure that often consisted of two hard points near the elevation axis and two softer points in the vicinity of the elevation wheel at about 90 deg from the elevation axis points. The Bonn support consists of members of equal stiffness to support a set of regularly spaced reflector backup radial rib trusses. The support members are generators of an inverted cone with the base attached to the radial trusses and a common junction at the apex. The apex point, which is below the elevation axis, is supported by an independent structure suspended from the elevation axis and is also driven in elevation by a conventional large elevation wheel with sector gear attached to its rim.

III. Configuration for New Antenna Studies

A. Backup Structure

The reflector backup consists of the conventional rib and hoop construction. There are 48 main rib trusses and 48 alternating intermediate ribs equally spaced within the 360-deg aperture. The rib trusses are braced by 11 circumferential hoop trusses. A schematic layout is shown in Fig. 1, where it also can be seen that the backup comprises replicate sectors of 15-deg modules. The main ribs are spaced at 7.5 deg within each module, and every other main rib has a cone generator bar to support it from below at ring 4. The intermediate ribs, which consist of a single top bar supported by the hoop trusses are omitted at ring numbers lower than ring 6, and the unsupported main ribs are omitted between rings 1 and 2. As shown in Figs. 1b and 1c, the hoop truss members occur in three categories: top, bottom, and diagonal bars. As shown in Fig. 1d, the rib members occur in four categories: top, bottom, diagonal, and post bars. Three additional categories of inter-rib bracing are: top surface diagonal bracing between adjacent rib tops, bottom surface diagonal bracing between adjacent rib bottoms, and inclined bracing from the top of one rib to the bottom of the next adjacent rib. Consequently, all members of the reflector backup structure can be classified within only 10 distinct category types. To emphasize manufacturing economy by means of replication, all members of the same category that occur at the same ring or within the same ring annulus are assembled into the same design variable group. Each member within a design group can be designed by the IDEAS program to have the same structural cross section. As an illustration, this particular antenna backup model, which has over 5000 individual bar members, requires less than 130 detailing variations to manufacture all of the bars.

The layout of ribs and hoops in Fig. 1 was arranged to provide a support at the four corners of each reflecting surface panel. The ring spacing and rib subdivisions were patterned to require surface panels of about the same size as used in the Mars antenna. The rib truss depths (Fig. 1d) are also similar to the Mars rib depths. A noticeable difference here, however, with respect to the Mars antenna is that the radial distance to rib truss panel points is the same for a given ring for all of the 96 rib trusses. The required type of symmetry that allows this repetition is destroyed within the Mars antenna because of an integral hub of reinforcing trusses that are arranged in a rectangular pattern. This reinforcing hub, which is used to support the backup, is, in general, skewed to the rib trusses. In the structure of Fig. 1, the function of the hub is replaced by the 24 cone generator support bars (bars A–S in Fig. 1d) and the central post (bar A–B). Because of the great emphasis on symmetry and repetition in this design, data generation is readily automated. Most of the data input required for subsequent design and analysis is generated within a special computer program in less than a minute of 1108 computer central processing unit (CPU) time. There are about 4000 data card images, which are computer produced on the basis of a relatively small number of input parameters that give key dimensions plus configuration and arrangement options. Another computer program automatically generates data to describe wind loading on the structure by interpolating from our existing wind tunnel pressure data.

B. Backup Structure Support

A diagram of the backup support is shown in Fig. 2. This supports the reflector backup ribs at the points marked "S" in the figure by means of the cone-generator bars that have a common apex at node 3 of the figure. The support carries the forces from the cone apex to the elevation bearing at node 4. The elevation bearing is supported by the alidade, for which redesign is not being investigated within this discussion. The apex of the cone is also supported in the longitudinal direction (parallel to the Y-axis) by a constraint that simulates the elevation drive pinion, as shown in Fig. 2b.

An independent structure, which is not shown on the figure, provides a separate support to bring the quadripod loads to the elevation axis. The quadripod structure is isolated from the reflector backup by its support to avoid load concentrations that would be incompatible with homology.

Before proceeding with the backup structure and support design, a preliminary design was performed for the support structure alone with simulated backup structure loadings. The purpose was to design the support to have sufficient stiffness for natural frequency requirements of the system. After this design was completed, some of the key supporting members were not allowed to change their properties when subsequently included with the entire structure. Had this exclusion not been made, designs to promote homology for the backup might have reduced the support stiffness excessively.

C. Computer Model

Symmetry of the antenna structure and gravity loading about the vertical plane perpendicular to the elevation axis (Y–Z plane, Fig. 1a) permits the analytical model to consist of only one-half of the structure. Consequently, only the structure contained between ribs 1 and 49 is

needed for the computer model. The individual members contained on these two ribs are represented by bars that have half the cross-sectional areas of the actual members. In the case of wind loading, which is not necessarily symmetrical, this half-model can treat winds only directly into the face or back of the reflector, since these can be assumed to be symmetrical with respect to the model. However, since the structure is also symmetrical with respect to a plane containing its focal and elevation axes, the response to winds from side directions will be exactly the same as the response to face or back winds.

IV. Computer Design Execution

To illustrate how the computer design can progress, Fig. 3 shows a sample design history for the reflector backup structure. The objective in this case is to reduce the average rms deflection for gravity loading over the elevation angle range from 0 to 90 deg.

The horizontal scale at the bottom gives the design cycle number; the top horizontal scale gives the elapsed CPU time on an 1108 computer. The vertical side scale is a relative scale used for both structure weight and performance objective. At the starting cycle, the structural weight was greater than a specified maximum. The weight was reduced to specification at the first design cycle, but the objective became worse as a result of the weight reduction. In succeeding cycles, the weight was maintained as specified and the objective rms improved, so that at the last cycle, it is three times better than at the start.

The initial analysis and five succeeding design analysis cycles were completed by the IDEAS program in about 15.5 min of CPU time. A similar problem required about the same time for a single analysis cycle on the NASTRAN program. Depending upon the time of the week when the run is made, the computer charges vary from $30.00 at the off-hours weekend night rate to about $330.00 at the prime weekday rate.

The amount of improvement that occurs for a design process of several cycles, such as shown in Fig. 3, depends to a large extent on the starting point. If there is a good starting point, for which member properties have been well chosen to produce a reasonably good objective, the amount of improvement by reproportioning these members would be expected to be relatively small. If, on the other hand, the starting member sizes were chosen more arbitrarily so that they did not produce a reasonably effective objective, there are more opportunities for improvement and a greater reduction of the objective can be expected. The design in Fig. 3 started from an arbitrary point in which the member sizes were chosen by empirical rules built into the code of the data generating program; hence, the 300% improvement. By the end of the second cycle, the new member sizes derived by the program had improved substantially from the arbitrary starting sizes, and from then on, the rate of improvement was slower.

In this particular case, the gravity objective rms was considerably better than required for X-band operation. A subsequent design was performed for which a lower maximum structural weight was specified to permit a larger but still acceptable rms. Figure 4 shows the history of a design process resuming from the results of the lower-weight subsequent design that was just described. This illustrates an antenna backup structure design that is a compromise for the not necessarily compatible requirements for performance for wind and for gravity loading.

This is done in two stages. In the first stage, the objective loading is a particular case of wind loading that is assumed to be critical, and the design objective is to minimize the rms deflections for this wind loading with a maximum weight specified to be somewhat less than would eventually be accepted. The progress of the first stage takes place over the first four design cycles that are shown in the figure. Notice that the wind objective is reduced from about 7.5 units to about 5 units, while a weight specification of 3 units is maintained. However, in this design, the gravity response deteriorates appreciably.

During the next stage, which is covered by the last four cycles in the figure, gravity performance was the objective. The weight specification is increased to 3.6 units, and no member is allowed to decrease in size to guarantee that the wind objective previously achieved will not be degraded. The gravity objective is then effectively reduced, the wind objective improves slightly, and the specified weight is maintained through the last cycle. In the final design, the gravity and wind objective have both been improved to about two thirds of their initial values. In view of the initial point, which in itself was relatively effective, being the result of prior design improvements, the achieved improvement of about 33% is considered to be substantial.

V. Design Results

A. Basic Configuration

A number of design variations were explored for the structure described in Figs. 1 and 2. In each of the explorations, the variations were made for alternative objectives with respect to the choice of either gravity or

wind loading as the design case, or selections from among preceding designs that were used as the starting points, or specified maximum total member weight, or relatively minor adjustments that related to groupings of members and establishment of initial minimum sizes. Each of these designs proceeded through four or five redesign cycles and produced restart member property cards to permit continuing designs that could resume from their best results. Four loading cases were used to establish minimum sizes required for stress integrity and to provide alternative choices of design objective for rms minimization:

(1) The gravity weight applied in the direction of the focal axis (Z-axis loading).

(2) The gravity weight applied in planes parallel to the aperture plane and acting perpendicular to the elevation axis (Y-axis loading).

(3) A survival wind load with the antenna at 90-deg elevation simulating a wind speed of 54 m/s (120 mph).

(4) A maximum operational wind load with the antenna at 60-deg elevation with wind from the rear and a wind speed of 34 m/s (77 mph).

The first two loading cases provide sufficient information to compute the gravity loading, and consequently the rms surface accuracy, at every elevation angle between the horizon and zenith. The second two wind loadings have been found to be the significant wind loading conditions for the Mars antenna.

In evaluating the performance of the new designs, the existing Mars antenna is used as a frame of reference for surface accuracy and tipping structure weight. Table 1 shows the Mars antenna data that are used for comparison.

As shown in Table 1b, the Mars antenna performs better with the wind from the front or rear than it does for the same wind loading applied from the side. This performance difference is the result of its unsymmetrical supporting configuration and does not have a preferential direction with respect to wind azimuth. Consequently, it seems reasonable to compare the performance of the new antenna designs with the average wind rms of the Mars antenna, which is also shown in this table.

Table 2 contains a summary of results for five new designs selected as the most promising from a much larger set of cases. These are listed in the order of their tipping weights, which were from 61% to 74% of the Mars antenna. All of these designs had considerably better performance with respect to gravity, but they did not always perform as well for the two wind loading cases. A composite rating factor is shown in the last three columns of the table, which gives a measure of design that takes weight and rms into account simultaneously. The factor is defined as the product of relative weight and relative rms. Factors less than unity are associated with designs that are more efficient than the Mars antenna; that is, designs with ratings less than unity would either weigh less for the same rms or would have a better rms for the same weight. In the particular case of wind loading, increasing the weight of the members by a common factor to bring the weight up to the weight of the Mars antenna would result in a design with an rms no more than the rating factor times the Mars antenna rms. Or equivalently, the antenna with additional reinforcing to have the same wind rms as the Mars would have a weight no more than its rating times the Mars antenna weight. In the case of gravity loading, where weight and rms response do not have a linear relationship but depend on the particular distribution of member properties, no such simple projections are possible.

In evaluating the relative performance merits of these alternative designs, it seems reasonable to consider the gravity performance to be more significant than the wind performance. The gravity loading is always present, while the joint occurrence of significant wind speeds and wind vector orientation relative to the antenna is statistical. Depending upon mission tracking requirements of the antenna system, it could be wasteful of material to reinforce the structure to maintain high performance for the occasional conditions of high wind speeds at unfavorable orientations. Either of design cases 64D-5 or 64E-5, which represent material savings of 39% and 35%, respectively, might be considered acceptable. Both of these designs are better for gravity performance than the Mars antenna, although the wind performance for the lighter of them is as much as 63% worse. Table 3 shows a comparison of weights of major components for these two antennas with the weights of the corresponding components of the Mars antenna (see Table 1).

B. Variations From the Basic Configuration

Several design variations from the basic configuration were explored to obtain guidance in establishing an eventual preferred configuration. The results of these are summarized below.

1. Reduced Number of Support Bars. As shown in Figs. 1 and 2, the alternate main ribs of the basic design are supported by a total of 24 cone support bars (marked A–S). As a variation, two out of every three of these bars

were removed to investigate an opportunity to simplify fabrication and to increase clearances that would allow greater latitude in the alidade and support structure layouts. Removal of these bars tests the ability of the hoop trusses to distribute the loads in the circumferential direction from the unsupported ribs to the nearest supported ribs. In the basic design, there is only one unsupported main rib between supported ribs, while in the present variation, there are five unsupported ribs between any pair of supported ribs. With fewer supports, a small but noticeable deflection wave in the circumferential direction was found at radii near the radius of the support ring. However, progressing radially outwards towards the rim, this wave damps out rapidly because of the hoop truss action. The results of several trial designs show that for equivalent tipping structure weight, removal of the support bars provides no significant penalty of gravity rms but in some cases, increased the wind rms by from 15% to 50%. With additional design trials and the acceptance of some minor weight penalty, the wind rms undoubtedly could be brought closer to that obtainable with the basic number of supports.

2. Alternative Focal Length to Diameter Ratios. The focal length-to-diameter ratios (F/D) of the Mars antenna and the basic design are 0.423. Several other antennas in use have smaller ratios, which result in more sharply curved surfaces. A variation in F/D ratio was investigated to see if there is a structural advantage in using shorter focal lengths. The additional ratios investigated were $F/D = 0.33$ and $F/D = 0.25$. Figure 5 shows envelope sketches and dimensions for comparison. To provide for equitable design comparisons, envelope dimensions were established to provide the same alidade clearance at the breakpoint (change in slope of the bottom of the truss main rib) for all variations. The truss depth at the vertex was maintained exactly the same, and the maximum truss depths at the breakpoints were approximately the same. The smaller F/D ratios bring the vertex and focal point closer to the elevation axis, but the parabola rim is farther from the axis because of the increased curvature. Table 4 contains summary comparison results for two designs with these new F/D ratios and repeats the summary information for design 64D-5, which has a similar weight. From Table 4 we find no clear preference for either of the alternative F/D ratios. These and other designs not summarized in the table indicated slightly better gravity rms for the smaller F/D ratios and slightly worse wind rms.

3. Configuration Modifications. The support structure configuration of the basic design was chosen to be nearly compatible with the alidade structure of the Mars antenna. As a result of an examination of feasible configurations for new alidades, it was found that the vertex of the reflector could be brought closer to the elevation axis than it is shown to be in Fig. 1a. Specifically, a layout of a new alidade was developed to reduce the distance from the elevation axis to the bottom of the rib trusses at the vertex by about one half. This provides the advantage of bringing the structure closer to the elevation axis, reducing the counterweight, and reducing moments of inertia for driving about the elevation axis. It was also decided to reduce the number of structural members by doubling the spacing between main ribs, reducing their number by one half. With this new spacing, some of the surface panels are supported directly on the top hoop members with no supporting diagonal members to assist in carrying the load. This adds a small but acceptable amount of additional bending deflections at these points. The lower number of ribs also implies a total of only 12 rather than 24 cone support points. However, it was shown previously that as few as 8 support bars could be sufficient. A top view of the corresponding framing of the top surface of the half antenna model is shown in Fig. 6.

Preliminary results obtained so far for this model indicate promising opportunities for weight reductions. Therefore, studies of this modified configuration are continuing, and further refinements of the layout and design are being developed. Table 5 contains a comparative summary of two initial designs that have been developed. The first case represents the lowest weight that has been achieved in a design for a gravity rms objective. The gravity rms and low weight are promising, but the relatively high wind rms indicates that further reinforcement may be necessary for improvement. The second case in the table represents a heavier design but, nevertheless, is lighter than any of the basic configuration designs. This second case indicates that further development is also needed to improve its wind performance.

VI. Summary

Conceptual studies of new 64-m antenna reflector backup and support structures are performed efficiently using new special-purpose software to generate, analyze, and design the structures. New designs are assembled and processed rapidly and economically in investigations of design improvements to be achieved through parameter and configuration variations.

Design studies performed for a basic model of a new antenna result in tipping weights with respect to the elevation axis of from 61% to 74% of the corresponding

weight for the existing Mars antenna. In addition to these weight savings, the emphasis in the new designs upon modular repetition of structural component members will produce additional economies in manufacture. The new designs have better accuracy and RF performance for gravity loading than the Mars antenna, although their accuracy for wind loadings tend not to be as good in view of their lighter weights. Nevertheless, because gravity loading is always present and significant wind loading is only occasionally present, the importance of performance for gravity loading predominates over the importance of wind loading performance.

A special study to investigate reducing the focal length-to-diameter ratio of the reflector, which would produce more sharply curved surfaces, indicates no major advantages in the structure design. It was found that shorter focal lengths are a little better for gravity loading and a little worse for wind loading.

Initial investigations found a promising modification of the basic configuration design that provides additional weight reductions resulting in weights in the neighborhood of half of the Mars antenna weight. The modification has about half the ribs of the basic configuration, which would further simplify fabrication. It would require, however, a different alidade configuration from the basic model. The basic model, on the other hand, is more closely compatible with the Mars alidade. Design studies are currently continuing for further refinement of this newest design.

References

1. *The NASTRAN User's Manual (Level 15.0)*, NASA SP-222(01). C. W. McCormick, editor (May 1973).
2. Levy, R., "Iterative Design of Antenna Structures," *The Deep Space Network Progress Report*, Technical Report 32-1526, Vol XII, Jet Propulsion Laboratory, Pasadena, California, pp. 100–111 (Dec. 15, 1972).
3. Von Hoerner, S., "Homologous Deformations of Tiltable Telescopes," *J. Structural Div., Proc. ASCE.* Vol. 93, No. ST-5, Proc. Paper 5529, pp. 461–485 (Oct. 1967).
4. Hachenberg, O., Grahl, B., and Wielebinski, R., "The 100-Meter Radio Telescope at Effelsburg," *Proc. IEEE*, Vol. 61, Sept. 1973, pp. 1288–1295.
5. Ruze, J., "Antenna Tolerance Theory-A Review," *Proc. IEEE*, Vol. 54, No. 4, April 1966, pp. 633–640.
6. Utku, S., and Barondess, S. M., *Computation of Weighted Root-Mean-Square of Path Length Changes Caused by the Deformations and Imperfections of Rotational Paraboloidal Antennas*, Technical Memorandum 33-118, Jet Propulsion Laboratory, Pasadena, California, March 1963.

Table 1. Mars 64-m comparison data

a. Components

Item	Mass, kg	Weight, kips
Reflector backup	315	695
Elevation wheel, reflector support and counterweight	751	1655
Quadripod and subreflector	25	55
Feed cone	27	60
Surface panels	26	58
Total tipping structure	1144	2523

b. Surface accuracy

	rms distortion	
	mm	in
Gravity, maximum	0.51	0.020
Survival wind, 90-deg elevation		
From front	4.54	0.179
From side	9.09	0.358
Average	6.82	0.269
Operational wind, 60-deg elevation		
From rear	1.93	0.076
From side	3.86	0.152
Average	2.90	0 114

Table 2. Summary of five new alternate designs

Run number	Tipping weight relative to Mars	Surface rms relative to Mars			Composite rating		
		Worst gravity	Survival wind	Operational wind	Worst gravity	Survival wind	Operational wind
64 D-5	0 61	0.55	1.32	1.63	0.34	0.81	0.99
64 E-5	0.65	0 83	0.97	1.19	0.54	0.63	0.77
64 D-1	0.67	0 40	1.35	1.66	0.27	0.91	1.11
64 F-2	0.71	0.64	0.89	1.09	0.45	0.61	0.77
64 F-5	0.74	0.40	0.86	1.05	0 29	0.63	0.78

Table 3. Component weight comparisons with respect to Mars antenna

Item	Run number	
	64 D-5	64 E-5
Reflector backup	0.50	0.57
Elevation wheel, reflector support and counterweight	0.61	0.64
Quadripod and subreflector	1.12	1.12
Feed cone	1.00	1.00
Surface panels	1.00	1.00
Total tipping structure	0.61	0 65

Table 4. Summary of designs for alternative F/D ratios

Run number	F/D	Tipping weight relative to Mars	Surface rms relative to Mars			Composite rating		
			Worst gravity	Survival wind	Operational wind	Worst gravity	Survival wind	Operational wind
64 D-5	0 423	0.61	0.55	1.32	1.63	0.34	0.81	0.99
33 B-4	0.333	0.62	0.37	1.43	1 74	0.23	0 89	1.08
25 B-4	0.250	0.62	0.55	1 42	1.72	0 34	0.88	1 07

Table 5. Sample design summaries for modified configuration

Run number	Tipping weight relative to Mars	Surface rms relative to Mars			Composite rating		
		Worst gravity	Survival wind	Operational wind	Worst gravity	Survival wind	Operational wind
02-5	0 44	0.95	2.42	3.79	0 42	1.06	1.67
02-I	0.58	0 49	1.42	2.18	0.28	0.82	1.26

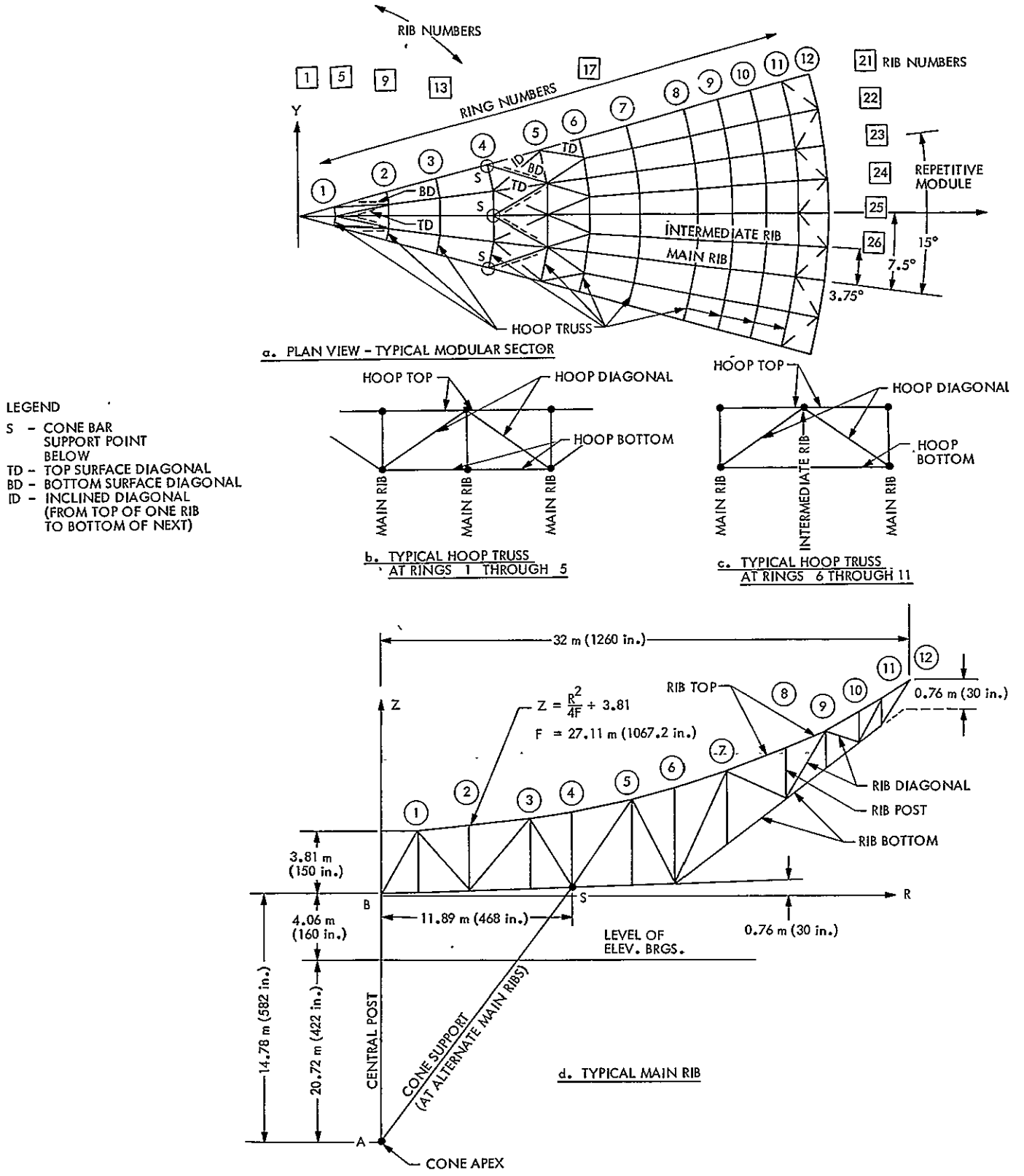

Fig. 1. Backup structure framing members

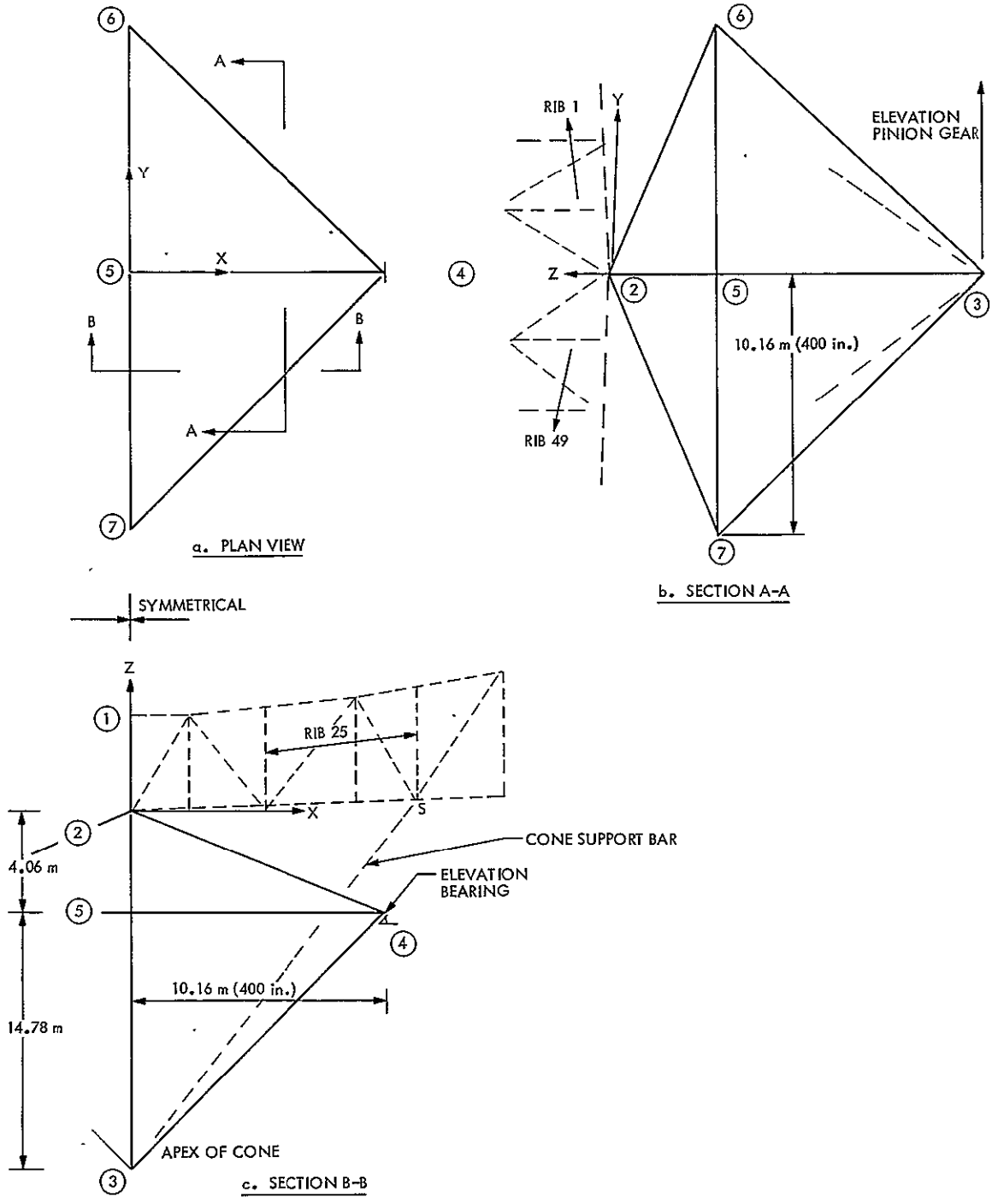

Fig. 2. Support structure for backup

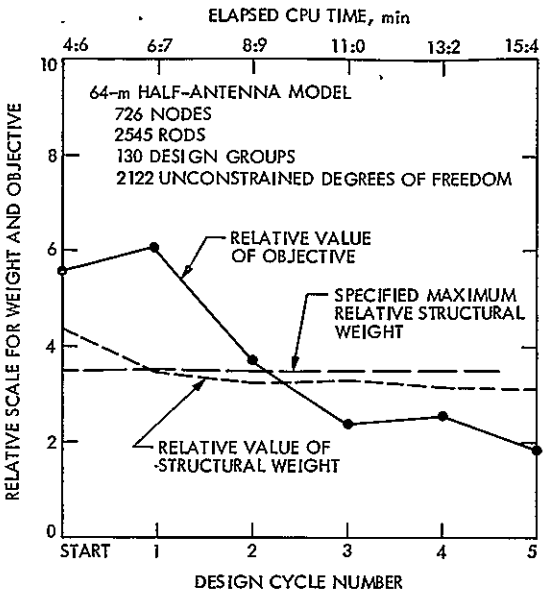

Fig. 3. Design history for 64-m antenna structure

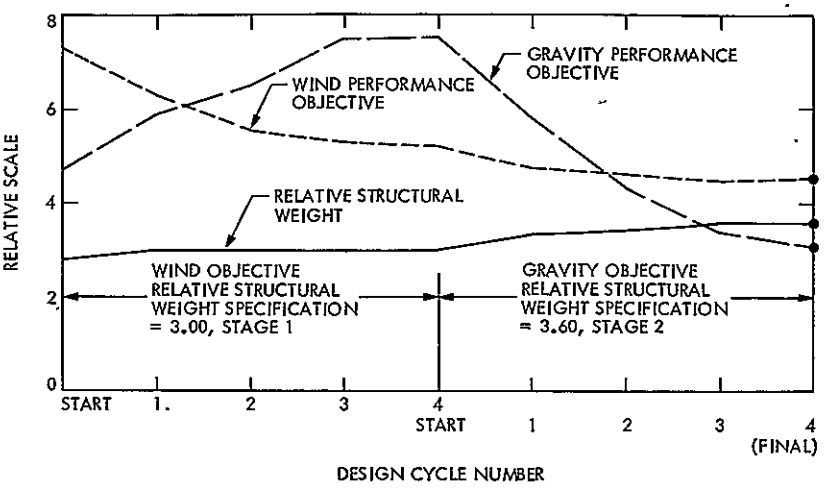

Fig. 4. Wind/gravity design history

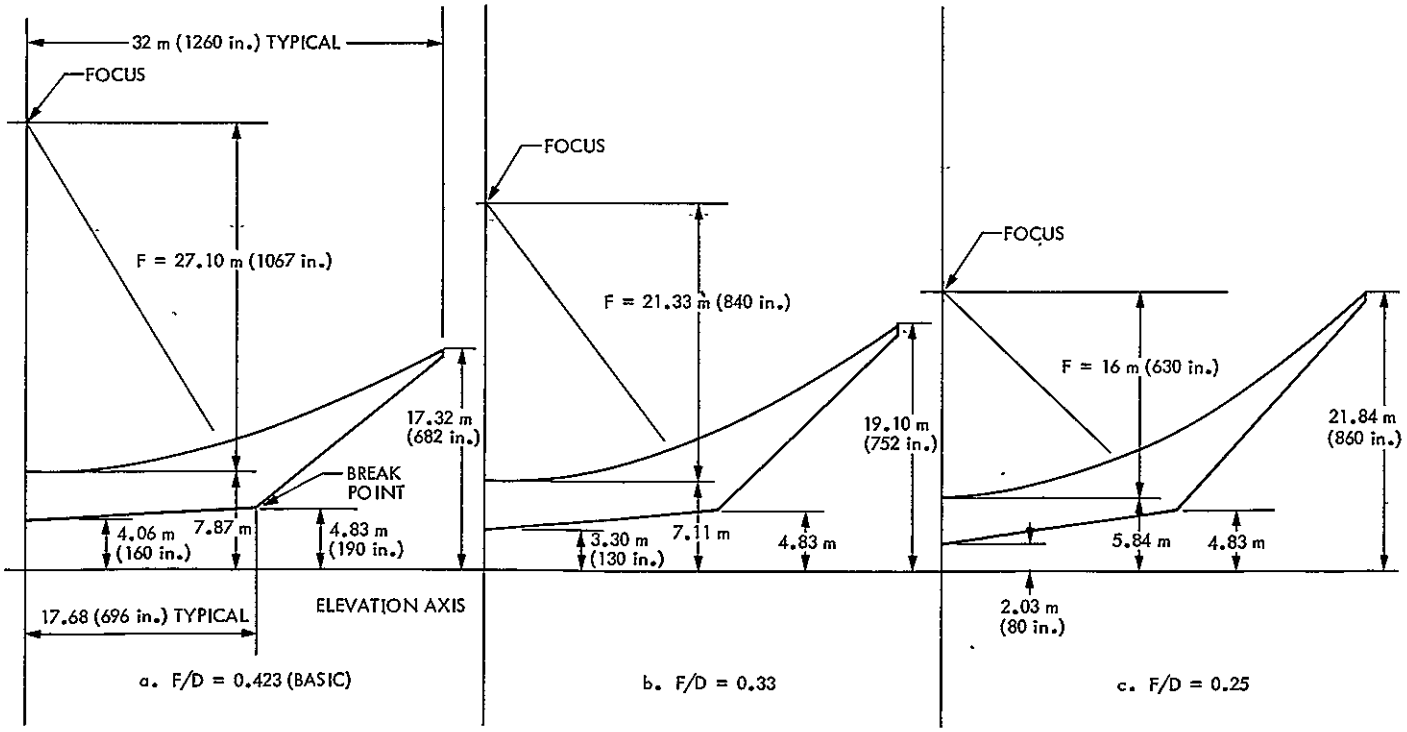

Fig. 5. Envelope dimensions for focal length-to-diameter variations

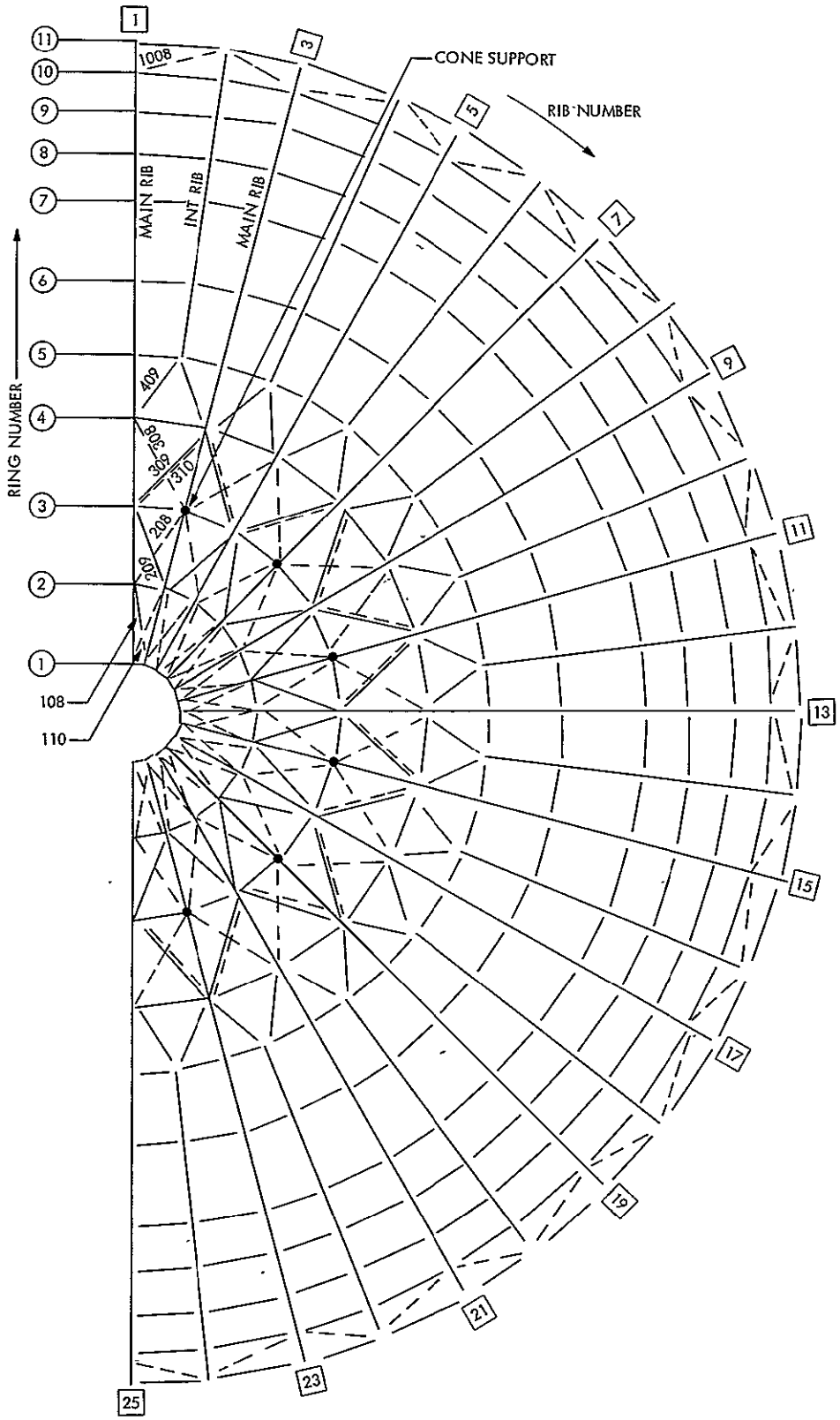

Fig. 6. Modified configuration top surface framing

DSS 14 Operating Noise Temperature During Helios 1 Near-Sun Tracking

C. T. Stelzried and D. Girdner
Communications Elements Research Section

When spacecraft are tracked near the line-of-sight of the Sun, the ground antenna sidelobes "see" the solar noise. The solar noise increases the ground system operating noise temperature and degrades the downlink RF reception performance. At specific antenna azimuthal angles relative to the Sun, noise peaks and nulls occur periodically throughout a day's tracking pass due to the quadripod support leg-generated sidelobes. This article documents this effect while tracking Helios 1, illustrates the time of the peaks, and compares the predicted time of the noise temperature peaks with the measured data.

I. Introduction

The ground antenna sidelobes "see" solar noise when tracking a spacecraft near the Sun line-of-sight. The solar noise increases the ground system operating noise temperature and degrades the downlink sensitivity. This occurs when the Goldstone Mars Deep Space Station (DSS 14) 64-m antenna operates at 2.2 GHz and the Sun–Earth–probe (SEP) angles are less than about 5 deg. Periodic peaks and nulls occur in the operating noise temperature (T_{op}) during a day's track. This is shown in the idealized curves of Fig. 1 and results from the Sun passing through the sidelobe positions of the ground antenna pattern as distorted by the quadripod support legs (Refs. 1 and 2). The azimuthal angle ϕ is defined in Fig. 2 for the northern hemisphere. (Reverse N–S and E–W on the figure in the southern hemisphere; all other figures assume northern hemisphere.)

II. Prediction of T_{op} Peak and Null Times of Occurrence

Figures 3 and 4 show plots of the "Sun path" for DSS 14 & 63 and DSS 43, respectively, computed from the Sun and Helios 1 spacecraft difference declination and difference right ascension as obtained from station-supplied computer polarization predicts and The American Ephemeris and National Almanac. These data are listed in Table 1 for Helios 1 for the period April 8 to May 12, 1975. The solid straight lines represent the values of ϕ (60, 120, 240, 300 deg) for the sidelobe peaks previously discussed. The

dashed straight lines, offset 12 deg from these peaks, are required to predict peak temperature duration times. Also shown is a typical sidelobe–Sun angle (SSA) representing the azimuthal difference angle between the sidelobe and the Sun applicable at meridian transit only:

$$\text{SSA} = \text{sidelobe angle} - \text{Sun path angle}$$

For this example (Fig. 3) on May 8, SSA = −13 deg for ϕ = 280 deg. The graph is used to read off values for SSA over the time period April 8 to May 12, 1975 and listed in Table 2. SSA is always less than 60 deg.

Figure 5 shows a graph useful for predicting the approximate polarizer setting as a function of spacecraft right ascension and declination and antenna hour angle. The polarizer predicts at meridian transit are used with SSA to predict the time of peak T_{op} (Philco memo M-0875-110, 27 August 1975). This has been calculated and tabulated for Helios 1 in Table 3.

Figure 6 shows a plot of DSS 14 T_{op} measurements while tracking Helios 1 in the near-Sun region as a function of time of day. Also shown are the predicted times of maximum T_{op}.

Figure 7 shows a plot of the DSS 14 T_{op} measurements as a function of Sun–Earth–probe angle comparing peak and minimum values for Pioneer 6 data (near solar cycle maximum) and Helios 1 data (near solar cycle minimum).

References

1. Bathker, D. A., "Large Ground Antenna Performance with Solar Noise Jamming," *Proc. IEEE*, Vol. 54, p. 1949, Dec. 1966.
2. Stelzried, C. T., *A Faraday Rotation Measurement of a 13-cm Signal in the Solar Corona*, Technical Report 32-1401, p. 33, Jet Propulsion Laboratory, Pasadena, Calif., July 15, 1970.

Table 1. Sun/Helios 1 position angle differences for first superior conjunction

Day of year (1975)	Right ascension, deg	Declination, deg
98	4.475	1.872
102	3.270	1.332
108	1.933	0.749
112	1.311	0.488
116	0.870	0.310
120	0.611	0.201
124	0.454	0.147
128	0.445	0.134
132	0.547	0.150

Table 2. Sun/sidelobe angle (SSA) azimuthal position for Helios 1 (applicable at meridian transit only)

Day of year (1975)	DSS 14 and DSS 63		DSS 43	
	SSA (for peak of ϕ = 300°), deg	SSA (for peak of ϕ = 240°), deg	SSA (for peak of ϕ = 60°), deg	SSA (for peak of ϕ = 120°), deg
98	52.8	−7.2	−7.2	52.8
102	52.2	−7.8	−7 8	52.2
108	51.5	−8.5	−8.5	51.5
112	50.0	−10.0	−10.0	50.0
116	49.5	−10.5	−10.5	49.5
120	48.6	−11.4	−11.4	48.6
124	47.8	−12.2	−12 2	47.8
128	47.0	−13.0	−13.0	47.0
132	46.4	−13.6	−13.6	46.4

Table 3. Calculated peak T_{op} for Helios 1

SEP, deg	Day of year (1975)	Time, GMT								T_{op}, kelvins	
		ϕ = 300°				ϕ = 240°					
		Start	Peak	End	Duration, min	Start	Peak	End	Duration, min	Peaks (both)	Low
1.25	113	≈13:33	17:00	18:11	278	19.34	20:01	20.28	54	130	45
0.83	117	13:32	17:17	18:13	281	19:36	20:02	20:28	52	280	100
0.58	121	13:32	17:26	18.15	283	19:38	20:03	20:28	50	610	270
0 53	122	13:31	17:36	18:17	286	19:38	20:03	20:28	50	850	410
0.48	124	13:31	17:42	18:20	289	19:40	20:04	20:28	48	1200	630
0.47	125	13.30	17:45	18:23	293	19:40	20:04	20:28	48	1400	770
0.46	127	13:30	17:51	18:27	297	19.41	20:03	20:27	46	1800	850
0.48	129	13·29	18:02	18:30	301	19:42	20:03	20:26	44	1340	720
0.51	130	13:28	18:03	18.34	306	19.42	20:02	20:25	43	1050	520
0.61	133	16:38	18.04	18:39	121	19.43	20:01	20:25	42	540	250
0.66	134	17:25	18:10	18:41	116	19:44	20.01	20:24	40	460	190

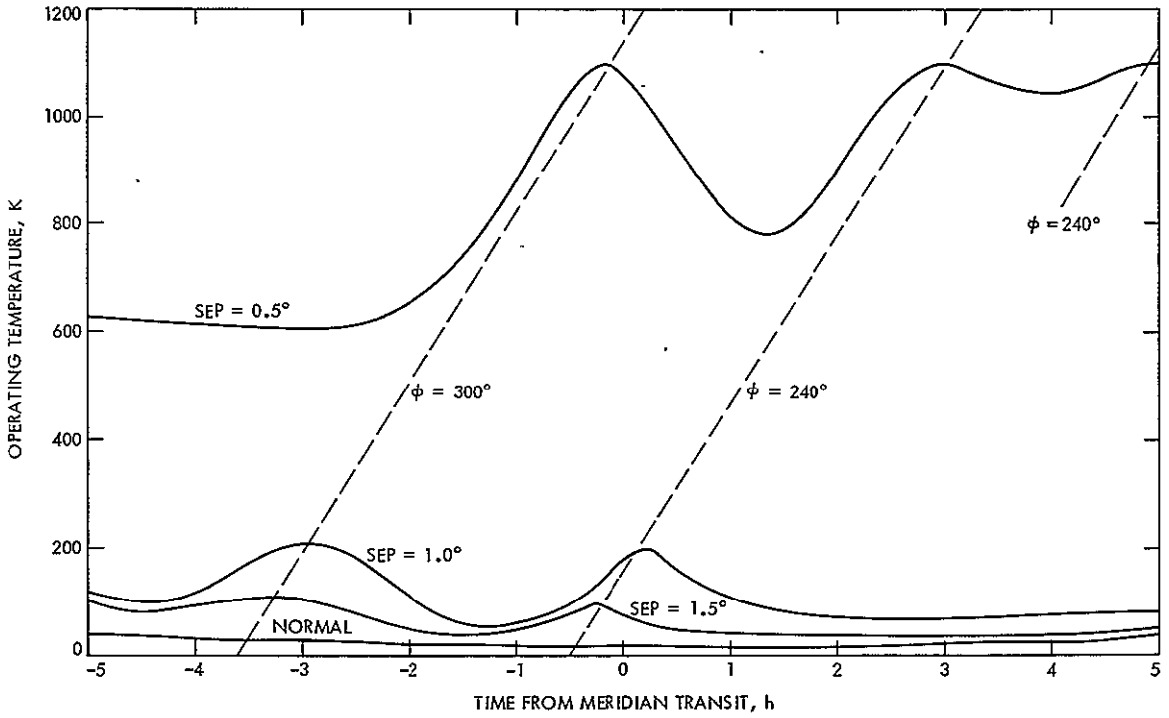

Fig. 1. Idealized curves showing system operating noise temperatures when tracking near the Sun

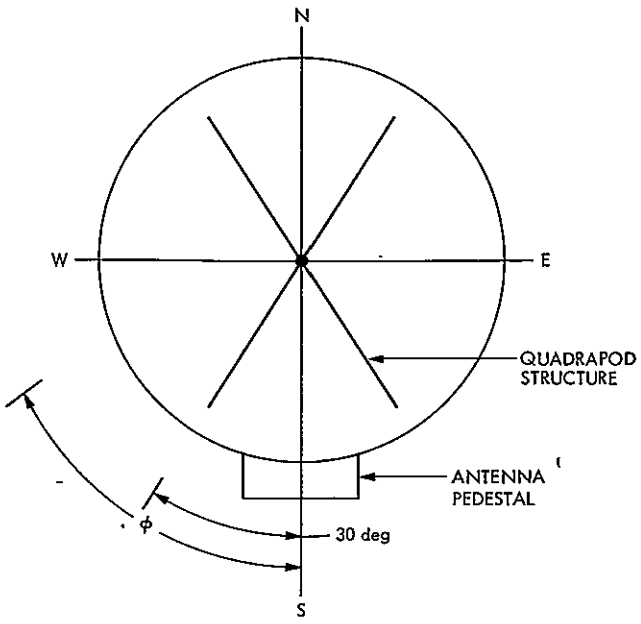

Fig. 2. Reflector coordinate system (looking toward dish) defining azimuthal angle ϕ

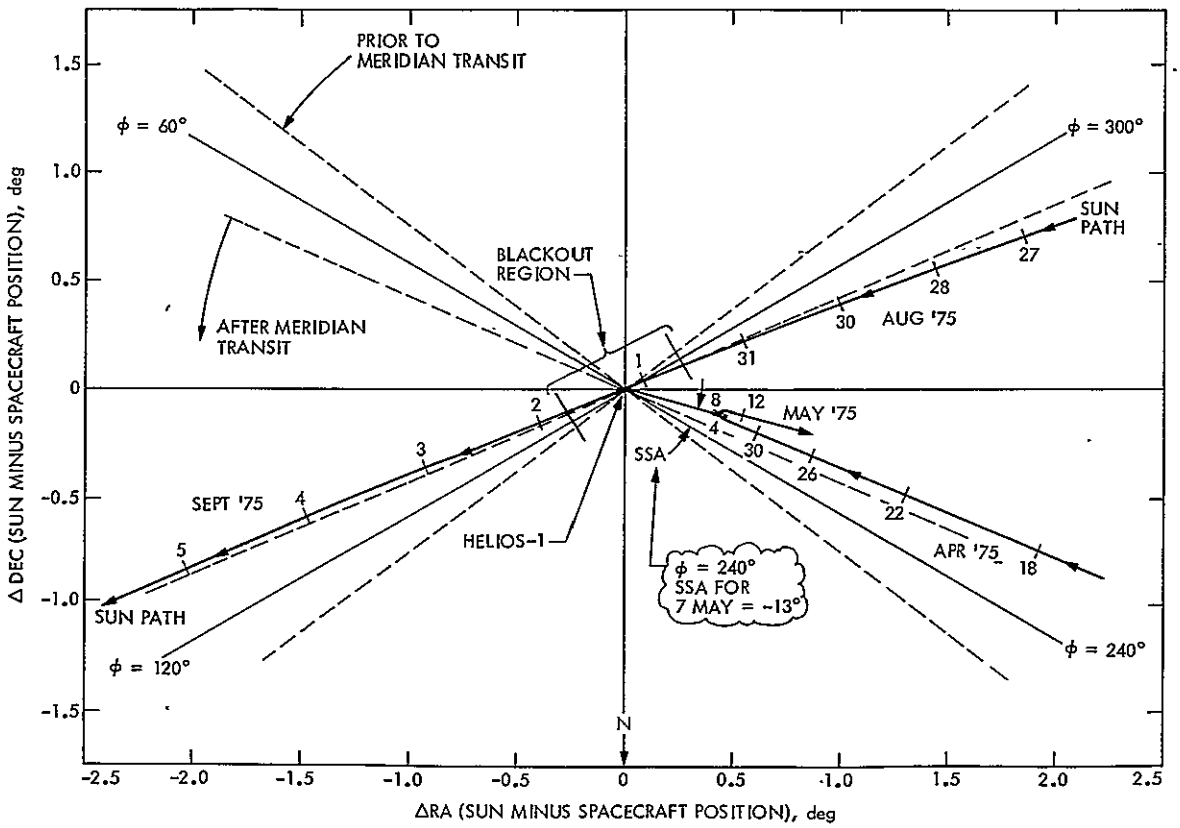

Fig. 3. Plot of position relative to Helios 1 for DSS 14/63

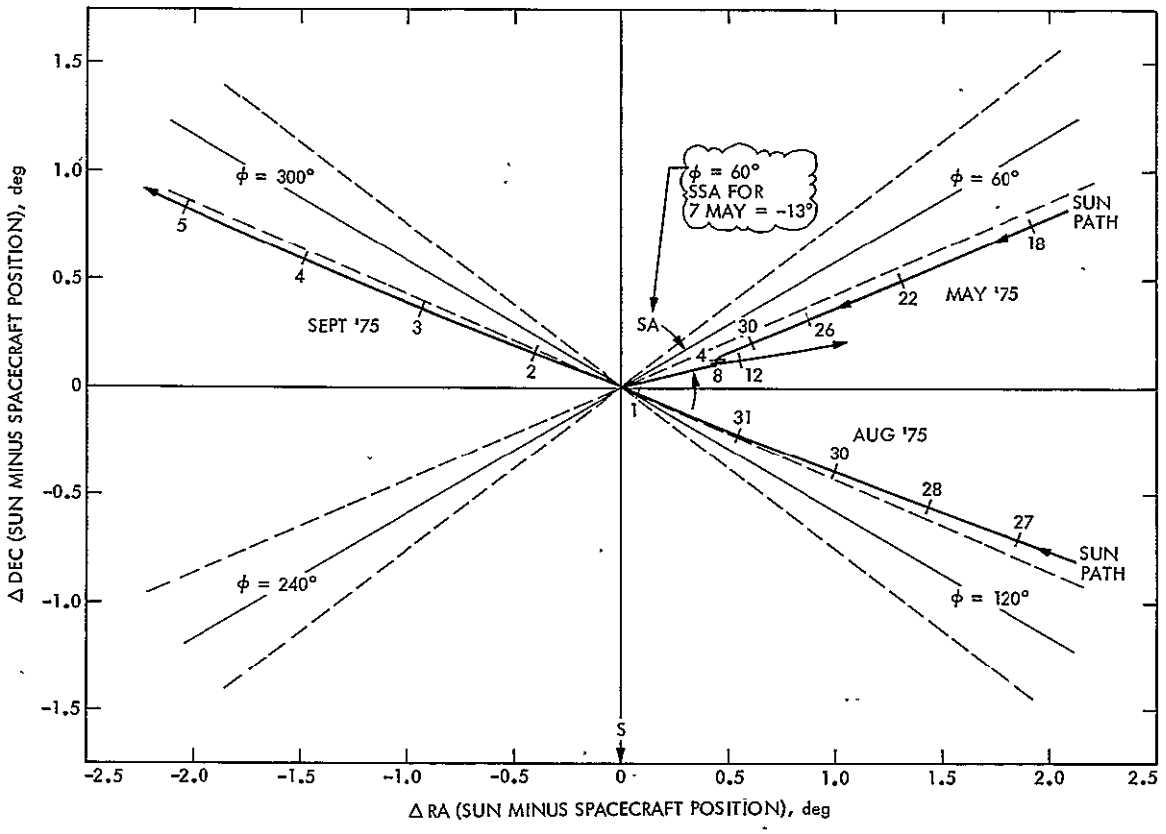

Fig. 4. Plot of position relative to Helios 1 for DSS 43

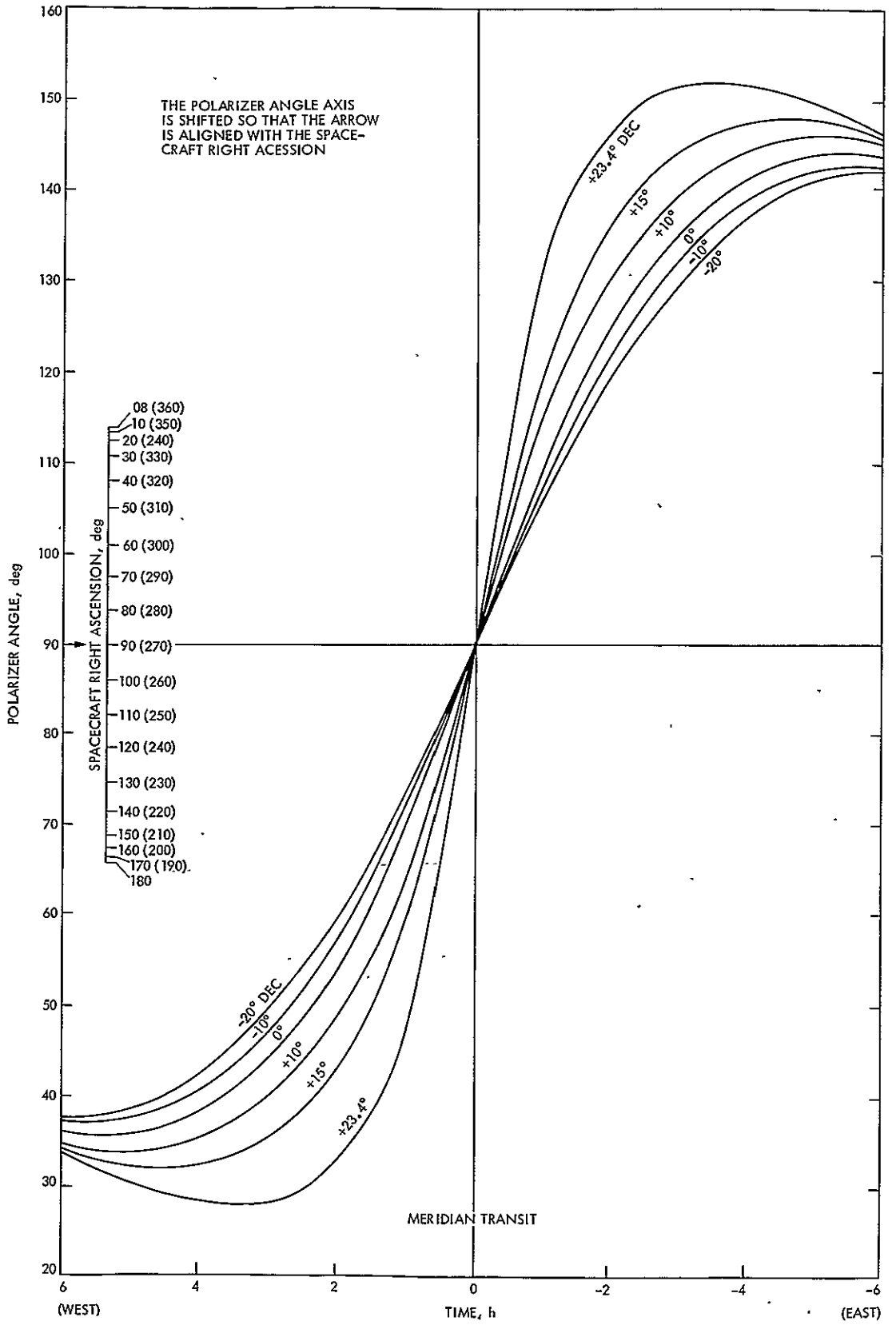

Fig. 5. Polarization angle prediction graph for DSS 14/63

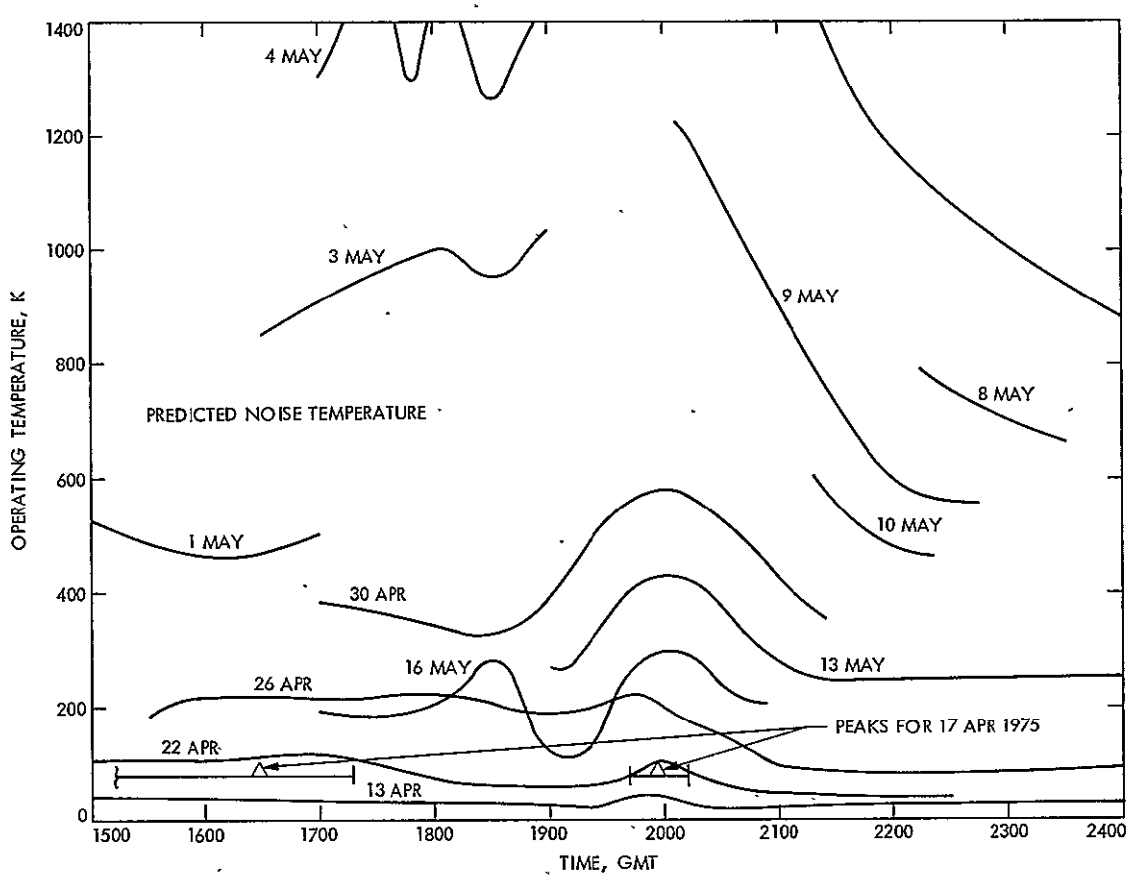

Fig. 6. System operating noise temperature during Helios 1 track in the near-solar region as a function of time of track

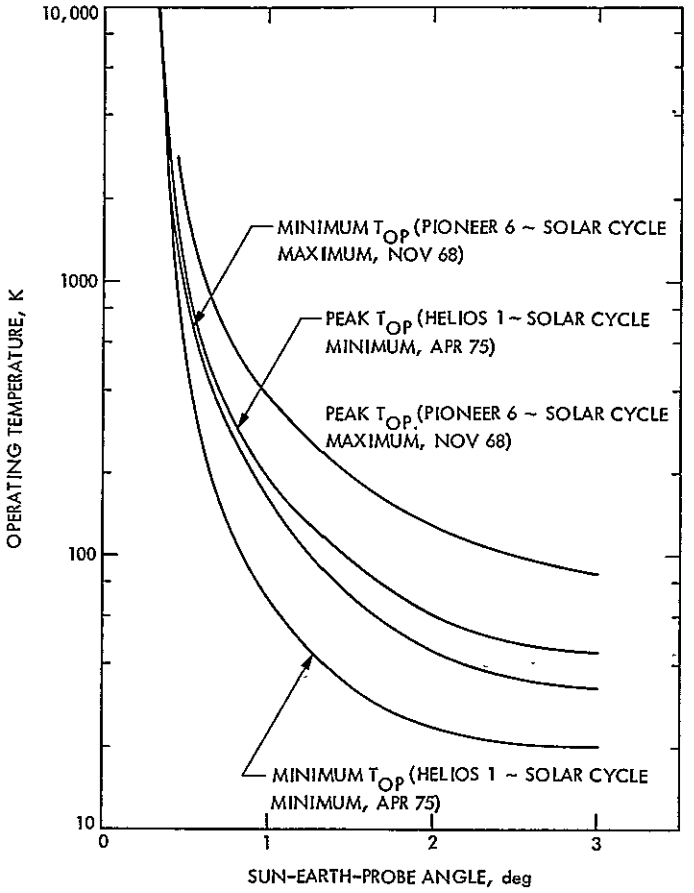

Fig. 7. System operating noise temperature during Helios 1 track in the near-solar region as a function of Sun-Earth-probe angle

Development of a Water Vapor Radiometer to Correct for Tropospheric Range Delay in DSN Applications

P. D. Batelaan, T. Sato, S. D. Slobin, and H. Reilly
Communications Elements Research Section

The rationale for a Water Vapor Radiometer (WVR) as an aid in predicting tropospheric delay correction is presented. Included is a block diagram and a description of the present developmental WVR with the semiautomated operating sequence outlined. A brief summary of field tests at El Monte airport and Pt. Mugu is given.

I. Introduction

Continued improvements in spacecraft navigation and radio interferometry have resulted in lowering the uncertainties that are contributed by various error sources. As a result of this, the uncertainty caused by tropospheric delay has come under consideration. This delay can be conveniently separated into two components, dry and wet. The dry, nearly constant atmospheric component is well understood and because of its relationship to easily measured surface parameters, it can be readily accounted for. The wet, variable atmospheric component varies from a delay of nearly zero, for dry air, to about 30 cm for saturated air at zenith (Ref. 1). A means of remotely sensing the integrated value of the total water that causes this delay, in the line of sight, is microwave radiometry. This knowledge can then lead to an RF delay correction for the wet component for use in spacecraft navigation or various forms of interferometry.

This RF delay is primarily due to the dielectric effects of water vapor and is only slightly coupled to water droplets. However, the converse is true of the radiometric emission qualities; the radio noise is largely due to liquid water (when present in the form of rain and clouds), and only slightly to water vapor. This means that in a single measurement of total water radiometric emission for the purpose of sensing delay-causing vapor, the noise from the vapor is dominated by the noise from the liquid component. This problem has been overcome by using a two-frequency radiometer with one channel at 18 GHz and the other channel at 22.2 GHz. The 22.2-GHz channel is largely sensitive to water vapor because this is a resonant frequency of the water vapor, while the 18-GHz channel responds largely to liquid water as previously described. This allows separation of the contaminating liquid component signal from the desired vapor component signal in the data stream (Ref. 2).

II. Description

The Water Vapor Radiometer (WVR) presently under development for Earth-based/DSN applications benefited from the previous accomplishments of the Science Division radiometers for use on NIMBUS satellites (Refs. 3, 4). Because the present effort was started as an upward-looking, ground-based philosophy rather than a nadir-viewing, spacecraft-based one, some aspects of the design were changed. These changes and their rationale will be described in detail in a future article.

The frequencies selected allow use of a single corrugated right circular polarization (RCP) horn of about 8-deg beamwidth. As shown in the block diagram (Fig. 1), this horn is followed by a waveguide switch that allows receiver selection of the three receiver loads; horn, ambient calibration, or cold calibration. Next is a coupler to inject the noise for the Noise Adding Radiometer (NAR) (Ref. 5). A mixer, intermediate frequency (IF) amplifier, dual Gunn-diode local oscillators and a local oscillator (LO)-select switch complete the receiver. The receiver package, including the coupler onward, is enclosed in a temperature-controlled box. A special effort has been made to use commercially available components and assemblies wherever possible. Exceptions to this are the horn antenna, the cold calibration load, and the load-select waveguide switch. The horn was required to have small size combined with high beam efficiency. The load-select switch needed to be low loss, low voltage standing wave ratio (VSWR), very repeatable, and with three positions. The cold calibration load subassembly required a portable, reliable, refrigeration scheme combined with a high-quality waveguide load. The requirements for these could not be met by any known commercial items.

The operation of the radiometer is semiautomated. A JPL-developed microprocessor/controller selects local oscillator frequencies, loads, controls the NAR, and receives and outputs data to a teletype and paper tape punch.

The radiometer is presently mounted on a commercial, small antenna positioner with remote manual readout and control (Fig. 2). For field operations this assembly is placed atop a trailer with the several racks of support equipment, and space for personnel, inside (Figs. 3, 4).

Briefly, the WVR automatically sequences as follows:

(1) At 18 GHz, the relative RF noise and the physical temperature of the ambient calibration load are measured and recorded.

(2) At 18 GHz, the relative RF noise and the physical temperature of the cold calibration load are measured and recorded.

(3) At 18 GHz, the relative noise from the horn is measured and recorded.

(4–6) Repeat Steps 1–3 at 22.2 GHz.

Also recorded are azimuth, elevation, day, and time. The nonreal time data reduction corrects the relative RF noise mesurements of ambient load, cold load, and horn, for match and loss, scales the corrected RF noise values for hot load and cold load to their measured physical temperatures, and outputs absolute radiometric sky temperature.

III. Operations

To date the instrument has gone through one upgrade in its design as a result of its first field test at El Monte Airport in May 1975. It has also recently (March 1976) been field tested at the Naval Pacific Missile Test Center (PMTC) at Pt. Mugu. Both tests were accomplished in conjunction with the Mission Analysis and Space Sciences Divisions.

At El Monte, the WVR was operated for side-by-side comparisons with two Space Sciences Division instruments, the Scanning Microwave Inversion Layer Experiment (SMILE) and the Nimbus-E Microwave Spectrometer (NEMS) (Figs. 5, 6). In addition, Division 39 arranged for an aircraft (provided under contract with MRI, Inc.) instrumented with various water-sensing equipment to fly radial vectors at several elevation angles. While the aircraft instruments recorded the line-of-flight water data, the radiometers simultaneously recorded at the same azimuth and elevation vectors. In addition, data from the U.S. Weather Service radiosondes, launched twice daily at El Monte Airport, were made available. In all, four flight tests were conducted during the one month that the three radiometers remained at this location. Data for radiosonde comparison were taken twice daily, and various other operational techniques and tests were conducted.

The March 1976 tests at Pt. Mugu were also conducted side-by-side with SMILE. The MRI aircraft was again flown along various vectors, but with improved instrumentation aboard. Radiosonde data were made available from twice-daily flights made by Pt. Mugu personnel. These

sondes (technically Rawinsondes) and their associated ground receivers and instrumentation, were of much better accuracy than the units at El Monte. The Navy also furnished an aircraft, fitted with a microwave refractometer (AN/AMH-3), which flew the same vectors as the MRI aircraft. The aircraft flight tests were conducted during four days over a two-week period. During the remainder of the two-week time, the WVR was used to conduct various other tests and develop operational techniques.

IV. Results

Reductions and analysis of the data taken at El Monte showed that several problem areas existed, some equipmental and some operational.

Equipment difficulties encountered were: poor LO stability on the 18-GHz channel, unstable match on the LO select switch, calibration load match uncertainties, and calibration load radiometric temperature uncertainties.

Operations at El Monte demonstrated the need to better understand the nature of how water is distributed in the air, and the best way to measure this phenomenon for use as a range correction. Based on this, the instrument was upgraded to correct the deficiencies mentioned above, and the tests at Pt. Mugu were conducted.

The Pt. Mugu data are presently being reduced and will be reported in the near future. Preliminary examination shows much improved stability over previous data.

References

1. Waters, J., "Atmospheric Effects on Radio Wave Phase and the Correction of Vapor-Caused Phase Fluctuations by Radiometric Measurements of Water Vapor Emission," VLA Scientific Memo No. 8. National Radio Astronomy Observatory, Charlottesville, Va., September 15, 1967.
2. Webster, W. J., "On the Determination of Atmospheric Path Length by Passive Microwave Radiometer," X-922-75-107. Goddard Space Flight Center, Greenbelt, Md., May 1975.
3. Staelin, D. H., et al., "The Nimbus-E Microwave Spectrometer," *The Nimbus-5 Users Guide*, Goddard Space Flight Center, November 1972.
4. Staelin, D. H., et al., "The Scanning Microwave Spectrometer Experiment," *The Nimbus-6 Users Guide*, Goddard Space Flight Center, February 1975.
5. Batelaan, P. D., et al., "A Noise-Adding Radiometer for Use in the DSN," *The Deep Space Network*, Space Programs Summary 37-65, Vol. II, Jet Propulsion Laboratory, Pasadena, Calif., September 1970.

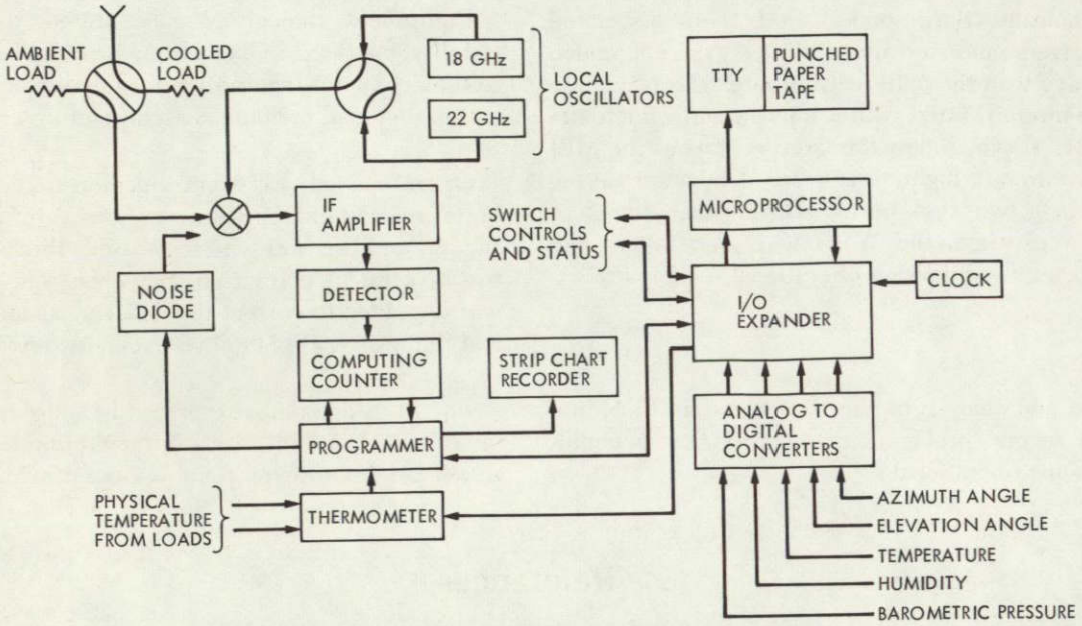

Fig. 1. Block diagram of developmental Water Vapor Radiometer

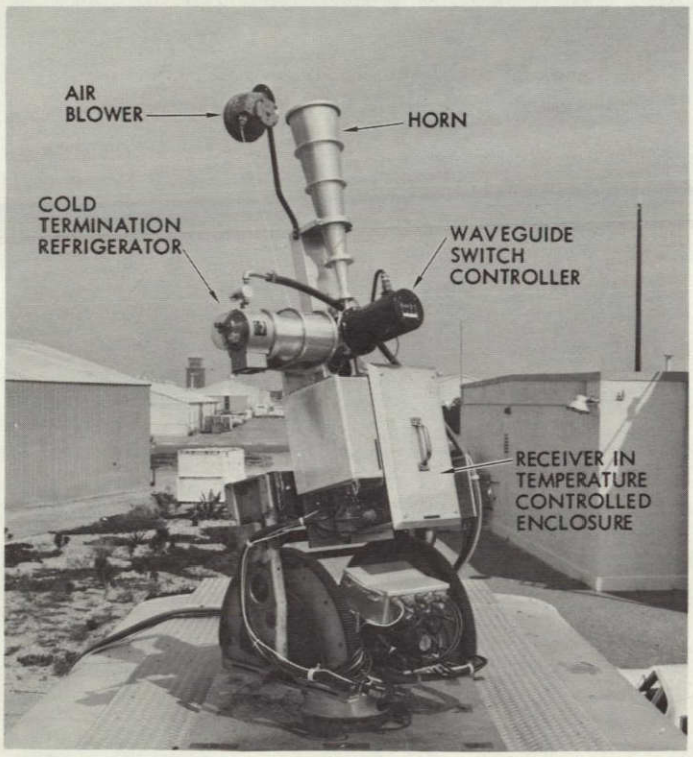

Fig. 2. The Water Vapor Radiometer. In the background is the Pt. Mugu Flight Control Tower

Fig. 3. The Water Vapor Radiometer mounted on its trailer for field testing

Fig. 4. Control monitor and recording equipment for the Water Vapor Radiometer located inside trailer

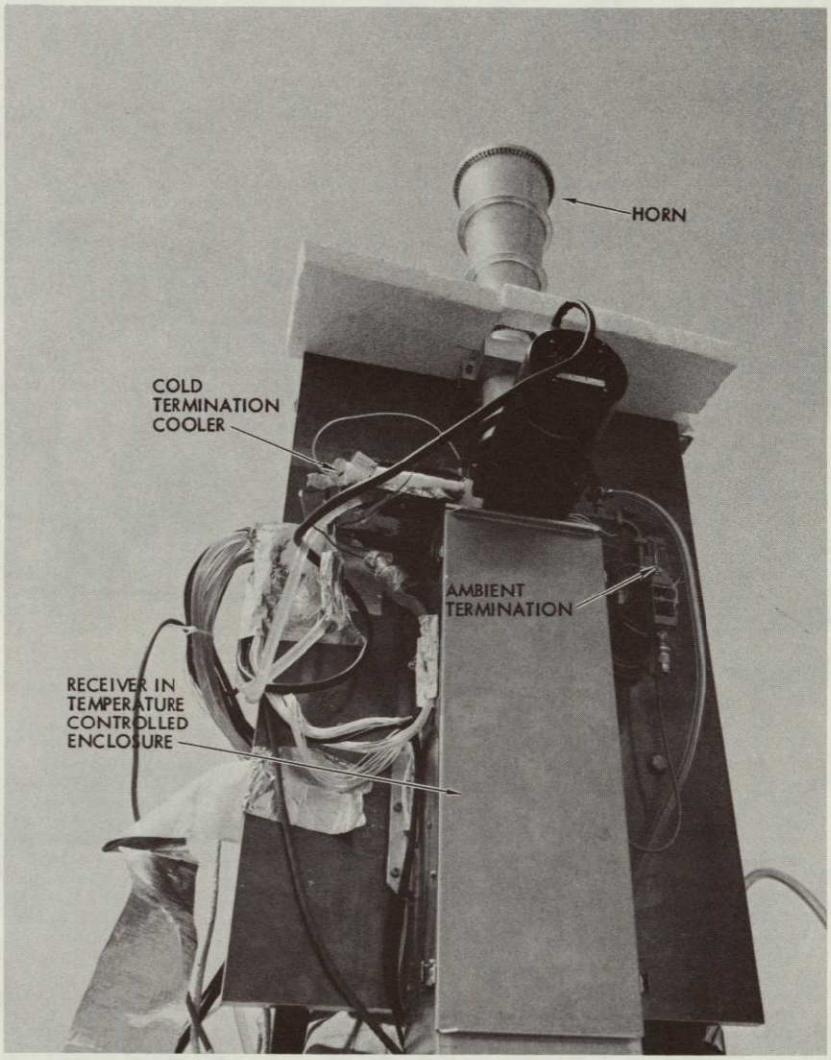

Fig. 5. The Water Vapor Radiometer configured for the May 1975 tests at El Monte Airport

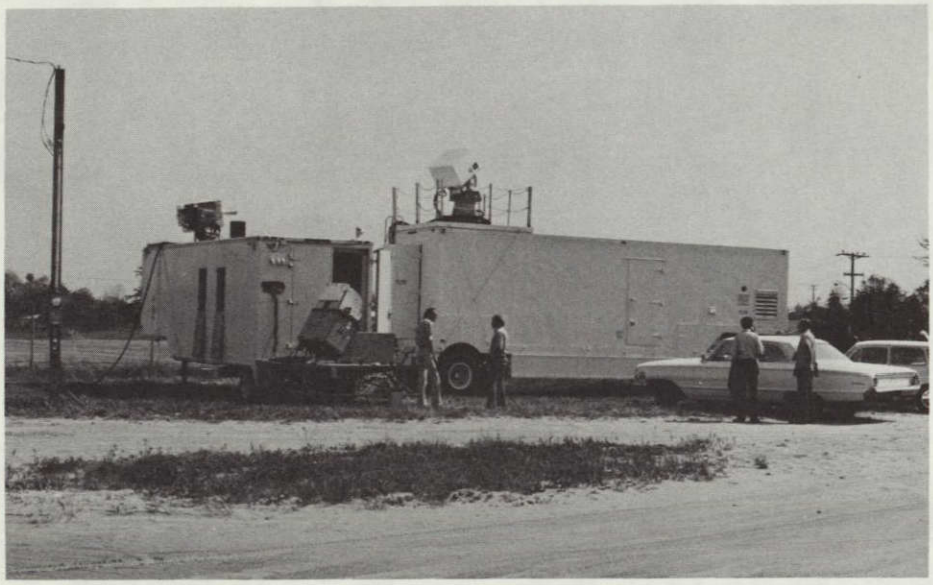

Fig. 6. The Telecommunications Division Water Vapor Radiometer and the Space Sciences Division SMILE and NEMS Radiometers (left to right) at El Monte Airport

Simple Intuitive Models of Programming

R. C. Tausworthe
DSN Data Systems Development Section

This article hypothesizes that mathematical models of the programming process can be formulated to gauge the sensitivities of that process to various given parameters, and that such models can be calibrated on an empirical basis and used as guides toward maximizing productivity, documentation quality, and programming reliability. The article then presents three oversimplified models as illustrations.

I. Introduction

The computer is a medium of artistic expression in the hands of a creator; it permits its user to fulfill, to the maximum extent of his human capability to communicate, almost any computational desire which can be codified into a programming language. And so, programming is truly an art form for many who are afforded the luxury of such a willing servant, but with little obligation to produce something industrially useful. To those of us, however, who view the computer as a tool, an integral part of our daily lives for the accomplishment of organizational goals and for the solution of problems we were hired to solve, the "art" of programming needs to be a science, or at least an engineering discipline.

There are many of us who classify ourselves as "nonprofessional programmers," but who have used programming as a research tool (in the author's case, to probe communications-theoretic problems, such as the threshold behavior of phase-locked receivers, the design of planetary ranging systems, the performance characteristics of telemetry systems, and so forth). The power of computers to describe, model, simulate, and solve very complicated mathematical problems has, in effect, catapulted the frontiers of science, so that we can now not only predict systems performance with amazing accuracy, but also optimize systems parameters to enhance that performance.

To develop a mathematical model which portrays a system and predicts, with some degree of fidelity, its per-

formance figure of merit, is a matter of professional training and the application of that training in a disciplined approach to problem solving. Standard mathematical techniques aided by computers normally yield system parameters which produce optimum or enhanced performance, if any such parameters exist on a practical basis.

Even when systems have a stochastic element in them (such as those found in space communications), their performance can be quantified: one learns to cope with randomness on an everyday, friendly basis, because even randomness exhibits certain reliable macroscopic regularities, in spite of microscopic unpredictability. One learns what things are mathematically ascertainable about stochastic processes, and what things are not. One learns to compensate, at the design level, for the adverse effects of noise and randomness in communications channels, through characterization of the environment in which the communication must take place. Space communications is thus no longer an art, but a bona fide engineering discipline.

Computer programming itself is a stochastic process, just as much as deep-space communications is, and perhaps more. However, to my knowledge, it has not been studied as such, nor characterized as fully as it needs to be to lift it from the "art" category to the "discipline" category. Whereas computer programs have been written to describe, model, and/or simulate very complicated mathematical problems and almost every other conceivable kind of system and/or process, there does not seem to be much effort in developing a mathematical theory or computer program which explains what is knowable about the process of programming. There are, however, some models of program reliability [1,2].

Many have perhaps scoffed at the prospects for formalizing the analysis of programming, both as a mathematical possibility, as well as an enterprise from which any useful information could be gained. Nevertheless, *it is the hypothesis of this paper that mathematical models of the programming process can be formulated to gauge the sensitivities of that process to various given parameters. Such models can be calibrated on an empirical basis and used as guides toward maximizing productivity, documentation quality, and programming reliability.*.

The first steps in demonstrating this hypothesis are to characterize some of the measurable aspects of software development and to postulate how various of the parameters correlate with one another and with reality.

II. Mathematical Modeling

Models of complex systems are seldom exact, especially when there are unknown factors. In such cases, the answers obtained must be weighed against intuition and observable data. Interpretations of results obtained from a model are often used to build levels of intuition; however, one must trust intuition only insofar as it reinforces physical evidence or aids in the creation of a more adequate mathematical model, or explains results coming from that model.

At times, it will be necessary to make outlandish simplifying assumptions just to arrive at an approximate first result. Such simplicity only tends to temper how much one can believe about that which the model tells as a general truth. If the response is favorable, then more detailed theories can be sought, more complicated models developed, until answers are known in believable precision.

This article therefore develops three outlandish, simple "beginning" models for certain aspects of the programming process, based on intuitive hypotheses and intuitive "proofs;" conclusions reached are therefore only approximate truths—but truths that are refinable by extended modeling and measurement.

When more precise models of programming someday come into existence, the process of programming can be optimized more scientifically. Until then, we are stuck with using more subjective means, opinion, and "gut-feeling" intuition to better the process.

III. Productivity Model

The first model is one of programming team efficiency. Let us suppose that there are W workers in a team who have just completed and delivered a documented, bug-free program. Each worker has spent time T_i, $i = 1, \cdots, W$ in the project, and each has an individual productivity p_i, $i = 1, \cdots, W$, expressed in some arbitrary common team production units. The average time T spent by each worker in the project is

$$T = (T_1 + \cdots + T_W)/W$$

and the average individual productivity P_I is

$$P_I = (p_1T_1 + \cdots + P_WT_W)/TW$$

Individual productivities p_i are measures of how much each worker has contributed to the deliverable final product per unit of time when unencumbered by the team structure. That is, when working alone, fully informed, each worker is capable of turning out p_i units per day.

However, for a team to function, there must (of necessity) be some time spent in interfacing and coordinating activities between workers, during which, nothing deliverable is produced. This fraction of time thus constitutes a loss factor insofar as productivity goes.

Let us suppose that each worker has spent only the *necessary* fraction t_i, $i = 1, \cdots, W$, of his time in such activities, and that the remainder of his time was spent producing at his normal, unencumbered rate. The average fractional time $t(W)$ spent in non-production is then defined as the *team-interaction factor*,

$$t(W) = (p_1 T_1 t_1 + \cdots + p_W T_W t_W)/P_I W T$$

The value of $t(W)$ is almost certainly an increasing function of W, since (intuitively) the more workers there are, the more likely that interfaces between individuals will exist.

The overall team production rate P_T is now given by the simple formula

$$P_T = P_I W[1 - t(W)]$$

This is a universal formula for team productivity, not merely one applicable to programming efforts. The implications one may gain from it are thus widely applicable to a multitude of management decisions concerning project organization.

A. What Lessons Can Be Learned From This Model?

It is obvious from the P_T equation that the critical parameter is the team-interaction factor, which must be kept as small as possible in order to maximize productivity (we did not need a mathematical model to tell us this, but the equation above verifies our intuition very well).

The team-production-rate equation shows very clearly what a project manager can manipulate to optimize his team's effort. If he is interested in high efficiency, he must attempt to keep $t(W)$ low by structuring the jobs into tasks which minimize the time each individual spends in interfacing his product with those of the rest of the team.

If he is interested in having a job then proceed at its highest rate, the manager must, in addition, choose the proper number of workers (with the requisite skills).

To give a simple example, suppose a manager were to divide a given programming development job, which includes design, coding, testing, documenting, quality assurance, and supervision functions into tasks such that each worker must interface with every other worker. In this case we can take

$$t(W) = (W - 1)\tau$$

where τ is the average time spent by each person interfacing with each of the others. The team production rate equation

$$P_T = P_I W[1 - (W - 1)\tau]$$

clearly has a maximum value (Fig. 1) as a function of W, at

$$W_{opt} = (1 + \tau)/2\tau \approx 1/2\tau$$

and the team efficiency at this figure is only

$$\text{efficiency} = (1 + \tau)/2 \approx 50\%$$

Adding more workers to a project already of size W_{opt} slows things down!

This behavior parallels the "maximum power transfer" law in electricity, and I refer to it as the "maximum team production rate" law: *A team producing at the fastest rate humanly possible spends half its time coordinating and interfacing.* The law holds true not just in the simple case we have assumed here, but also in any instance where $t(W)$ is roughly proportional to W. Only when this proportionality constant, τ, can be made very small does W_{opt} turn out to be so large as never to be attainable in practice.

B. Maximizing Productivity

Having identified that it is the time spent in communicating, interfacing, and integrating that lowers productivity (in this simple study), we can ask, what can be done to counteract this lessened production rate? The answer is simple in principle: *organize personnel tasks into team efforts which minimize the time individuals need to spend interfacing (and redoing their work because of improper interfacing).* Said differently: break the job into pieces which separate cleanly into parts which humans can handle easily, and whose solution then fits together well into an integrated whole.

Structured Programming (Ref. 3) using Chief Programmer Teams (Ref. 4) is one such concept which attempts to do just this for production programming. The team is divided into areas of expertise and the program is modularized so that both program and personnel interfaces are imposed top-down, in development sequence, and documented directly in the program code.

A wider concept than the Structured Programming/Chief Programmer Teams approach above, which extracts the essential features, but extends to a total development, may be described as the top-down, hierarchic, modular, structured approach to design, coding, testing, and documentation (Ref. 5). In this discipline, the design is created principally from the top-down in a modular fashion, in which each module is expanded in detail at each succeeding hierarchic level. Each design module can then be coded and tested, in that order. By making the interfaces between personnel coincide with interfaces between activities, and by making these interfaces be the *required documentation* deliverables, concurrently produced along with the program, then such interfaces tend to be totally productive, the documentation is forced to be produced and sufficient, and management has visibility into the software development process by merely monitoring the interface activity.

C. Conclusions About Productivity

The conclusion at this point, then, is that the simple one-parameter model of productivity explains the need for an organized approach in defining the development team makeup and in setting the software production discipline. It further gives one who has not yet fully appreciated the benefits of modern structured programming reason to believe that such methods can be made to work for him or for his organization.

IV. Program Readability Model

The next model is one relating to the level of documentation required for a program to be readable. Surely "readability" is a highly subjective quantity, and probably extremely variable across an ensemble of readers; but let us address the response of an "average" reader, as if there were one.

Let the program consist of L lines of compilable statements, divided into "blocks" of approximately B lines each. The uniform block size is somewhat artificial, but makes the problem easier to grasp. Let us further suppose that each block is accompanied by documentation which details its *function* i.e., a description of what the block computes, or its purpose), and also then provides additional information, which I shall call the block *rationale.* The latter contains descriptions of such things as the assumed entry and exit conditions, the significance of certain operations within the block, and relationships among data items. Such documentation may take the form of comments inserted directly into the code, or as flowcharts and narrative in some external document accompanying the code, or any other form easily understood by the intended readers.

The documentation level parameters of interest in the model are

f = the fraction of blocks having a functional description

t = the fraction of a block's total function described, when given

r = the fraction of blocks having rationale supplied

q = the fraction of a block's quantity of rationale needed, when supplied

Let it be assumed that functional and rationale descriptions within each block can be separated so as to be independent, nonoverlapping data about what is going on in the code, that is, the functional description is to be devoid of rationale, and vice versa. This is purely a mathematical necessity for what follows, and need not be in effect in actual practice; in actuality, the two may be intermixed, and correlated in any meaningful way.

There are several durations of interest when reading a block:

T_L = time to read and comprehend the action of a line of code.

T_F = time to read and comprehend a complete function description.

T_R = time to read and comprehend a complete rationale description.

$T_{CF}(x)$ = time to create a fraction x of the missing function description needed, from fraction $1 - x$ given.

$T_{CR}(x)$ = time to create a fraction x of missing rationale description needed, from fraction $1 - x$ given.

The latter two time factors arise when there is something missing that the reader needs, in order to understand the

program. If only a fraction t of an entire functional description is given, the remaining fraction $1 - t$ must be recreated by the reader if there is to be full understanding, and the same is true concerning rationale. Both $T_{CF}(0)$ and $T_{CR}(0)$ are zero, by definition.

In order to recreate missing material, the reader may make inferences and analyses based on material supplied as part of the given block, as well as material provided outside that block. However, I will assume that a functional description should pertain entirely to the code within that block, and I shall therefore further assume that the understanding of the functional behavior of a block depends wholly on information supplied for that block. Recreating rationale may, however, require inferences based on information outside the block.

Now let us assume that if only a fraction t of the complete functional statement is given, then the time to read that functional statement is tT_F, and let similar statements describe the other reading times, as well. In such circumstances, the total average time required to read and understand a block of code will be

$$T_B = BT_L + f[tT_F + T_{CF}(1-t)] + (1-f)T_{CF}(1) + r[qT_R + T_{CR}(1-q)] + (1-r)T_{CR}(1)$$

This expression is comprised of terms, in sequence, which (1) relate the time to read the code in a block line-by-line; (2) read a functional description, when it is given; (3) and (4) recreate any missing functional information; (5) read the rationale statement, when given; and (6) and (7) recreate any missing rationale.

The same type of formula and parameters can also probably be developed to describe how long it takes one to develop a block of code in the first place, but I have not explored such an equation, as yet.

A. Documentation of Block Function

Intuitively, the time to recreate a fraction x of the functional description (by reading the code, head scratching, etc.), must increase with x—the more there is missing, the longer it takes to figure out what is going on. The curves shown in Fig. 2 represent conceptual readability indices associated with understandability of block function.

It seems intuitive that, for most computer languages, there surely must exist some minimal block size B_F such that $T_F < T_{CP}(1)$, that is, such that the time to read and understand a given complete, adequate functional description is less than the time it takes to divine that function when no such statement is provided at all. (I shall reexamine this hypothesis more a little later.) Based on such a presumption, we may conclude that for all block sizes $B > B_F$, the optimum value of f cannot be zero. That is, some fraction $f > 0$ of the blocks should always have some form of functional description, each with level of detail t. A similar reasoning shows that if blocks are larger than some value B_R, then some fraction $r > 0$ of the blocks should always have rationale supplied.

By differentiation, we can next study the sensitivity of T_B to the documentation-level parameters f, t, r, and q. First, with respect to f (the density of functional descriptions), to answer what density of the blocks should contain functional statements:

$$\frac{\partial T_B}{\partial f} = tT_I - [T_{CF}(1) - T_{CF}(1-t)]$$

Since there is no dependency upon f in this derivative, then T_B takes its extreme values at either $f = 0$ or $f = 1$ For $B > B_F$, the value $f = 0$ has been ruled out; in addition, since there exists a value of t (namely $t = 1$) such that the derivative is negative, then T_B assuredly is maximized at $f = 1$.

That is, for every program with block size $B > B_I$, *every block should have a functional description.* Moreover, if $T'_{CF}(1-t) = T_I$ has a solution in (0,1), there may be an optimum level of detail, $t_{opt} < 1$. Otherwise, the function should be described completely ($t_{opt} = 1$). The sensitivity of T_B to t is gauged by

$$\left.\frac{\partial T_B}{\partial t}\right|_{f=1} = T_F - T'_{CF}(1-t)$$

The shape of $T_{CF}(x)$ is, of course, unknown; but one may speculate on its form, and conceptually, measurements could even be made to determine the characteristic. It seems reasonable that $T_{CF}(x)$ should have an increasing positive derivative; that is, that the amount of time required to figure something out should require a disproportionately longer amount of time, the more that there is to be figured out. If such were the case, and, in addition, if $T_F > T'_{CF}(0)$, then there will exist an optimum, $t_{opt} < 1$.

An optimum level of documentation detail t_{opt} less than unity (total detail) appears at that point for which an individual's reasoning facility overtakes his reading comprehension speed. It is thus advisable to leave out obvious

details and easily understood, but difficult-to-explain concepts from functional statements. Such are symptoms of overdocumentation.

B. Documentation of Block Rationale

Considerations for rationale documentation in a program run a parallel course to the functional documentation described above, but the rationale-recreation process within the reader is a different mechanism, and therefore there are some differences in the level required.

For one thing, it seems intuitive that the time required to understand the reasons for having a certain function, and the significance and relationships of block operations, variables, and data depend, to a great extent, on how well one understands the entire program surrounding the block (we have assumed function and rationale descriptions are independent within a block, but this may not necessarily hold globally).

Consequently, the time required to recreate any missing rationale needed for understanding probably depends both on q (the level of description detail in the rationale provided) as well as r (the density of blocks outside the block under scrutiny having rationale provided). In more complicated models, it probably also depends on f and t (and a number of other parameters), as well.

Investigation into proper levels for r and q is thus more intricate than the previous analysis, and, regretfully, too lengthy for inclusion here. In fact, I have not yet carried these to a point where meaningful conclusions can be drawn. However, I conjecture that the answers must be $r = 1$, $q = q_{opt} < 1$, just as was true for function: rationale should accompany *every* block larger than some B_R, and there will exist a level of detail at which reasoning rate overtakes the rate at which the volume of material needed can be read.

C. Self-documenting Programs

The reasoning above indicates that if functional blocks are too large, then every block should possess both functional and rationale descriptions. The equations also seem to indicate, in addition, that below some critical block size, no code documentation may be needed at all, other than the code itself. However, such can be true only if the program blocks are properly segmentized into understandable functional units and the rationale for and about such functions is clear, from the code statements themselves.

Is such a segmentation of a program possible? Is self-documentation of program code (in a suitable higher-level language) attainable?

The answer is probably, "No, not entirely." But again, top-down, hierarchic, modular, structured programming in a language which permits long label names goes a long way towards achieving this end. Program functional blocks can be limited to a size conducive to understanding, with a hierarchy of links to other functional (sub) blocks.

Particularly, these functional blocks can be labeled, using long enough labels, to state both the function and rationale of each given block. Contrast, for example, the following linkages to a subfunction invoked by the keyword DO; the remaining text following each DO is the subfunction label. The subfunction code is the same in each case:

```
DO  3048;
DO  S;
DO  SORT;
DO  BUBBLE SORT;
DO  BUBBLE SORT ARRAY A OF SIZE N;
DO  BUBBLE SORT ARRAY A OF SIZE N,
      BECAUSE IT IS SIMPLEST AND FAST
      ENOUGH HERE;
```

Similarly, contrast the following predicate tests, all of which refer to the same condition:

```
IF(X>Y) . .
IF(VAL>MAX) . . .
IF(INPUT VALUE>MAXIMUM ALLOWED)
IF(INPUT IS TERMINATED AS SIGNALLED
      BY AN INPUT VALUE GREATER THAN
      THE MAXIMUM ALLOWED) . . .
```

In the last example, the predicate statement may be realized as a linkage to a subfunction (perhaps a macro) which computes any of the first three predicates.

Studies (Refs. 6 and 7) have indicated that the optimum block-size with respect to intellectual manageability and comprehension, contains between 5 and 10 elements. Hence, if self-documentation is attainable, the program blocks should probably be no larger than this size.

D. Conclusions About Readability

The conclusions drawn from the readability model are that, if functional blocks are too large, then they must *always* have functional and (probably) rationale descriptions. Functional blocks falling below a certain critical size have the potentiality of being self-documenting. Finally, top-down, hierarchic, modular, structured programming using long descriptive names for subfunctions and operations provides a means whereby this potential is largely achievable.

V. Program Development Model

The final model I give here is one dealing with how programs should be developed (top-down, bottom-up, inside-out, etc.) so as to minimize the programming costs. The first step toward developing the program model is to depict the program as a sequence of control graphs; each graph represents the set of program blocks at a given time as nodes with directed links to subordinate blocks (nodes), as illustrated in Fig. 3 for structured programs.

The sequence begins with G_0, the null graph, and winds up, K stages later, at $G = G_K$, the entire program graph. For convenience, I will assume that each of the stages of work in between increases the size of the graph by $1/K$-*th* of the total final program graph size; that is,

$$|G_k| - |G_{k-1}| \approx \frac{|G|}{K}$$

Now let me define the scope of control $C_k(n)$ of a node n on G_k as

$$C_k(n) = \{m | \text{ a path exists from } n \text{ to } m \text{ on } G_k\}$$

Similarly, I shall define the scope of error $S_k(n)$ of a node n on G_k as

$$S_k(n) = \{m | \text{ an error in } n \text{ requires changing } m \text{ on } G_k\}$$

In words, the scope of control of a node n is the set of all nodes whose corresponding code is connected with the evaluation of the function represented by N. The scope of error of a node n is the set of all nodes whose corresponding code must be altered, should an error be found at n.

Intuitively, it seems reasonable that $S_k(n)$, more often than not, contains $C_k(n)$, because if an error is found at n, then all subfunctions of n will probably have to be reexamined, as well as some other nodes connected to n in ways other than control. In a highly modular program, we can, in fact, probably estimate $S_k(n) \approx C_k(n)$.

A. Development Cycle

Let us now suppose that the program at stage $k-1$ has resulted in G_{k-1}, and that the extension to G_k is about to commence. Then iteratively, let a version, call it G'_k, of G_k be developed and evaluated until no errors are found, whereupon we rename G'_k as G_k, as shown in Fig. 4. Now define

$$\Delta G_k = (G_k \cup G_{k-1}) - (G_k \cap G_{k-1})$$

and separate ΔG_k into altered old code $S_k(e_1, \cdots, e_{b_k})$ and added new code, ∇G_k; the nodes $e_1 \cdots, e_{b_k}$ were found to be in error during the work stage.

Let now the cost of this stage be represented by the formula

$$\text{Cost}(k) = \$_0 |\nabla G_k| + \$_1 |S_k(e_1, \cdots, e_b)|$$

This cost presumes that both new code and alterations (in total lines of code) can be produced at uniform cost rates per program node, different cost rates apply when writing new code than repairing erroneous code.

The total cost to produce a program of N nodes under these assumptions is then

$$C_{\text{tot}} = \$_0 N + \$_1 \sum_{k=1}^{K} |S_k(e_1, \cdots e_{b_k})|$$

The number of nodes N a program contains should not be so much a function of the production method as the function that is to be performed; hence, the minimization of programming cost is effected primarily by reduction of the second term in the cost equation.

B. Error Penetration

For large programs, it seems intuitive, except for nodes near the bottom of the graph, that the magnitude of the scope of control of a node n is approximately related to the graph size in an exponential way, where the exponent is roughly the fractional number of levels between that node and the "bottom" of the subgraph dominated by n, in relation to the total number of levels in the graph. This is illustrated in Fig. 5. In a modular program, since

$S(n) \approx C(n)$, the same can probably be said about the scope of error, as well. Hence, let us define $\lambda(n)$, the *error-penetration level* of node n in the graph G_k, as

$$\lambda_k(n) = \frac{\ln|S_k(n)|}{\ln|G_k|}$$

so that we can write

$$|S_k(n)| = |G_k|^{\lambda_k(n)}$$

where $0 \leq \lambda_k(n) \leq 1$

Now since the development cycle found no errors in G_{k-1} prior to embarkation towards G_k, errors found subsequently in G_{k-1} arise mainly from assumptions made at stage $k-1$ not supportable at stage k. It is thus the addition of new nodes that has allowed the discovery of errors

Let it therefore be assumed that the number of discovered errors is proportional to the number of added nodes (N/K) at stage n, and that the errors have non-overlapping scopes:

$$b_k = bN/K$$

$$|S_k(e_1, \cdots, e_{b_k})| = \sum_{j=1}^{N/K} |G_k|^{\lambda_k(e_j)}$$

$$= \sum_{j=1}^{N/K} [kN/K]^{\lambda_k(e_j)}$$

Now, let it be supposed that the development process can maintain a uniform (average) error penetration throughout the implementation activity; that is, suppose $\lambda_k(e_i) \approx \lambda$. Then the total development cost would be

$$C_{tot} = \$_0 N + \$_1 \frac{bN^{1+\lambda}}{1+\lambda}[1 + 0(1/K)]$$

and is independent of K, the number of development stages, insofar as first-order effects are concerned. The cost, of course, is least when $\lambda = 0$ (zero error penetration), but I don't know of any development process that can achieve this. If N is very large, it is easy to see that the principal development costs come from the "debugging term," which could increase as rapidly as N^2, were the improper development disciplines to be in effect.

C. Minimizing Development Costs

The way to minimize the cost is to find a development procedure which maintains a uniformly low error penetration coefficient. This coefficient λ is roughly the fractional number of levels an erroneous node e lies between the top and the bottom of the subgraph controlled by e, when the scope of control can be made the same as the scope of error.

It then seems intuitive, from the above model, that one should strive to augment G_{k-1} to reach G_k by some method which adds those new nodes to G_{k-1} which have the least scopes of error inside G_{k-1} and maximum outside; one should strive also to keep the error scope within the scope of control as nearly as possible, and the starting work stage should choose G_1 as that set of nodes having the greatest scope of error in G, since these will have zero scope in G_0 (the null graph). This minimization procedure is only intuitive, I haven't actually gone through a proof that it does, in fact, minimize the cost. Such a proof is probably academic anyway, since I can't actually compute or measure scopes on *a priori* bases. However, it seems unlikely that the optimum strategy will be too different than the intuitive guidelines above.

The cost-minimizing strategy above is sometimes called "hardest-out" programming; it depends on being able to evaluate or estimate error penetration levels on *a priori* basis Such evaluations or estimations are often possible if there is a preliminary design or baseline to work from.

If node penetration levels are not known *a priori*, then the top-down development procedure is probably the best that one can follow for several reasons. First, overall program correctness can conceivably be checked at each stage. Since the top node is the one with the greatest scope of control, it is probably then also the one with the greatest error scope. Adding nodes to the bottom of the graph at each stage keeps the scope of control of the added nodes to a minimum (zero), and thus, errors are not apt to be errors in control, but in connections between nodes other than control. If top-down structured programming is performed using a modular (in the connectivity sense) approach, then the error scopes are further reduced.

Hence, top-down hierarchic, modular, structured programming seems to be the intuitive ideal approach toward increasing programmer productivity (considering cost as being proportional to programming time) when no *a priori* estimates of error penetration levels of a program are available.

VI. Summary

I did not intend, at the outset, to make this article one extolling the virtues of Structured Programming, but rather, to illustrate that models of programming are possible and that these models can tell us something about the way programming projects should be approached for increased effectiveness. Yet it is interesting to see, at least it was for me, that in each case, Structured Programming, as discipline, was capable of delivering the optimum according to the model.

Oversimplified models can, of course, lie if they don't include enough of the real world in them. Intuitive models tend only to verify intuitive truths, and perhaps this is why Structured Programming seemed so optimum in the analyses. Did my personal bias toward Structured Programming drive me to the models and to the assumptions used in getting the solution, or vice-versa. I truthfully don't know. I do know I was trying to be objective.

I realize it is very easy to argue with oversimplifications, hypotheses, and assumptions. I realize that intuition is not proof, and that perhaps several interpretations of the results, in conflict with my own; are possible.

However, I now feel confident that basic studies, empirical measurements, statistical analyses, and applied research can someday provide less intuitive, more accurate, more sophisticated, rigorous models and simulations of the programming process. From such analyses, precise guidelines and disciplines will be discovered for improving future software developments beyond our current practical limitations, perhaps someday to their ultimate imminent theoretical maxima.

References

1. Craig, G. R., et al., "Software Reliability Study," AD-787 784, TRW Systems Group, Redondo Beach, Calif., Oct. 1974.
2. Richards, F. R., "Computer Software: Testing, Reliability Models, and Quality Assurance," AD/A-001 260, Naval Post Graduate School, Monterey, Calif., July 1974.
3. Dijkstra, E. W., Dahl, O. J., and Hoare, C.A.R., *Structured Programming*, Academic Press, New York, 1972.
4. Baker, F. T., "Chief Programmer Teams: Principles and Procedures," Report No. FSC 71-6012, IBM Corp., Gaithersburg, Md., Feb., 1972.
5. Tausworthe, R. C., *Standardized Development of Computer Software*, Jet Propulsion Laboratory, Pasadena, Calif., (to be published).
6. Miller, G. A., "The Magical Number Seven, Plus or Minus Two: Some Limits on Our Capacity for Processing Information," *Psychological Review*, Vol. 63, pp. 81–97, 1956.
7. Weinberg, G. M., *The Psychology of Computer Programming*, Van Nostrand Reinhold Co., New York, pp. 28–40, 1971.

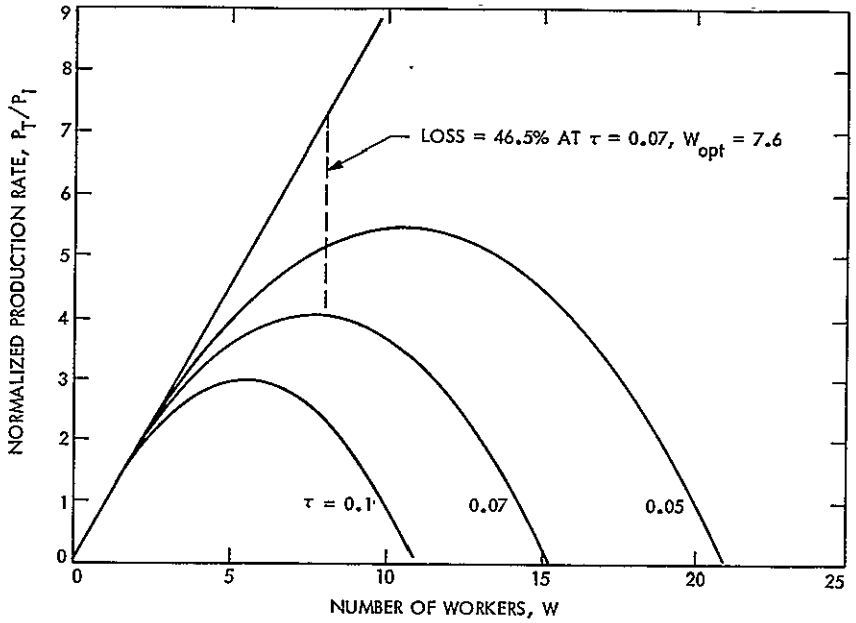

Fig. 1. Normalized team production rate as a function of team size, with communications

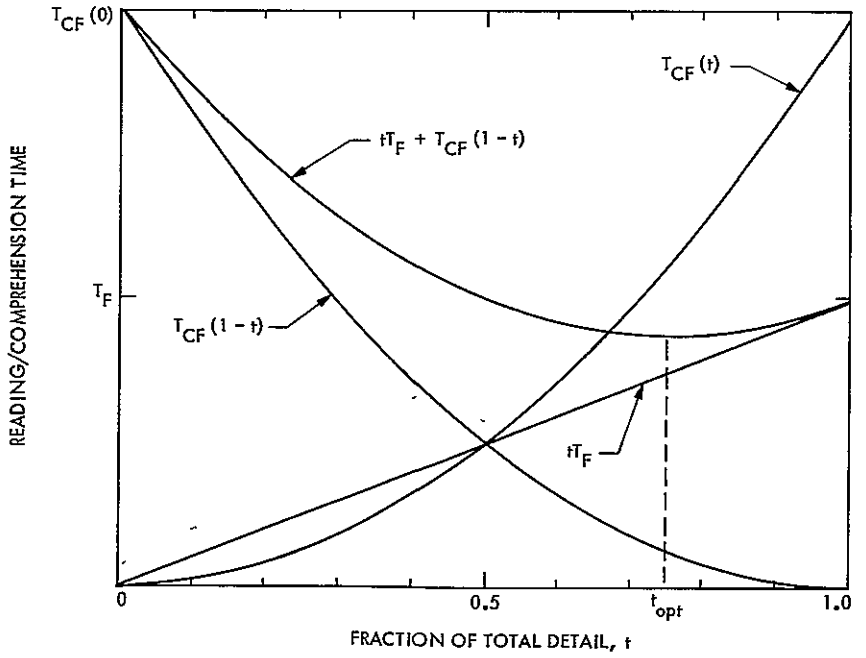

Fig. 2. Conceptual forms for readability indices for comprehension of block function

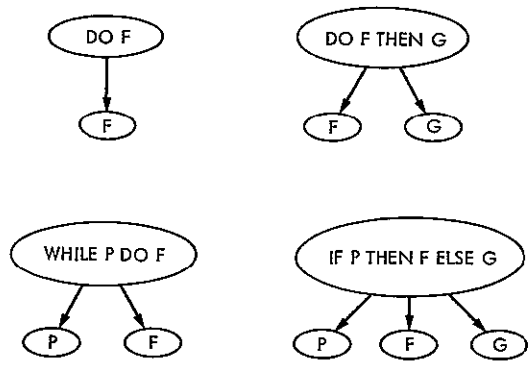

Fig. 3. Representation of a structured program as a graph in which nodes represent control connections. Each of *P*, *F*, and *G*, may have further expansion

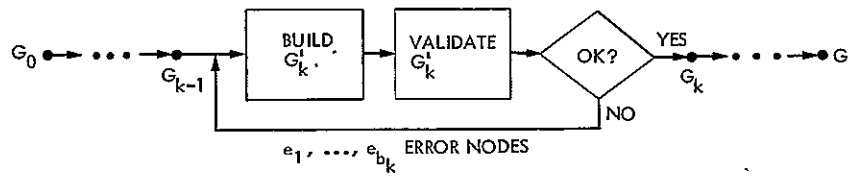

Fig. 4. Program development cycle

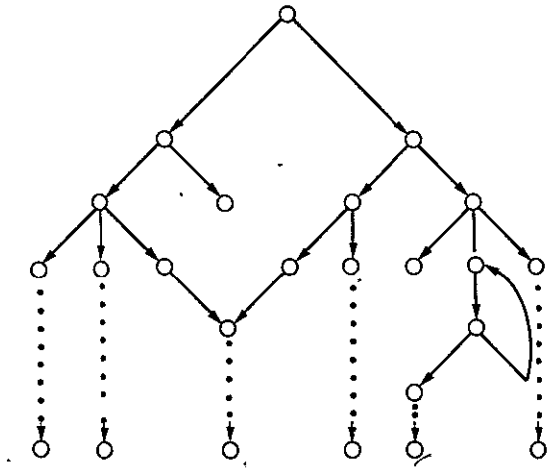

Fig. 5. Program graph which shows an almost exponential relation between node levels and the scope of control

Software Production Methodology Testbed Project

R. C. Tausworthe
DSN Data Systems Development Section

This article reports the history and results of a 3-1/2-year study in software development methodology. The findings of this study have become the basis for DSN software development guidelines and standard practices. The article discusses accomplishments, discoveries, problems, recommendations and future directions.

I. Introduction

Since November 1972, the DSN has been engaged in the development of a software production methodology, a set of Standard Practices which implement this methodology, and a set of languages and aids for software implementation, which together form the DSN Programming System. The software methodology development was principally an empirical bootstrapping from emerging theories in software production through a testbed implementation project into a viable modern software engineering discipline.

The testbed project was the complete redesign of an MBASIC language processor (Ref. 1) under controlled conditions which could be altered to observe effects. Design and management methods which produced favorable effects were recorded for future projects in the form of a two-volume "software methodology textbook" (Ref. 2). At this writing, both the testbed project and the textbook Volume I, exposing the methods used to effect the completion of the testbed, are complete. This article discloses the key final project guidelines, the key design concepts, the machine-independent design philosophy, the testbed methodology accomplishments and discoveries, the testbed project statistics (including team productivity), some problems not solved during this testbed activity, some recommendations for future projects, and some future needs indicated by the testbed project.

II. History

In November 1972, the Telecommunications Division and the Tracking and Data Acquisition Planning Office formed a joint team to establish a viable advanced engineering activity in development and application of a standard DSN language and the development and promulgation of engineering and technical management standards for the implementation of software for operational use in DSN facility subsystems and in DSN

technical management and administration. Later that month, this team initiated the machine-independent design of an MBASIC language processor, to be designed and documented by National Information Systems, Inc. (NIS), of Los Altos, California, to JPL standards with respect to design methodology, documentation format, level of detail, quality, and management.

A prototype version of the MBASIC processor had, at that time, just become operational (Fig. 1) on the Univac 1108 in the General-Purpose Computing Facility, having been implemented by International Computer Equipment, Inc., private consultants, and NIS. This prototype was not suitable for transfer to other host systems, was not documented to an effective level, and was probably not extendable to the intended full MBASIC language without an almost complete rewrite. Structured programming and other forms of modern software engineering, in their infancy, had not been used.

The MBASIC machine-independent design (MID) was therefore originally commissioned to fulfill the following work statement (October 1972):

(1) The design would be machine-independent down to a set of subroutines whose design would be machine-dependent.

(2) The level of design detail would extend only to that degree sufficient to permit determination of trade-offs for programming in assembly language on 16- and 32-bit hosts.

(3) Decision tables would be used to the maximum extent.

(4) Data structures and module interfaces would be specified in detail.

(5) Top-down, hierarchic, structured design principles would be applied, and documentation of the design down to five levels, plus a narrative overview, would be delivered.

Subsequent to this statement of work were several redirections of effort, the most significant of which was the transformation of the MID effort into a modern software engineering methodology testbed project, and this single redirection was the basis for all other redirections. By means of such a testbed on a software development of significant size, it was possible to formulate, implement, observe, and tune software design, documentation, coding, testing, and technical management methodologies to observe their effects in a clinical way.

The methodology instructions began in November 1972 as a set of memoranda sent to NIS; by January 1973, enough of these had been issued that, at the request of the Tracking and Data Acquisition Office, they were compiled into a "standards methodology working paper." This working paper was augmented and revised continually as the development guidelines evolved, and always kept current. It was distributed at several junctures in draft form.

In order for others to be able to use the working paper and to apply the methodologies in their own projects, it was found necessary to add tutorial material to the working paper. By June 1975, the paper had taken on the appearance of a methodology textbook, had gone through seven drafts, each including more and more tutorial detail, and had split into two volumes, methods and standards. The first volume is currently being typeset, and the second volume is drafted through most of its textual chapters and a few of its appendices.

The textbook drafts enjoyed a wide exposure to the programming community, both at JPL and outside, being used as texts for JPL seminars and classes, and for classes taught by the author and others as a graduate course to professional programmers through West Coast University. Feedback from these exposures and from members of the JPL Committee on Modern Programming (COMP), the DSN Software Management Seminar, and the DSN Programming System Steering Committee continually influenced the textbook material.

By the first part of December 1972, the first two levels of the design had been delivered and reviewed. This constituted what at the time was considered to be an "architectural overview," dealing with the technical aspects of the program procedure only. Several objections were raised with the material presented, principally with respect to the readability, detail level, and format of the design documentation.

By this time, too, a QA audit of the prototype (U1108) processor had revealed that its documentation was faulty, so the designers, over the next 3 months, were diverted from the MID until the U1108 documentation was brought up to date.

Once the U1108 documentation was up to date, there was then an intense trial and error, instruct and observe, modify and review activity over the next 6 months to develop the principal design and documentation practices which would remain in effect for the remainder of the MID project. From October 1973 through January 1974,

all flowcharts and narrative explanations of the processor down through level 3 (50 flowcharts) were prepared, reviewed, reprepared, and finally reviewed in mid-February by a formal review board.

The board concurred that design criteria (see Section III) were being fulfilled, whereupon the major design work began. Design milestones during the next 2 years are shown in Fig. 1. Figure 2 is a graphic display of the team cumulative productivity over the same period. Four of the significant milestones, to be discussed later, also are shown on the figure: a changeover of personnel, from high-level program architects to less experienced programmers, in November of 1974; the commencement of concurrent coding of the design by JPL personnel on the Caltech Decsystem-10 in March 1975; the delivery of all flowcharts and narratives in November 1975; and the formal completion of the design activity in March 1976, whereupon the MBASIC cognizant development engineer (CDE) was made responsible for the repair of minor errors detected in coding and testing the design.

III. Final Development Guidelines

The development guidelines in effect at the formal termination of the design phase were, first and foremost, that the design be hierarchically modular, limited in control connectivity to sequence, DOWHILE, WHILEDO, IFTHENELSE, and CASE (Ref. 2) structures, and readable (and developed principally) from the top down. Only one nonstructured termination form for a module was permitted, namely that for processing error messages and returns back to the MBASIC command mode.

Design documentation was in the form of flowcharts and accompanying narrative keyed to each flowchart. Additionally, tables, formats, data structures, error messages, and a glossary formed necessary reference appendices. Such documentation detail was, on a flowchart by flowchart basis, to fulfill three criteria:

(1) Adequacy for coding by remote coders without consultation, without functional ambiguity.

(2) Adequacy to assess correctness and for carrying on the design with no major redirections necessary.

(3) Adequacy of final document for use as principal sustaining document.

In order for the MBASIC CDE to review the design with respect to these three criteria, it became necessary for him to code the design on the Caltech Decsystem-10 and perform checkout measures on a flowchart by flowchart basis. These checkout measures consisted of informal top-down tests of the evolving programming dummy stubs for as yet uncoded or undesigned features, and executing the program in a special debug-monitor mode provided by the Decsystem-10.

Although such checkout tests were designed and performed informally, the guidelines for testing were explicit: submit the embryonic processor to input conditions that cause the traversal of each flowline on each flowchart newly added to the program, at least once.

All items submitted by NIS were kept under strict project control. Flowcharts and other items contained "signature control boxes," in which were placed initials of the designer, a concurring peer, and the accepting CDE, such items were given "accepted" status and so logged. Only items once accepted could be coded and tested; such modules having errors detected were changed in the log to "rework" status and returned to NIS for correction. All code was a direct translation of the flowcharts, box for box.

Items supplied by NIS on an information-only basis (lookahead design items) and items formally submitted but not yet approved by the CDE, were logged as "awaiting disposition." These modules could be coded only for use as dummy stubs, if needed. Errors detected in the use of such dummies were fed back to NIS, but no change in status resulted.

Items having been identified (as, for example, by a striped module on a flowchart) but not delivered yet in any form were marked "unseen" and logged.

Figure 2 displays the rate at which modules awaiting disposition and above were delivered (upper line), and the rate at which the modules received accepted status (lower line). In mid-1975, the status monitor of logged modules was computerized, which accounts for the appearance of increased detail during the latter part of the project.

IV. Machine-Independent Design Concepts

Because the MID was to be implementable on a range of host computers, the design had to be documented using higher-level, machine-independent descriptors of algorithms, data structures, and operating system services and interfaces. For this reason, flowcharts were chosen as the medium for expression of procedure, with narrative written to explain each flowchart, material keyed to each box on the chart. A set of precisely defined conventions for operations within flowchart boxes was adopted, and

these were inserted into the design documentation as programming standards.

These conventions were so rigorously defined that, had a compiler been available to recognize them, the translation from flowchart to code would have been automatized.

The machine-independent design extended from the top-level flowchart (called Chart 1) downwards through the program hierarchy to a set of stubs whose algorithm was felt to be potentially machine-dependent but whose interface with the remainder of the design (outside these stubs) was still machine-independent. These stubs were said to form the "environmental interface" with the host system, and were labeled "E-routines."

Figure 3 shows the separation of the MBASIC processor into the Fundamental language (that portion being the subject of Vol. I of Ref. 1) processor, herein called the MID, together with the machine-independent design of extensions to the full language (MIDX) and the machine-independent design of the compiled-code, or batch, processor (MIDB). The machine-dependent design (MDD), MDDX, and MDDB portions are machine-dependent designs needed to interface the machine-independent algorithms to the host operating system (e.g., for I/O).

In many instances, algorithms for processing MBASIC statements were deemed to be machine-dependent only because of certain constants which were likely to vary from host to host. Such algorithms were included into the MID by defining parameterized values for the constants, giving these a special notation (mnemonic name prefixed by "%") so as to be discernible to implementors.

To implement MBASIC on a host, the flowcharts comprising the MID can be coded immediately in host assembly language, manually, or perhaps using a set of portable macros (Ref. 3). The remainder of the job is to perform the machine-dependent design of the E-routines, and then to code and test these. Machine-dependent variation in performance of each implementation is to be tolerated only as permitted within the program specification (Ref. 1).

V. Testbed Methodology Accomplishments

Among the accomplishments of this testbed activity may be listed the firm establishment of procedures forming the central core of current DSN standard practices, which advocate the use of top-down structured design methods and sound engineering practices. The project demonstrated that the design documentation was, in fact, adequate for coding by remote coders; that the top-down approach can accommodate personnel changeovers with a minimum project impact; and that, in fact, junior design-level personnel can replace senior architect-level personnel without adverse effect once the major program structure and higher-level design decisions have been worked out.

As may be noted in Fig. 2, the pure-design rate (before rework starts coming back from the CDE) is much higher than a design-plus-correctness-assessment rate is apt to be. This is evidenced by the "sprint" of modules generated at the beginning and after new personnel were brought on board. This demonstrates that design to establish a program architecture is feasible without the need for coding when detail correctness is not an issue.

However, as demonstrated by the increased slope of the acceptance line, concurrent coding is an aid to correctness assessment early in a project and a necessity (the jagged falloff) in its latter stages.

The curves in Fig. 2 demonstrate that meaningful quantitative monitors of programming progress exist, based on public programming practices. The public programming practices here consisted of regular submittals of flowcharts, narratives, tables, etc. (completed and lookahead), and the logging of such items by completion category. The missing item needed to make early predictions of costs and schedules was only the top asymptote, not known in the present case until almost mid-project (July 1975).

Recommendations to improve progress monitors appear in Section IX.

VI. Testbed Project Statistics

The MID specification consists of about 950 flowcharts (plus narrative) and E-routine interface descriptions, plus tables, the glossary, etc. By considering all documentation items uniformly distributed over the 950 module deliverables, one may compute that, over approximately 1250 man-days, approximately 3/4 of a module was designed and documented per man-day from the go-ahead review in February 1974 until project completion in March 1976. The low productivity rate is principally a reflection of the difficulty of doing an extremely intricate processing task in a machine-independent way, as opposed to doing the same task in a machine-dependent way.

In corroboration of this, the Decsystem-10 figures are 1.7 modules per man-day for a 525 man-day total,

including design, coding, debugging, and testing. The MID coding took only 100 man-days to code but another 175 man-days coding and testing to get the MID error-free. Of significant note is that only 18% of the time was spent in coding and debugging, and 82% in design.

The total expenditure for the development and first implementation (MID + MDD) was about 2050 man-days, or about 8.2 man-years. This represents about 13 lines of code per man-day.

However, the total next-time effort may be expected to be only 625 man-days, or about 2.5 man-years (525 + 100 man-days). The implementation on the next host is therefore only about 30% of the initial development effort, or about 45 lines of code per man-day.

VII. Methodology Discoveries

At the beginning of the project, a strict top-down discipline was a stated requirement, imposed on the design team to verify claims in the literature (Ref. 4) that strict top-down methods were profitable. It was soon discovered that, while the submission of formal design items, documentation, and delivery of codable flowcharts from the top-down was of great merit, strict adherence to the top-down development discipline was having an adverse effect both on achieving a good design and on securing a high initial correctness.

On modifying the development guidelines, it was learned that a lookahead design effort to supplement the top-down method and to establish the program architecture was of great benefit as a precursor to the formal top-down detailed design, documentation, and subsequent coding. Such lookahead, it was found, did not need to be absolutely correct in detail, so long as the designers' intentions were recorded, work tasks identified, and the overall program size estimated. Coding to assess correctness by the designers was *not* needed, and, in fact, would probably have been a hindrance if done. Some coding might have been useful to make certain performance tradeoffs, however.

Once the formal top-down development began, however, coding was found to be needed, not only to prove program correctness but also to reinforce the designers psychologically.

Coding and checking design items soon after submission and project acceptance was found to avert the "correctness paranoia" syndrome which tends to set in when the design gets too large for mental retention of intricate details. Rather, when designers *know* what they have produced thus far is correct, they stop worrying about it and go on to more productive things.

The design effort got off to a slow slow start, it seemed, for several reasons, principal of which was a general lack of familiarity with the top-down, modular, hierarchic, structured programming methodology. Indeed, at that time, much of the methodology had not been developed yet, and was in the process of being developed as a result of this design work. However, it was found, as new personnel were brought in, that they, too, required a period of training in the methodology before they could do an effective job.

Another aspect of the design task, which not only decreased initial productivity, but which was generally believed to be unachievable to begin with, was the requirement for a machine-independent design. Structuring a program for machine-independence in all but a set of environmental stubs was clearly not a production task, but one which required applied research. The philosophies and methods developed in this area will be the subject of a future article.

However, in retrospect, it now appears that at least half of the algorithms in an entire implementation can fall into this machine-independent design category. Moreover, these algorithms form the entire upper-level structure of the MBASIC processor. The machine-dependent items are relegated to environmental interfacing stubs whose implementations do not require personnel with language-processor-design skills.

Because the architectural overview and overall processing philosophy of the program were, unfortunately, not made an early part of the formal design supplied to the Decsystem-10 and MODCOMP-II implementation teams (JPL and contractor personnel), we found that there was a great need for this type of information early in the coding and testing phases.

The first correctness test procedures were very formal and very detailed. It was soon discovered that such procedures are difficult to write, lengthy, and require great expenditures of time, and at no discernible increase in level of correctness over less formal procedures, given standard guidelines. The standard guideline was to execute the program modules under test using the entire program (or major segment) as a driver, with dummy stubs for modules not yet coded and with path monitors adequate to trace the control flow; to select input data to cause the program to traverse each flowline in each module under test at least once, plus extreme-value data, out-of-bounds

data, and randomly chosen valid data; to run the program with its stubs using the selected input; and to exercise human judgment whether or not the trace information indicated that the intended functions were being accomplished.

Selection of detailed procedures and test data, as well as the criteria for judgment of correctness, were left to the discretion of the individual implementors. Testing using the standard guideline proved to be very efficient, quick (with respect to more formal methods), and thorough.

The method used to log flowcharts, described earlier, proved very useful in gauging the current status of delivered items. Because an entire lookahead was not done prior to the commencement of the formal detailed design, however, the ultimate number of modules was unknown until quite late. Thus, incremental progress could be seen on a regular basis, but estimated percentage of completion was unavailable. Had a complete architectural (lookahead) design been done and from this, a work breakdown structure generated, we can now see in retrospect that it would have been possible to monitor percentage completion figures right from the beginning of the formal phase, and to report progress as milestones defined in the work breakdown structure.

VIII. Documentation Discoveries

The principal documentation of the MID processor was in the form of flowcharts and narratives. Flowcharts were hand-drawn using templates with ANSII-standard symbols, labeled by typewriter. All flowcharts conformed to rigid structured programming and detail requirements. There was a separate page or two of narrative for each chart, supplied to explain each step in the charted procedures, its significance, and its rationale. Such documentation was initiated in rough draft form by the NIS designers, then typed and drafted by clerical personnel before submission to JPL.

It was found that this documentation format was excellent with respect to communications between designers and coders. We had achieved the goal that flowcharts were codable by remote personnel without consultation. The quality of the documentation was generally excellent, although there was a relatively high volume of paper for the amount of information it contained.

However, the documentation medium proved to be cumbersome in the sense that the design process tended to get in series with the limited clerical personnel available and assigned to the task. For this reason, turn-around time for effecting changes was slow. In the end, we wound up working much of the time from red-lined charts returned to NIS in "rework" status, having discovered errors by coding and testing and repaired these ourselves in red-line form.

The level of documentation, with respect to detail, seemed to follow the inequality

DESIGNER < SUSTAINING < CO-LOCATED CODER < REMOTE CODER

The level required [so-called Class A (Ref. 4), adequate for remote coders] was therefore deemed adequate for later sustaining of the design. However, the differential between the level of detail required by the designer and that needed by others was very great. Designers could get by very well with little detail, and getting them to supply this detail, at times, was somewhat of a problem. Writing down all the details was not a creative job but something, we learned, that could be provided by relatively junior design-level personnel.

Generally, then, the higher-level architects developed the major algorithms in flowcharted sketches, which the more junior designers then supplied with details and narratives. In so doing, the junior-level designers learned enough of the design and methodology that, midway in the project, they were able to replace their more expensive colleagues altogether. The senior people were free for more creative and less drudging tasks.

The fact that there is a rather routine, drudging part of the documentation task, which tends to avert creative people from doing it, is an indication that much can be done to improve the design medium to bring it into closer alignment with what is needed by coders.

For one thing, it was found that once an overview of the processing, data structuring, and architecture of the program was gained by coders, they tended not to need the detailed narratives supplied. Rather, they coded directly from the charts, which were explicit enough for that task without narrative recourse. Hence, probably a lot of work went into creation of narratives which could have been avoided had a suitable overview been insisted upon and provided in the beginning. The overview, incidentally, was the last-produced piece of documentation.

The overview was requested (but not insisted upon) early but was felt at the time not to be a high-priority item. Developing it, too, must have been viewed a drudging job by the architects, who then would have had to write it themselves if it were to be among the first-

produced deliverables. Some recommendations for future projects are contained in the next section.

The final documentation discovery discussed here is felt to be of major significance: comment-free code. Alarming as it sounds, coding the MID (and MDD as well) had, by project standards, almost no narration in the assembly code listings. The comment fields of the assembly listing were limited to cross-reference annotations of the flowchart number, title, and box number. This cross-referencing made it very easy to correspond lines of code with actions in the design for coding, debugging, and later QA audits. Only when special coding was used, or when it was otherwise not clear how a certain function on a flowchart was achieved by the code, were narrative comments permitted. Since the level of detail required produced explicit coding implications, virtually no such narratives were needed.

The practice permitted fast, routine coding; coders did not have to make up comments, except in rare instances, and made no design decisions (in coding the MID at least). But more importantly, it virtually forced the *design* medium (flowcharts + narrative) to also become the *debugging* medium. Any corrections to be made were first identified, then entered on the flowchart (red-lined), and then inserted into the code, rather than vice-versa. Because of this, the documentation was always kept up to date as a natural consequence of the program development, not as an after-the-fact, error-prone process. A great deal of expense had gone into producing quality documentation, and comment-free code proved a way of not subverting that quality by creating a processor maintainable at the code level alone.

IX. Recommendations

In future testbed activities (specifically, the MBASIC extension to full language capability), we intend to, and recommend that other projects also, perform an entire lookahead design (no coding and detailed correctness not at issue) down to a sufficient level to establish the architecture and the number of modules and schedule to an accuracy goal of 10%. The architecture documentation will consist predominantly of hand-drawn flowcharts and other graphics, including sketches of major data structures (narratives also permitted but not required). The idea is to permit the architect to carry the design through all the way to that point needed to size the job, to gauge the number of flowcharts in the final design to 10%. We currently estimate that about 20-25% of the total development time will be spent in this activity.

Additionally, the designer will then be asked to produce a work breakdown structure defining interim milestones, tasks, personnel assignments, and determination of critical-path items.

During this architectural phase, the evolving flowchart module tree will be recorded, as well as estimated completion percentages of other architectural tasks, at regular (biweekly) intervals.

Once the architecture is complete, and a Software Definition Document written and reviewed per DSN Standard Practice, the formal development of detailed, high-initial-correctness flowcharts, narratives, and other items will begin.

The concurrent coding effort will begin early in the post-architecture phase so as to reduce design-error risk, but not so early as to constrain the design prerogatives.

Comment fields in the code listings will continue to contain documentation references only, except in special circumstances. Coding will continue to be a direct translation of the flowcharts, in 1 to 1 correspondence, box for box.

Testing for correctness (as opposed to acceptance testing) will continue to be performed on an informal basis but in conformance with the formal guideline given earlier.

Because the MIDX design is to extend the MID, the same documentation guidelines will be in effect (for uniformity). However, overview material will be insisted upon early.

X. Problems not Solved by the Testbed Methodology

Perhaps the most noticeable failure of the testbed was in the area of minimizing problems due to non-colocation between design and coding teams, principal of which was the inability to maintain the desired visibility into the partial-progress status of the design team. Regular progress reporting was unenforceable; submitted reports, when they came, generally provided no quantifiable status information. Because status monitors were faulty, we were unable to predict schedules. It is hoped that better status monitors will be forthcoming in the MIDX follow-on because of the explicit architectural phase and work breakdown structures to be generated.

As mentioned earlier, the documentation medium (more than the documentation format) proved inflexible and expensive, and required a comparatively long turn-around time to correct even minor bugs, cosmetics, or oversights.

The clerical burden of supplying drudging narrative detail to support flowcharts tended to "burn out" design team members, especially those with the more senior capability. Because of the fear of having to renarrate (added drudgery) items found by later coding to be in error, and by emphasis placed on original correctness in the design, there seemed to be a correctness paranoia. This led to hiding of design items, or reluctance to deliver flowcharts and narratives on a piecemeal basis. This countered the "public programming" goal and decreased visibility into how much of the design we actually had at any particular point in time. We hope that the separate architectural phase (during which correctness in minor details is not at issue), the use of concurrent coding to check design details early, and the improved status monitors will avert future difficulties of this type.

XI. Future Needs Indicated by Testbed Project

Probably the single thing most needed to raise productivity at this point is a more flexible, easier-to-maintain, less expensive but equally descriptive and graphic form of program documentation. The documentation produced by designers needs to be sufficient for remote coders as a natural outcome of the documentation method; that is, the documentation method needs to narrow the gap between what the designer wants to produce and what the remote coder actually needs. (We refuse to accept designers doing the coding themselves as a method of achieving this, as it tends to produce software not maintainable by individuals other than the originators.)

The second major need is that for better project visibility producing methods during the design and implementation. Suitable methods for cost and schedule prediction will probably result when this need is fulfilled.

Perhaps the best way to increase the level of public programming (and thereby, project visibility) is to merge the design and documentation media via automation. If design media are computer-based, processing a design into readable and needed documentation can potentially be done automatically—fulfilling the first need above—and at the same time, can provide a viable status probing capability—fulfilling the second need also.

To avert human fallibility in the informal correctness testing and to speed up the path-identification and corresponding input data generation, there is a need for computer aid. The generation of tests and test data conforming to the earlier guideline is almost a clerical task in itself, tantamount to tabulation of various paths in the design and determination of data (and stub designs) to drive the coded program through those paths. Although human judgment may be needed at points in this procedure, certainly the computer is capable of scanning the design, analyzing and tabulating paths and conditions to be met for the human then to consider.

Other aids can readily be wished for. The creation of such development supporting software must always be guided by expectation or demonstration of feasibility, cost, and potential gain.

XII. Summary

The methodology developed as a result of this testbed has become the foundation of the current DSN software development guidelines and standard practices. The quality of the testbed design and of the documentation produced by it is unmistakable. There is room for yet more improvement, however, chiefly in the areas of increased productivity and project manageability. Both of these enhancements can be achieved by putting the computer to work to solve the very problems people have in creating programs for the computer.

At the beginning of this project, the development of quality software was truly an art masterable by only a few of its practitioners. The application of the methodology used and derived by this testbed demonstrates that production programming may be a passing art form. Such a passage is not lamentable, however, for it will be replaced by an effective engineering discipline. Whereas artforms are generally mastered by a few but appreciated by many, the engineering discipline will be both practiced and appreciated by an entire community of adherents.

References

1. *MBASIC*, Vol. I—Fundamentals, Vol. II—Appendices, Jet Propulsion Laboratory, Pasadena, California, 1973 (JPL internal document).
2. Tausworthe, Robert C., *Standardized Development of Computer Software*, Vol. I—Methods, Vol. II—Standards, Jet Propulsion Laboratory, June 1976 (JPL internal document).
3. Riggins, M. C., "Portability of the MBASIC Machine Independent Design," *DSN Prog. Report 42-24*, Jet Propulsion Laboratory, Dec. 15, 1974, pp. 100–106.
4. Tausworthe, Robert C., *Standard Classifications of Software Documentation*, Technical Memorandum 33-756, Jet Propulsion Laboratory, Pasadena, California, Jan. 15, 1976.

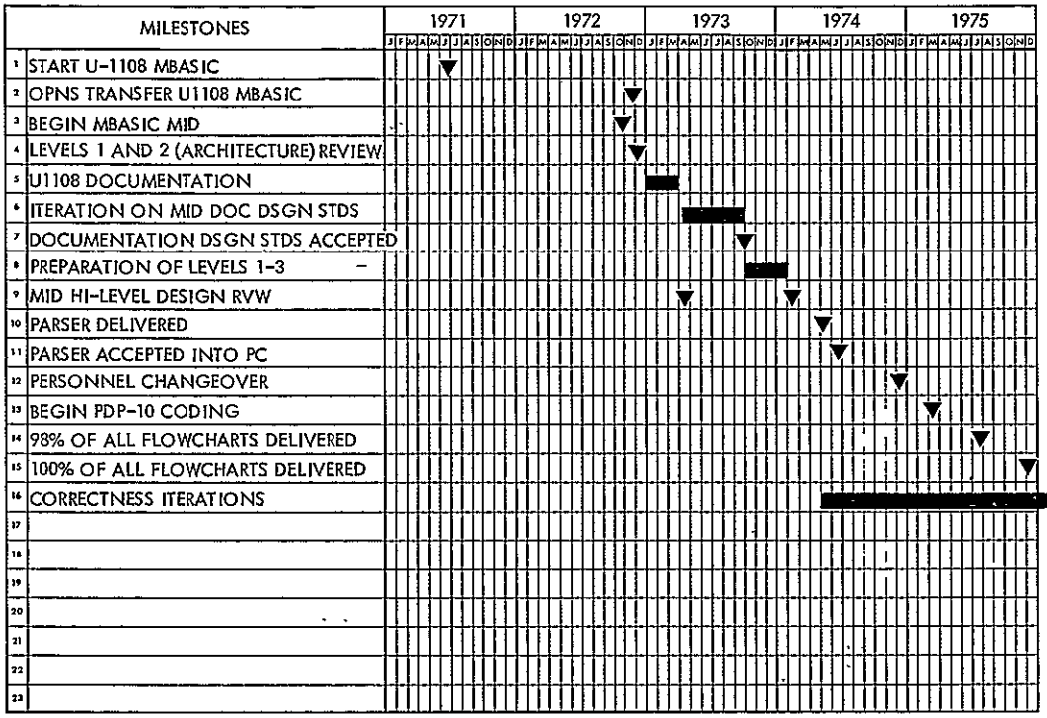

Fig. 1. MBASIC development history

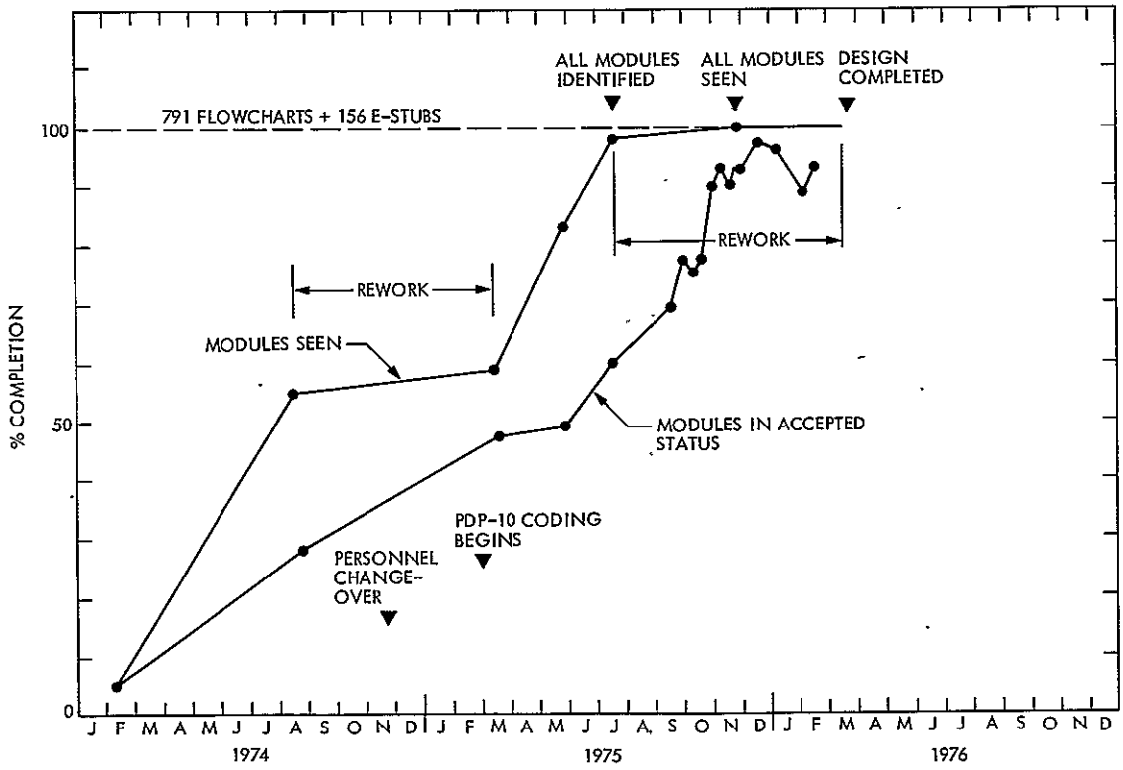

Fig. 2. MBASIC-MID module development history

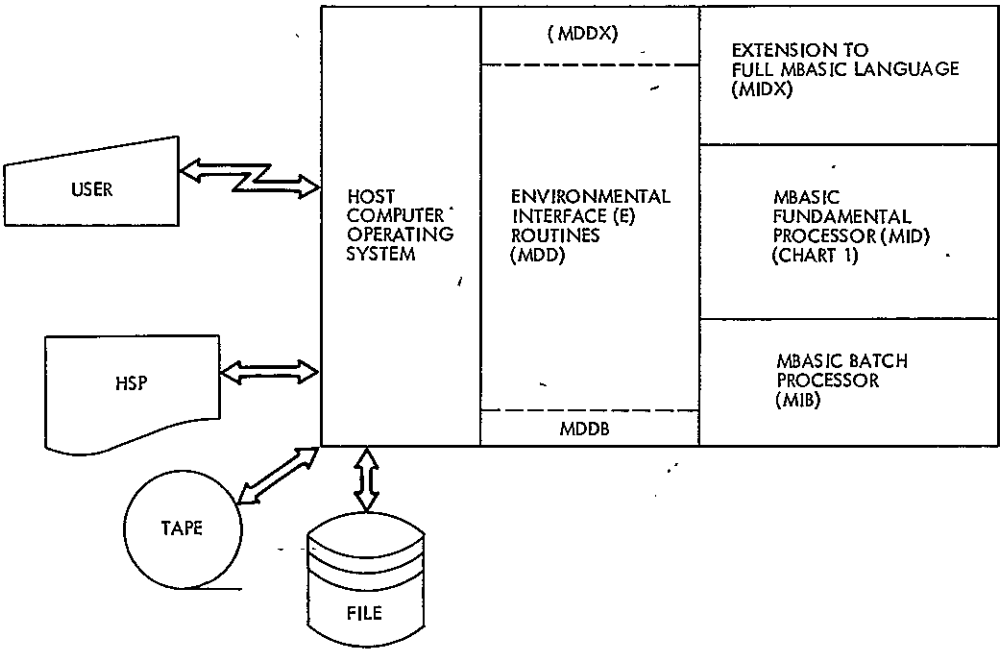

Fig. 3. MBASIC machine-independent design configuration

Standard Interface – Twin-Coaxial Converter

W. A. Lushbaugh
Communications Systems Research Section

The Network Operations Control Center standard interface has been adopted as a standard computer interface for all future minicomputer-based subsystem development for the Deep Space Network. A previous article in this report series presented a discussion of an intercomputer communications link using a pair of coaxial cables. This unit is capable of transmitting and receiving digital information at distances up to 600 m with complete ground isolation between the communicating devices. This article describes a converter that allows a computer equipped with the standard interface to use the twin-coaxial link.

I. Introduction

A twin-coaxial intercomputer communications link (Ref. 1), capable of communicating at distances up to 600 m (2000 ft), has been operational for over three years. The advantages of such a link include complete ground isolation between communicating computers as well as the capability of operating in a noisy environment.

When the Network Operations Control Center (NOCC) Standard Interface Adaptor (SIA) was adopted as a standard computer interface for all minicomputer-based subsystem development for the DSN, it was decided to develop a converter to enable any computer equipped with an SIA to interface with, and communicate across, a twin-coaxial link. This article provides a description of the operational characteristics of such a converter.

II. Review of the Twin-Coaxial Link

The twin-coaxial link was designed as an intercomputer link, i.e., the signaling format and priorities are identical at both ends of the link. The link functions in a half-duplex mode; i.e., it can transmit data in either direction, but only one way at a time. Signals on the two coaxial cables are balanced and transformer-isolated to minimize effects of ground-level imbalances between the two communicating devices. The two cables each carry signals in one direction only. The cable connected to the transmit connector at one end of the link must be connected to the receive terminal at the other end.

When the link is inactive, there is no signal in either cable. From the inactive state, the switching on of a 1-MHz carrier by one of the computers (say, computer A)

constitutes a 1-bit message to computer B that communication is desired, and when computer B returns a similar carrier, it acknowledges that message. Symmetrically, the switching off of the carrier is an emphatic "I quit!" message used to terminate transmission or which could be used to reinitialize from erroneous link operation.

Transmission over the link is, in fact, bit-serial, but it is conceptually on a byte-by-byte basis. Bits are transmitted by deleting one cycle of carrier, with the phase of the last cycle of carrier determining the value of that bit. Eight data bits (one byte) and an associated parity bit are sent in consecutive 2-μs intervals. When the receiving computer has room in the buffer associated with the link, it sends a 2-bit control message as a request for the next byte. This "transmit-byte/receive-control packet" handshaking provides synchronization between the communicating controlling software in both computers that accommodates the link data rate to the capabilities of the computers.

Since nine bits are transmitted per byte and two received before the next transmission, a minimum of 22 μs are needed to send each byte. This converts to a maximum rate of 45 kbytes per second but due to computer interrupt timing and software overhead only 25 kbytes have been achieved in practice.

III. Review of the Standard Interface

The NOCC standard interface output consists of fourteen signals and a power sense line. The fourteen signals consist of eight data signals, two function code signals, and four control or handshaking signals. Three of the four combinations of function codes are available for tagging data transmission while the fourth, the 1 1 condition, is reserved for commands out of the computer or status in from the device connected to that computer. Two of the control signals are used as stimulus signals; one from computer (stimulus from computer (STC)) and one from the device (stimulus from device (STD)). Both of these signals are unidirectional and go true for the complete duration of a message. The remaining two signals are bidirectional control signals called response (RSP) and ready (RDY), which control the handshaking of data across the interface. Response and ready each make one complete cycle (false to true to false) for each byte transferred across the interface.

Computer and device SIAs have been assigned different access priorities (Ref. 2). The computer has the highest priority when it wants to send a command. The device has the next two priority levels: first, when it wants to send a status byte to the computer, and next when it wants to transfer data. The lowest priority is the data output mode for the computer. The converter described in this article has the device priority assignment.

IV. Converter Control Signals

Control of the twin-coaxial link through the converter and an SIA is accomplished by sending commands and receiving status. Table 1 shows how the 8 bits of a command are interpreted in the hardware and which bits are returned as status from the converter. D1 is the least significant bit. Following is a detailed description of each bit in the command and status.

D1 **Command** When a 1 is received in this bit position, it will cause the twin-coaxial link to start transmitting if the carrier enable flip-flop has been or is simultaneously set (see D3) and the link is not in the busy receiving mode.

D2 **Command** Unassigned.

D3 **Command** This bit controls the carrier enable flip-flop for the twin-coaxial link. When set to zero, the link is disabled. It must be set to 1 before transmitting or receiving is possible.

D4 **Command** When this bit is set to a 1 in a command, a reset pulse is developed which resets the end-of-message flag and any error flags in the twin-coaxial hardware.

D5 **Command** This bit steers the control message flip-flop. This flip-flop determines the value of the two-bit control message sent by the twin-coaxial link in the receive mode. Normally, the control message is 0 0 while the 1 1 value is used for errors or buffer overflow conditions. (See D7 Status.)

D6 **Command** Unassigned.

D7 **Command** There are eight pairs of outputs from the twin-coaxial driver–receiver unit. A multiplexer has been provided to select one of these. The loading of the multiplexer register is controlled by D7. When D7 is a 1, D1 through D4 are copied into this 4-bit register, and not used otherwise; D5 and D6 are ignored. The extra bit in the multiplexer address register allows future expansion to 16 channels.

D8 Command This bit, when set to 1, asks the converter to immediately return its present status. When this bit is set, D1 through D6 are ignored.

D1 Status A one in this position signifies that the twin-coaxial link received a packet of bits of the wrong length; i.e., not 2 or 9 bits.

D2 Status A one in this position signifies that the twin-coaxial link received a bit while it was in the process of transmitting a bit.

D3 Status This bit is a copy of the carrier enable flip-flop.

D4 Status When this bit is a one, it signifies that an incoming carrier has terminated.

D5 Status This bit is a copy of the control message flip-flop.

D6 Status A one in this position signifies a parity error in the received byte.

D7 Status A one is set in this position when the twin-coaxial link receives the control message 1 1.

D8 Status This bit is a 1 or 0 depending on whether the incoming carrier is on or off, respectively.

V. Automatic Control Features

The twin-coaxial link was originally designed to be on a direct I-O port of a computer. It was found that with the SIA between the programmer and the twin-coaxial link, it was more convenient for the programmer if some automatic features were added to the twin-coaxial link converter. These automatic features are:

(1) The converter automatically sends a status byte to the computer when an incoming carrier is detected. This will happen in both the transmitting and receiving modes.

(2) The twin-coaxial hardware is automatically reset when the status byte with the end message flag set (D4) is taken by the SIA. This reset has the same effect as the reset generated when the computer sends a command with the reset bit (D4) set, and, in addition, the carrier enable and control message flip-flops are also cleared.

(3) When the program terminates a transmission, the standard interface will drop its stimulus signal STC. The last byte delivered to the converter may still be there, however, since the twin-coaxial link has to wait for a control message from the device with which it is communicating. To accommodate this case the converter saves the last byte until it is requested, and then terminates the transmission. The software will be notified at the end of transmission, when the carrier coming in to the converter is cut off, generating a status byte delivery to the computer.

(4) Any twin-coaxial error condition (D1, D2, D6, D7 described above) causes a status byte to be delivered to the SIA. Since these error flags are not cleared until a reset pulse is generated in the hardware, an inhibit was provided to let the error status condition be sent only once.

(5) To facilitate programming, the controller can be commanded (by bit D8 in a command) to return its present status to the computer.

VI. Conclusion

An SIA-to-twin-coaxial converter has been built. It will enable any computer equipped with an SIA to interface with the twin-coaxial intercomputer communications link and communicate over ground-isolated coaxial cable up to 600 m. Two complete units have been built to date, one with an eight-way multiplexer at the driver and receiver interface of the twin-coaxial link, which allows the SIA to selectively communicate over one of several coaxial links. Both converters have been successfully tested between an SIA in a Modcomp II computer and a twin-coaxial unit in an XDS 920.

References

1. Lushbaugh, W. A., "A Driver/Receiver Unit for an Intercomputer Communications Link" in *The Deep Space Network Progress Report*, Technical Report 32-1526, Vol. XV, pp. 109–114, Jet Propulsion Laboratory, Pasadena, CA, June 15, 1973.

2. *Detailed Specifications for Deep Space Network Standard Interface*, Specification No. ES508534, Rev. B, Nov. 26, 1974 (JPL internal document).

Table.1. Status and command bytes

	Command from computer	Status to computer
D1	Start transmitting	Error number bits received
D2	—	Bit received while transmitting
D3	Carrier enable flip-flop	Carrier enable flip-flop
D4	Reset	End message flag
D5	Control message flip-flop	Control message flip-flop
D6	—	Parity error
D7	Multiplexer select*	Control message 1 1 received
D8	Request status return	Incoming carrier on

*When a command is received with D7 set to 1, a multiplexer register is loaded with bits D1 through D4.

Final Report on DSN Telemetry System Performance With Convolutionally Coded Data: Maximum Likelihood Decoding

B. Benjauthrit
DSN Systems Engineering Office

This report finalizes the analysis of DSN telemetry system performance based on the convolutionally coded data for the short constraint length 7:½ codes at low-bit rates, 8 to 2048 bits per second, obtained from CTA 21 for the block III type, S-band configuration. The results indicate that a loss of one or more decibels in the system performance may be expected due to system degradation. Also, burst error lengths up-to 100-bits may not be unusual in actual operational situations.

I. Introduction

This is a final report on DSN telemetry system performance with the convolutionally coded data obtained from the Compatibility Test Area (CTA 21) during the 1975 calendar year (Ref. 1). The report focuses on the test results analyzed for the short constraint length 7:½ codes to be employed by outer-planet Mariner spacecraft such as the Mariner Jupiter–Saturn (MJS). Analysis of the telemetry system for the long constraint length 32:½ codes is presented separately elsewhere in this issue of the DSN Progress Report (Ref. 2). The tests cover bit rates ranging from 8 to 2048 bits per second (b/s) and modulation indexes (MI) from 37.2 to 75 deg.

To obtain the performance characteristics, a stream of fixed, known symbol pattern that can be decoded by both the Pioneer 32:½ and MJS 7:½ decoders, generated by the Simulation Conversion Assembly (SCA), was modulated on the subcarrier and passed to the test transmitter, where the carrier was modulated (See Fig. 1a). The microwave equipment (UWV) routed the transmitted carrier to the receiver (RCVR), where a Y-factor was used to calibrate the input signal-to-noise ratio (Ref. 3). The symbol stream was demodulated in the Subcarrier Demodulator Assembly (SDA) and sent to the Symbol Synchronizer Assembly (SSA) for synchronization and quantization. The eight-bit A–D conversion of each symbol was recorded on magnetic tape by the Telemetry & Command Processor (TCP) in octal. On the UNIVAC 1108, the octal symbols were converted to FIELDATA characters before they were preprocessed to three-bit symbols (See Fig. 1b). The three-bit symbols were then processed and analyzed by the Viterbi Decoding Program (Ref. 4) to provide the final results for this report.

II. Methodology and Analysis

DSN telemetry system performance may be described in terms of bit signal-to-noise ratio (E_b/N_0), bit error rate (BER), or bit error probability (BEP), and bit error distribution. To obtain such parameters, the corrupted eight-bit symbols recorded on magnetic tape are converted to three-bit symbols, which are acceptable by the Viterbi Decoding Program that was designed to simulate as closely as possible the actual JPL Maximum Likelihood Convolutional Decoder (MCD). The program decodes the symbols and compares the result with the original data bits.

To reduce the amount of the decoded bits to a size that can be handled, the decoded bits and the original data bits are exclusive-ored and packed into a sequence of integers:[1]

$$g = (g_1, g_2, \cdots, g_n)$$

where each g_i is the count of good bits (it will be referred to here as an error-free run, EFR), and n is the total number of EFRs for the test. In this notation, two consecutive errors occur when g_i equals zero. For example, the sequence (2,5,1,7;0,1,3) represents the event (0010000010100000001101000), where each 1 designates an error and each 0 designates a good bit. Since the decoded data stream ends with or without an error, this end bit will not be considered.

Now, if E is the total number of errors, then

$$E = n - 1$$

Representing the total number of good bits by G, we have

$$G = \sum_{i=1}^{n} g_i$$

Hence, the total number of decoded bits, D, for the test is

$$D = G + E$$

Next, if we denote an integer guardspace by g_s, a burst of bit errors is defined as a subsequence of g whose elements assume values less than g_s. That is, the EFR sequence of a burst b is of the form:

$$g_i, b, g_{i+k}$$

where

$$g_i, g_{i+k} \geqq g_s$$

and

$$b = (g_{i+1}, g_{i+2}, \cdots, g_{i+k-1})$$
$$g_j < g_s \text{ for } i+1 \leqq j \leqq i+k-1$$

The total number of errors in b, ϵ, is then

$$\epsilon = (i+k) - i = k$$

The total number of good bits contained in b, δ, is

$$\delta = \sum_{j=1}^{k-1} g_{i+j}$$

and the total number of bits in b, burst length, is

$$\epsilon + \delta$$

In general, g is of the form:

$$g = (g_1, b_1, g_2, b_2, \cdots, b_m, g_m)$$

where $g_i \geqq g_s$ and each b_j contains $g_k < g_s$. The average burst length of the sequence g is

$$b_{ave} = \frac{b_1 + b_2 + \cdots + b_m}{m}$$

and the average number of errors within a burst is

$$\epsilon_{ave} = \frac{\epsilon_1 + \epsilon_2 + \cdots + \epsilon_m}{m}$$

where ϵ_i is the number of errors within the ith burst. Note that the burst definition given above also includes isolated bit errors. However, the results described in Section IV do not consider isolated errors as bursts.

Now for an EFR r_i, let f_i denote its frequency of occurrence, c_i denote its cumulative number of f_i, and p_i denote its cumulative probability of c_i. Then,

$$(r_1, r_2, \cdots, r_{k-1}, r_k)$$
$$(f_1, f_2, \cdots, f_{k-1}, f_k)$$
$$(c_1, c_2, \cdots, c_{k-1}, c_k)$$
$$(p_1, p_2, \cdots, p_{k-1}, p_k)$$

[1] An alternate way which was employed in Ref. 2 is to produce a sequence of integers $(k_1, k_2, \cdots, k_n)$, where k_i is the number of consecutive good bits if i is even, otherwise k_i is the number of consecutive bad bits

are defined by

$$c_k = f_k, c_{k-1} = c_k + f_{k-1}, c_i = c_{i+1} + f_i, \cdots, c_1 = c_2 + f_1$$

and

$$p_k = c_k/c_1, p_{k-1} = c_{k-1}/c_1, p_i = c_i/c_1, \cdots, p_1 = c_1/c_1$$

where r_j are sorted as $r_1 < r_2 < \cdots < r_k$ and k is the total number of distinct EFRs. The cumulative probability p_i is the probability that an EFR r_i is being exceeded; it is a sample distribution function of EFRs or, for short, an EFR sample distribution.

III. Viterbi Decoding Performance of Memory Path Lengths 36 and 64

In the early phase of data processing, memory path length (MPL) was set to 36. However, it was later found that the JPL MCD uses MPL 64. To make certain that the results already processed are compatible and comparable to subsequent results, an investigation was conducted to determine the discrepancy between the performances of the two values. The investigation reveals that the difference in performance between these two values appears to remain within 0.2 dB and is much less at high-bit SNRs. This finding also assures that the results obtained from Deep Space Station (DSS) 62 (Ref. 2) are valid for use in the MJS flight project design. Note that the decoder used at the DSS 62 is an off-the-shelf LV7015 from LINKABIT, which employs MPL 36.

The performance of the Viterbi decoding algorithm for MPLs 36 and 64 was investigated via the Viterbi Decoding Program (Ref. 4), using data generated from another 1108 program. The results are tabulated in Tables 1 and 2 for values of $E_b/N_0 = 2,3,4$, and 4.3 dB. Figure 2 provides the plots, E_b/N_0 vs BEP, of the data. For comparison, the figure also includes the baseband performance curves of the JPL functional requirements and of the prototype MCD acceptance test data at 250 kb/s. The figure shows that the Viterbi decoding performance of MPL 64 is everywhere better than that of MPL 36. This is especially true for low SNRs. The improvement in the performance diminishes towards high SNRs. Nonetheless, the overall improvement appears to be less than 0.2 dB. Observe that the majority selection performance improves significantly with MPL.

Figure 3 provides the curve of EFR size R vs probability that R is exceeded for $E_b/N_0 = 3$ dB. The curve reveals that large-sized EFRs have a higher probability to occur for MPL 64 than for MPL 36.

IV. Test Results and Discussions

The complete test plan for the project was provided in Ref. 1. It consisted of 6 series of tests, A through F, with a total of 33 tests. Series A and B tests had 6 tests each, 1 to 7, except 5. There were 5 tests in series C, E, and F, and 6 tests in series D. The data rates of the tests ranged from 8 to 2048 b/s and modulation indexes from 37.2 to 75 deg. And only Block III RCVR/SDA type was used in the test setup.

Again, the Y-factor method is employed to calibrate E_b/N_0 to the receiver. Since this type of calibration usually lacks precision, the data output at the TCP are not recorded until the system is adjusted so that the SSA symbol error rate (SER) printouts are averaged to the theoretical SER, obtained from a Telemetry Analysis Program. Consequently, DSN telemetry system performance is described here in terms of the E_b/N_0 derived from the output SSA SER vs BEP of the decoded bits, and the EFR sample distribution.

Since the SSA SER is only an estimate of the input SER due to noise in transmission, the derived E_b/N_0 is also an estimate of the input E_b/N_0 to the receiver.

The test results are now given. The plots of E_b/N_0 vs BEP for test series A through F are depicted in Fig. 4. Again, the JPL functional requirements for the MCD and the prototype MCD acceptance test data at 250 kb/s are included in the plots. The plots also provide the corresponding system performance curves for majority selection. Figure 5 shows the ERF sample distribution plots of the above tests. The test descriptions and burst error statistics, including burst rate, average number of errors per burst, average burst length, average EFR length, and maximum burst error and burst length, are tabulated in Table 3. A burst rate is defined as the ratio of the number of bursts to the number of decoded bits.

In what follows, we shall, for simplicity, call each test and the data file of each test by only the test name. For example, test A and the data file of test A will be referred to as A.

The results of A1, A2, A3, and A6 satisfied the functional requirements. The first part of A1, up to bit 780012, was not included in the plot due to large burst errors; some burst lengths were as large as 88, which resulted in as high a BEP as 5.75×10^{-4}. After decoding up to 587608 bits, a burst error of length 50 occurred in A4. This was the only burst error found in the data file. Test A7 contained 3 EFRs, which ranged from 4.8×10^5 to 7.3×10^5 bits.

The results of B1, B2, and B6 remained pretty much within the functional requirements. The early portion of B2 effected a rather low BEP, as low as 5×10^{-6}. All in all, B2 was a good file. For B3, a burst of length 36 occurred after bit 1222432; this made the BER of B3 high. Large burst errors and EFRs tended to occur more towards the end of B7, otherwise, decoding of B7 proceeded normally.

Over one million bits were decoded for C1 and C4, and their BEPs remained within the functional requirements. No errors were found in C2, within 1.8 million bits. But two errors occurred in C3, immediately after bit 106768. Since E_b/N_0 of C3 was above 6 dB, at least 10^7 bits were required to provide a meaningful result; however, C3 had only 1.4 million bits. The same may be said about C5. Note that due to large burst errors, the first and last portions of C5 were not included in the BEP calculation; the former bursts were as large as 34, and the latter bursts were even worse, as large as 100. The graph of the EFR sample distribution of the series C tests is shown in Fig. 5c. Observe that the curves elevate with E_b/N_0.

The series D test results deviated, towards the worse side, uniformly from the functional requirements, as much as one or more decibels. Nevertheless, the decoding of these tests proceeded normally.

Only E1 and E5 were obtained for the series E tests. It was not possible to get the receiver for E2 in lock, and, consequently, no data were recorded for this test. Similar to the series D tests, the results of E1 and E5 were noticeably worse than the functional requirements. Note that E3 contained no decoding errors, and E4 had an unrecognizable bit pattern.

For the series F tests, only F1, F2, and F3 were run. The results of these tests were also worse than the functional requirements. Due to large burst errors, F1-2 was terminated before an end of file was reached. The decoder did not, however, encounter such a difficulty in F1-1. Similarly, no major difficulty was faced in F2. Also, no decoding errors were detected in the entire file of F3.

Finally, the following observations may be made about the EFR sample distribution curves in general:

(1) The depth of each curve indicates the quantity of EFR, the deeper the greater.

(2) The extent (to the right) of each curve indicates the size of its EFRs, the farther the larger.

(3) Each transition signifies an EFR.

V. Conclusions

The task undertaken was complicated by many intermediary steps in setting up the test equipment in the Compatibility Test Area and in processing the test data. However, the final test results appear to reveal that the performance of the DSN telemetry system seems to satisfy the system functional requirements, at least at the bit rates considered which range from 8 to 2048 b/s and under the various test conditions prescribed in this report. System performance degradation of one or more decibels in actual operations under certain conditions may be expected, especially at low-bit rates. Also, though the average burst lengths are generally less than 10, within our range of analysis, error burst lengths up to 100 may not be unexpected. Lastly, MCD performance improves with memory path length. But an improvement of not more than 0.2 dB may be expected when changing from memory path length 36 to 64. Also, MCD performance of best metric selection is almost always better than that of majority selection.

Acknowledgment

The work presented in this report was a combined effort of many individuals in the advanced engineering group of the DSN Systems Engineering section, led by B. D. L. Mulhall. Without their assistance and cooperation, this work would have been impossible.

References

1. Mulhall, B. D. L., *et al.*, "DSN Telemetry System Performance With Convolutionally Coded Data," in *The Deep Space Network Progress Report 42-30*, pp. 184–199, Jet Propulsion Laboratory, Pasadena, Calif., Dec. 15, 1975.

2. Greenhall, C. A., "DSN Telemetry System Performance With Convolutionally Coded Data: Sequential Decoding Update," in *The Deep Space Network Progress Report 42-33* (this issue), Jet Propulsion Laboratory, Pasadena, Calif., June 15, 1976.

3. Baumgartner, W. S., *et al.*, "Multiple-Mission Telemetry System Project," in *The Deep Space Network*, Space Program Summary 37-60, Vol. II, pp. 152–169, Jet Propulsion Laboratory, Pasadena, Calif., Nov. 30, 1969.

4. Benjauthrit, B., Mulhall, B. D. L., and Wong, J. S., "A Viterbi Decoding Program for DSN Telemetry System Analysis," in *The Deep Space Network Progress Report 42-28*, pp. 5–10, Jet Propulsion Laboratory, Pasadena, Calif., Aug. 15, 1975.

Table 1. Data used for comparison between memory path lengths 36 and 64

MPL	E_b/N_0, dB	Total			Bit errors		Symbol errors	Bit error rate		SER, %	Best metric				Largest burst	Largest burst length
		Decoded bits	Bursts	EFR	Best metric	Majority		Best metric	Majority		Burst rate	Average, bits				
												Errors/ burst	Burst length	EFR length		
64	2.0	35937	35	272	271	293	7518	7.54×10^{-3}	8.15×10^{-3}	10.46	9.74×10^{-4}	7.43	12.21	123.38	27	37
36	2.0	34272	53	390	389	505	7152	1.14×10^{-2}	1.47×10^{-2}	10.43	1.55×10^{-3}	7.23	11.57	86.88	37	58
64	3.0	215937	29	195	194	204	34191	8.98×10^{-4}	9.45×10^{-4}	7.92	1.34×10^{-4}	6.66	10.83	1106.37	19	26
36	3.0	215965	40	229	228	387	34197	1.06×10^{-3}	1.79×10^{-3}	7.92	1.85×10^{-4}	5.60	9.40	942.08	19	26
64	4.0	215937	1	6	5	5	24571	2.32×10^{-5}	2.32×10^{-5}	5.69	4.63×10^{-6}	5.00	7.00	35988.67	5	7
36	4.0	215965	1	6	5	15	24575	2.32×10^{-5}	6.95×10^{-5}	5.69	4.63×10^{-6}	5.00	7.00	35993.33	5	7
64	4.3	539937	0	1	—	—	54548	—	—	5.05	—	—	—	539937	—	—
36	4.3	539965	0	1	—	5	54550	—	9.26×10^{-6}	5.05	—	—	—	539965	—	—

Table 2. JPL prototype MCD acceptance test data at 250 kb/s[a]

MPL	E_b/N_0, dB	Total bits	Total bit errors	Bit error rate	
				Test data	Requirements
36	2.0	—	—	1.00×10^{-2}	—
64	3.0	4.10×10^{8}	3039	7.41×10^{-4}	9.00×10^{-4}
64	4.0	4.10×10^{9}	1621	3.96×10^{-5}	6.00×10^{-5}
64	5.0	6.55×10^{9}	89	1.36×10^{-6}	2.50×10^{-6}

[a]From M. Alberda, DSN Data Systems Development Section.

Table 3. Results for test series A through F

Test ID	MPL	E_b/N_0, dB	No. of Decoded bits	Bit errors		MI, deg	Bit error rate		SER, %	Best metric							
				Best Metric	Majority		Best Metric	Majority		No. of Bursts	No. of EFR	Burst rate	Largest errors/ burst	Largest burst length	Average, bits: Errors/ burst	Burst length	EFR length
A1	36	3.75	500256	69	147	55	1.38×10^{-4}	2.94×10^{-4}	6.18	17	70	3.40×10^{-5}	8	14	3.88	6.71	9254
A2	36	4.54	800000	4	7	55	6.95×10^{-5}	1.25×10^{-4}	4.58	1	5	1.25×10^{-6}	4	8	4.00	8.00	246831
A3	36	4.75	933120	5	5	55	5.36×10^{-6}	5.36×10^{-6}	4.21	1	6	1.07×10^{-6}	5	7	5.00	7.00	66538
A4	64	5.42	2877630	26	26	55	9.04×10^{-6}	9.04×10^{-6}	3.11	1	27	3.48×10^{-7}	26	50	26.00	50.00	22601
A6	64	4.61	1000000	7	7	67.6	7.00×10^{-6}	7.00×10^{-6}	4.46	2	8	2.00×10^{-6}	4	6	3.50	5.50	124999
A7	64	5.48	1800000	13	13	75	3.72×10^{-6}	3.72×10^{-6}	3.02	3	14	1.67×10^{-6}	6	10	4.333	6.33	128570
B1	36	3.41	600000	140	287	55	2.33×10^{-4}	4.78×10^{-4}	6.93	29	141	4.83×10^{-5}	21	28	4.79	7.29	4477
B2	36	3.93	2000000	65	65	55	3.25×10^{-5}	3.25×10^{-5}	5.81	16	66	8.00×10^{-6}	6	14	4.00	6.88	—
B3	64	4.94	2463901	109	116	55	4.42×10^{-5}	4.71×10^{-5}	3.88	16	110	6.49×10^{-6}	22	36	6.75	10.88	22398
B4	64	5.40	3736025	0	0	55	0.00	0.00	3.14	0	1	0.00	—	—	—	—	—
B6	36	5.19	3946180	6	6	67.6	1.52×10^{-6}	1.52×10^{-6}	3.46	2	8	5.06×10^{-6}	4	6	3.00	4.00	49370
B7	36	5.38	1600000	65	65	75	4.06×10^{-5}	4.06×10^{-5}	3.17	10	52	6.25×10^{-6}	11	21	5.30	8.40	28424
C1	36	4.56	1010880	11	12	55	1.08×10^{-5}	1.19×10^{-5}	4.56	2	12	1.98×10^{-6}	6	10	4.50	7.50	64799
C2	64	5.25	1861801	0	0	55	0.00	0.00	3.37	0	1	0.00	0	0	0.00	0.00	1861801
C3	64	6.32	1384209	2	2	55	1.45×10^{-6}	1.45×10^{-6}	1.93	1	3	1.45×10^{-6}	2	2	2.00	2.00	461402
C4	36	3.96	1010880	55	88	42	5.44×10^{-5}	8.71×10^{-5}	5.74	11	56	9.89×10^{-6}	8	16	4.91	8.64	18050
C5	64	5.32	1580038	5	5	67.6	3.00×10^{-6}	3.00×10^{-6}	3.26	2	6	1.20×10^{-6}	2	4	2.00	3.00	283100
D1	36	5.04	1123885	21	23	55	1.87×10^{-5}	2.05×10^{-5}	3.70	4	22	3.56×10^{-6}	12	28	4.75	9.50	51084
D2	64	5.49	1199457	8	8	55	6.67×10^{-6}	6.67×10^{-6}	2.98	3	9	2.50×10^{-6}	3	5	2.33	3.33	133272
D3	64	6.63	1000000	1	1	55	1.00×10^{-6}	1.00×10^{-6}	1.61	0	0	0.00	0	0	0.00	0.00	499999
D5	64	6.20	1200096	1	1	58.4	8.33×10^{-7}	8.33×10^{-7}	2.06	0	0	0.00	0	0	0.00	0.00	600048
D6	64	5.83	999873	444	444	66.5	4.44×10^{-4}	4.44×10^{-4}	2.52	85	445	8.50×10^{-5}	7	14	3.29	5.29	2245
E1	36	3.50	233280	89	187	42	3.82×10^{-4}	8.02×10^{-4}	6.74	18	78	4.50	9	20	4.50	8.17	2830
E2	Not available																
E3	36	5.71	315468	0	0	42	0.00	0.00	2.69	0	0	0.00	0	0	0.00	0.00	315468
E4	Unrecognized pattern																
E5	64	4.56	330561	27	27	45	6.24×10^{-5}	6.24×10^{-5}	4.56	6	28	1.82×10^{-5}	4	6	3.50	4.67	11804
F1-1	64	4.19	201465	68	68	42	3.38×10^{-4}	3.38×10^{-4}	5.26	15	69	7.50×10^{-5}	7	15	4.47	6.87	2918
F1-2	64	3.50	250000	89	92	42	3.56×10^{-4}	3.68×10^{-4}	6.74	16	78	6.40×10^{-5}	11	23	4.81	8.69	2830
F2	64	4.34	160209	14	14	42	8.00×10^{-5}	8.00×10^{-5}	4.98	4	15	2.50×10^{-5}	5	7	3.50	3.75	10679
F3	64	4.92	116865	0	0	42	0.00	0.00	3.90	0	1	0.00	0	0	0.00	0.00	116865

(a) TELEMETRY TEST SETUP CONFIGURATION (IN CTA 21)

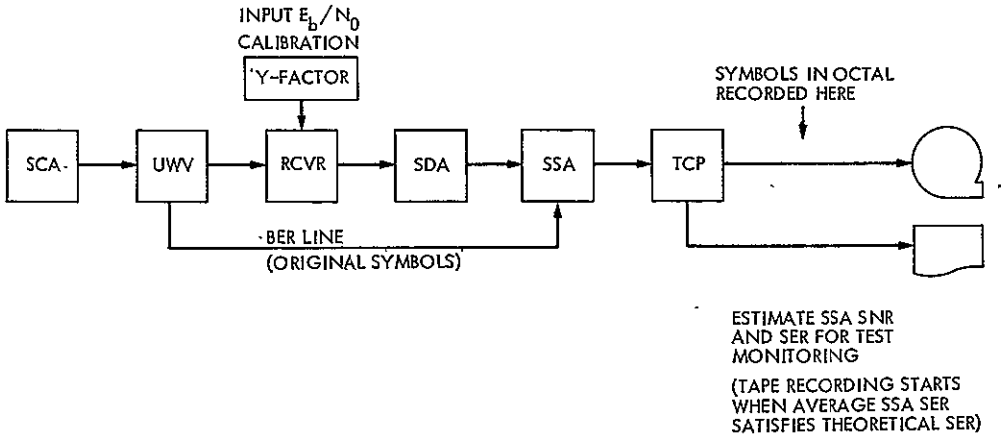

(b) TELEMETRY TEST DATA PROCESSING CONFIGURATION (UNIVAC 1108)

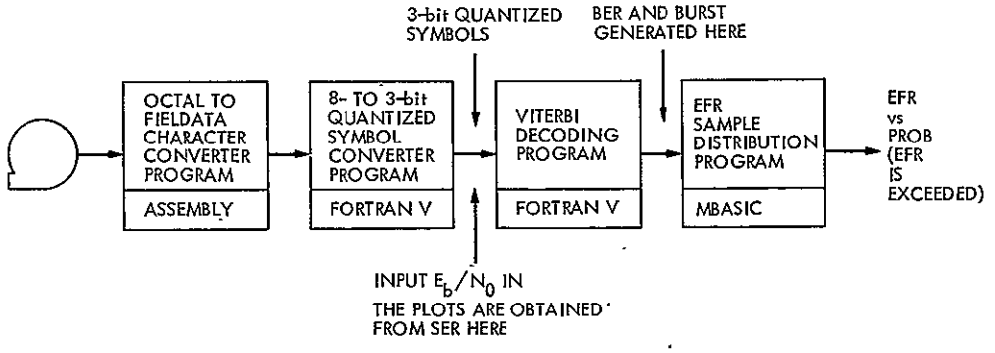

Fig. 1. Telemetry test setup and data processing configurations

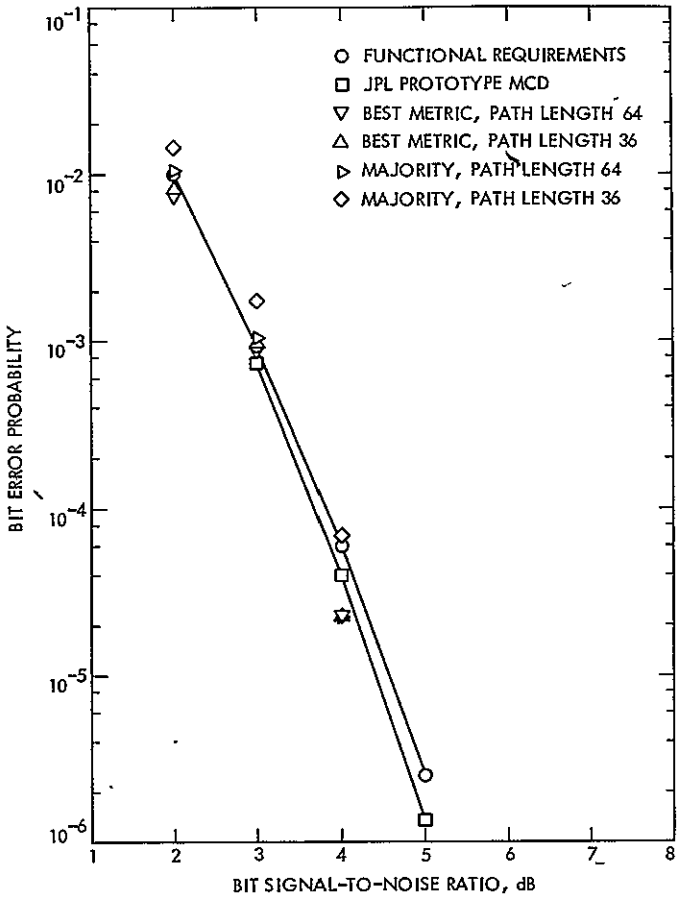

Fig. 2. Bit signal-to-noise ratio vs bit error probability

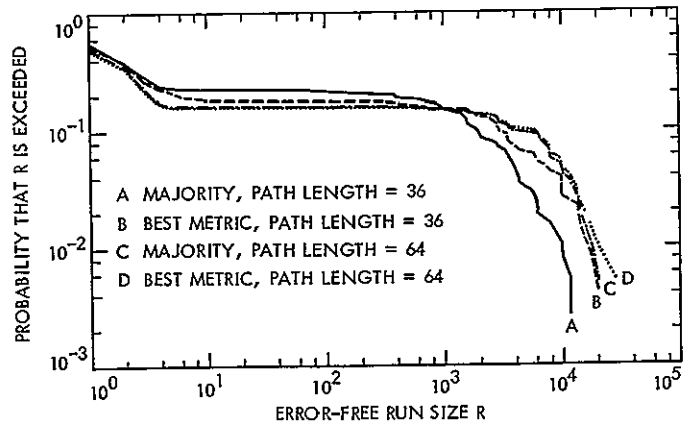

Fig. 3. Error-free run size R vs probability that R is exceeded

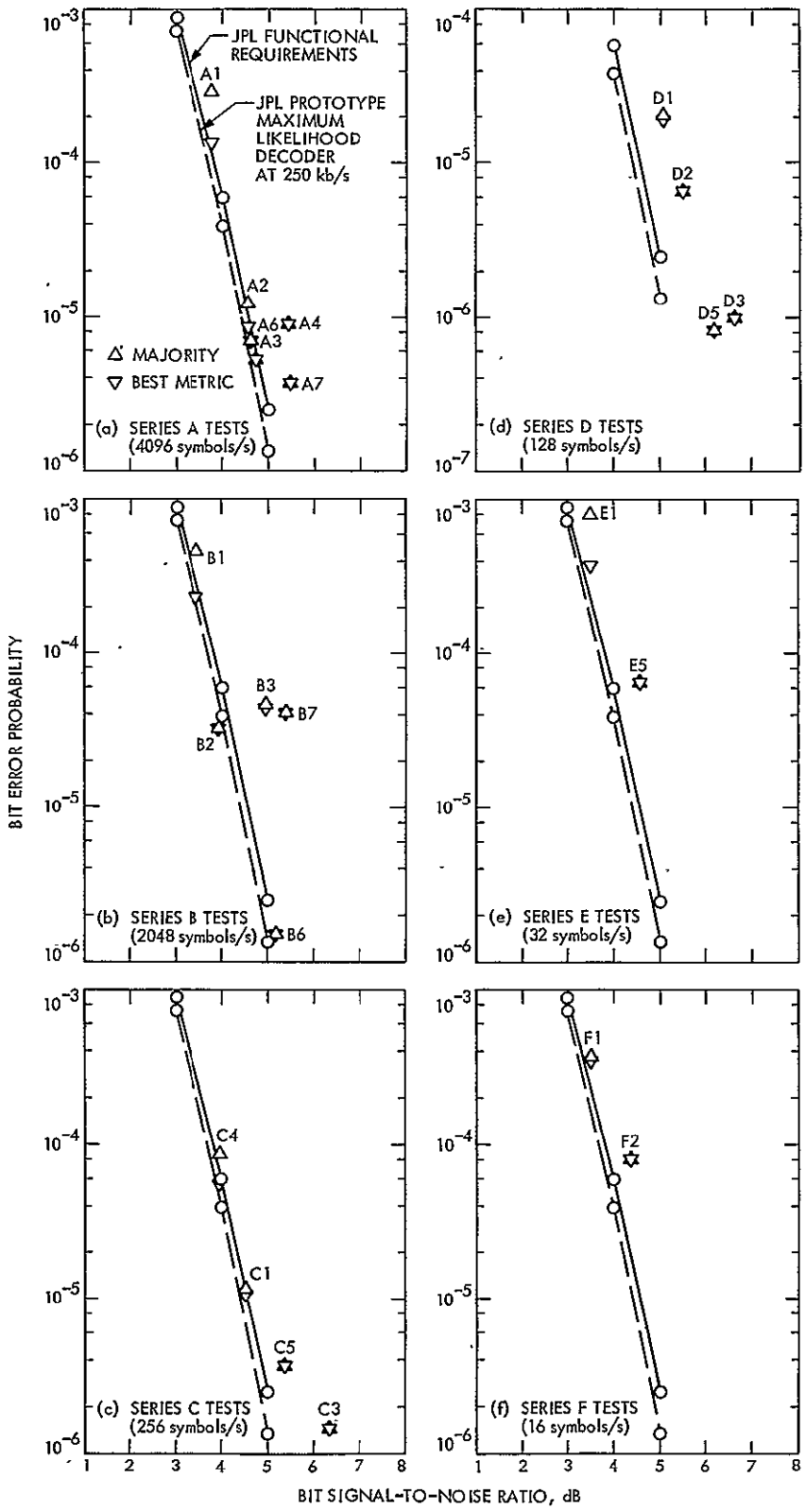

Fig. 4. Bit signal-to-noise ratio vs bit error probability for test series A through F

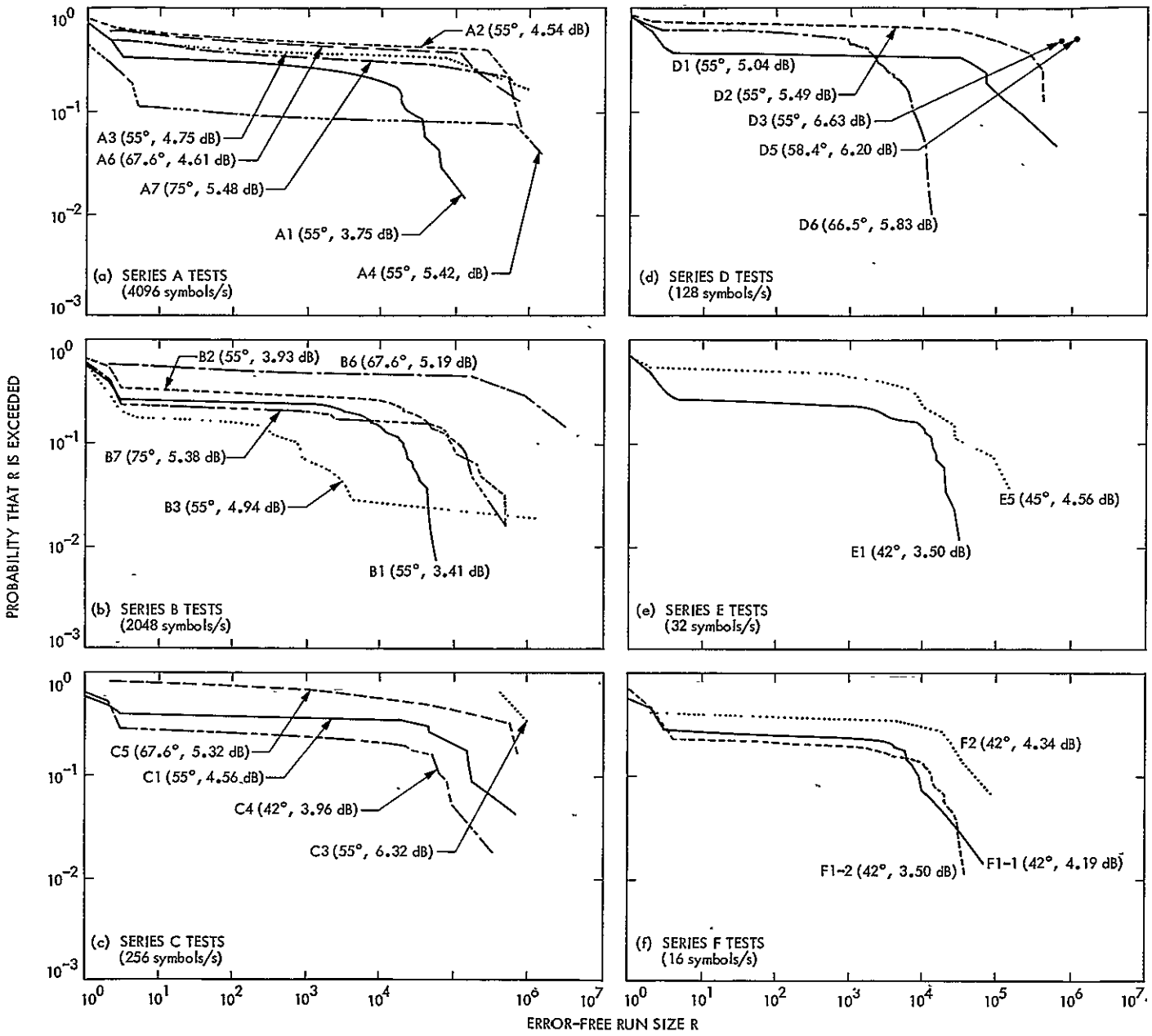

Fig. 5. Error-free run size R vs probability that R is exceeded for test series A through F

DSN Telemetry System Performance With Convolutionally Coded Data: Sequential Decoding Update

C. A. Greenhall
DSN Systems Engineering Office

DSN Telemetry System performance in decoding convolutionally coded data by both sequential and maximum-likelihood techniques is being determined by testing at various Deep Space Stations. This article describes corrections and refinements to the sequential decoding tests.

I. Introduction

Reference 1 described an ongoing program of tests designed to measure the performance of the DSN on convolutionally coded data. Both sequential and maximum-likelihood decoding techniques were tested. The former is used by the Pioneer and Helios projects, and the latter will be used by Mariner Jupiter–Saturn.

The present article is an update of Ref. 1 in the area of sequential decoding. It describes changes in the offline decoding program, improved estimates of signal-to-noise ratio (SNR), progress toward the determination of optimal modulation indexes, and comparisons between online and offline decoding tests.

II. Changes in the Decoding Algorithm

Since Ref. 1 was written, we have made some corrections to our offline sequential decoding algorithm to bring it more into line with the program in the Data Decoder Assembly (DDA) and to eliminate undetected bit errors. All test files were redecoded with the corrected program. The corrections are:

(1) A computation is counted when either the decoder steps forward along a best branch, or the decoder steps backward and does not immediately step forward again. Sideward steps are not counted. (A sideward step is a backward step along a best branch followed by a forward step along a worst

branch.) This change improved the comparison between online and offline decoding tests.

(2) The known bits in the tail (usually the last 32 bits of each frame) are "forced." In other words, the code tree ceases to branch once the tail is reached. Furthermore, the threshold is not tightened while the decoder is in the tail. This forces the decoder to back directly out of the tail if it turns out that errors were made in the bits immediately before the tail. This handling of the tail[1] eliminated the undetected bit errors reported in Ref. 1.

III. Tabular Summary of Tests

Each block of tests in Table 1 identifies a particular bit rate. The "nominal cutoff" is the nominal DDA sequential decoding computation rate of 20480 computations per second, referred to the given bit rate.

For each test we show

(a) The modulation index (MI).

(b) The observed symbol error rate (SER).

(c) The values of total power to noise spectral density ratio (P_t/N_0) and symbol energy to noise spectral density ratio (E_s/N_0) inferred from SER by a method explained in the next section. These are estimates of SNR before system degradations.

(d) Frame deletion rates for online and offline tests at the nominal cutoff. Where both online and offline deletion rates are shown, the two types of tests were run either at the same time or one right after the other. For blocks A to E, the SER was taken from the offline tests. The Block F online tests were performed at DSS 62, Madrid, Spain; for these tests, SER was available.

The frame length for the online tests is 192 bits; for the offline tests it is 180 bits (since the offline decoding program requires frame length to be a multiple of 36). An exception is test B1, where both online and offline tests use an 1152-bit frame. All tests use a 32-bit tail sequence.

For the cases with at least 10 deletions, an estimate of standard error is given. If there are k deletions, the error is $100/\sqrt{k}\,\%$ of the deletion rate.

[1]Suggested by J. W. Layland.

IV. Inference of Signal-to-Noise Ratio

As Ref. 1 noted, it has been difficult to determine the value of P_t/N_0 at the receiver. We therefore presented results using observed symbol error rate as an indicator of test conditions. (Decoder bit energy to noise spectral density ratio (E_b/N_0) was deduced by inverting the complementary error function.) For the present report, we ran a telemetry analysis program[2] with trial values of E_s/N_0 and observed the output SER. Using our *measured* SER, we could interpolate a value for input E_s/N_0 and, hence, for P_t/N_0.

Figure 1 shows the inferred P_t/N_0 versus modulation index for test blocks A through F.

It will be rather difficult to determine optimum modulation indexes from the tests run so far, for one does not find many tests with nearly the same P_t/N_0 but different modulation indexes. The next section discusses the conclusions that can be drawn about goodness of modulation indexes.

V. Choice of Modulation Indexes

Figure 2 shows sample distribution functions of the number of computations per bit for selected tests. Each vertical line is an approximate 90% confidence interval for the value of the distribution function. If p is the value of the function, and there are a total of n data, the confidence interval is

$$p\left(1 \pm \frac{1.65}{\sqrt{np}}\right)$$

We use this formula only for $np \geq 10$ data.

Referring to Figs. 1 and 2, we consider each test block (data rate) in turn.

Block A—2048 bits/s

Test A6 has lower power than A2 or A7, yet the A6 curve is lower than the others. It is not much lower, but the hypothesis that the A6 curve is above the A2 curve (at one point) is rejected by a statistical test at the 90% level. Thus, an MI of 67.6 deg is better than 55 or 75 deg.

Block B—1024 bits/s

B6 has less power than B3 or B7, and its curve is lower. Again, 67.6 deg is better than 55 or 75 deg.

[2]Written by G. Dunn.

Block C—128 bits/s

C4 has about 0.1 dB more power than C2, but the C2 curve is below the C4 curve up to 20 computations/bit. Beyond 20, there are not enough data, and we cannot say anything about the deletion rate at the nominal cutoff of 160 computations/bit. Nevertheless, it appears that 55 deg is better than 42 deg.

Block D—64 bits/s

D4 has more power than D1, but D4's performance is much poorer. An MI of 42 deg is simply much too low here—there is not enough power in the data.

D6 has more power than D5, but D6 is useless for telemetry. The shape of the distribution near its left end does not give a hint of the extremely heavy tail. It appears that an MI of 66.5 deg is much too high. There is not enough power in the carrier, and receiver phase jitter causes symbol errors to appear in bursts. Large numbers of computations become more likely.

Block E—16 bits/s

E5 has more power than E1, and its MI is higher. Although it is impossible to predict which would have the higher deletion rate at 1280 computations/bit, the curve for E5 appears to have the heavy tail characteristic of an MI that is too high. We cannot choose between 42 and 45 deg here.

The E3 and E4 curves show identical performance from MIs of 37.2 and 42 deg.

Block F—8 bits/s

The obvious comparisons—F2 with F5, and F3 with F4—fail to show any advantage of one MI over another.

Comments. We can make some qualitative remarks about the effect of modulation index on the distribution of computations. If MI is too low, the distribution curve has a knee near 1 computation/bit. Nearly perfect frames are unlikely because the SER is high. As MI increases, the knee disappears, the slope of the curve becomes steeper, and the curve approximates a Pareto (x^{-a}) distribution. The optimum MI is probably found in this range. As MI continues to increase, the curve becomes convex. Although the initial part of the curve is not much affected, the tail of the distribution becomes heavier as receiver phase jitter causes the symbol errors to become dependent.

We have not been able to pin down a clear optimum MI (within, say 1 deg) for any of these bit rates. This is partly because the P_t/N_0 values did not come out as intended. What is needed is a sequence of tests in which the Y-factor, which controls P_t/N_0, is kept accurately constant for a whole sequence of tests, while the MI is varied from test to test. It does not matter that it is difficult to relate *true* P_t/N_0 to the *observed* Y-factor. The true P_t/N_0 can be estimated later as we did in Section IV or by using the Symbol Synchronizer Assembly estimate of E_s/N_0. The important thing is that P_t/N_0 be kept constant (whatever its value) while varying MI.

VI. Comparison of Online and Offline Sequential Decoding

Purposes of offline decoding tests are (a) to measure performance when parameters such as frame length, tail length, and deletion cutoff are changed, and (b) to detect when something is seriously wrong with the online tests and to provide a backup in this case. It is thus necessary to find out how well the offline decoding program simulates the DDA decoder. Figure 3 shows some comparison plots, with some 90% confidence intervals attached to the distribution curves. The functions never disagree by more than a factor of 4 (until the statistics become unreliable). The offline B1 (frame length 1152) distribution function has more of a knee than the online function, but otherwise tracks the online function faithfully.

Since the offline tests are under better control than the online tests, we have rejected those online tests whose distribution curves differ *radically* from those of the corresponding offline tests. For example, as Table 1 shows, we rejected all Block D online tests except D6.

For Block F, however, the *offline* tests were rejected. It was difficult to get enough data at this low rate, and results differed widely from run to run.

Reference

1. Mulhall, B. D. L., *et al.*, "DSN Telemetry System Performance With Convolutionally Coded Data," in *The Deep Space Network Progress Report 42-30*, pp. 184–199, Jet Propulsion Laboratory, Pasadena, Calif., Dec. 15, 1975.

Table 1. Telemetry conditions and deletion rates

Test label	Modulation index, deg	SER, %	P_t/N_0, dB s^{-1}	E_s/N_0, dB	Deletion rate ($\times 10^{-4}$) Online	Offline
Block A. 2048 bits/s; nominal cutoff 10 computations/bit						
1	55.0	6.19	38.79	0 93		150 ± 6%
2	55.0	4.58	39.57	1.71	6 0 ± 25%	2.0
3	55.0	4 09	39.82	1.96	59 ± 8%	2.5
4	55.0	3.21	40.35	2.49	1.8	0.5
6	67.6	3 50	39 24	2.43	24 ± 13%	0.4
7	75.0	3.12	39.27	2.85	2.0	4 2 ± 30%
Block B. 1024 bits/s; nominal cutoff 20 computations/bit						
1[a]	55.0	6.99	35.55	0.70	33 ± 20%	44 ± 30%
2	55.0	5.84	36.05	1.20		6.7 ± 30%
3	55 0	3 92	37.00	2.15	5.6 ± 30%	10 ± 20%
4	55.0	3.11	37.49	2.64		0
6	67.6	3.47	36.40	2.61		0
7	75.0	3.16	36 53	3.12		6.1
Block C. 128 bits/s, nominal cutoff 160 computations/bit						
1	55 0	4.56	28.33	2.51	0	0
2	55.0	3.33	28 97	3.15	0.8	<2.5
3	55.0	2.33	29.60	3 78	0	0
4	42.0	5.88	29.09	1.52	3.0	<1
Block D. 64 bits/s, nominal cutoff 320 computations/bit						
1	55.0	3.70	26.25	3.45		<5
2	55 0	2.99	26.63	3.83		0
3	55.0	1.61	27.60	4.80		0
4	42 0	5.77	26.43	1.87		20 ± 30%
5	58.4	2.06	27 16	4 69		0
6	66.5	2.52	27.22	5.40	45 ± 35%	124 ± 12%
Block E. 16 bits/s, nominal cutoff 1280 computations/bit						
1	42.0	6.8	21.2	2.7		7
3	42.0	~3.0	~22.7	~4.2		<10
4	37.2	3 88	22.86	3.44		0
5	45.0	4.56	21.80	3.74		<17
Block F. 8 bits/s; nominal cutoff 2560 computations/bit						
1	42.0	6.43	19 36	3.83	13	
2	42.0	4.14	20.03	4.50	0	
3	42 0	2 69	20.66	5.13	0	
4	37 2	3.73	20.62	4.21	0	
5	45.0	3.10	20.31	5.26	2.0	

[a]Frame length = 1152 bits.

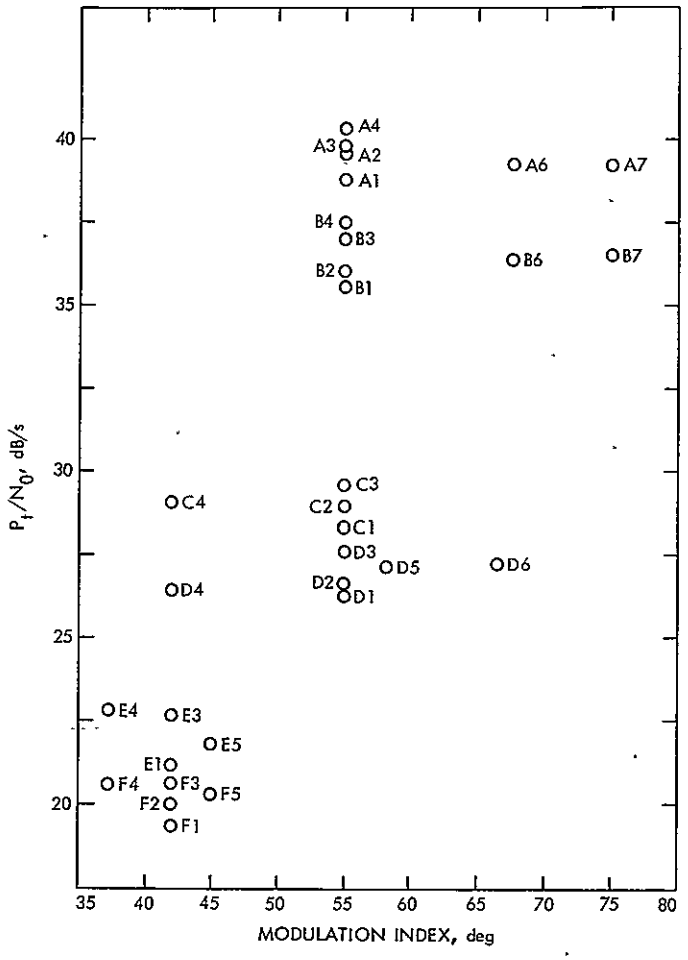

Fig. 1. Test conditions

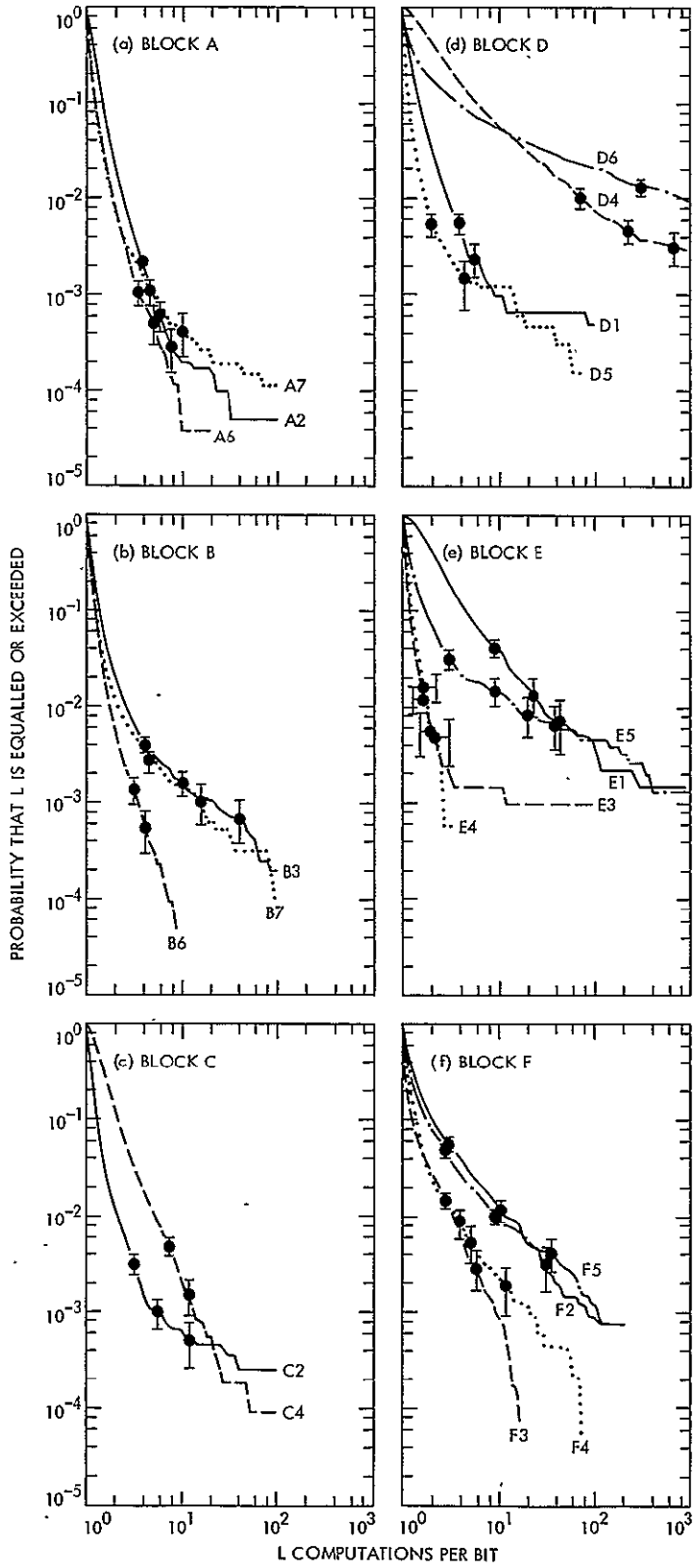

Fig. 2. Sample distribution functions of computations per bit

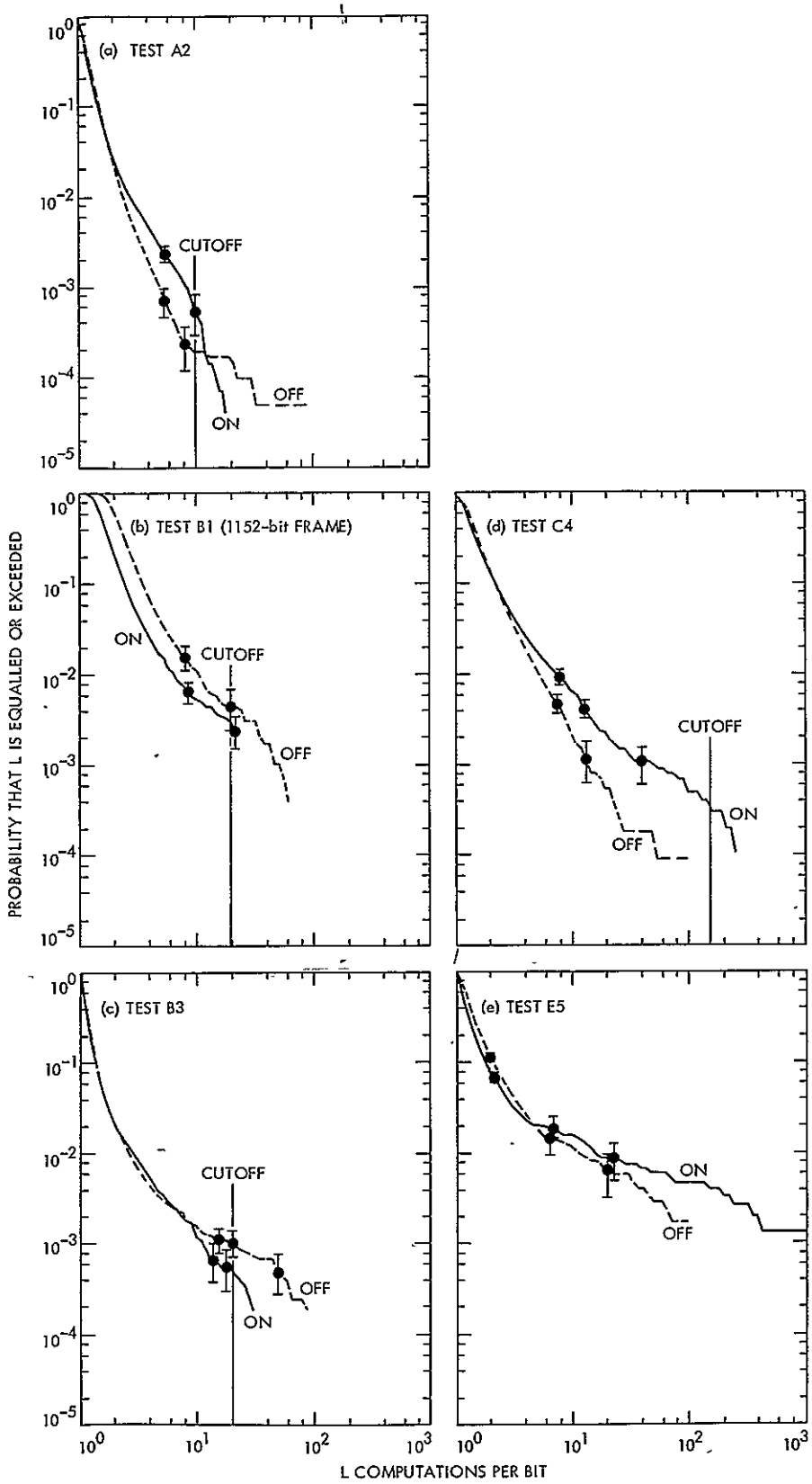

Fig. 3. Online and offline sequential decoding

DSN Performance Tests of a Maximum Likelihood Decoder

J. M. Urech
Station Director, Cebreros, Spain

L. D. Vit
Operations Manager for the Robledo Station

C. A. Greenhall
DSN Systems Engineering Office

Viterbi decoding tests were carried out at DSS 62, Madrid, Spain. Results of bit error rate, burst statistics, and estimation of signal-to-noise ratio are presented.

I. Introduction

The present report[1] covers the results of the Madrid DSN engineering task: DSN Performance for Convolutional Decoding. This work was undertaken by personnel from Deep Space Stations (DSSs) 62 and 63 at Madrid, Spain, in a joint effort with Section 430. A preliminary report has already appeared (Ref. 1).

The objective of the task was to determine the performance of the DSN in convolutional coding when using a maximum likelihood decoder.

The study required the integration of a maximum likelihood convolutional encoder-decoder model Linkabit LV7015 into the DSS Telemetry and Command Data Handling Subsystem (TCD) and the evaluation of its performance at a medium data rate. It also included the development of the appropriate testing software and a real-time performance estimator algorithm.

[1]Based on an internal report by the first two authors.

The task began with the receipt of the LV7015 unit at the end of June 1975. After its physical integration into the DSS 62 TCD Subsystem, a preliminary testing and calibration phase was carried out in parallel with the test software development. The actual system testing was initiated early in October 1975 and was terminated in December 1975. The evaluation of the system performance was carried out simultaneously with the data gathering.

This report covers the overall task results including the integration phase, algorithm development, software description, and test results.

II. Test Plan

The test strategy was to determine telemetry performance as a function of several ratios of total power to noise spectral density (P_t/N_o) and different modulation indexes for each P_t/N_o (these values are related to the Mariner Jupiter-Saturn Mission). The tests were run at

2560 bits per second with an actual error rate of approximately $5 \cdot 10^{-5}$, using Block III receiver (RCVR) and Block III and subcarrier demodulator assembly (SDA).

The tests were grouped into blocks corresponding to specific values of P_t/N_o and subdivided into runs for different values of modulation indexes (Table 1).

Figure 1 shows a reordering of runs as a function of the ratio of bit energy to noise spectral density (E_b/N_o). Most of the runs are in the 5 to 6 dB range where the theoretical bit error rate ranges approximately from 10^{-6} to 10^{-8}.

The analysis of the test results is presented in Section II of this report.

A. Test Configuration

The main configuration characteristics are summarized as follows:

1. Simulation Conversion Assembly (SCA) Configuration

SCA control:	Manual
Bit Rate:	2560 bits/s
Bit pattern:	Repetitive 111010
Modulation:	Biphase
Subcarrier:	22.5 kHZ
Data Type:	Fixed
Data Format:	Uncoded NRZ level

2. RF configuration

Maser:	To cold start
S-Band channel:	20
RCVR bandwidth:	Narrow
Automatic gain control bandwidth:	Narrow
SDA bandwidth:	Per test plan
Carrier suppression:	Using 50-MHz Y-factor

The carrier suppression adjustment allowed an accuracy of about 0.1 dB. The SDA-RCVR phasing was performed at a strong signal level and by adjusting the SDA modulation index attenuator for 280 mV peak to peak.

The E_b/N_o calibrations were also done by means of the Y-factor.

3. Digital configuration.

The digital configuration is summarized in Fig. 2. A detailed explanation of Phases I and II is given in Subsection II-B-3.

B. Test Software Description

A primary objective of this DSN engineering task was to evaluate DSN performance with convolutionally coded data when using the LV7015 unit. Some DSN projects already use convolutional coding but are decoded by a Fano-type algorithm. The present case, which is oriented to the Mariner Jupiter-Saturn Mission, uses convolutional data decoded by the Viterbi maximum likelihood decoding criteria. Then, since all the existing testing software was designed for a sequential Fano decoder, a new program was developed for the evaluation of the DSN performance with the Viterbi algorithm.

The main concern when decoding with the Viterbi algorithm is the decoded data bit error rate. With the Fano algorithm the main concern is the probability of erasing a block of coded data, that is, the probability of being unable to process a data frame before the next frame is ready for decoding. Therefore, in the present case the overall testing philosophy consists precisely in analyzing the bit error patterns.

1. Bit error characteristics. The Viterbi decoder algorithm does not proceed on a per block basis like the Fano algorithm nor does it consider past bit decisions. The decoded bits may be in error in a certain path length and yet able to remerge with a good path at a certain node and remain correct thereafter. Therefore, the decoder always proceeds forward and may depart from the correct path occasionally depending on channel noise characteristics. The bit errors occur in bursts whose characteristics are to be determined for the testing conditions. The burst approach suggests two definitions.

(1) An error-free run is a sequence of consecutive correct bits. Two different types of runs will be considered: Type 1 includes runs of length 0 to 5 ($R < 6$), and Type 2 includes runs of length 6 or greater ($R \geq 6$).

(2) An error-burst is a sequence of decoded bits which begins with a bit in error, ends with a bit in error, contains only Type 1 runs, and is surrounded by Type 2 runs. The shortest burst has length 1 (a single isolated error).

The statistical analysis of runs will then distinguish between correct bits within a burst assuming there is a

run of length zero between two consecutive bits in error, and runs of correct bits not in a burst; that is, 6 or more consecutive good bits.

The main point thereafter is to identify the bits in error, proceed with their classification into bursts and runs, and then analyze the clustering of errors and correct bits within the bursts.

2. Data compression. In order to handle the previously mentioned conditions, the following approach is taken: A bit error pattern is obtained by direct comparison of the original data and the decoded bits. Therefore the *ones* in this pattern represent bits in error in the decoded data. Instead of operating directly with this binary error pattern, a preprocessing step is first carried out. The number of consecutive *ones* and consecutive *zeros* in the error pattern are counted. The binary pattern is compressed into a sequence of integers where the odd terms correspond to consecutive *zeros* in the error pattern while the terms of even order correspond to consecutive *ones* in the error pattern. Note that the alternative choice could have been made as well. However, since it is much more likely that the actual sequence will begin with a run, the former approach is selected. This preprocessing (Phase I) greatly reduces the data storage required, the search time, and also simplifies the statistical evaluation (done in Phase II). Therefore, given an error pattern of the form

$$\underbrace{0\ldots.0}_{K1}\quad\underbrace{1\ldots.1}_{K2}\quad\underbrace{0\ldots.0}_{K3}\quad\underbrace{1\ldots.1}_{K4}$$

the corresponding sequence of integers would be

$$K1, K2, K3, K4 \qquad Ki \in N$$

where N is the set of non-negative numbers.

In general, the runs of ones and the runs of zeros are transformed into a sequence of integers

$$(a_i); \qquad i \in N$$

where the subsequence of odd terms

$$(a_i); \qquad i = 2K - 1,\ K = 1,2,3, \cdots$$

represents the respective lengths of the runs of zeros, and the subsequence of even terms

$$(a_i); \qquad i = 2K \qquad K = 1,2,3, \cdots$$

represents the respective lengths of the runs of ones. All the considerations concerning error bursts and runs are taken directly from the sequence (a_i).

3. Software characteristics. As previously stated, the overall process is carried out in two phases.

During Phase I the data are gathered in real time as per the configuration depicted in Fig. 2. The high-speed data (HSD) blocks are classified and the decoded data are synchronized and compressed as explained in Subsection II-B-2. A quick-look display of signal level, Symbol Synchronizer Assembly (SSA) signal-to-noise ratio (SNR), normalization rate, and bit error rate (BER) is optional through TTY or line printer for a preliminary test verification. The final product of Phase I is then a classified and compressed error pattern.

The actual data analysis is performed during Phase II, and the mag tape Digital Original Data Record (DODR) recorded during Phase I is processed as follows:

(1) The mag-tape records are classified into in-sync or out-of-sync status, matrix records, statistics records and end of runs.

(2) The statistical analysis and outputs are carried out and displayed on the line printer.

III. Test Results

A brief review of the test plan setup conditions reflects a concentration of SNRs especially in the 5- to 6-dB range (Fig. 1) which corresponds to very small variations of modulation indexes for relatively close values of P_t/N_o. The resulting variations from one test to another are in most cases smaller than the intrinsic uncertainties of the evaluating algorithms. It is then difficult to determine whether the deviations relative to the expected values are due to set-up errors or actual degradations. For a better presentation of the results, a table has been assigned to each block of runs. These tables (Table 1) contain the following data extracted from the test printouts:

(1) E_b/N_o (TH): Theoretical values from the test plan.

(2) $\Delta E_b/N_o$ $(\overline{N}_c)$: The difference E_b/N_o (TH) $- E_b/N_o$ $(\overline{N}_c)$, where E_b/N_o $(\overline{N}_c)$ is the estimation of the bit energy-to-noise density through the normalization rate algorithm developed in Section IV.

(3) $\Delta E_b/N_o$ (SSA): The difference E_b/N_o (TH) $- E_b/N_o$ (SSA), where E_b/N_o (SAA) is the SNR estimator by the SSA, unbiased for values over 5 dB and incre-

mented by 3 dB to represent bit energy-to-noise density ratio.

(4) The total number of bits in the run.

(5) The bit error rate directly obtained from the error pattern.

(6) $\Delta E_b/N_o$ (BER): The difference between E_b/N_o (TH) and the value of E_b/N_o which theoretically gives the observed BER.

(7) Average length of runs ≥ 6.

(8) Average length of burst.

(9) Average number of errors per burst.

(10) Average density of errors in a burst. This is simply the average number of errors per burst/average length of burst.

The test results are analyzed next from two different aspects:

(1) In terms of system degradation.

(2) In terms of statistics on runs and bursts, and other parameters.

A. System Degradation

The system performance in terms of degradation is evaluated in three different steps:

(1) The SSA SNR which shows the performance at the decoder input.

(2) The bit error rate which is actually the basic parameter reflecting decoder performance.

(3) The normalization rate which reflects the specific characteristic of the decoder. This study is made in Section IV.

1. SSA SNR algorithm. Figure 3 represents the differences between E_b/N_o (TH) and E_b/N_o (SSA) for each run. These results are typical representations of the SSA SNR statistical variations. It may be noted for instance, that for blocks H, I and J having practically the same P_t/N_o, a slight average degradation increase is observed as the SDA bandwidth is increased. Also, there seems to be a very small increase in degradation for the highest modulation indexes in each block.

As will be emphasized later on, the SSA SNR values are very poorly correlated with the actual decoder behavior in terms of bit errors since large increments in the number of errors are not reflected by the SSA algorithm.

2. System performance versus BER. All the results concerning the bit error rate are of great importance for the system performance evaluation. The decoder behavior will be reflected in the number of errors for each test condition. Figure 4 shows the difference between E_b/N_o (TH) and E_b/N_o derived from experimental values of the bit error rate. There is a striking difference with Fig. 3 in that the BER shows a rapid increase for runs with higher modulation indexes in a given test block. This degradation effect (actually at the highest data SNR) is justified by the corresponding receiver jitter increment at lower receiver margin values. For a given total power, at higher modulation indexes the increased carrier suppression causes a slowly varying (compared to bit rate) jitter which affects system performance by introducing additional degradation. It must be noted though that the optimum working point is not to be derived from the results plotted in Fig. 4. Instead it is more convenient to analyze the behavior of the bit errors as a function of the modulation indexes and establish the optimum point by choosing (for each P_t/N_o) the carrier suppression yielding the lowest error rate. This is done in Fig. 5 for each of the test blocks.

It is clearly seen that there exists a minimum degradation point on the order of 70 degrees, while above these values the degradation due to jitter greatly overcomes the increase of data power obtained from higher carrier suppressions. Of interest is the comparison of these results with those presented on page 173 of Ref. 2; the experimental results are compatible with the theoretical model. There also appears to exist a correlation between the results in Figs. 4 and 5 as expected. The family of curves of Fig. 5 are also compatible with the test conditions in terms of total power-to-noise density ratios. Several conclusions are then available at this point:

(1) The increasing values of modulation indexes cause an increasing degradation due to jitter when surpassing a certain optimum modulation point in the range of 70 degrees.

(2) The corresponding bit error rate increase is not reflected by the SSA SNR algorithm which shows very small increments in degradation.

It must be brought out again that the close proximity of test setup conditions and the normal algorithm dispersions make a neat evaluation of the optimum conditions difficult, but approximate values are possible with an

acceptable definition. Evidently, the optimum modulation indexes could be pinned down more precisely if more tests were run between 65 and 70 degrees.

B. Statistical Results on Bursts and Runs

The results developed in the previous paragraph would be conclusive as far as optimum working conditions if the bit errors at the decoder output were randomly distributed. However, this is not the case for a maximum likelihood decoder where the errors tend to concentrate into bursts Therefore, although an optimum point has been derived from experimental results, this situation must now be confirmed in terms of the statistical behavior of bursts and runs.

1. Theoretical considerations. The definition of burst is tied closely to the choice of code and method of decoding. The convolutional code has constraint length 7; the state of the decoder consists of the last 6 bits shifted into it. (See Ref. 3 for an exposition of Viterbi decoding.) We can consider the correct path through the trellis as being the all 0's path, and assume that all paths ultimately fail to survive except one. The state of the ultimate surviving path differs from the state of the correct path whenever there is a 1 in the state bits of the shift register, and returns to the correct state as soon as a run of 6 0's has appeared. Thus, there is a one-to-one correspondence between the sequence of bursts and the sequence of excursions of the surviving path from the correct path. An excursion M branches long will yield a burst of length $M - 6$. If there are n wrong bits in this burst, there are $M - 6 - n$ correct bits grouped in runs <6.

The fixed path memory of the decoder can cause additional errors not included in this scheme; the decoder will occasionally choose a bit not belonging to the ultimate survivor path.

2. Error bits in bursts and burst lengths versus BER. We shall now select the BER as a variable and study its effects on the number of errors in a burst and the burst length. Let

P_1 = probability that a burst has length 1

L = average length of a burst

D = average density of errors in a burst

D_i = average density of errors in the interior of a burst

= total number of interior errors/total number of interior bits

The interior of a burst consists of the burst minus its endpoints (which are always bad bits). Bursts of length 1 or 2 have empty interior. The relation

$$D = D_i\left(1 - \frac{2 - p_1}{L}\right) + \frac{2 - p_1}{L}$$

is a direct consequence of the definitions.

Figures 6, 7, and 8 are scatter diagrams of L, D, and D_i, respectively, versus BER. The L and D plots show slow increasing and decreasing trends, but D_i fluctuates about a constant level of about 0.48 for $5 \cdot 10^{-6} < \text{BER} < 2 \cdot 10^{-3}$. (For $\text{BER} < 5 \cdot 10^{-6}$ the data are scanty and the statistics poor.) More information on the behavior of the interior bits could be obtained from the distributions of runs of length <6. We have not yet done this; nevertheless, we will tentatively model a burst as having a length whose mean depends slowly on the BER, and an interior error density whose mean is constant and slightly less than ½.

3. Statistical results on runs. The average run length ($R \geq 6$) is directly related to the BER. Let $\overline{R}$ be the average length of the runs $R \geq 6$. Then $\overline{R}$ = (number of bits − total burst length)/number of $R \geq 6$. Since total burst length $<<$ number of bits, and number of $R \geq 6$ = number of bursts + 1, we get

$$\overline{R} = \frac{\text{L} \cdot \text{D}}{BER \cdot (1 + 1/N_b)} \tag{1}$$

where N_b = number of bursts. This applies to average values, but does not reflect the statistical behavior of runs. The statistical analysis carried out by the test software includes the distribution function of $R \geq 6$. These curves for Block H tests are shown in Fig. 9.

The plots seem to add some additional information to the curves in Fig. 5. The optimum range in the family of curves is not as broken as in the case of Fig. 5 and even defines a broader range of appropriate values.

The same degradation effects observed at different modulation indexes upon the BER are also affecting the average run length in a similar manner. The effect of the increasing total power-to-noise density according to the test plan is reflected as expected by longer runs of error-free bits.

However, for each family of curves the optimum choice seems, as stated before, less broken than in Fig. 5. As a

matter of fact, tests J, H, G and K yield the longest runs at modulation indexes in the range corresponding to about 71 or 72 degrees. The distribution plot of Test I appears to be quite correlated with the results in Fig. 5 and the best curve in the latter is the deepest point in the former plotting. Tests L did not yield sufficient statistics as to allow a plotting of a curve.

These run length distributions are the distributions of waiting time between bursts. As a trial hypothesis, we might suppose that the positions of the bursts form approximately a Poisson process on the time axis. If this is so, then we should have

$$P = e^{-(r-6)/(\bar{R}-6)}$$

where P is the probability that a run of length ≥ 6 is not less than r, and $\bar{R}$ is the average length of runs ≥ 6. (We pretend that we are dealing with a continuous distribution.) Treating the 6's as negligible, we rewrite the above as

$$\log_{10} \ln (1/P) = \log_{10} r - \log_{10} \bar{R} \qquad (2)$$

Figure 10 is a log-log plot of ln $(1/P)$ versus r for most of the curves of Fig. 9. The dashed lines are from Eq. (2) using the values of $\bar{R}$ from Table 1. The fit is good; we conclude that at least for $r > 10^3$ the distributions are exponential and are thus determined by their means $\bar{R}$.

It is then appropriate to plot $\bar{R}$ versus modulation index for each block. This we have done in Fig. 11. The result is essentially an upside-down version of Fig. 5, with slight differences. (Eq. (1) would lead us to suspect this.) It is apparent that either run length distributions or BER can be used to locate optimum-modulation indexes.

4. Statistical results on bursts. Figure 12 represents selected burst length distribution curves[2] for Block H tests. As expected, these curves are similar and do not present significant deviations. They depend slightly on the signal-to-noise condition with longer bursts at higher bit error rates.

It must be noted, however, that the maximum burst lengths (not shown in this article) are in some cases much longer than expected. In these test runs there is a large gap between the maximum and next to maximum values. This has not been explained fully but there are a few indications that they might be caused by random malfunctions in the SSA coupler.

[2]Only the bursts of length ≥ 2 are included.

IV. System Performance Evaluator

It is convenient to derive the system performance evaluation from some parameter directly related to the decoder operation and the only parameter which may be made available to the operational program is the normalization counter. The following presentation justifies the use of the normalization values as performance evaluator.

A. Normalization Rate

The Viterbi decoder algorithm behaves basically as a progression along the trellis by pairwise comparisons of paths and the elimination of less probable paths, following a metric criterion. The pairwise comparisons are made at each bit time and the metric values are derived from the channel symbol quantizations provided by the SSA, and the branch symbols hypothesized by the so called "normalization rate" mechanism.

The normalization mechanism may be visualized as being composed of a set of 4-stage buffers which, at each bit time, are incremented by a metric value and then compared pairwise as per the trellis structure. To simplify the scheme it may be assumed that the path holding the lowest metric is considered to be the "best" path. However, during the decoding process all paths including the "best path" will accumulate metric values so as to saturate their corresponding buffers (assuming a significant noise level). In the decoding range of operation the "wrong" paths will nevertheless accumulate at a much faster rate than the "best" path. A *normalization* occurs when the logic detects that all the "wrong" paths have a high metric ($M >> 4$) and that the best path has just reached or surpassed a threshold of 4. At this time all the buffers are reduced (normalized), and this fact (normalization) is registered in a counter.

B. Theoretical Model

Figure 13 represents schematically the density function of the SSA output, together with the schemes for quantizing the output and computing the metric increment m. It is assumed that a "0" symbol was sent and that the best path also outputs a "0" at this point. If the BER is low, we can assume that for most of the time, the best path symbol agrees with the symbol that was sent. Then the accumulation of metric by the best path, i.e., the normal-

ization rate, will reflect the ratio of symbol energy to noise spectral density (E_s/N_o) seen by the decoder.

The normalization per bit N_b is just half the accumulation of metric per symbol time by the best path. In terms of the probabilities p_i shown in Fig. 13, the *mean* normalization per bit, $\bar{N}_b$, is given by

$$\bar{N}_b = 1/2 \sum_{j=1}^{4} j p_j \tag{3}$$

Let $P_e(E_s/N_o)$ be the probability of a hard-decision symbol error for any given E_s/N_o. Let $K = M/Q$, where M is the integration mean and Q the quantization interval. Then Eq. (3) becomes

$$\begin{aligned} \bar{N}_b &= 1/2 \sum_{i=0}^{\infty} P_e((E_s/N_o)(1 + i/K)^2) \\ &= f(E_s/N_o, K) \end{aligned} \tag{4}$$

Now the question arises: Will the model depart from experimental results at low E_s/N_o when the bit error rate is significant? How will the model be adapted to the system operating conditions?

In order to answer the above questions a series of tests were run with a standard configuration, sampling the normalization counter for different E_s/N_o and assuming a value of K corresponding to the optimum SDA/SSA setting of 280 mV. We have determined experimentally that this value of K is 2.5.

C. An Algorithm for Performance Evaluation

The mathematical model developed in the previous section seems to be accurate enough to constitute the basis for a performance evaluator. The requirements may be summarized as a need to evaluate decoder performance (or the system performance) from the normalization rate. A convenient performance estimator could be one which would evaluate the bit error rate or, more simply, the energy per bit-to-spectral noise density. In our case the problem will be reduced to relating the normalization counter values to the bit energy-to-spectral noise density, E_b/N_o.

The function f in Eq. (4) was evaluated numerically for a range of E_s/N_o and for several values of K. Then, with K set equal to the optimum value, the function was inverted graphically to give $E_b/N_o = E_s/N_o + 3$ dB as a function of $\bar{N}_b$. However, since the normalization counter is transferred to the operational program every 192 bits, it was thought that it would be preferable to use normalization counts ($\bar{N}_c$) instead of the normalization rate ($\bar{N}_b$) as the variable. Thus, a final change was made where

$$\bar{N}_c = 192 \times \bar{N}_b$$

and finally

$$E_b/N_o, dB = g(\bar{N}_c)$$

was obtained.

For the practical purposes of using the relationship as a computerized algorithm, a rational function was fitted to the numerical values of $g(\ )$. The final expression adopted for the algorithm was then

$$E_b/N_o, \text{dB} = \frac{2.9664}{\bar{N}_c + 0.08} + 5.1218 - 0.2252\,\bar{N}_c \tag{5}$$

This expression will, therefore, convert the normalization counts as transferred from the decoder into the corresponding channel E_b/N_o, dB. Figure 14 is a plot of expression (5) and is compared to the values of $g(\ )$. The fit has an error lower than 0.3 dB in the range $1 < \bar{N}_c < 15$. Although the fit is poor for $\bar{N}_c < 1$, the approach is not useful anyway in this region. The statistics become very poor at E_b/N_o over 7 dB, since extremely few normalizations will occur and the conversion into E_b/N_o becomes less relevant.

D. Experimental Results

The experimental results obtained from the test runs are now analyzed to prove the practical validity of the algorithm. The E_b/N_o values derived from the normalization rate are compared to the corresponding SSA SNR algorithm. Fig. 15 shows the difference in dBs between the normalization algorithm values and the SSA values. The normalization algorithm values have been adjusted to correct the curve fitting error of Fig. 14. For most of the runs, the normalization and SSA estimates agree within 0.2 dB. The conclusion is that the normalization algorithm behaves very much as the SSA algorithm.

Finally, in Fig. 16 we plot BER versus E_b/N_o ($\bar{N}c$) for the test runs having optimum modulation index (lowest BER for each block). The SNR values have again been corrected according to the curve fit error in Fig. 14. The plotted points show rather good agreement with a theoretical curve of BER versus E_b/N_o. Thus the normalization rate algorithm seems to give a good estimate of the SNR that the decoder actually sees.

Acknowledgments

This study represents the combined effort of several members of the Madrid Space Station staff including A. Chamarro (Operational Software Integration and Linkabit Model LV 7015 Integration); J. L. Morales (Testing Software Development); M. S. Cristobal and A. M. Rosich (Testing Preparation and Coordination); and J. L. Alonso, A. Cancela, and F. Sanz (Hardware Interface Design and Implementation). The contributions of the DSS 62 personnel who configured and ran the tests are also acknowledged.

References

1. Urech, J. M. et al., "Preliminary Results of DSN Performance for Convolutional Codes With a Viterbi Decoder," in *The Deep Space Network Progress Report 42-32*, pp. 222-240, Jet Propulsion Laboratory, Pasadena, Calif., April 15, 1976.
2. Edelson, R. E., ed., *Telecommunications Systems Design Techniques Handbook*, Technical Memorandum 33-571, Jet Propulsion Laboratory, Pasadena, Calif., 1972.
3. Viterbi, A., "Convolutional Codes and Their Performance in Communications Systems," *IEEE Transactions on Communications Technology*, Vol. COM-19, No. 5, 1971.

Table 1. Summary of test conditions and results (1.2E3 = $1.2 \cdot 10^3$)

Run	Mod index, deg	E_b/N_o (Th)	$\Delta E_b/N_o$ ($\overline{N}_r$)	$\Delta E_b/N_o$ (SSA)	No of bits	BER	$\Delta E_b/N_o$, BER	Average run length ≥ 6	Average burst length	Average no. of errors per burst	Average density of errors in burst
Block H, P_T/N_0 = 39 67 dB, RCVR/SDA bandwidths: 12 Hz/Narrow											
1	55	3.85	0.75	0.72	9.9E6	7.31E-4	0.7	5.16E3	6.06	3.77	0.623
2	65	4.73	0.87	0.92	9.0E7	1.13E-4	1.1	3.05E4	5.61	3.45	0.615
3	69	4.99	0.71	0.57	9.0E6	1 19E-5	0.6	1.96E5	3.66	2.38	0.652
4	70	5.05	0.65	0.48	4.9E7	2 04E-5	0.9	1.87E5	5.96	3.83	0.643
5	70.6	5 08	0.94	0.97	9.1E7	4.81E-5	1.1	7.67E4	5 82	3.69	0.634
6	71	5 10	0.57	0.50	4.4E7	1.35E-5	0.8	2.58E5	5.76	3.50	0 608
7	72	5 15	0.83	0 77	9.9E6	2 39E-5	1.0	1.54E5	5.80	3.74	0.644
8	73	5.20	0.85	0.80	9.4E6	8.11E-5	1.4	4.71E4	6.15	3.84	0 624
9	74	5.24	0 84	0.79	1 0E7	6.86E-5	1.4	6.19E4	6.94	4.27	0 615
10	76	5.33	0.80	0.69	9.4E6	7.13E-5	1.6	6.08E4	7 46	4.36	0.585
11	78	5.40	1.21	0.91	1.0E7	3.32E-4	2 1	1.68E4	9.50	5.59	0.588
12	80	5 45	0.88	0.75	9.0E6	7.37E-4	2.3	8.4E3	10.7	6.20	0.577
Block I, P_T/N_0 = 39.77 dB, RCVR/SDA bandwidths. 12 Hz/Medium											
1	55	3.95	0.64	0.62	1.0E7	4.13E-4	0.6	9.3E3	6 28	3.84	0.612
2	65	4.83	0 83	0 83	9.7E6	4.67E-5	0.9	7.7E4	5.84	3.62	0.621
3	69	5 09	0.70	0 56	8.8E6	8.0E-6	0 6	3.7E5	4.58	3.08	0.672
4	70	5.15	0.89	0.84	8 1E7	2.5E-5	1.0	1.4E5	5.42	3.51	0.646
5	70.7	5.19	0.82	0.80	7.1E7	2 58E-5	1.1	1.5E5	6.13	3.88	0 633
6	71	5.20	0.82	0 78	6.9E7	3.88E-5	1.2	9.7E4	6.05	3.77	0.623
7	72	5.25	0.91	0.82	1.3E7	5.17E-5	1.3	7.6E4	6.44	3.95	0.614
8	73	5.30	0.82	0.73	1.1E7	5.17E-5	1.4	8.4E4	7.18	4.38	0 609
9	74	5.34	0.81	0.75	1.0E7	4.11E-5	1.4	9.8E4	6.71	4.07	0 606
10	76	5.43	0.82	0.74	9.0E6	4.91E-5	1.5	9.8E4	7.86	4.86	0.619
11	78	5.50	1.67	0.94	7.4E6	5.36E-4	2.3	1.0E4	9.08	5.37	0 591
12	80	5.55	1.30	1.14	9.0E6	1.95E-3	2.8	3.8E3	13 0	7.41	0.572
Block J, P_T/N_0 = 39.82 dB, RCVR/SDA bandwidths: 12 Hz/Wide											
1	55	4.00	0.82	0.67	1.1E7	6.39E-4	0.8	6.0E3	6.30	3.84	0.609
2	65	4 88	0.91	0.95	1.1E7	7.09E-5	1.1	5.18E4	5 63	3.69	0.655
3	69	5.14	1.16	0 81	9.5E7	3.45E-5	1.1	9.89E4	5 43	3.42	0.629
4	70.8	5.24	1.01	1.0	4.7E7	4.56E-5	1.3	8 28E4	6.06	3.78	0.624
5	71	5.25	1.02	0.91	4.5E7	3.4E-5	1.2	1.18E5	6.41	4 02	0.627
6	72	5.30	0.91	0.81	9.4E6	4.71E-5	1.4	8.3E4	6.54	3.94	0.603
7	73	5.35	0.92	0.81	9.1E6	3 48E-5	1.3	1.02E5	5.59	3.59	0.642
8	74	5.39	0.91	0.88	9.4E6	5.43E-5	1.5	7.7E4	6.85	4.22	0.616
9	76	5.48	1.02	0.87	9.6E6	6.46E-5	1.5	6.28E4	6.63	4.08	0.616
10	78	5 55	1.28	0.93	9.0E6	1.97E-4	2.1	2.44E4	8.17	4.82	0.590
11	80	5.60	1.24	1.07	9.2E6	1.58E-3	3.0	4.53E3	12.5	7.16	0.574

Table 1 (contd)

Run	Mod index, deg	E_b/N_o (Th)	$\Delta E_b/N_o$ ($\overline{N_c}$)	$\Delta E_b/N_o$ (SSA)	No. of bits	BER	$\Delta E_b/N_o$, BER	Average run length ≥ 6	Average burst length	Average no of errors per burst	Average density of errors in burst
Block G, $P_T/N_0 = 40.26$ dB, RCVR/SDA bandwidths. 12 Hz/Medium											
1	55	4.44	0.61	0 62	9.9E6	7.92E-5	0.7	4.4E4	5.40	3.50	0.648
2	65	5.32	0.82	0.65	1.0E7	6.55E-6	0 8	5.5E5	6.05	3 81	0.630
3	69	5.58	0.87	0 61	8.4E6	3 55E-6	0.9	7.67E5	4 50	3 00	0 666
4	70	5.64	0.97	0.69	8.0E6	4.48E-6	1.0	4.66E5			
5	71	5.69	0 83	0.63	7.4E7	5 47E-6	1.1	6.7E5	6 23	3.70	0.594
6	72	5.74	0.87	0.59	4.3E7	6.33E-6	1.2	5.8E5	6.11	3.72	0.610
7	73	5.79	0.98	0.76	3.9E7	2.63E-5	1.7	1.8E5	7.57	4 76	0 628
8	74	5 83	0.97	0.72	1 1E7	2.02E-5	1.6	2.0E5	6.41	4.12	0.642
9	75	5.88	1.2	0.64	9.0E6	9.03E-6	1.4	4.2E5	6.14	3 98	0 648
10	78	5 99	1 29	0.80	9 1E6	8.87E-5	2.3	5.5E4	7 97	4 91	0 616
11	80	6.04	1.02	0.77	8.6E6	3.0E-4	2 6	1.9E4	9.89	5 71	0 577
Block K, $P_T/N_0 = 41$ 26 dB, RCVR/SDA bandwidths. 12 Hz/Medium											
1	55	5 44	0 83	0 78	9.6E6	8.37E-6	1.0	5.8E5	8.58	5.17	0.602
2	65	6.32	1 0	0.72	8 5E6	2.29E-7	0.8	4.3E6	2.00	2.00	1.00
3	72	6.74	0 98	0.46	9 0E7	1.13E-7	1.1	2.2E7	5.60	3.30	0.589
4	73 5	6 81	1.27	0.81	8.6E7	3.88E-7	1.5	6 2E6	3.75	2.59	0.691
5	74	6.83	0.96	0.70	8.5E7	3.77E-7	1.5	6 25E6	3.78	2.54	0 674
6	75	6.88	1.22	0.94	9 3E6	6.31E-7	1.7	3.16E6	5 50	3.02	0 549
7	76	6.92	0 89	0.54	9.4E6	1.73E-6	2 0	3.1E6	11.0	8.00	0.727
8	77	6 95	0.87	0 56	9.0E6	1.54E-6	2.0	1.5E6	4.36	2.77	0.636
9	80	7.04	1.31	0.85	8.5E6	1.45E-4	2.5	3.8E4	9.44	5 53	0.587
Block L, $P_T/N_0 = 42.76$ dB, RCVR/SDA bandwidths: 12 Hz/Medium											
1	55	6 94	0 80	0.47							
2	65	7.82	0.23	0.42							
3	73	8.29	−0.52	0 39							
4	74	8 33	−4.1	−0.37							
5	75	8 38	0.33	0.72							
6	75.2	8.38	0.15	0.63							
7	76	8.42	0.21	0.69							
8	77	8.45	0.27	0.77							
9	78	8.49	1.07	0 85							
10	80	8.54	−0.03	0.69		2.3E-6	3.7				

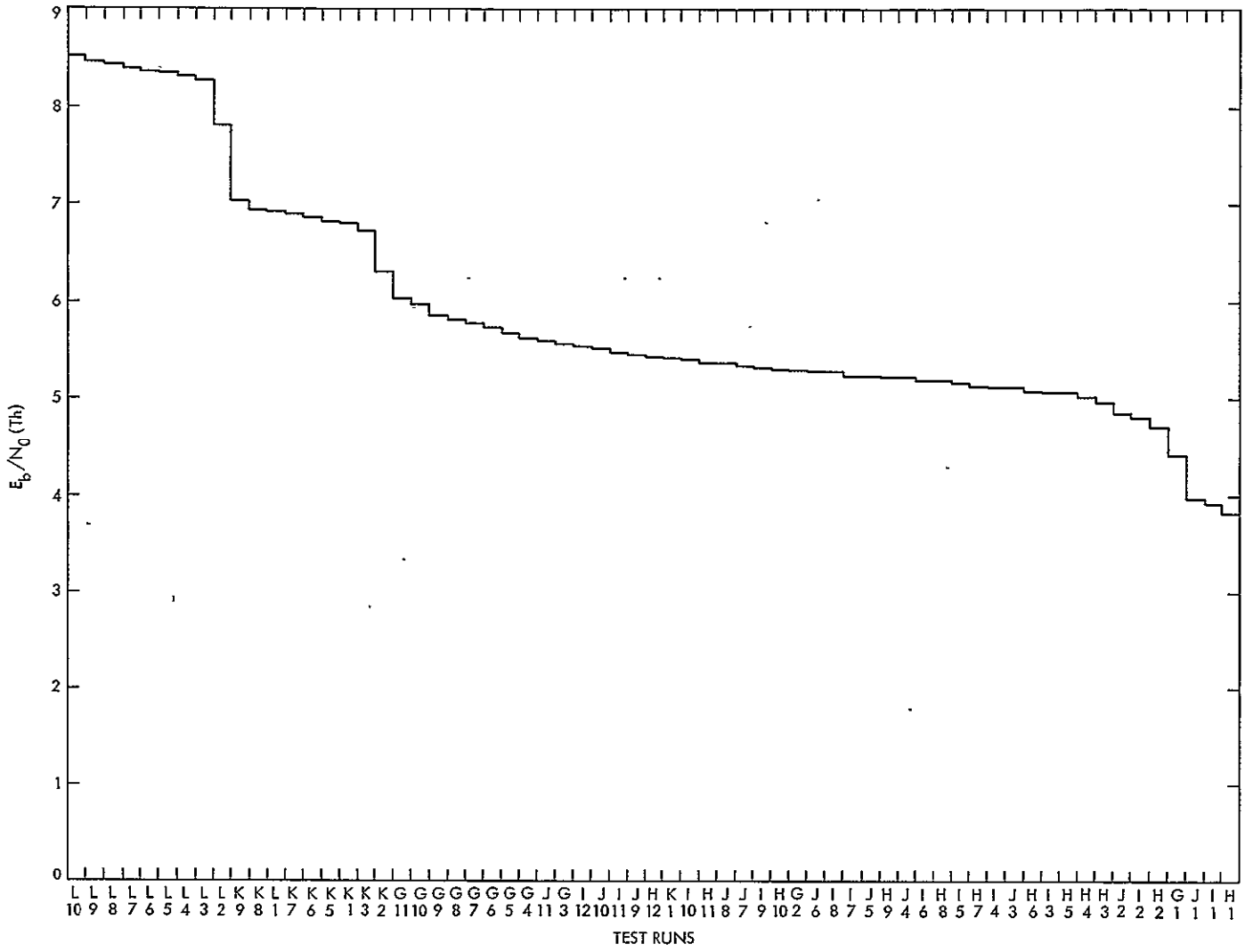

Fig. 1. Display of E_b/N_o

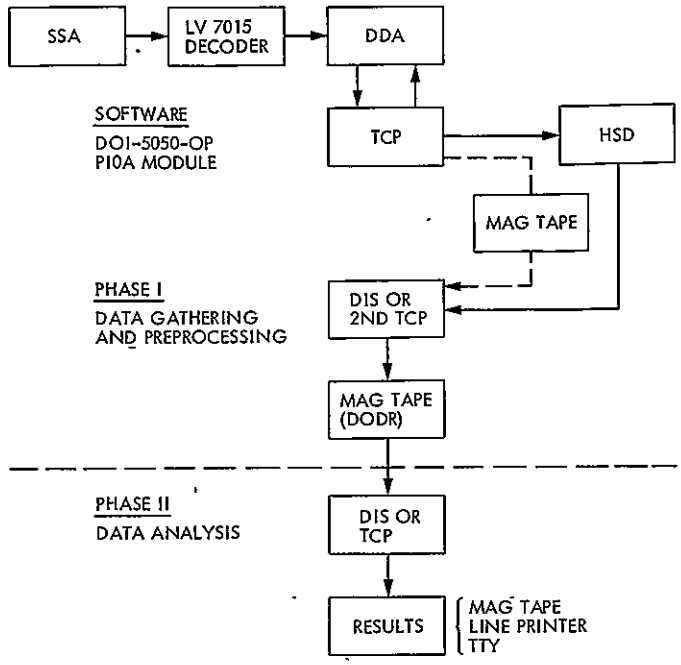

Fig. 2. Digital configuration

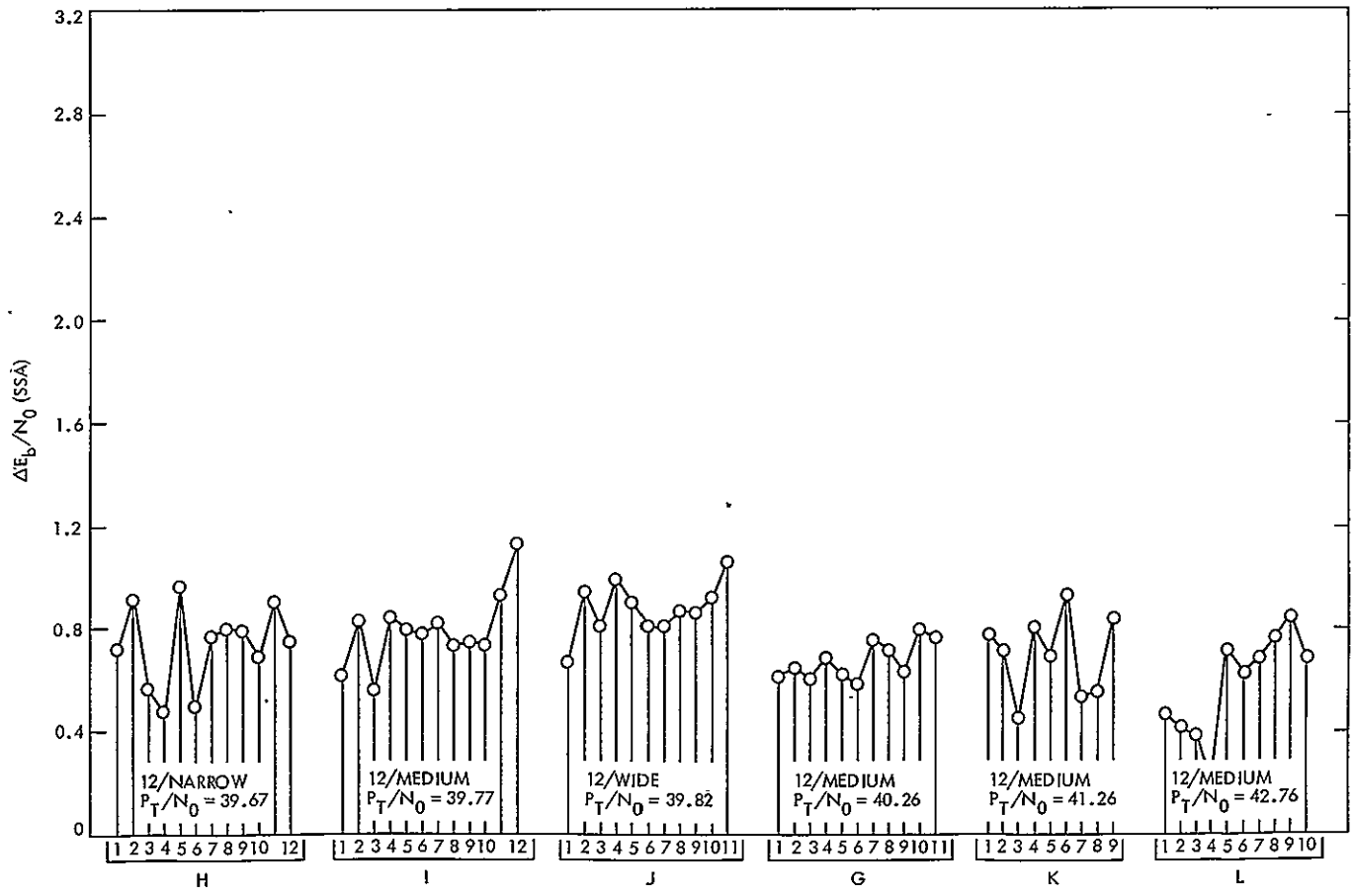

Fig. 3. Difference between E_b/N_o (Th) and E_b/N_o (SSA)

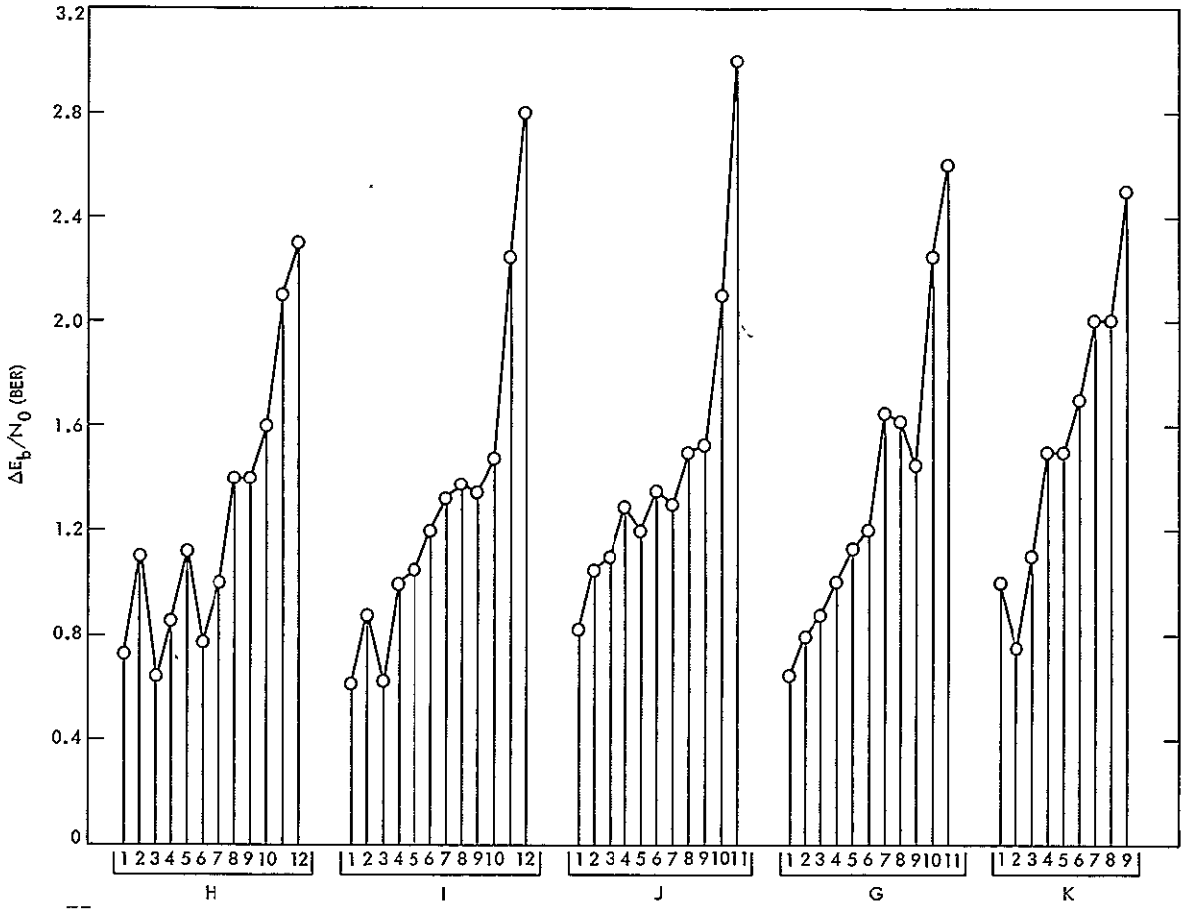

Fig. 4. Difference between E_b/N_o (Th) and E_b/N_o (BER)

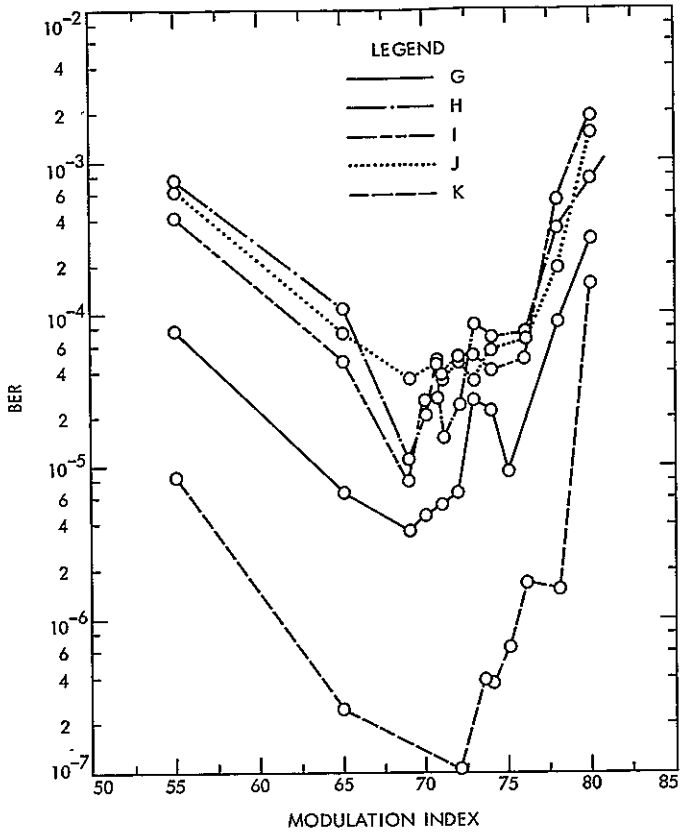

Fig. 5. Bit error rate versus modulation index

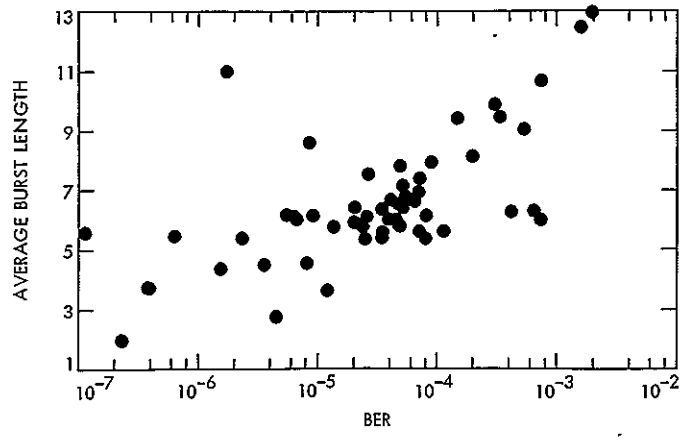

Fig. 6. Average burst length versus bit error rate

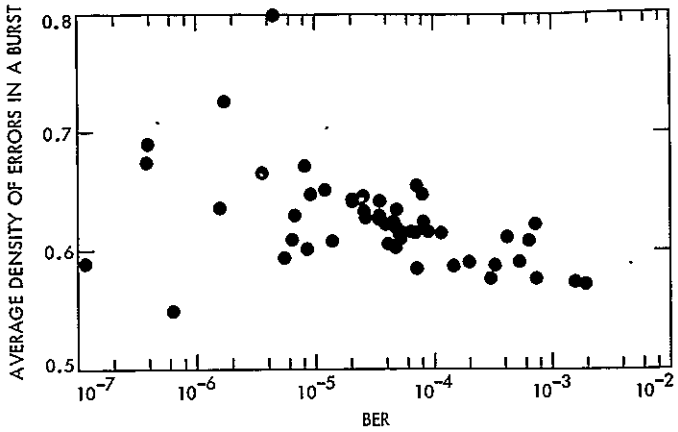

Fig. 7. Average density of errors in a burst versus bit error rate

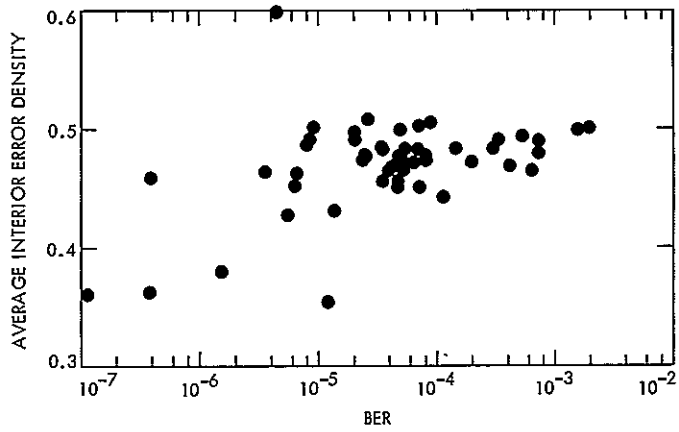

Fig. 8. Average interior error density-versus-bit error rate

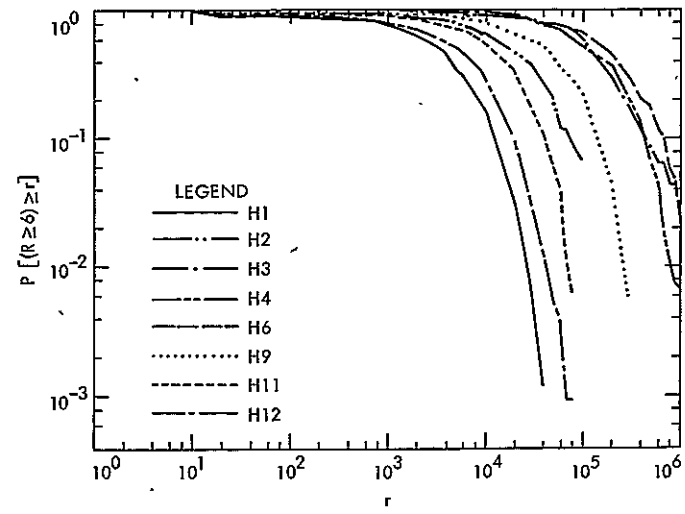

Fig. 9. Sample distribution functions of run length ($R \geq 6$)

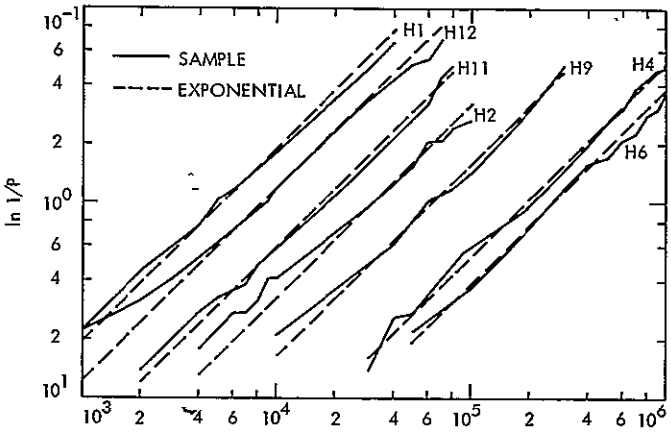

Fig. 10. Comparison of sample distributions of runs with exponential distributions

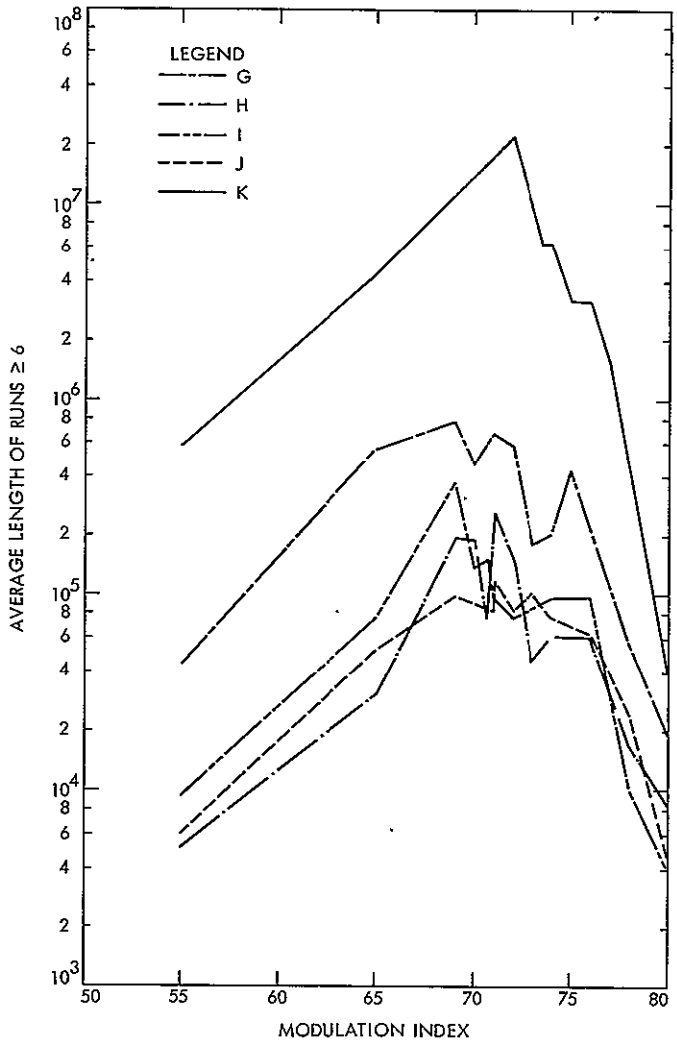

Fig. 11. Average length of runs ≥ 6 versus modulation index

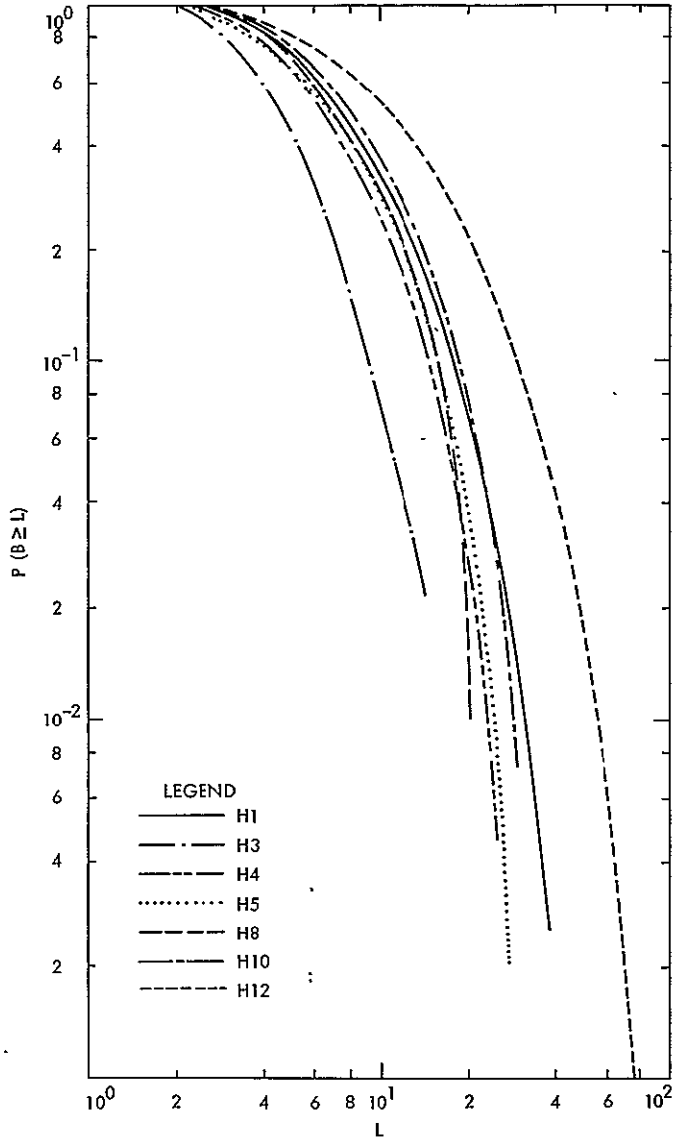

Fig. 12. Distribution functions of burst length

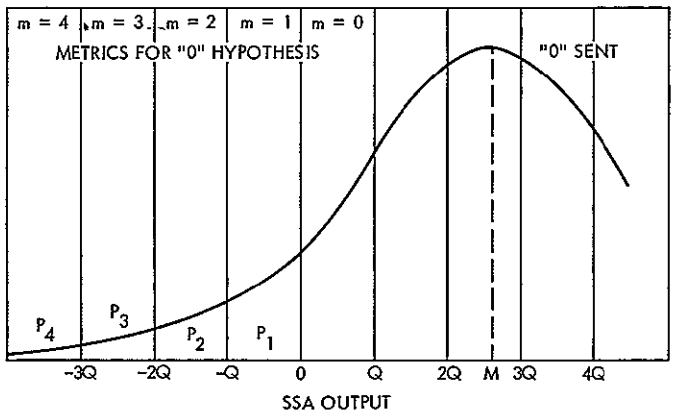

Fig. 13. Quantization and metric schemes

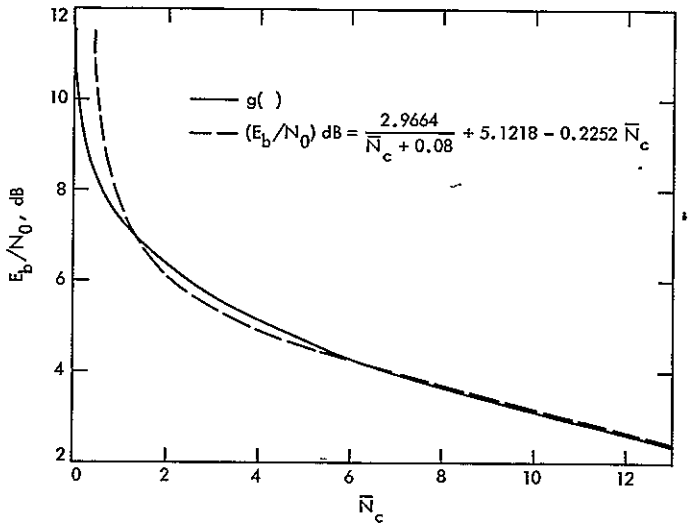

Fig. 14. E_b/N_o versus normalization counts

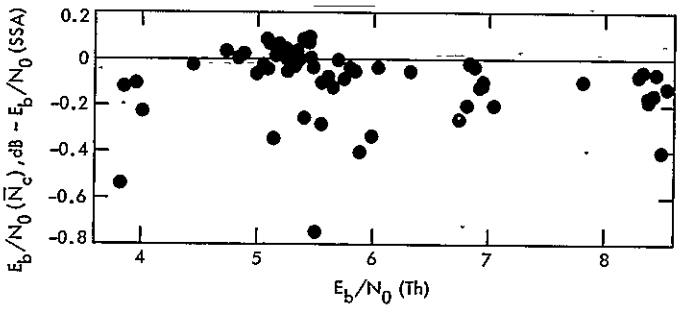

Fig. 15. Comparison of normalization and SAA estimates of E_b/N_o

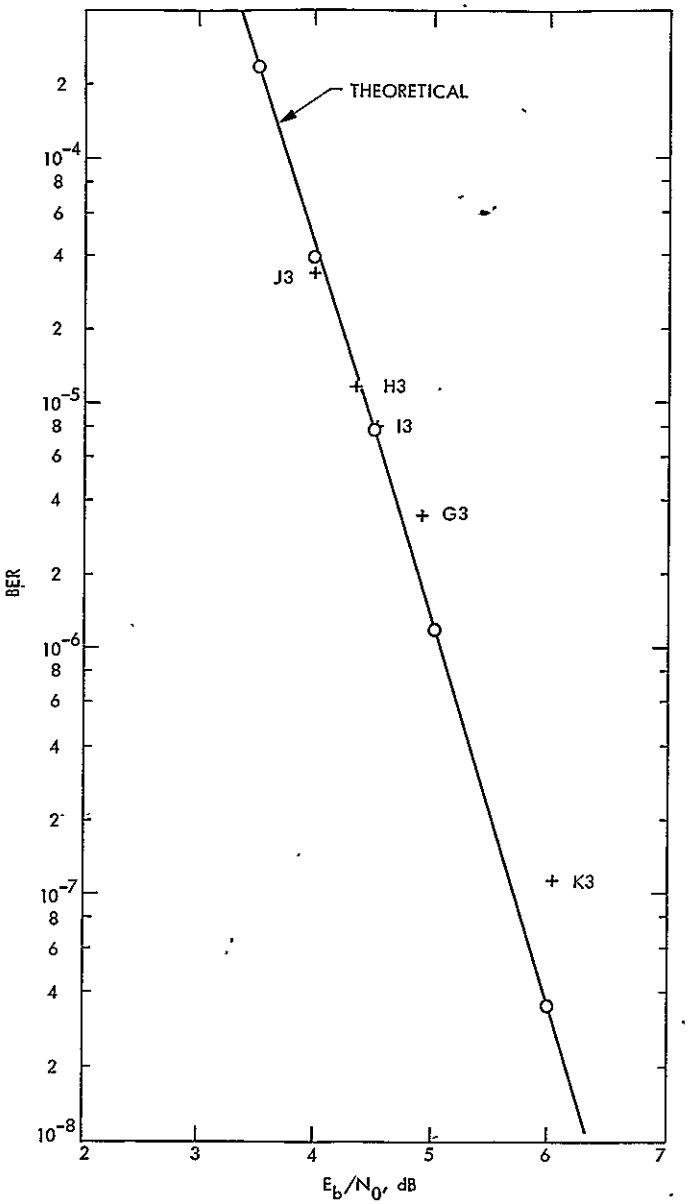

Fig. 16. Bit error rate versus E_b/N_o $(\overline{N}_c)$ for runs having optimum modulation indexes

Modification of Moore Measuring Machine/Leitz Microscope

H. A. Greth and L. Brubaker
Quality Assurance DSN and Mechanical Hardware Section

Quality Assurance Mechanical Inspection, anticipating the need for improved measuring techniques for the various Laboratory programs, has perfected a modification of the Leitz Microscope for the Moore Measuring Machine that has the capability of significantly reducing inspection time with increased reliability.

I. Introduction

To inspect hardware requiring high accuracies, some hardware even too delicate to handle or touch, a microscope with a measuring stage was needed. Up to now the only available instrument was the projection comparator, which does not give a true image of the part, only a shadow or a reflection from the part. Too much of the required accuracy is lost in this method.

II. Innovation From Existing Equipment

The Mechanical Inspection Department has adapted or modified a Leitz microscope capable of attaching directly to the spindle of the Moore Measuring Machine. The precision that is built into the Leitz microscope and the attaching of it to the Moore has given us accuracies to 0.5 micron (20 millionths of an inch) (100% more accurate than a projection comparator). In essence, we now have a tool maker's microscope, but on a 30-cm × 45-cm (12-in. × 18-in.) table. Also, the Leitz microscope provides six different magnifications from 10× to 150×, an internal 360-deg optical protractor, as well as built-in master charts of 30 thread profiles, 28 circles, and 32 radii, all usable in different magnifications. Also, a removable magazine is provided for special charts and templates.

Shown below are some applications of this instrument and a few of the services the Metrology Laboratory is called upon to do for Flight, DSN, and R&D programs.

(1) Measuring the form, angle, pitch, and diameter of threads.

(2) Checking form tools, milling cutters, gears, shapes, gages, templates, cross-sections, fittings, and various small parts and contours.

(3) Surface inspection of machined work, holes, pits, scratches, and fractures.

(4) Accurate determination of center distances between drilled holes, threaded holes, or pins.

(5) Dimensions of impressions and ball diameters.

(6) Laying out and spotting of precision parts.

(7) Measuring from edges to holes or radii, slots, lengths, widths, tensile specimens, glass-enclosed electrodes, filaments, coils, and items too delicate to handle or touch.

III. Summary

Modifying the Leitz Microscope and adapting it to the Moore Measuring Machine with its various accessories has provided one of the most versatile instruments for precision measurements, and has greatly increased the measurement accuracies of parts that are too delicate to stage and handle.

A Procedure for Preliminary Reduction of Bandwidth Synthesis Data

George Purcell
Tracking Systems and Applications Section

The procedure described here provides a fast, flexible, and inexpensive way to reduce and evaluate bandwidth synthesis observations before committing them to a more complex general-purpose fitting program. It enables the user to apply various corrections to the data, to resolve integer-cycle ambiguities, to calculate preliminary values of the baseline vector and source positions, and to assess the quality of the observations.

I. Introduction

Reference 1 outlines the first steps in a procedure for analyzing bandwidth synthesis observations in radio interferometry. At present, a typical observing session for this purpose includes perhaps twenty separate observations of ten compact extragalactic radio sources, made simultaneously at two or more stations. Each observation lasts about ten minutes and contains data in two or more (usually three) S-band frequency channels, which are sampled sequentially at intervals of one second. Each channel is nominally 24 kHz wide, and the channel-to-channel separations are at present normally 2, 8, and 10 MHz. The observations at each station are recorded digitally at 48,000 bits per second on standard 1.27-cm (1/2-in.) computer tapes, which are later brought together for analysis.

After the initial steps of cross-correlation, fringe-stopping, and phase-tracking, discussed in Ref. 1, the observer has, for each observation on a given baseline (that is, between two particular stations), the following intermediate results:

(1) From each channel, a measurement of the residual fringe rate

(2) From each channel, a measurement of the residual delay based on the bitstream alignment performed during cross-correlation (in the present system a relatively crude measurement, not used in the subsequent analysis)

(3) From each *pair* of channels, another measurement of the residual delay obtained by bandwidth synthesis. These measurements contain integer-cycle ambiguities (see formula 27 and the following discussion in Ref. 1) that have to be resolved before the data can be analyzed further.

The "residual" delays and fringe rates listed above are in each instance the difference between an observed value and the value predicted for that measurement by a model. This model is an analytic function of the presumed values of the baseline vector, the direction to the radio source, and the properties of Earth's troposphere. Consequently, the residuals can be used to compute corrections to small errors in the original estimates of the model parameters. Although the functions involved are highly nonlinear, the parameters are in general so well known that the residuals are very small. In this case, a linearized model is entirely adequate, and a straightforward application of the method of least squares yields the desired corrections.

To obtain the best results with this method, it is desirable to reduce simultaneously a large number of observations, comprising numerous observing sessions and many sources. A fitting procedure that performs this function will be the subject of a forthcoming report. It can solve simultaneously for an arbitrary number of model parameters including baselines, source positions, tropospheric delays, clock offsets, and clock rate offsets. Changes in the resulting baselines, in turn, can be interpreted in terms of polar motion and fluctuations in the rate of rotation of Earth. However, this sophisticated procedure is necessarily complex, time-consuming, and expensive to use. To use it efficiently, one needs also a simpler program to preprocess subsets of the data: to apply various corrections, to remove integer-cycle ambiguities, and to perform at a less refined level many of the functions of the master program. The following sections describe the capabilities and operation of a program that has been developed for this purpose.

II. Description of the Program

The program is designed to handle conveniently the observations from a single observing session on one baseline. Its principal functions are:

(1) To resolve the integer-cycle ambiguities in the residual delays

(2) To calculate preliminary least-squares estimates of the baseline, clock parameters, and source positions

(3) To expose irregularities in the data, including bad points, discontinuities, and abnormal distributions of errors.

Table 1 lists the program's important input and output. The optional input allows the user to delete observations temporarily from the fit, to specify corrections to the parameters of the delay model, and to assign statistical weights to his initial estimates of the baseline and source positions.

The flow chart in Fig. 1 shows the principal operations performed by the program. Most of them are routine or self-explanatory, but two are not — the resolution of integer-cycle ambiguities in the synthesized delays, and the estimation of statistical errors.

For the program to resolve the integer-cycle ambiguities correctly for a particular channel pair, it is necessary for that part of each residual delay caused by errors in the model parameters to be substantially less than half the reciprocal of the difference between the two channel frequencies. Therefore the program ordinarily begins by processing the most closely spaced pair of channels (that is, the pair that permits the largest initial uncertainty in the model) and corrects the observations for all *known* errors in the original model before trying to resolve the ambiguities for that first channel pair. Having resolved the ambiguities, the program can calculate a first set of corrections to the model parameters, which it then uses to correct the observations from the channel pair with the next wider separation. Since the errors in the delays decrease as the separation between channels increases, the program can thus proceed iteratively to more and more widely spaced channel pairs, sufficiently refining its estimates of the baseline and source positions at each iteration to allow resolution of the ambiguities in the next iteration. If this scheme should break down, it is also possible to override the automatic procedure by specifying predetermined integer-cycle corrections in the input stream.

The other unusual feature of the program is the way in which it assigns errors and statistical weights to the data. (For a more thorough discussion see Ref. 2.) The process of phase-tracking produces along with each residual delay or fringe rate an estimate of its uncertainty due to sources of error that operate at relatively short time scales, up to a minute or so. These errors normally are entirely dominated by system noise with an autocorrelation time much less than a second. However, there are other sources of error, including some instrumental drifts and changes in the propagation media, that operate on time scales from minutes to hours and can contribute significantly to the scatter in data over the length of an observing session. The program attempts to account for these errors by assigning an additional fringe rate error and an additional delay error to each channel pair, and adding them in quadrature to the system noise errors. Then, after fitting the observations in a particular channel pair, the program uses a chi-square test to determine whether the residual scatter

is consistent with the assigned total errors. If not, the program adjusts its estimates of the additional errors accordingly, recomputes the statistical weights, and repeats the fit.

The program uses the data from the last channel pair — that is, the one with the widest channel separation — to calculate its best estimates of the baseline vector, clock parameters, and whatever source positions it was asked to find, along with estimates of the errors in those quantities. By comparing these results with other measurements, and by examining the printer plots of the residuals after fitting, the user can then gauge the quality of the observations and determine possible sources of difficulty for the master fitting program. If he wants to, he can run the program again with dubious data deleted, or with different constraints on the parameters of the model.

III. A Sample Experiment

As an example of the use of the procedure, consider the observations made in Spain at DSSs 61 and 63 between UT 0500 and 0900 on January 9, 1976. There were eleven observations of five sources, and the channel frequencies were 2285, 2287, and 2295 MHz.

Figure 2 shows the residual delays at successive stages of the reduction. (The residual fringe rates, not shown, follow a similar progression except for the resolution of the integer-cycle ambiguities.)

Figure 2a shows the raw data for the most closely spaced pair of channels, at 2285 and 2287 MHz. The large scatter is the result of an intentional error of about 50 meters in the z component of the a priori baseline, along with smaller errors in the x and y components. Despite the large size of this baseline error, no compensatory corrections were necessary, and the program proceeded directly to resolve the integer-cycle ambiguities. For this pair of channels, 2-MHz apart, the cycle time is 500 nanoseconds, and so an observed difference of at least 250 nanoseconds between successive observations would be required to induce a correction. Since the largest change turned out to be only about 115 nanoseconds, however, no corrections were made. (Notice that if the error in the baseline had been a little more than two times as large, the largest difference would have exceeded 250 nanoseconds, and a "correction" would have been applied — incorrectly. For such a large baseline error it would have been necessary to apply at least a partial baseline correction to the data before resolving the integer-cycle ambiguities.)

The least-squares fit of the data in Fig. 2a gave a clock offset of 247 nanoseconds and corrections of 6.0, 2.6, and -48.7 meters to the x, y, and z components, respectively, of the baseline. Figure 2b shows the residuals after fitting of the data in Fig. 2a. The error bars here (and in Fig. 2f) are the estimates of system noise derived from phase tracking. Since the residuals are small, no additional sources of error had to be invoked.

The results for the 2287 and 2295 MHz channel pair are not shown. Figure 2c gives the raw data for the last channel pair to be analyzed, 2285 and 2295 MHz, with a separation of 10 MHz and a cycle time of 100 nanoseconds. Here again, the large scatter is due almost entirely to the incorrect a priori baseline. Now, however, the program can use the baseline corrections computed for the previous channel pair (2287 and 2295 MHz) with the results shown in Fig. 2d. Here the total scatter is even larger (note the change in scale between plots), but the distribution of delays is almost discrete, with values separated by 100 nanoseconds. The program then resolves the integer-cycle ambiguities and obtains the final residuals before fitting shown in Fig. 2e. Finally, Fig. 2f shows the residuals after fitting. The improvement between Figs. 2e and 2f is not dramatic, because the baseline corrections computed for the previous channel pair were already quite accurate.

References

1. Thomas, J. B., "An Analysis of Long Baseline Interferometry, Part III," *The Deep Space Network Progress Report*, Technical Report 32-1526, Vol. XVI, pp. 47–64. Jet Propulsion Laboratory, Pasadena, Calif., Aug. 15, 1973.
2. Thomas, J. B., et al., "A Demonstration of an Independent-Station Radio Interferometry System with 4-cm Precision on a 16-km Baseline," *J. Geophys. Res.*, Vol. 81, pp. 995–1005, Feb. 1976.

Table 1. Input and output of fitting program

Required input (punched cards)
A priori baseline (the one used for cross-correlation)
Channel frequencies and pairings
Intermediate results for each observation (punched by previous step of the reduction):
Identification, date and time, source name
Observed residual delays and associated errors
Observed residual fringe rates and associated errors
Partial derivatives of observed delays and rates with respect to model parameters (for least-squares design matrix)
Program-control options (control use of optional input and output)
Optional input (punched cards)
Corrections to a priori baseline
Corrections to a priori source positions
Corrections to a priori estimates of polar motion and UT1 – UTC
Corrections to tropospheric delays at zenith
Arbitrary corrections to the observed residual delays
Estimates of errors in the a priori baseline and source positions
Initial estimates of scatter in the data due to sources of error other than system noise
Predetermined integer-cycle corrections to the observed residual delays
List of sources for which corrected positions are to be calculated
List of data to be deleted from the fit
Output for each channel pair (line printer)
List of active program-control options
Estimates of observational errors other than system noise both before and after fitting
Summary of the observations
List of data deleted from the fit
Table of raw data, corrections, and corrected data
List of phase-turn corrections, predetermined or computed by the program
List of least-squares adjustments to the fitted parameters
Table of residuals before and after fitting
Printer plots of the delay and rate residuals after fitting
Fitted values of the baseline, clock parameters, and source positions, and their errors

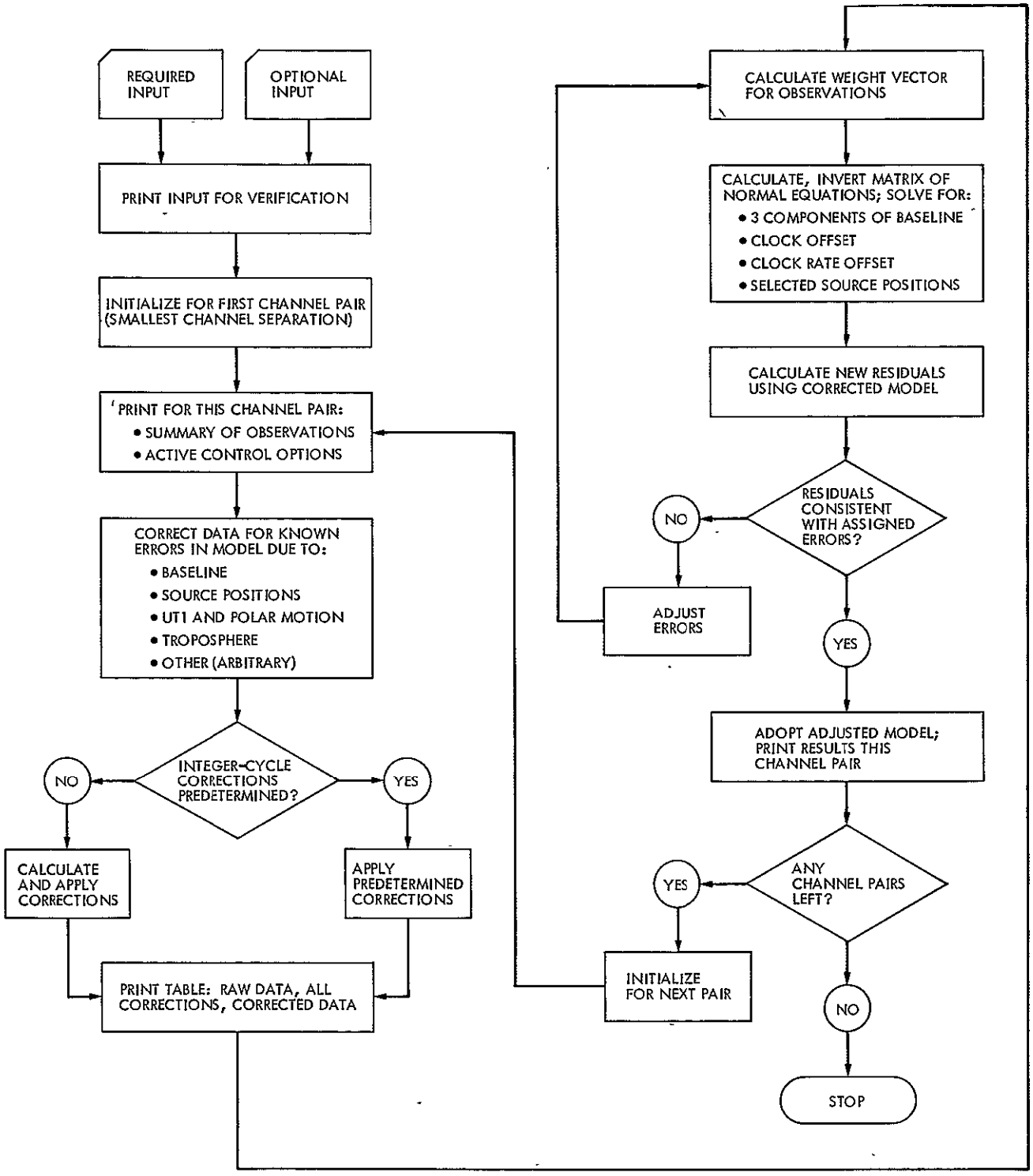

Fig. 1. Flow chart of fitting program

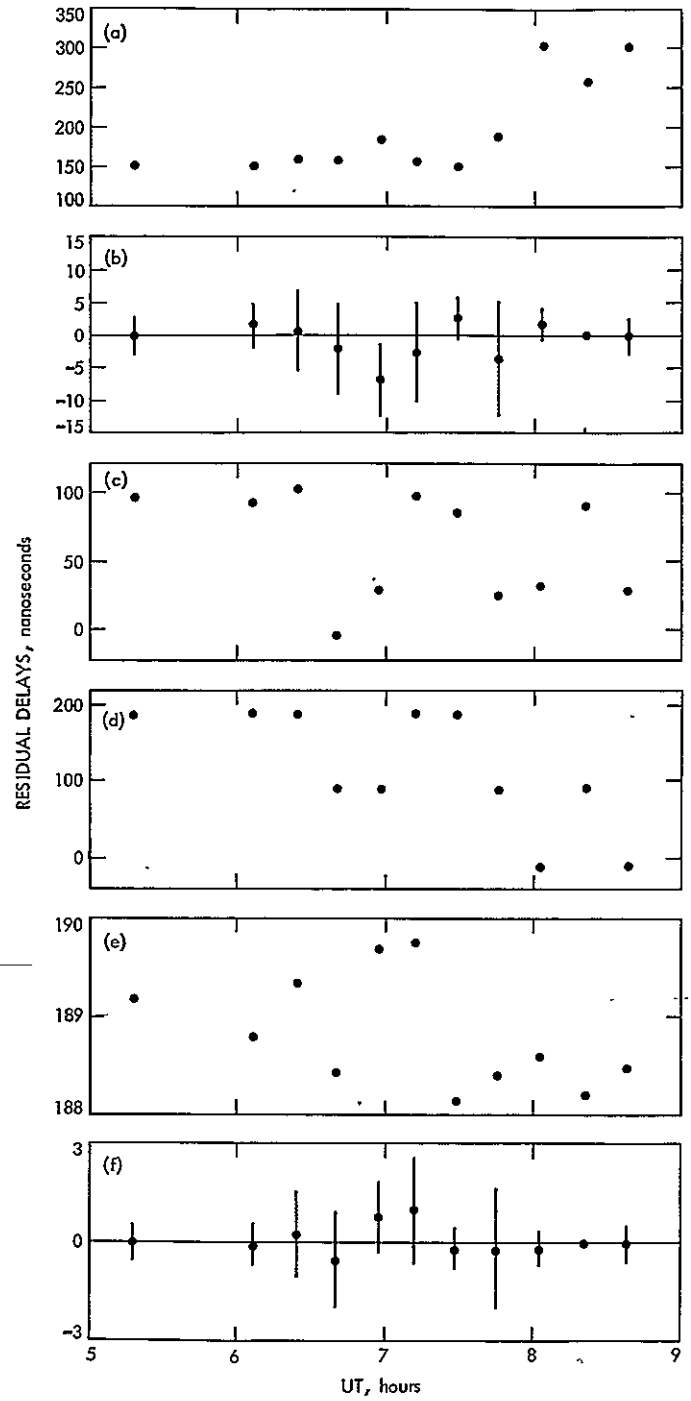

Fig. 2. Residual delays at successive stages of a sample reduction: (a) raw data for channel separation of 2 MHz; (b) residuals after fitting for channel separation of 2 MHz; (c) raw data for channel separation of 10 MHz; (d) data after baseline correction, channel separation of 10 MHz; (e) data after integer-cycle correction, channel separation of 10 MHz; (f) residuals after fitting for channel separation of 10 MHz.

Pioneer Venus Entry Simulator

C. E. Johns
R. F. Systems Development Section

To assure successful tracking of the four Pioneer Venus probes, it is necessary for the deep space station receiver operators to be familiar with the characteristics of the received signals. As an aid for training the operators for this mission, signal simulators have been developed which completely duplicate the probe signals. This article describes the method used for generating these test signals.

I. Introduction

During the entry phase of the Pioneer Venus mission (Ref. 1), the one large and three small probes will be tracked with both closed- and open-loop receivers. Only one opportunity exists to have a successful track. It is important, therefore, that adequate operator training be provided to assure successful tracking. To aid in operator training, a simulator is being developed that completely duplicates the characteristics of all four probe signals. The method of simulating one of the characteristics, the doppler frequency profile of these probes, is discussed in this article.

II. Doppler Profile Generators

Voltage-controlled crystal oscillators (VCXOs) are used as the simulation signal sources. Doppler frequency simulation is obtained by generating a control voltage profile for the VCXOs that is identical to the desired frequency profile. Applying this voltage profile to the VCXO input generates a simulation signal with the desired frequency profile. A typical doppler profile is shown in Fig. 1. To simplify the design, the profile has been divided into two segments: the first segment from time t_0 to t_1, the second segment from t_1 on.

A. Segment 1

Using the method of averages, a second order polynomial was derived which closely approximates each doppler profile curve. The polynomial is in the form of

$$E_1(t) = a_0 + a_1 t + a_2 t^2 \tag{1}$$

Each of the terms of this equation is generated independently as shown in Fig. 2. A step voltage is first generated by means of a relay closure, which is applied to the input of a double integrating circuit. This step voltage, E, can be defined as:

$$E \equiv b_0 \tag{2}$$

The output of the first integrator (point A) is:

$$V_1(t) = \frac{E}{RC}\int_0^t dt = \frac{Et}{RC} \equiv b_1 t \qquad (3)$$

This is then integrated a second time yielding (point B):

$$V_2(t) = \frac{-E}{R^2C^2}\int_0^t t\,dt = \frac{Et^2}{2R^2C^2} \equiv b_2 t^2 \qquad (4)$$

The input step voltage and the integrator outputs are then resistively summed, using appropriate attenuations, for reducing the "b" coefficients in expressions (2), (3), and (4) to the "a" coefficients of expression (1). The voltage developed across the common summing resistor R4 is the desired waveform, but reduced in amplitude. The voltage across R4 is then amplified to the required VCXO control level by an inverting operational amplifier (A1).

B. Segment 2

To generate the second portion of the profile after time t_1 (Fig. 1), another voltage approximation was made using the circuit shown in Fig. 3. When the relay is closed shortly after t_2, a step voltage E is applied to a resistive divider, R5 and R6. The voltage across R6 (E_{R6}) is then applied to the series network R7, R8 and capacitor C. The output voltage $E_2(t)$ across R8 and C is then:

$$E_2(t) = E_{R6}\left[1 - \frac{R_8}{R_7 + R_8}\exp\left(t/(R_7 + R_8)C\right)\right] \qquad (5)$$

When the relay first actuates the output is a step:

$$E_2(t) = E_{R6}\frac{R_8}{R_7 + R_8} \qquad (6)$$

at which time the capacitor starts charging at a rate determined by the time constant $(R_7 + R_8)C$ and becomes asymptotic to a final value of E_{R6}. Actual circuit values used are shown in Fig. 3. Circuit performance and the predicted doppler profile are plotted together in Fig. 4 to show their propinquity.

The voltage $E_2(t)$ is isolated by a unity gain operational amplifier whose output is summed with $E_1(t)$ at the input of amplifier A1 (Fig. 2). The output from A1 is, therefore, the composite of the two voltages that is used for controlling the VCXO frequency.

The voltage E_1 is short-circuited at time t_1, and E_2 is enabled at t_2. During the interval between the two times, the test signal is temporarily turned off to duplicate the loss of the received signal during the entry phase of the probes.

III. Conclusion

A method for generating test signals which closely duplicate the characteristics of the received signals from the Pioneer Venus probes has been completed. Using these methods, a breadboard unit, which duplicates one of the small probes, has been constructed and successfully tested.

Reference

1. Miller, R. B., "Pioneer Venus 1978 Mission Support," in *The Deep Space Network Progress Report 42-27*, pp. 28–35, Jet Propulsion Laboratory, Pasadena, Calif., June 15, 1975.

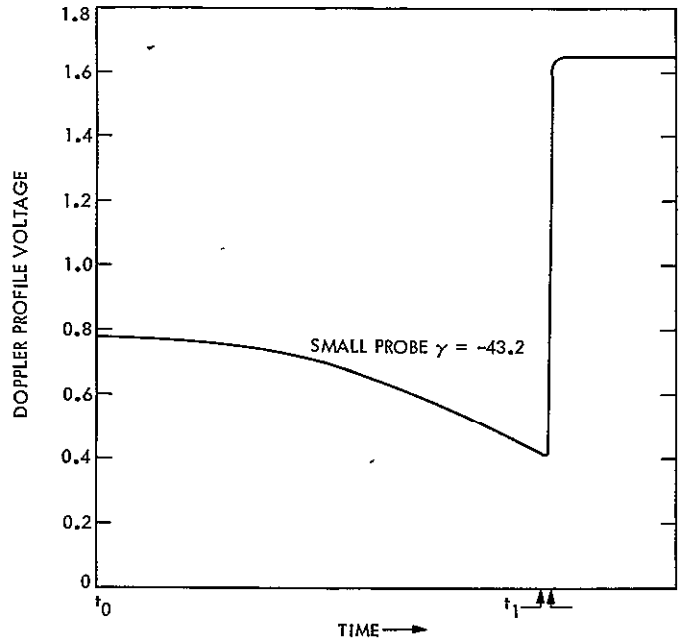

Fig. 1. Doppler profile voltage vs time

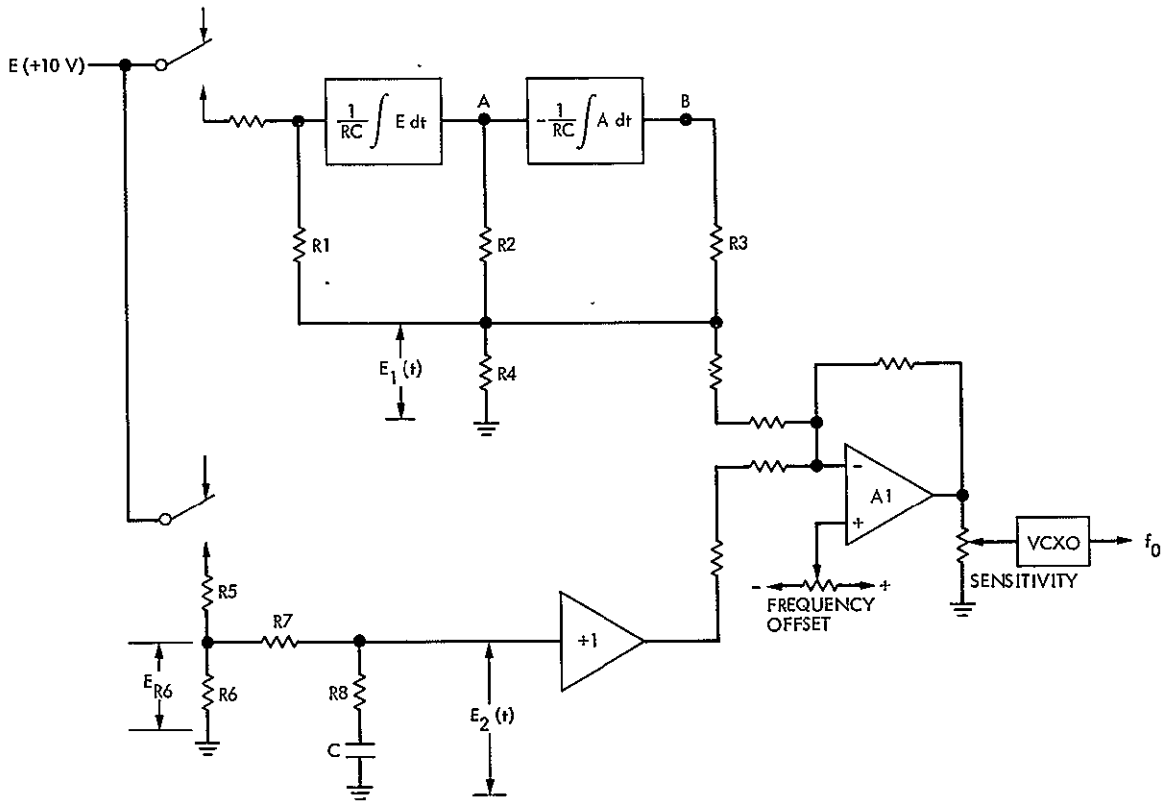

Fig. 2. Simplified diagram of the doppler profile generator

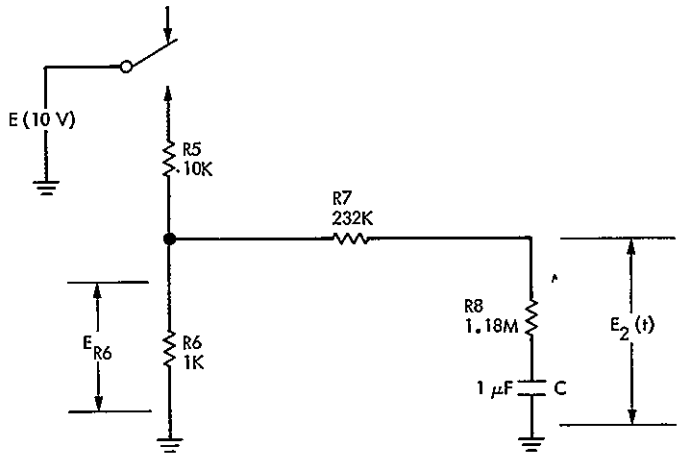

Fig. 3. Circuit for generating post-entry doppler profile

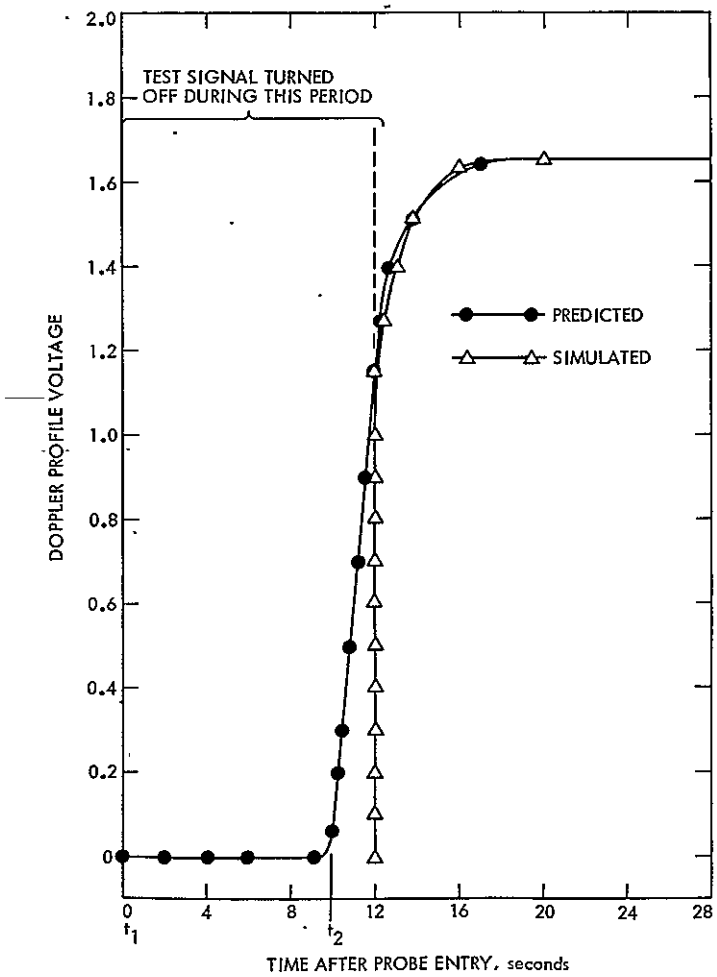

Fig. 4. Predicted and simulated doppler profiles

Doppler Noise Considered as a Function of the Signal Path Integration of Electron Density

A. L. Berman and J. A. Wackley
Network Operations Section

This article advances the hypothesis that observed doppler noise during solar conjunctions is proportional to total columnar electron content along the signal path. This assumption leads directly to a geometrical model ("ISED") for observed doppler noise which is shown to be in very good agreement with doppler noise data accumulated during the 1975 Pioneer 10, Pioneer 11 and Helios 1 solar conjunctions. An augmented model ("RISED") is constructed which quantitatively indicates correlation between Earth observed Sunspot activity and systematic, cyclical deviations from the ISED model. Applications expected from this effort are: (1) Ability to validate generation of doppler data during solar conjunctions, (2) Ability to predict solar corruption of doppler data during mission critical phases which occur during solar conjunctions, and (3) Possibility of extracting electron density information from observed doppler noise.

I. Introduction

In 1975, A. L. Berman and S. T. Rockwell, after studying the (1975) solar conjunctions of the Pioneer 10, Pioneer 11, and Helios 1 spacecraft, proposed (see Reference 1) a geometrical doppler noise model (NOISE_p) as follows:

$$\text{NOISE}_p(Hz) = \begin{cases} 0.003; & ISI \leq 223 \\ K_1(ISI)^{1+K_2}; & ISI > 223 \end{cases}$$

where

$$ISI = \frac{\beta}{\sin \alpha}$$

α = Sun-Earth-probe angle (SEP), deg

β = Earth-Sun-probe angle (ESP), deg

$K_1 = 2.8 \times 10^{-6}$

$K_2 = 2.9 \times 10^{-1}$

Basically, the NOISE$_p$ model was derived by noting that possible sources of solar corruption of doppler data, such as electromagnetic energy flux and charged particles, had densities roughly proportional to the inverse square of the distance from the Sun, and then hypothesizing that the total effect leading to an increase in doppler data noise would be obtained by integrating the density of corrupting sources along the signal path:

$$\text{doppler noise} = K\int \frac{1}{r^2}\, dR$$

where

r = Sun–signal path distance

R = Earth–spacecraft distance

K = arbitrary constant

with the result that

$$\int \frac{1}{r^2}\, dR = \frac{1}{r_e}\left(\frac{\beta}{\sin\alpha}\right)$$

A better fit to actual (observed) doppler noise data[1] was obtained by raising *ISI* to the 1.29 power, thus leading to the final model form (NOISE $_p$).

It was subsequently concluded that the derived parameter *ISI* was extremely similar to expressions given for total (solar) electron content along the signal path. For instance, L. Efron and R. J. Lisowski (Ref. 2) give the identical (functional) expression for total signal path electron content

$$I_e = \int N_e(r)\, dR = \frac{N_1}{r_e}\frac{\beta}{\sin\alpha}$$

where

I_e = total electron content along signal path

$N_e(r)$ = electron density function

N_1 = electron density at $r = r_e$

r_e = Earth-Sun distance (AU)

It was then considered that perhaps a better model could be obtained if one used a more precise expression (i.e., not simply $1/r^2$) for the electron density function. A great many expressions to define the solar electron density as a function of distance from the Sun have been advanced during the last several decades, and they are all somewhat similar. Typical examples are (with r = distance from the Sun):

Van De Hulst: $N_e(r) = \frac{A}{r^6} + \frac{B}{r^{2.3}}$ (Ref. 3)

Hollweg: $N_e(r) = \frac{A}{r^6} + \frac{B}{r^2}$ (Ref. 4)

Muhleman: $N_e(r) = \frac{A}{r^6} + \frac{B}{r^{2.3}}$ (Ref. 5)

The Muhleman formulation above was selected, and Section II proceeds to evaluate the following expression:

$$I_e = \int N_e(r)\, dR = \int\left(\frac{C_1}{r^6} + \frac{C_0}{r^{2.3}}\right) dR$$

II. Signal Path Integration of the Muhleman Electron Density Function: The "ISED" Model

One wishes to obtain I_e:

$$I_e = \int\left(\frac{C_1}{r^6} + \frac{C_0}{r^{2.3}}\right) dR = C_1\int \frac{dR}{r^6} + C_0\int \frac{dR}{r^{2.3}}$$

Figure 1 details the Earth-Sun-spacecraft geometry, with

$r^2 = R^2 + r_e^2 - 2Rr_e\cos\alpha$

$r_{s/c}$ = Earth-spacecraft distance

$R_{s/c}$ = spacecraft-Sun distance

Starting with the $C_0/r^{2.3}$ term, one has:

$$I_{e1} = C_0\int_0^{R_{s/c}} \frac{dR}{r^{2.3}} = C_0\int_0^{R_{s/c}} \frac{dR}{(R^2 + r_e^2 - 2Rr_e\cos\alpha)^{1.15}} = C_0\int_0^{R_{s/c}} \frac{dR}{([R - r_e\cos\alpha]^2 + r_e^2\sin^2\alpha)^{1.15}}$$

[1]All references to observed doppler noise will be taken to mean "pass average," good, two-way 60-second sample rate doppler data noise (see Refs. 1 and 7 for greater detail).

Let

$$x = R - r_e \cos\alpha$$

$$dx = dR$$

$$a = r_e \sin\alpha$$

so that

$$I_{e1} = C_0 \int_{-r_e\cos\alpha}^{R_{s/c}-r_e\cos\alpha} \frac{dx}{(x^2+a^2)^{1.15}}$$

$$= \frac{C_0}{a^{2.3}} \int_{-r_e\cos\alpha}^{R_{s/c}-r_e\cos\alpha} \frac{dx}{\left(1+\frac{x^2}{a^2}\right)^{1.15}}$$

Now let

$$\frac{x}{a} = \tan w$$

$$dx = a\sec^2 w dw$$

so that

$$I_{e1} = \frac{C_0}{a^{2.3}} \int_{\tan^{-1}\frac{(-r_e\cos\alpha)}{a}}^{\tan^{-1}\frac{(R_{s/c}-r_e\cos\alpha)}{a}} \frac{a\sec^2 w dw}{(\tan^2 w+1)^{1.15}}$$

$$= \frac{C_0}{a^{1.3}} \int_{\tan^{-1}\frac{(-r_e\cos\alpha)}{a}}^{\tan^{-1}\frac{(R_{s/c}-r_e\cos\alpha)}{a}} \frac{dw}{(\tan^2 w+1)^{0.15}}$$

and since

$$\tan^2 w + 1 = \sec^2 w = \frac{1}{\cos^2 w}$$

then

$$I_{e1} = \frac{C_0}{a^{1.3}} \int_{\tan^{-1}\frac{(-r_e\cos\alpha)}{a}}^{\tan^{-1}\frac{(R_{s/c}-r_e\cos\alpha)}{a}} (\cos w)^{0.3} dw$$

From Ref. 1, p. 237:

$$\tan^{-1}\left(-\frac{r_e\cos\alpha}{a}\right) = \alpha - \frac{\pi}{2}$$

and

$$\frac{R_{s/c}-r_e\cos\alpha}{r_e\sin\alpha} = \tan\left(\beta - \left[\frac{\pi}{2}-\alpha\right]\right)$$

$$\tan^{-1}\left(\frac{R_{s/c}-r_e\cos\alpha}{a}\right) = \beta - \left[\frac{\pi}{2}-\alpha\right]$$

$$= \beta - \frac{\pi}{2} + \alpha$$

so that

$$I_{e1} = \frac{C_0}{a^{1.3}} \int_{\alpha-\pi/2}^{\beta-\pi/2+\alpha} (\cos w)^{0.3} dw$$

Since the maximum contribution of the integral occurs at $x = 0$ (closest approach of signal to the Sun), a Maclaurin's series expansion is used for the integrand:

$$f(w) \cong f(0) + w\left(\frac{df}{dw}\right)_0 + \frac{w^2}{2!}\left(\frac{d^2f}{dw^2}\right)_0 + \frac{w^3}{3!}\left(\frac{d^3f}{dw^3}\right)_0 + \cdots + \frac{w^n}{n!}\left(\frac{d^nf}{dw^n}\right)_0 + \cdots$$

with

$$f(w) = (\cos w)^{0.3}$$

$$f(0) = 1$$

$$\frac{df}{dw} = -0.3\sin w(\cos w)^{-0.7}$$

$$\left(\frac{df}{dw}\right)_0 = 0$$

$$\frac{d^2f}{dw^2} = -0.3(\cos w)^{0.3} - 0.21\sin^2 w(\cos w)^{-1.7}$$

$$\left(\frac{d^2f}{dw^2}\right)_0 = -0.3$$

$$\frac{d^3f}{dw^3} = -0.33\sin w(\cos w)^{-0.7} - 0.357\sin^3 w(\cos w)^{-2.7}$$

$$\left(\frac{d^3f}{dw^3}\right)_0 = 0$$

$$\frac{d^4f}{dw^4} = -0.33(\cos w)^{0.3} - 1.302\sin^2 w(\cos w)^{-1.7} - 0.063\sin^4 w(\cos w)^{-3.7}$$

$$\left(\frac{d^1 f}{dw^1}\right)_0 = -0.33$$

$$\frac{d^2 f}{dw^2} = -2.505 \sin w(\cos w)^{-0.7} - 6.069 \sin^3 w(\cos w)^{-2.7} - 3.566 \sin^5 w(\cos w)^{-4.7}$$

$$\left(\frac{d^2 f}{dw^2}\right) = 0$$

$$\frac{d^4 f}{dw^4} = -2.505(\cos w)^{0.3} - 19.9605 \sin^2 w(\cos w)^{-1.7} - 34.218 \sin^4 w(\cos w)^{-3.7} - 16.762 \sin^6 w(\cos w)^{-5.7}$$

$$\left(\frac{d^4 f}{dw^4}\right)_0 = -2.505$$

$$(\cos w)^{0.3} \cong 1 + \frac{w^2}{2!}(-0.3) + \frac{w^4}{4!}(-0.33) + \cdots = 1 - 0.15w^2 - 0.01375w^4 + \cdots$$

The desired quantity then becomes:

$$I_{c1} = \frac{C_0}{a^{1.3}} \int_{\alpha-\pi/2}^{\beta-\pi/2+\alpha} (\cos w)^{0.3}\, dw$$

$$= \frac{C_0}{a^{1.3}} \int_{\alpha-\pi/2}^{\beta-\pi/2+\alpha} (1 - 0.15w^2 - 0.01375w^4 + \cdots)\, dw$$

$$= \frac{C_0}{a^{1.3}} \left[w - \frac{0.15w^3}{3} - \frac{0.01375w^5}{5} + \cdots \right]_{\alpha-\pi/2}^{\beta-\pi/2+\alpha}$$

$$\cong \frac{C_0}{a^{1.3}} \left[w - 0.05w^3 - 0.00275w^5 \right]_{\alpha-\pi/2}^{\beta-\pi/2+\alpha}$$

$$= \frac{C_0}{a^{1.3}} [(\beta - \pi/2 + \alpha) - (\alpha - \pi/2) - 0.05\{(\beta - \pi/2 + \alpha)^3 - (\alpha - \pi/2)^3\} - 0.00275\{(\beta - \pi/2 + \alpha)^5 - (\alpha - \pi/2)^5\}]$$

$$= \frac{C_0 \beta}{a^{1.3}} \left[1 - 0.05 \left\{ \frac{(\beta - \pi/2 + \alpha)^3 - (\alpha - \pi/2)^3}{\beta} \right\} - 0.00275 \left\{ \frac{(\beta - \pi/2 + \alpha)^5 - (\alpha - \pi/2)^5}{\beta} \right\} \right]$$

Defining:

$$A_0 = \frac{C_0}{(r_c)^{1.3}}$$

one arrives at the final expression for I_{c1}:

$$I_{c1} = A_0 \left[\frac{\beta}{(\sin \alpha)^{1.3}} \right] F(\alpha,\beta)$$

where

$$F(\alpha,\beta) = 1 - 0.05 \left\{ \frac{(\beta - \pi/2 + \alpha)^3 - (\alpha - \pi/2)^3}{\beta} \right\} - 0.00275 \left\{ \frac{(\beta - \pi/2 + \alpha)^5 - (\alpha - \pi/2)^5}{\beta} \right\}$$

One now wishes to evaluate the C_1/r^5 term:

$$I_{c2} = C_1 \int_0^{R_s/c} \frac{dR}{r^5}$$

Using notation similar to the previous integral, one has:

$$I_{c2} = C_1 \int_{-r_c \cos\alpha}^{R_s/c - r_c \cos\alpha} \frac{dx}{(x^2 + a^2)^3} = \frac{C_1}{a^6} \int_{-r_c \cos\alpha}^{R_s/c - r_c \cos\alpha} \frac{dx}{\left(1 + \frac{x^2}{a^2}\right)^3}$$

$$= \frac{C_1}{a^6} \int_{\tan^{-1}\frac{(-r_c \cos\alpha)}{a}}^{\tan^{-1}\frac{(R_s/c - r_c \cos\alpha)}{a}} \frac{a \sec^2 w\, dw}{(\tan^2 w + 1)^3}$$

$$= \frac{C_1}{a^5} \int_{\alpha-\pi/2}^{\beta-\pi/2+\alpha} \frac{dw}{(\tan^2 w + 1)^2} = \frac{C_1}{a^5} \int_{\alpha-\pi/2}^{\beta-\pi/2+\alpha} (\cos w)^4\, dw$$

which simply yields

$$I_{c2} = \frac{C_1}{a^5} \left[\frac{3}{8} w + \frac{1}{4} \sin 2w + \frac{1}{32} \sin 4w \right]_{\alpha-\pi/2}^{\beta-\pi/2+\alpha}$$

Because of the $(1/a^5)$ dependency, one only needs to consider the case:

$$\alpha \to 0$$
$$\beta \to \pi$$

Let

$$\alpha \equiv \Delta_\alpha \qquad \Delta_\alpha > 0$$
$$\beta \equiv \pi - \Delta_\beta \qquad \Delta_\beta > 0$$

One then has:

$$I_{e2} = \frac{C_1}{a^5}\left[\frac{3}{8}\{\beta - \pi/2 + \alpha - (\alpha - \pi/2)\} + \frac{1}{4}\{\sin[2(\alpha+\beta) - \pi] - \sin[2\alpha - \pi]\} + \frac{1}{32}\{\sin[4(\alpha+\beta) - 2\pi] - \sin[4\alpha - 2\pi]\}\right]$$

$$= \frac{C_1}{a^5}\left[\frac{3}{8}\beta + \frac{1}{4}\{\sin[\pi + 2(\Delta_\alpha - \Delta_\beta)] + \sin[\pi - 2\Delta_\alpha]\} + \frac{1}{32}\{\sin[2\pi + 4(\Delta_\alpha - \Delta_\beta)] + \sin[2\pi - 4\Delta_\alpha]\}\right]$$

Now

$$\sin[\pi + 2(\Delta_\alpha - \Delta_\beta)] \approx -2(\Delta_\alpha - \Delta_\beta)$$
$$\sin[\pi - 2\Delta_\alpha] \approx +2\Delta_\alpha$$
$$\sin[2\pi + 4(\Delta_\alpha - \Delta_\beta)] \approx +4(\Delta_\alpha - \Delta_\beta)$$
$$\sin[2\pi - 4\Delta_\alpha] \approx -4\Delta_\alpha$$

so that

$$I_{e1} = \frac{C_1}{a^5}\left[\frac{3}{8}\beta + \frac{1}{4}\{-2(\Delta_\alpha - \Delta_\beta) + 2\Delta_\alpha\} + \frac{1}{32}\{4(\Delta_\alpha - \Delta_\beta) - 4\Delta_\alpha\}\right]$$

$$= \frac{C_1}{a^5}\left[\frac{3}{8}\beta + \frac{4}{8}\Delta_\beta - \frac{1}{8}\Delta_\beta\right]$$

$$= \frac{C_1}{a^5}\left[\frac{3}{8}(\beta + \Delta_\beta)\right]$$

$$= \frac{C_1}{a^5}\left[\frac{3\pi}{8}\right]$$

Defining

$$A_1 = \frac{C_1}{(r_e)^5}\left[\frac{3\pi}{8}\right]$$

one has

$$I_{e2} = \frac{A_1}{(\sin\alpha)^5}$$

The model ISED (integrated solar electron density) is thus defined:

$$\text{ISED} = I_{e1} + I_{e2} = A_0\left[\frac{\beta}{(\sin\alpha)^{1.5}}\right]F(\alpha,\beta) + A_1\left[\frac{1}{(\sin\alpha)^5}\right]$$

with

$$F(\alpha,\beta) = 1 - 0.05\left\{\frac{(\beta - \pi/2 + \alpha)^3 - (\alpha - \pi/2)^3}{\beta}\right\} - 0.00275\left\{\frac{(\beta - \pi/2 + \alpha)^5 - (\alpha - \pi/2)^5}{\beta}\right\}$$

It is noteworthy to compare the above formulation with the NOISE_p model, which is in good agreement with the doppler noise observations presented in Refs. 1, 6, and 7:

$$\text{NOISE}_p = K_0\frac{\beta^{1.29}}{(\sin\alpha)^{1.29}}$$

Recall that the original hypothesis in Ref. 1($1/r^2$ dependency) led to the dominant variable:

$$\sim\frac{1}{\sin\alpha}$$

and that to obtain a better fit to the doppler noise observations, it was necessary to (empirically) adjust the power of the dominant variable:

$$\sim\frac{1}{(\sin\alpha)^{1.29}}$$

which is now seen to be in almost perfect agreement with the dominant variable in the first term of the ISED formulation. That an empirically adjusted model would prove to be in excellent (functional) correspondence with the actual electron content along the signal path (ISED), would certainly argue persuasively in favor of strong correlation between observed doppler noise and ISED. Addi-

tionally, this result should not be surprising, as it was certainly alluded to by Muhleman, et al., in Ref. 5, p. 100: "The phase jitter essentially depends on the electron density fluctuation, and the observing wavelength and the density fluctuations are approximately proportional to the mean density."

A further observation along these lines is provided by G. L. Dutcher, (Ref. 8, pp. 15–16), who also indicates that the electron density fluctuation is proportional to the mean electron density, and additionally, indicates the approximate constant of proportionality (p. 50):

$$\left[\frac{\text{electron density fluctuations}}{\text{mean electron density}}\right]_{RMS} \approx 0.02$$

The observed doppler noise data from 1975 Pioneer 10, Pioneer 11, Helios 1 (first) and Helios 1 (second) solar conjunctions, as presented in Refs. 1 and 7, were fit to the ISED model, thereby producing the following fit constants:

$$A_0 = 9.65 \times 10^{-1}$$

$$A_1 = 5 \times 10^{-10}$$

If the data were really representative of the electron density function, one would expect the ratio of the coefficients determined from the observed data (A_0, A_1) to be similar to the ratio of the coefficients presented by Muhleman in Ref. 5. Normalizing terms to one solar radii, Muhleman indicates two sets of coefficients (pp. 95–96):

$$A = 1.3 \times 10^{5}$$

$$B = 1.15 \times 10^{6}$$

$$\frac{A}{B} = 113$$

and

$$A = 0.8 \times 10^{5}$$

$$B = 0.51 \times 10^{6}$$

$$\frac{A}{B} = 157$$

For the ISED case (normalized to one solar radius):

$$A_1' = C_1[r_e \sin(0.27°)]^{-6}$$

$$A_0' = C_0[r_e \sin(0.27°)]^{-2\,3}$$

$$\frac{A_1'}{A_0'} = \frac{C_1[r_e \sin(0.27°)]^{2\,3}}{C_0[r_e \sin(0.27°)]^{6}}$$

$$= \left(\frac{C_1}{C_0}\right)\frac{1}{[r_e \sin(0.27°)]^{3\,7}}$$

$$= \frac{A_1(r_e)^5\left(\frac{8}{3\pi}\right)}{A_0(r_e)^{1\,3}}\,\frac{1}{[r_e \sin(0.27°)]^{3\,7}}$$

$$= \frac{A_1\left(\frac{8}{3\pi}\right)}{A_0[\sin(0.27°)]^{3\,7}}$$

$$= 179$$

It is reassuring that the ratio of the coefficients determined from the observed doppler noise data is similar to the ratio of the coefficients determined from other experimental observations.

As in Ref. 7, all comparisons of observed doppler noise (N_i) to the various proposed models will be cast in logarithmic form, or dB:

$$\text{Doppler noise residual, } dB \equiv 10 \log_{10}\left(\frac{N_i}{\text{MODEL}}\right)$$

Using this standard, the statistics for the combined data base (in excess of 500 "pass average" doppler noise observations), when fit to the ISED model, were as follows:[2]

	PN 10	PN 11	HEL-1st	HEL-2nd	All
σ (dB)	1.88	1.91	2.07	2.00	1.95
Bias (dB)	+0.06	−0.45	+0.54	+0.38	0.00

Scatter diagrams (observed noise vs the ISED model) can be seen in Appendix A as follows:

Fig. A1—Pioneer 10

Fig. A2—Pioneer 11

Fig. A3—Helios 1 first

Fig. A4—Helios 1 second

Fig. A5—Combined

[2]The standard deviation given by Muhleman (Ref. 5, p. 95) for the B term (0.51×10^6) is 0.30×10^6, or 2.15 dB, which is curiously similar to these numbers!

Qualitatively, the improvement of the ISED model over the previous $NOISE_p$ model can be seen by comparing the above figures to (respectively):

Fig. 8, Ref. 1

Fig. 9, Ref. 1

Fig. 10, Ref. 1

Fig. 7, Ref. 1

Fig. 3, Ref. 7

Improvement is most notably seen at very small SEPs and small ESPs. This is most probably a direct result of the following deficiencies in the previous $NOISE_p$ model:

(1) Lack of a $(\sin \alpha)^{-5}$ term (only applicable for SEP $\leq 1.5°$)

(2) $\beta^{1.29}$ versus the (correct) β.

Comparisons of the observed doppler noise versus the ISED model, as a function of day of year (DOY), are seen in Appendix B. Presentations are as follows:

Fig. B1—Pioneer 10

Fig. B2—Pioneer 11

Fig. B3—Helios 1 first

Fig. B4—Helios 1 second

Finally, the Muhleman Phase Jitter Model (from Ref. 5, Fig. 8, p. 100) has been frequently discussed and has always been found too small by an order of magnitude or more. What was not readily apparent was that the Muhleman model, as a function of the geometry, agrees with the observed doppler noise, except for a multiplicative constant! The following gives an approximate comparison of the ISED model and the Muhleman doppler phase jitter prediction:

SEP, deg	Muhleman model, Hz, one-way	ISED, Hz, two-way	Ratio ISED/ Muhleman
15.6	2.65×10^{-4}	1.33×10^{-2}	50
10.5	4.50×10^{-4}	2.27×10^{-2}	50
5.3	1.08×10^{-3}	5.60×10^{-2}	52
2.7	2.65×10^{-3}	1.34×10^{-1}	51
1.1	1.33×10^{-2}	6.60×10^{-1}	50

As can readily be seen, the models are extremely similar, when considered as a function of the geometry.

III. Correlation With Solar Activity: The RISED Model

In the previous section, observed doppler noise was modeled as a function of signal path electron content. However, as has already been pointed out in Refs. 6 and 7, systematic, cyclical deviations from the model appear when the residuals are viewed as a function of DOY. Additionally, these deviations display good correlation between different spacecraft, when the spacecraft signal paths are on the same side of the Sun (Ref. 7). Appendix C presents observed doppler noise residuals (in *dB*) from the ISED model as follows:

Fig. C1—Pioneer 10

Fig. C2—Pioneer 11

Fig. C3—Helios 1 first

Fig. C4—Helios 1 second

The question now arises, can observations of solar activity be used in some way to modify the ISED model and thus perhaps account for (in some fashion) the observed cyclical fluctuations about the ISED model? It is already well known that the electron density function fluctuates with the long-term solar cycle. For instance, Van De Hulst (Ref. 3) scales his electron density function by location within the solar cycle, with the maximum value approximately twice the minimum. Similarly, M. Waldmeier (Ref. 9) states: "For any heliographic latitude the electron density function is higher during sunspot maximum than during the minimum."

The ISED residuals seen in Appendix C frequently differ by 3 to 6 *dB* between neighboring maxima/minima. This would seem to be consistent with other observations of temporal changes in electron density; for instance, Dutcher (Ref. 8, p. 40) comments on changes by a factor of three (4.8 *dB*) over a period of days. Additionally, T. A. Croft, in Ref. 10, reports on variations of electron density which reappear approximately coincident with the solar rotation rate (p. 521): "The 27-day repetition is clearly seen in interplanetary electron content measurements obtained by the radio propagation experiment on the Pioneer spacecraft. . . . The measured electron content of the solar wind in mid-1970 exhibited a region of relatively high electron density that reappeared at intervals of about 27.8 days."

Considering the above, it was concluded that possibly the daily (Earth) observed Sunspot index (Zurich, R_Z) could be used in some fashion to adjust the ISED model and thereby attempt to lessen the magnitude of the systematic deviations of the observed doppler data from the model. If such a process were successfully executed, correlation could be demonstrated in a quantitative sense via a comparison to the previously presented ISED residual standard deviations (σ). To attempt this procedure, two separate aspects of the problem were addressed:

(1) *Phase.* An algorithm would be required to link in some internally consistent fashion the earth observation of solar activity, and the subsequent (or prior) effect on observed doppler noise.

(2) *Magnitude.* A function of R_Z would have to be empirically constructed to "scale" the ISED model.

The strongest correlation appeared to be between periods of zero sunspot activity and periods of very negative ($-3 \sim -4$ *dB*) residuals. Consideration of the time relationships between the two led to the following (strictly empirical) hypothesis (with the geometry as shown in Fig. 2).

Assume

(1) Each daily R_Z measurement is time centered (averaged) for a solar longitude = 0 deg.

(2) Variations in electron density "propagate" outward in a radial direction and at a constant speed (V_0) from a surface or corotating near surface region.

The above allows one to construct a consistent (but arbitrary) method of relating Earth observations of solar activity and signal path observations, as follows:

(1) Time to propagate from surface to signal closest approach:

$$t_\tau = \frac{1}{V_0}\{r_e \sin\alpha\}$$

$$= A_2 \sin\alpha$$

$$\cong A_2\alpha$$

(2) Time to rotate from Earth observation (0 deg longitude) to longitude of propagation region ($\gamma = \pi/2 - \alpha$ and ω_s = solar rotation period):

$$t_r = \frac{\omega_s}{2\pi}(\pm\gamma)\begin{cases} + \text{ signal west of Sun} \\ - \text{ signal east of Sun} \end{cases}$$

$$= \pm\frac{\omega_s}{2\pi}\left(\frac{\pi}{2} - \alpha\right)$$

$$\approx \pm\frac{27 \text{ days/rev}}{2\pi}\left(\frac{\pi}{2} - \alpha\right)$$

$$= \pm\left[6\tfrac{3}{4} - \frac{13.5}{\pi}\alpha\right]$$

Adding the two times together, one has

(1) West side

$$T = t_\tau + t_r = 6\tfrac{3}{4} + \alpha\left(A_2 - \frac{13.5}{\pi}\right)$$

(2) East side

$$T = t_\tau + t_r = -6\tfrac{3}{4} + \alpha\left(A_2 + \frac{13.5}{\pi}\right)$$

Finally, since the sunspot observations are a function of DOY, the phase time T is rounded to the nearest integer day:

$$n_t(\text{days}) \equiv \text{integer}\,(T + 0.5) \qquad T \geq 0$$

$$n_t(\text{days}) \equiv \text{integer}\,(T - 0.5) \qquad T < 0$$

The sunspot data are published as a function of DOY:

$$R_Z(\text{DOY})$$

Since the data exhibit sharp day to day fluctuations in addition to the longer term, higher magnitude fluctuations that are the primary concern here, the sunspot data were smoothed in the following manner:

$$YR_Z(\text{DOY}) = 0.1R_Z(\text{DOY} - 2) + 0.2R_Z(\text{DOY} - 1) + 0.4R_Z(\text{DOY}) + 0.2R_Z(\text{DOY} + 1) + 0.1R_Z(\text{DOY} + 2)$$

The smoothed phased sunspot value for a doppler noise observation on a given day (DOY) then becomes:

$$XR_Z(\text{DOY}) = YR_Z(\text{DOY} - n_t)$$

Finally, it was necessary to construct a function of XR_Z which could be used to scale the ISED model. Examination of the ISED residuals and the (phased) sunspot data

indicated a multiplicative function with the following general characteristics:

Sunspot activity (R_Z)	Multiplicative Characteristic
$0 \sim 10$	$\sim$0.5 for zero sunspots; quickly rising to about 1.0
$10 \sim 40$	$>$1.0 and very gradually increasing
$40 \sim 100$	gradually accelerating rate until $\sim$4.0 for 100 sunspots

To accomplish this, the following function was constructed:

$$WR_Z = (1 + A_4 XR_Z)\,(1 + A_5[XR_Z]^2) - A_6 \cos\left[\frac{\pi}{2}\left(\frac{XR_Z}{A_7 + XR_Z}\right)\right]$$

thus leading to the RISED (rotating integrated solar electron density) model, fully defined as follows:

$$\text{RISED} = WR_Z\left\{A_0\left[\frac{\beta}{(\sin\alpha)^{1.3}}\right]F(\alpha,\beta) + A_1\left[\frac{1}{(\sin\alpha)^5}\right]\right\}$$

with

$$F(\alpha,\beta) = 1 - 0.05\left\{\frac{(\beta - \pi/2 + \alpha)^3 - (\alpha - \pi/2)^3}{\beta}\right\} - 0.00275\left\{\frac{(\beta - \pi/2 + \alpha)^5 - (\alpha - \pi/2)^5}{\beta}\right\}$$

$$WR_Z = (1 + A_4 XR_Z)\,(1 + A_5[XR_Z]^2) - A_6 \cos\left[\frac{\pi}{2}\left(\frac{XR_Z}{A_7 + XR_Z}\right)\right]$$

$$XR_Z(\text{DOY}) = YR_Z(\text{DOY} - n_t)$$

$$YR_Z(\text{DOY}) = 0.1R_Z(\text{DOY} - 2) + 0.2R_Z(\text{DOY} - 1) + 0.4R_Z(\text{DOY}) + 0.2R_Z(\text{DOY} + 1) + 0.1R_Z(\text{DOY} + 2)$$

and

$$n_t = \begin{cases} \text{integer}\,(T + 0.5) & T \geq 0 \\ \text{integer}\,(T - 0.5) & T < 0 \end{cases}$$

where

$$T = \begin{cases} 6\tfrac{3}{4} + \alpha\left(A_2 - \dfrac{13.5}{\pi}\right) & \text{signal paths west of Sun} \\ -6\tfrac{3}{4} + \alpha\left(A_2 + \dfrac{13.5}{\pi}\right) & \text{signal paths east of Sun} \end{cases}$$

The observed doppler noise data from the Pioneer 10, Pioneer 11 and the Helios 1 first 1975 solar conjunctions, subject to the following (minor) restrictions: (1) data $<$ 30 deg heliographic latitude (the signal closest approach point) and (2) data such that ISED $>$ 0.003 Hz were fit to the RISED model, with the various A_n parameters varied to minimize the standard deviation of the residuals. This process yielded the following set of parameters:

$$A_0 = 9.153 \times 10^{-3}$$
$$A_1 = 1.2 \times 10^{-9}$$
$$A_2 = 1.2 \times 10^{+1}$$
$$A_4 = 9 \times 10^{-3}$$
$$A_5 = 1 \times 10^{-1}$$
$$A_6 = 4 \times 10^{-1}$$
$$A_7 = 5 \times 10^{-1}$$

The function WR_Z with the above A_4 through A_7 is plotted versus R_Z in Fig. 3. The statistics resulting from the determined parameter set were as follows:

	σ (dB)	Bias (dB)
Pioneer 10 east	1.58	+0.36
Pioneer 10 west	1.34	+0.18
Pioneer 11 east	1.57	−1.23
Pioneer 11 west	1.31	−0.17
Helios 1 first (west)	2.06	+0.44
Combined	1.55	0.00

By comparing these results to those obtained for the ISED case, a very substantial decrease in the (combined) standard deviation can be seen:

$\sigma = 1.86$ ISED[3]

$\sigma = 1.55$ RISED[3]

Basically, the RISED model very substantially improved the Pioneer 10 and Pioneer 11 results, (i.e., de-

creased the systematic deviations) and essentially left the Helios 1 (first) results unchanged. If only the (combined) Pioneer 10 and 11 results are compared, the improvement is even more dramatic:

$\sigma = 1.81$ ISED[3]

$\sigma = 1.38$ RISED[3]

A qualitative view of the improvement can be seen in Appendix C, where the following parameters are plotted as a function of DOY:

ISED residuals, *dB*

Smoothed, phased sunspots, XR_Z

RISED residuals, *dB*

and for the following cases:

Fig. C1—Pioneer 10

Fig. C2—Pioneer 11

Fig. C3—Helios 1 first

Additionally, Appendix D presents the observed doppler noise and the RISED model versus DOY for the following cases:

Fig. D1—Pioneer 10

Fig. D2—Pioneer 11

Fig. D3—Helios 1 first

while Appendix E presents the observed doppler noise versus the RISED model for the following cases:

Fig. E1—Pioneer 10

Fig. E2—Pioneer 11

Fig. E3—Helios 1 first

Fig. E4—Composite

When the Helios 1 second solar conjunction doppler noise data were fit to the RISED model with the fit parameters as previously determined, the results were quite disappointing—the RISED case producing a standard deviation very substantially worse than for the ISED case. It was noted that there occurred an extremely sharp peak in (observed) sunspot activity on DOY 218, and a correspondingly sharp peak in ISED residuals on DOY 234. Assuming that these events should correlate, a (constant) delay factor in the phasing relationship was introduced:

$$T(\text{west}) = 6\tfrac{3}{4} + \alpha\left(A_2 - \frac{13.5}{\pi}\right) + A_1$$

A new A_0 and A_1 were selected, yielding the following fit parameter set:

$A_0 = 7.6 \times 10^{-1}$

$A_1 = 5 \times 10^{-10}$

$A_2 = 1.2 \times 10^{+1}$

$A_3 = 8.25$

$A_4 = 9 \times 10^{-3}$

$A_5 = 1 \times 10^{-1}$

$A_6 = 4 \times 10^{-1}$

$A_7 = 5 \times 10^{-1}$

The statistics for the RISED model with this parameter set, as compared to the ISED model results, were as follows:

Helios 1 second (west)	$\sigma = 1.90$;	RISED
Helios 1 second (east)	$\sigma = 1.63$;	RISED
Helios 1 second (all)	$\sigma = 1.77$;	RISED
Helios 1 second (all)	$\sigma = 2.00$;	ISED

The RISED residuals, ISED residuals, and the smoothed, phased sunspots can be seen in Fig. C4, Appendix C; while the RISED residuals and observed doppler noise data versus DOY are seen in Fig. D4, Appendix D.

Although the standard deviation is significantly reduced for this RISED fit when compared to the ISED case, little significance can be attached to it because of the major alteration required to the basic RISED algorithm. This negative experience in projecting the RISED model forward to a new set of solar conjunction data leads one to (negatively) consider:

(1) Additional, currently unknown factors will have to be considered before a doppler noise model can incorporate observed solar activity in a quantitative fashion.

[3]For the "slightly" reduced data set, as previously defined.

(2) As a practical matter, it may not be possible to incorporate observed solar activity into a doppler noise model in a quantitative fashion.

Regardless of this failure to successfully project the RISED model forward, it is felt that the experience of the RISED model with the Pioneer 10, Pioneer 11, and Helios 1 (first) Solar conjunction doppler noise data represents an extremely strong, quantitative indication of correlation between Earth-observed solar activity and (assumed) fluctuations in electron density.

IV. Applications of the ISED Model

Applications of the work done to date in analyzing the 1975 solar conjunction observed doppler noise would appear to separate into two distinct categories, these being:

(1) Applications which only require doppler noise to be modeled as an arbitrary function of Earth-Sun-probe geometry, and which already appear to have a strong likelihood of successful realization.

(2) Applications which require the central hypothesis of the functional relationship between observed doppler noise and the signal path integration of electron density to be established, and hence, are less certain in terms of a successful realization.

These will be briefly expounded upon below in Subsections A and B.

A. Expected Applications

1. Validation of doppler data generation during solar conjunction phases. With the current ISED model, the real-time Network Analysis Team, Tracking (NAT TRACK) has a standard against which doppler noise can be compared, and which can be used to separate out possible Tracking System malfunctions. In support of this effort, the Network Operations Analysis Group, Tracking (NOAG TRACK) is currently providing NAT TRACK with ISED plots for any spacecraft in solar conjunction.

2. Planning for critical mission operations during solar conjunction phases. The ISED model can be used to quantitatively establish minimum requirements and trade-off factors for the planning of critical mission events within solar conjunction phases. For instance, as a function of time, one can easily compute:

$$\frac{d\text{ISED}}{dt} = \frac{\partial \text{ISED}}{\partial \alpha}\frac{d\alpha}{dt} + \frac{\partial \text{ISED}}{\partial \beta}\frac{d\beta}{dt}$$

where

$$\frac{\partial \text{ISED}}{\partial \alpha} \approx -\frac{1.3\,A_0 \beta\, F(\alpha,\beta)}{(\sin\alpha)^{2.3}}\cos\alpha - \frac{5\,A_1 \cos\alpha}{(\sin\alpha)^6}$$

$$\frac{\partial \text{ISED}}{\partial \beta} \approx \frac{A_0\, F(\alpha,\beta)}{(\sin\alpha)^{1.3}}$$

and where the quantities

$$\frac{d\alpha}{dt}, \frac{d\beta}{dt}$$

are easily obtainable from standard trajectory information. The rate of change of ISED with time could then be used quantitatively to establish tradeoffs of solar corruption of navigation data with other mission characteristics.

B. Possible Applications

1. Accurate measurement of long term (~months) average electron density levels. During any solar conjunction period, numerous measurements of doppler noise will be obtained, which when used in conjunction with the ISED model, might be expected to provide an accurate "average" electron density level.

2. Measurement of intermediate (~days/weeks) electron density fluctuations. Multiple doppler noise measurements per day combined with the ISED model might be expected to provide a reasonable measurement of intermediate fluctuations in the average electron density level.

3. Correlation of observed solar activity with fluctuations in electron density. The intermediate fluctuations in electron density might be expected to constitute a powerful tool in correlative studies of Earth observed solar activity (perhaps similar to the RISED effort).

V. Summary

This report suggests that observed doppler noise is a direct function of the total electron content along the signal path:

$$\text{doppler noise} = K\int_0^{R_{s/c}} N_e(r)dR$$

C.3

which directly leads to a geometrical model (ISED) for the prediction of doppler noise:

$$\text{ISED} = A_0\left[\frac{\beta}{(\sin\alpha)^{1.3}}\right]F(\alpha,\beta) + A_1\left[\frac{1}{(\sin\alpha)^5}\right]$$

$$F(\alpha,\beta) = 1 - 0.05\left\{\frac{(\beta - \pi/2 + \alpha)^3 - (\alpha - \pi/2)^3}{\beta}\right\}$$

$$- 0.00275\left\{\frac{(\beta - \pi/2 + \alpha)^5 - (\alpha - \pi/2)^5}{\beta}\right\}$$

A best fit of this model to the combined Pioneer 10, Pioneer 11, and Helios 1 1975 solar conjunction doppler noise produced the following fit parameters:

$$A_0 = 9.65 \times 10^{-4}$$

$$A_1 = 5 \times 10^{-10}$$

and a standard deviation about the ISED model of:

$$1\sigma = 2.0\,\text{dB}\ \{\text{factor of } 1.58\}$$

Attempts to correlate systematic deviations from the ISED model with observed solar activity (RISED) produced a substantial decrease in systematic model error (for a selected data set):

$$1\sigma = 1.6\,\text{dB}\ \{\text{factor of } 1.45\}$$

However, it was not possible to successfully project the RISED model forward to a new (Helios 1 second) data base.

Finally, certain benefits are expected to have strong likelihood of realization:

(1) Validation of doppler data generation during solar conjunction phases.

(2) Planning for future mission critical phases during solar conjunctions.

Additional, but far less certain, benefits may also accrue:

(1) Determination of long term (~months) electron density levels.

(2) Determination of intermediate (~days/weeks) fluctuations in electron density levels.

(3) Detailed electron density information (particularly of the inner corona) which might be useful in correlative studies of solar activity.

Acknowledgments

A hearty thanks is extended to two individuals who greatly aided in the bringing of this report to fruition: F. Almon, for her excellent rapid-fire typing, and M. Cates, for her pellucid eye-pleasing graphical illustrations.

References

1. Berman, A. L., and Rockwell, S. T., "Analysis and Prediction of Doppler Noise During Solar Conjunctions," in *The Deep Space Network Progress Report 42-30*, Jet Propulsion Laboratory, Pasadena, Calif., Dec. 15, 1975.

2. Efron, L., and Lisowski, R. J., "Charged Particle Effects to Radio Ranging and Doppler Tracking Signals in a Radially Outflowing Solar Wind," in Space Programs Summary 37-56, Volume II: *The Deep Space Network*, Jet Propulsion Laboratory, Pasadena, Calif., March 31, 1969.

3. Van De Hulst, J. C., "The Electron Density of the Solar Corona," *Bulletin of the Astronomical Institutes of the Netherlands*, Vol. XI, Number 410, Feb. 2, 1950.

4. Stelzried, C. T., *A Faraday Rotation Measurement of a 13 CM Signal in the Solar Corona*, Technical Report 32-1401, Jet Propulsion Laboratory, Pasadena, Calif., July 15, 1970.

5. Muhleman, D. O., Anderson, J. D., Esposito, P. B., and Martin, W. L., "Radio Propagation Measurements of the Solar Corona and Gravitational Field; Applications to Mariner 6 and 7," in *Proceedings of the Conference on Experimental Tests of Gravitational Theories*, California Institute of Technology, Pasadena, Calif., Nov. 1970.

6. Berman, A. L., and Rockwell, S. T., "Correlation of Doppler Noise During Solar Conjunction With Fluctuations in Solar Activity," in *The Deep Space Network Progress Report 42-30*, Jet Propulsion Laboratory, Pasadena, Calif., Dec. 15, 1975.

7. Berman, A. L., "Analysis of Solar Effects Upon Observed Doppler Data Noise During the Helios 1 Second Solar Conjunction," in *The Deep Space Network Progress Report 42-32*, Jet Propulsion Laboratory, Pasadena, Calif., April 15, 1976.

8. Dutcher, G. L., *A Communication Channel Model of the Solar Corona and the Interplanetary Medium*, CSRT-69-1, Center for Space Research, Massachusetts Institute of Technology, 1969.

9. Waldmeier, M., "Slow Variations in the Solar Corona," in *The Solar Corona*, edited by J. W. Evans, Academic Press, New York, 1963.

10. Croft, T. A., "Corotation of An Intermittent Solar Wind Source," in *Solar Wind*, edited by C. P. Sonett, P. J. Coleman, Jr., and J. M. Wilcox, Ames Research Center, National Aeronautics and Space Administration, Washington, D. C., 1972.

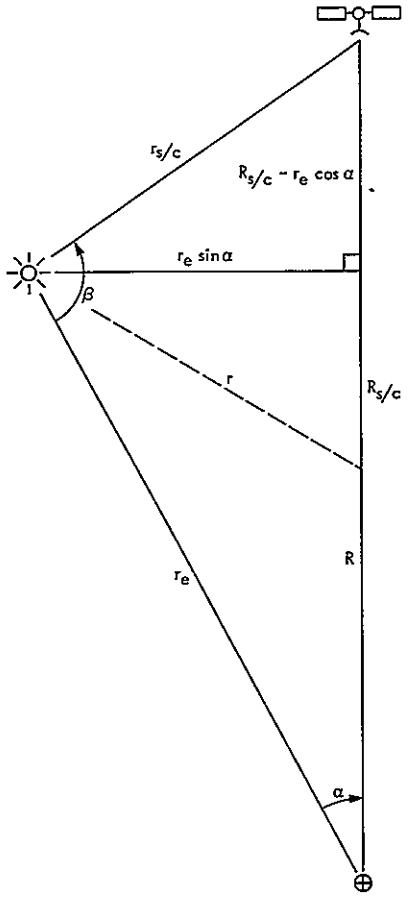

Fig. 1. Sun–Earth–spacecraft geometry

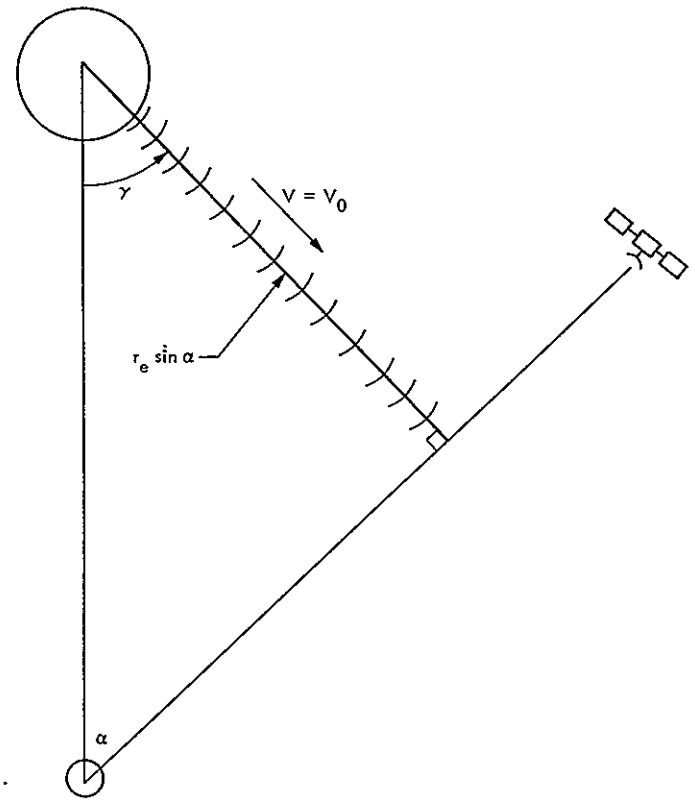

Fig. 2. Correlation phase geometry

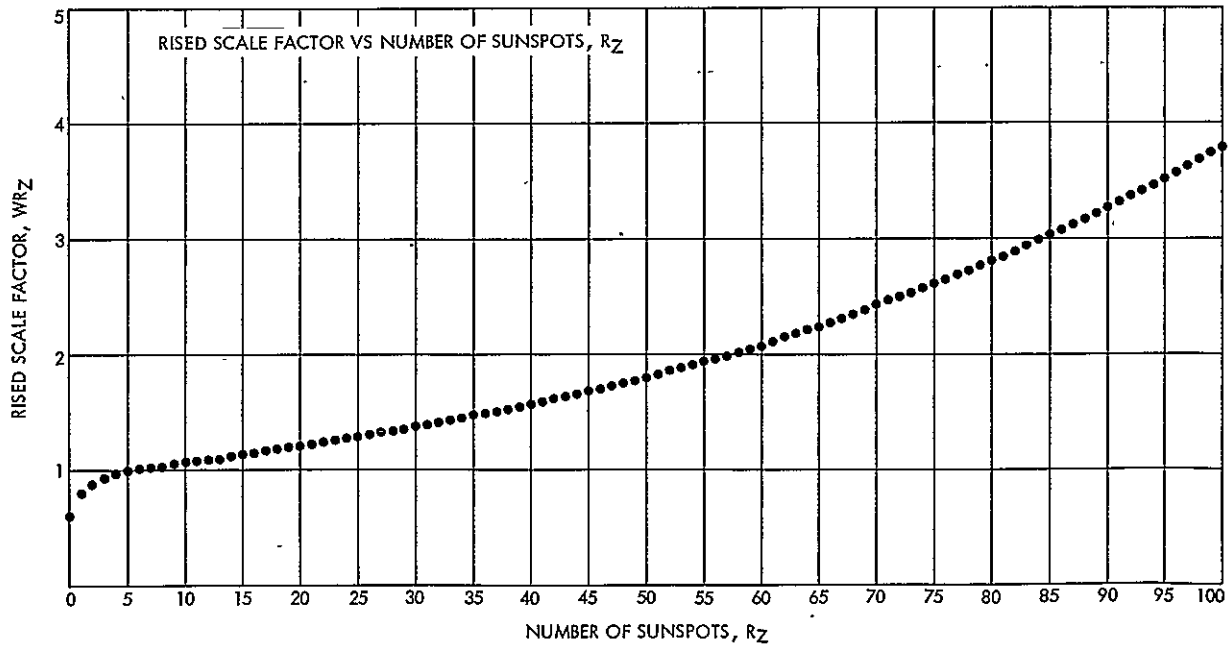

Fig. 3. RISED scale factor vs number of sunspots, R_Z

Appendix A

Observed Noise versus the ISED Model

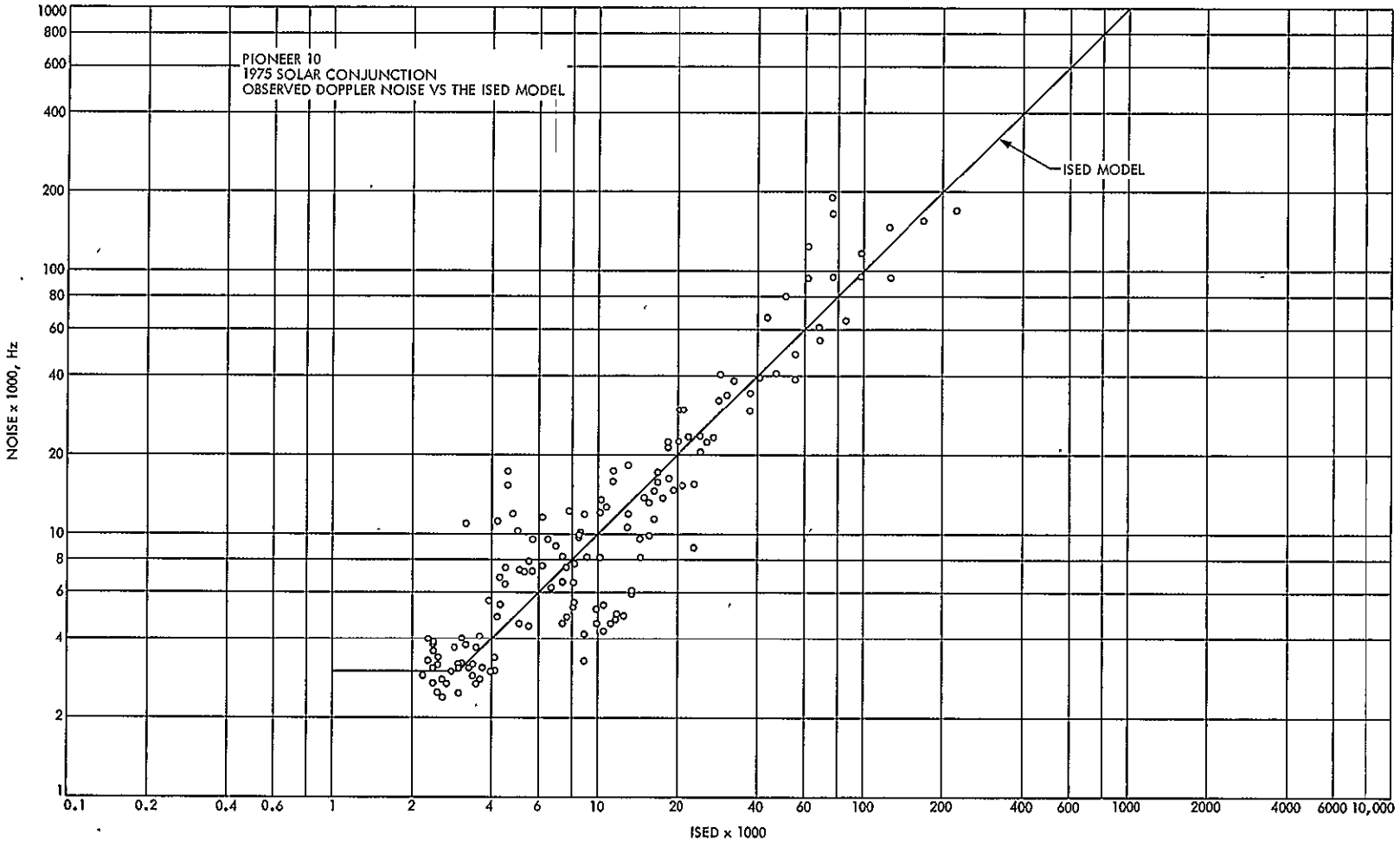

Fig. A-1. Pioneer 10 1975 solar conjunction observed doppler noise versus the ISED model

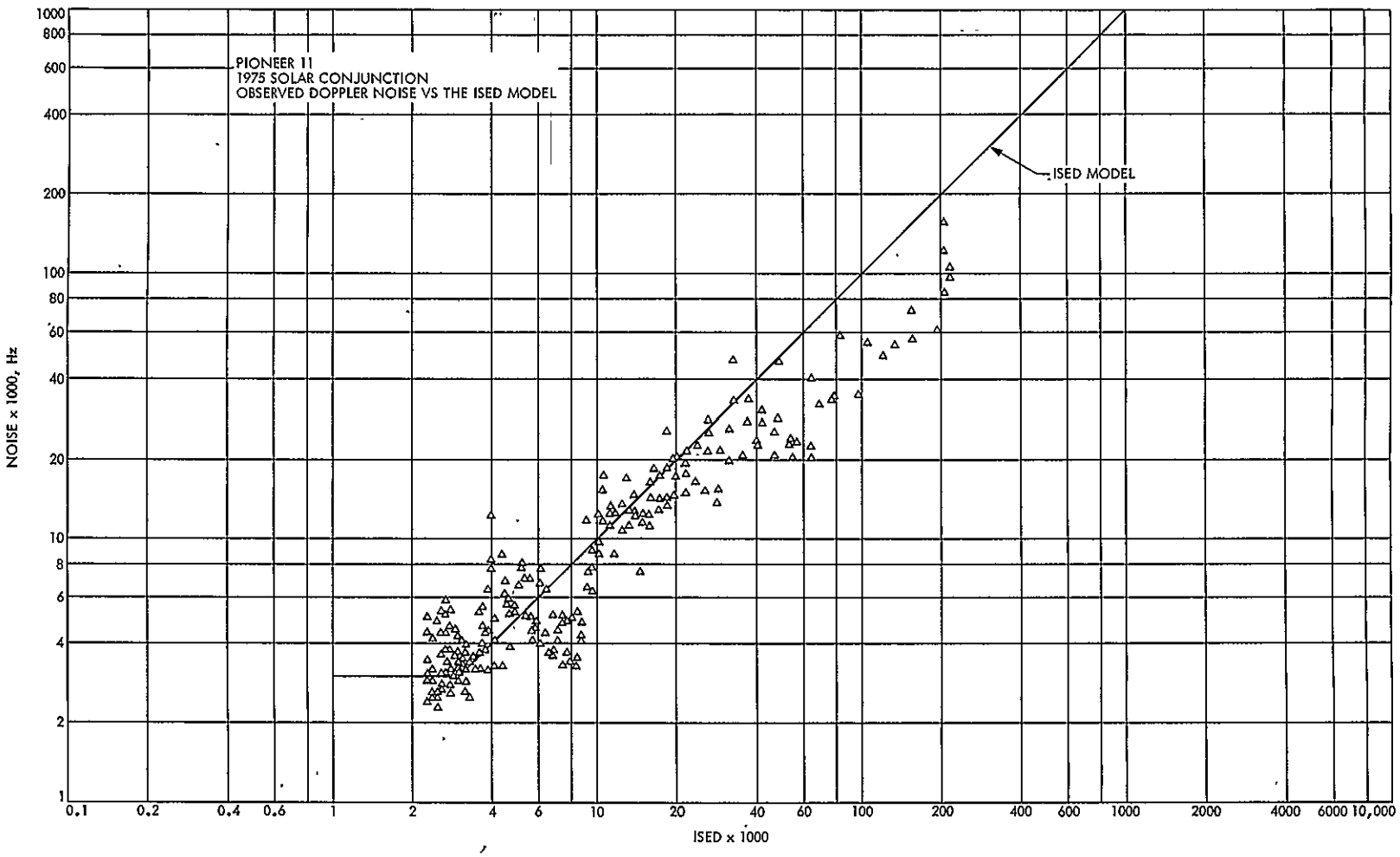

Fig. A-2. Pioneer 11 1975 solar conjunction observed doppler noise versus the ISED model

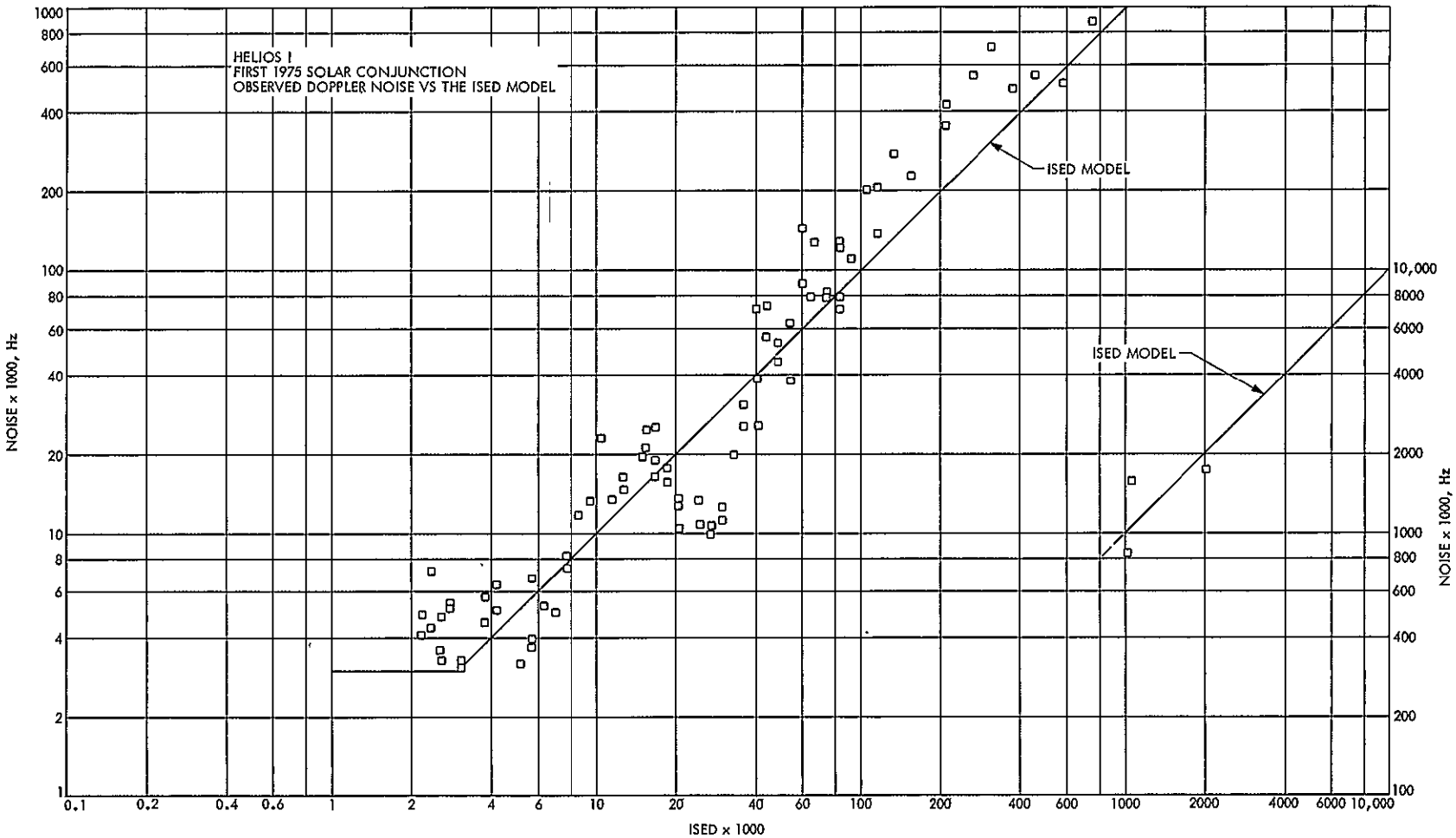

Fig. A-3. Helios 1 first 1975 solar conjunction observed doppler noise versus the ISED model

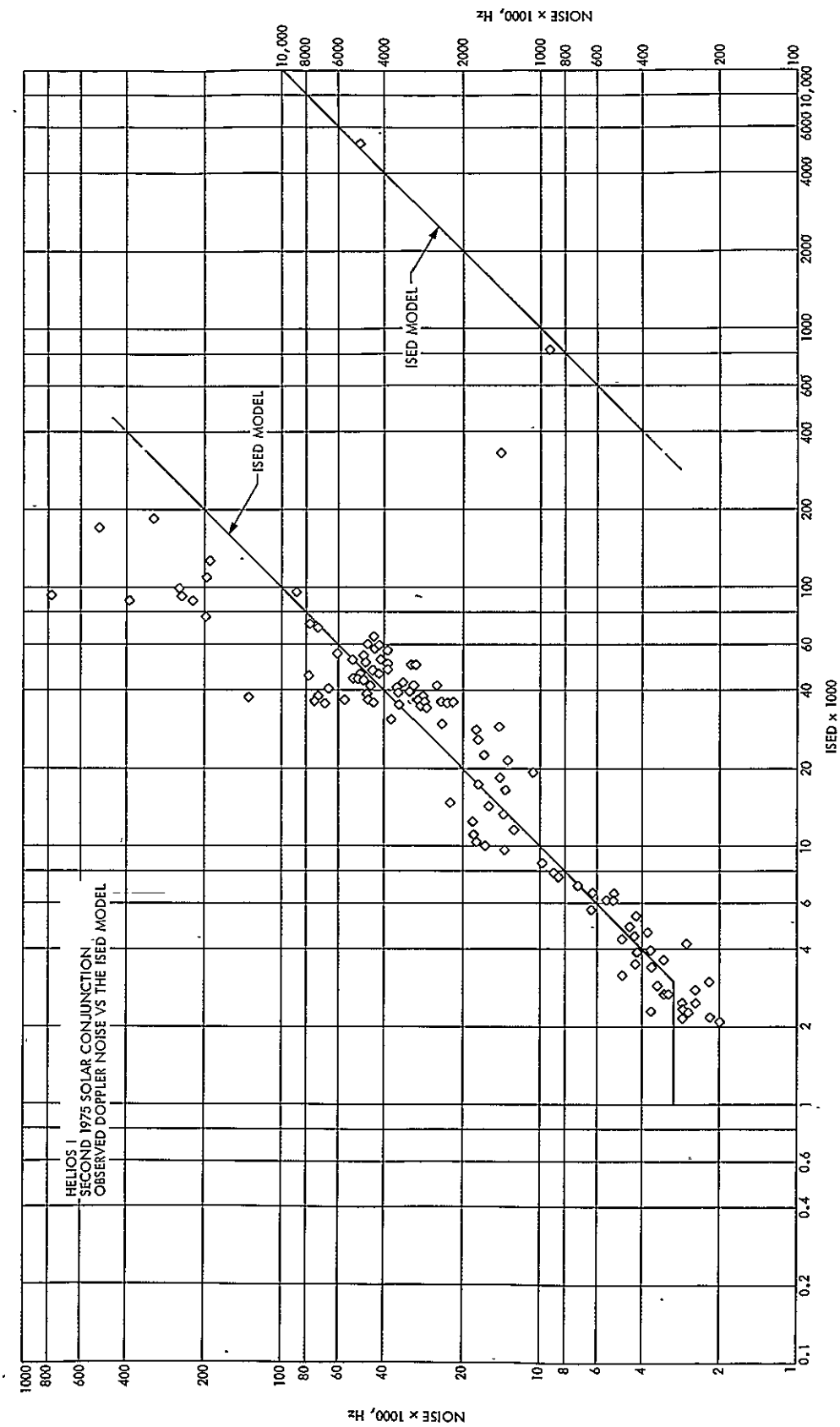

Fig. A-4. Helios 1 second 1975 solar conjunction observed doppler noise versus the ISED model

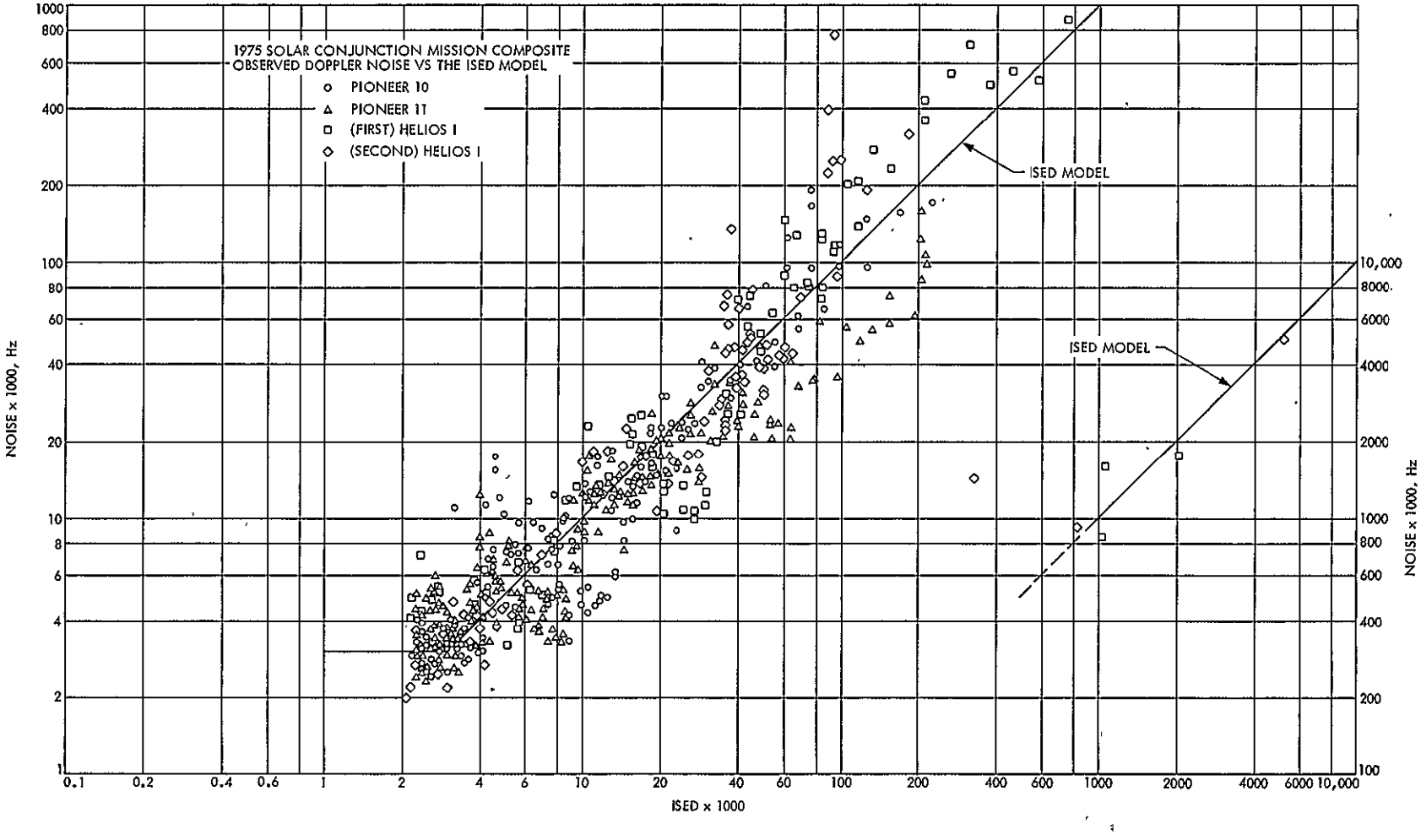

Fig. A-5. 1975 solar conjunction mission composite observed doppler noise versus the ISED model

Appendix B

Observed Noise and the ISED Model versus Day of Year

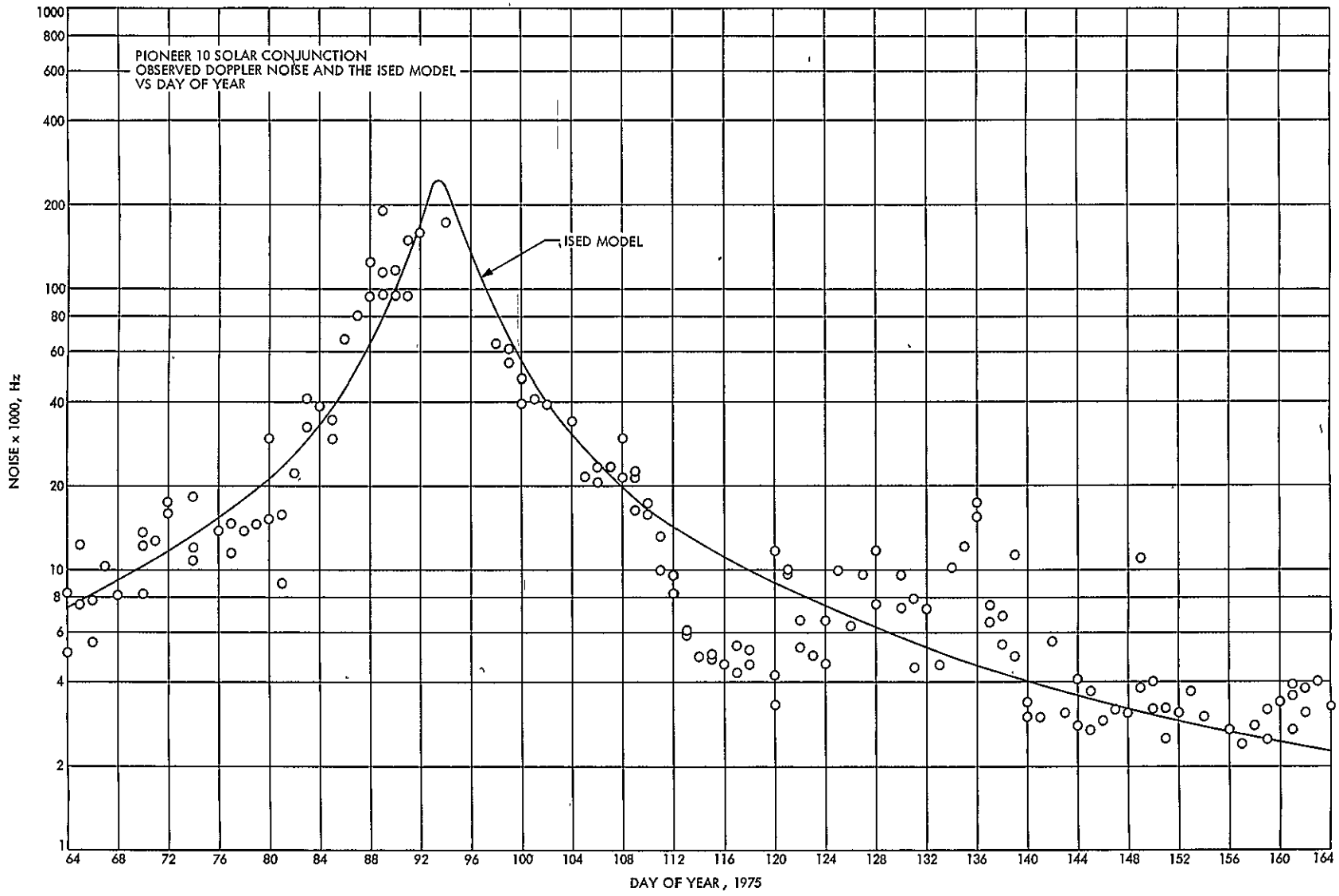

Fig. B-1. Pioneer 10 solar conjunction observed doppler noise and the ISED model versus day of year

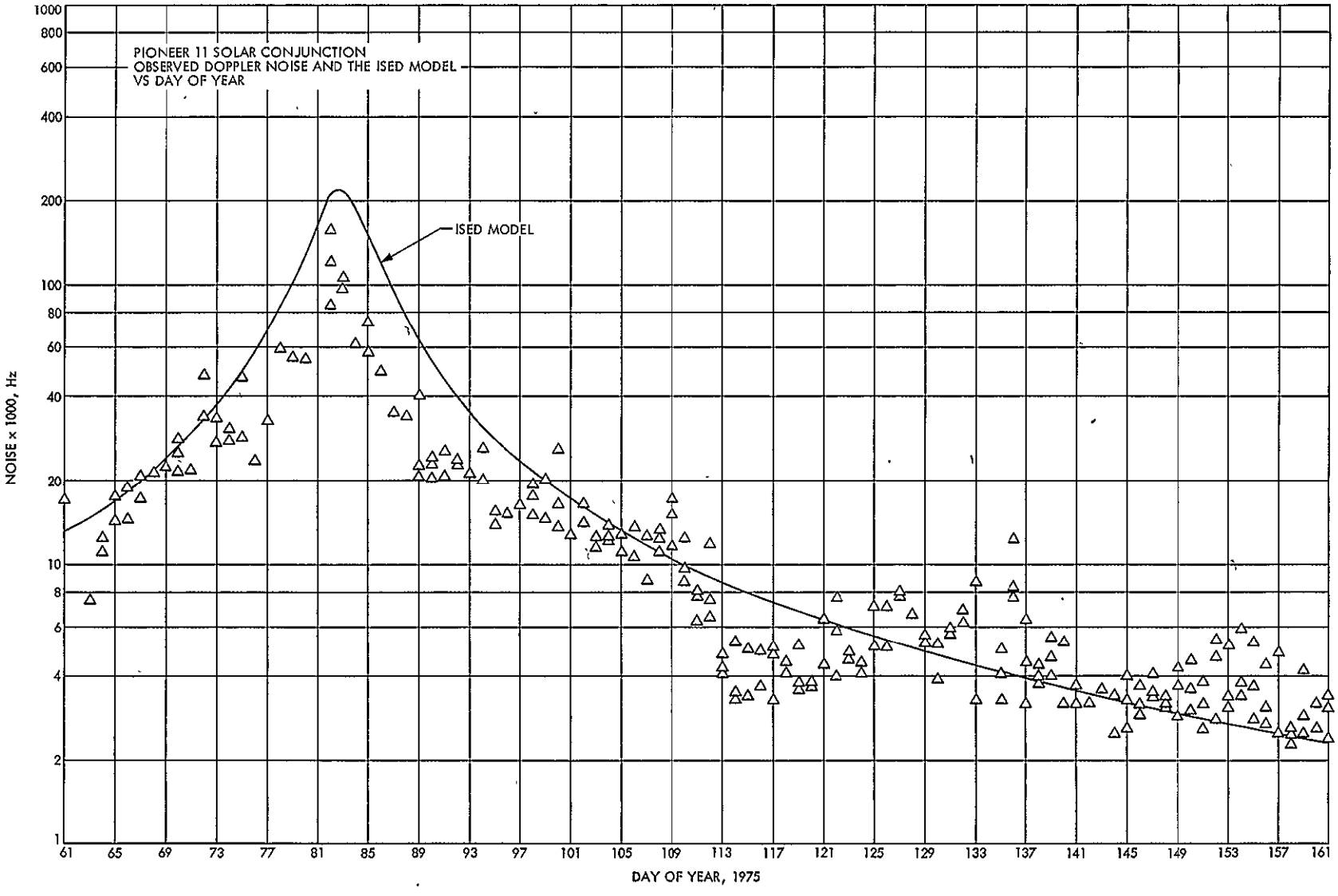

Fig. B-2. Pioneer 11 solar conjunction observed doppler noise and the ISED model versus day of year

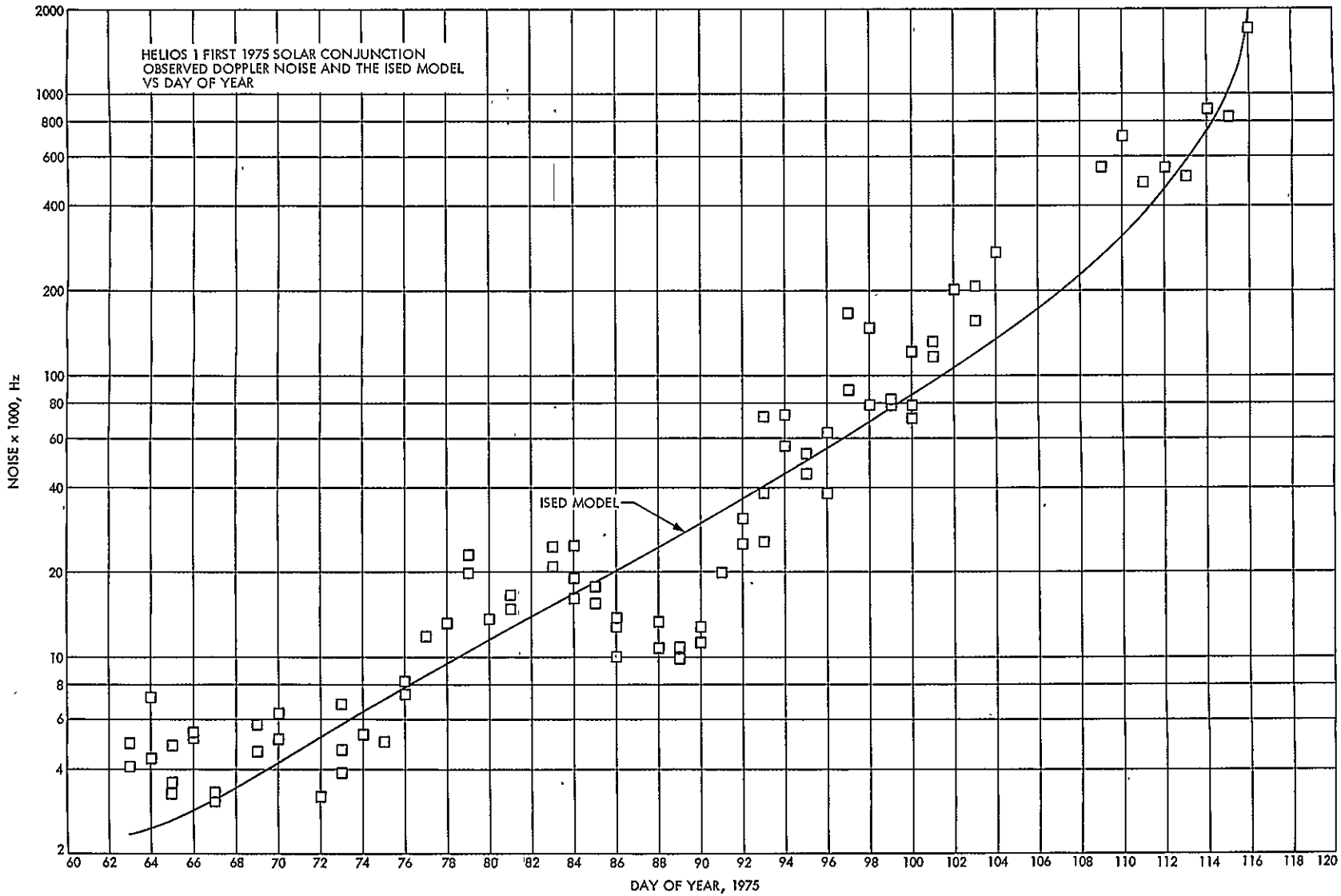

Fig. B-3. Helios 1 first 1975 solar conjunction observed doppler noise and the ISED model versus day of year

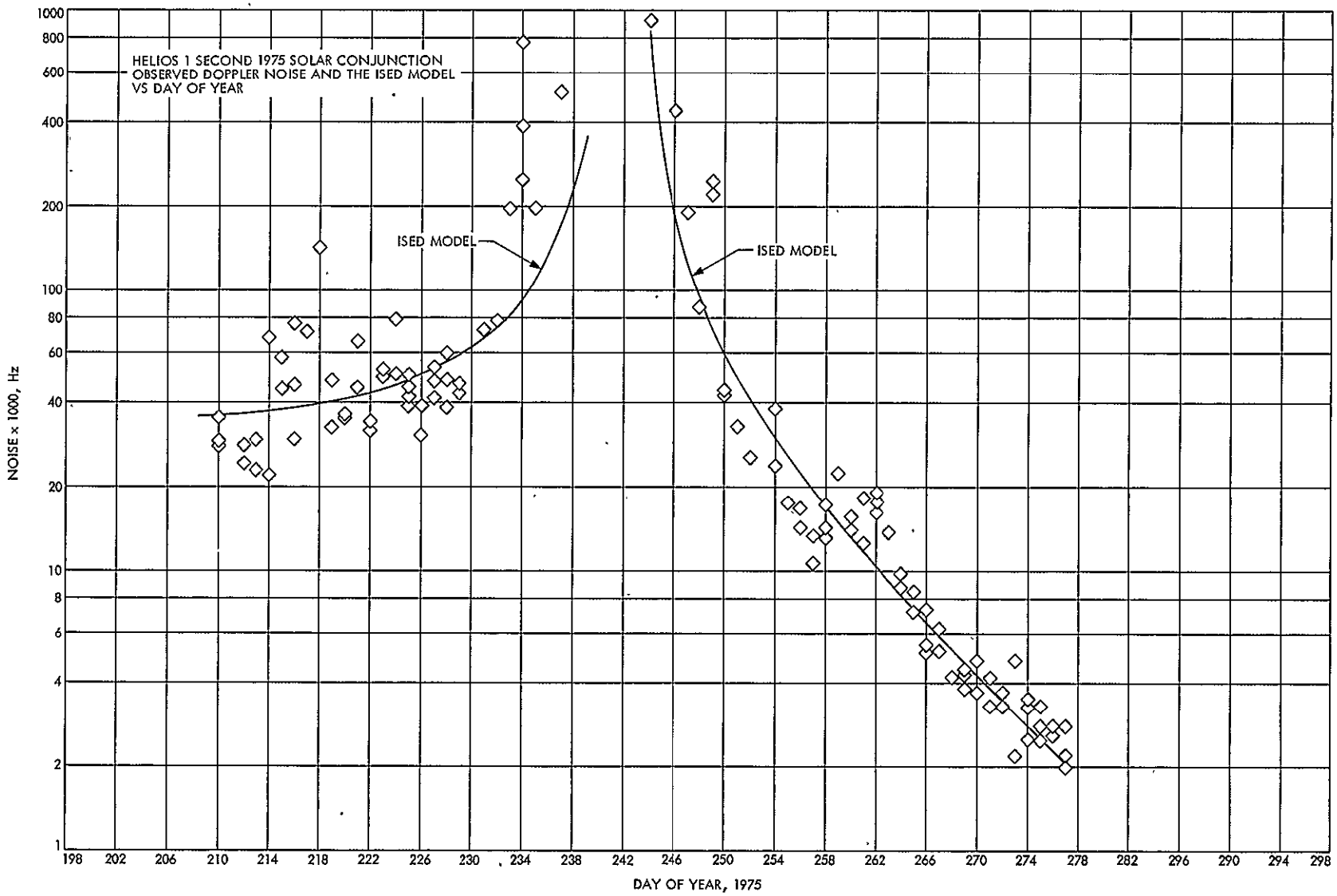

Fig. B-4. Helios 1 second 1975 solar conjunction observed doppler noise and the ISED model versus day of year

Appendix C

ISED Residuals, Smoothed/Phased Sunspots, and RISED Residuals versus Day of Year

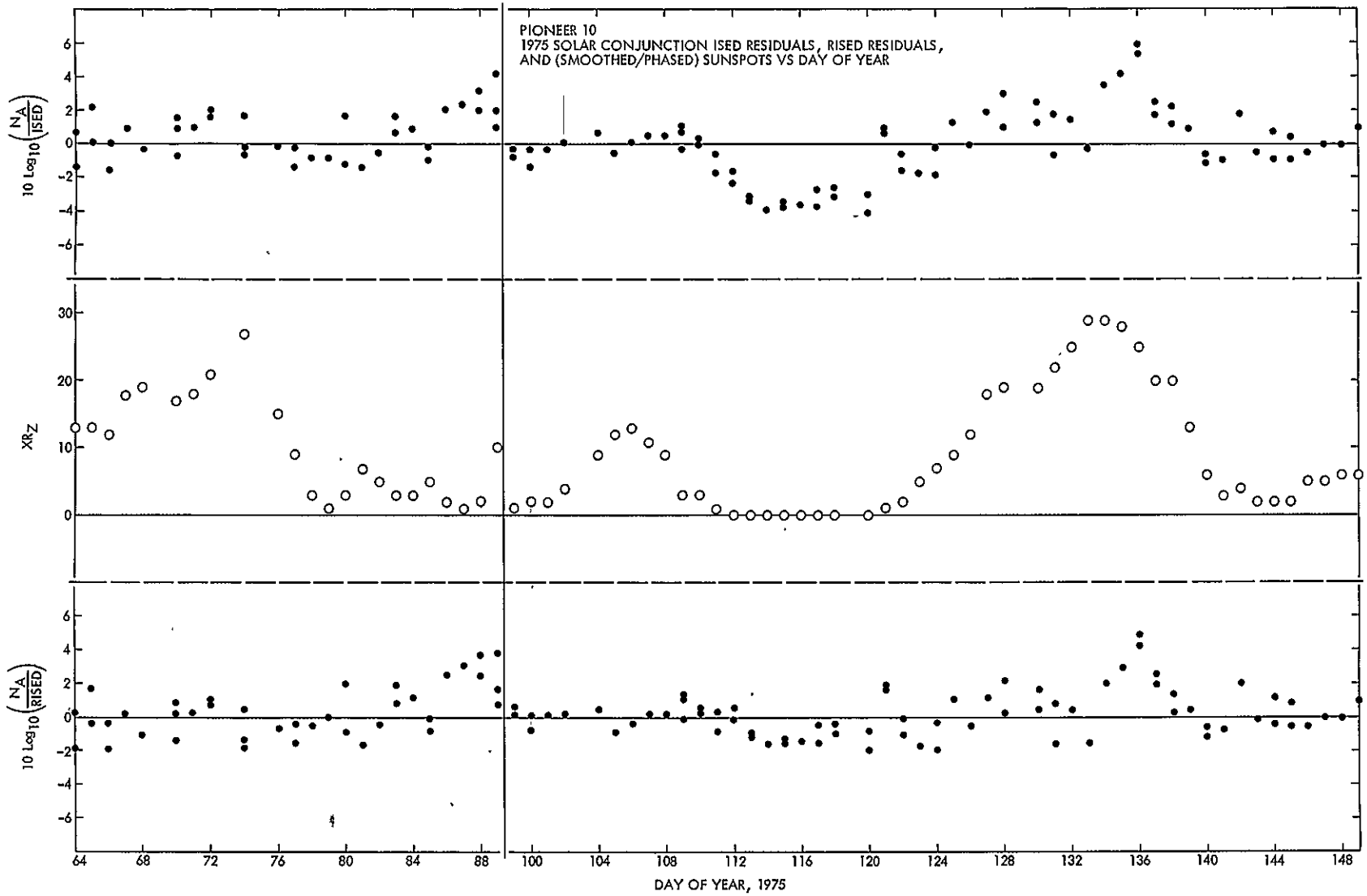

Fig. C-1. Pioneer 10 1975 solar conjunction ISED residuals, RISED residuals, and smoothed-phased sunspots versus day of year

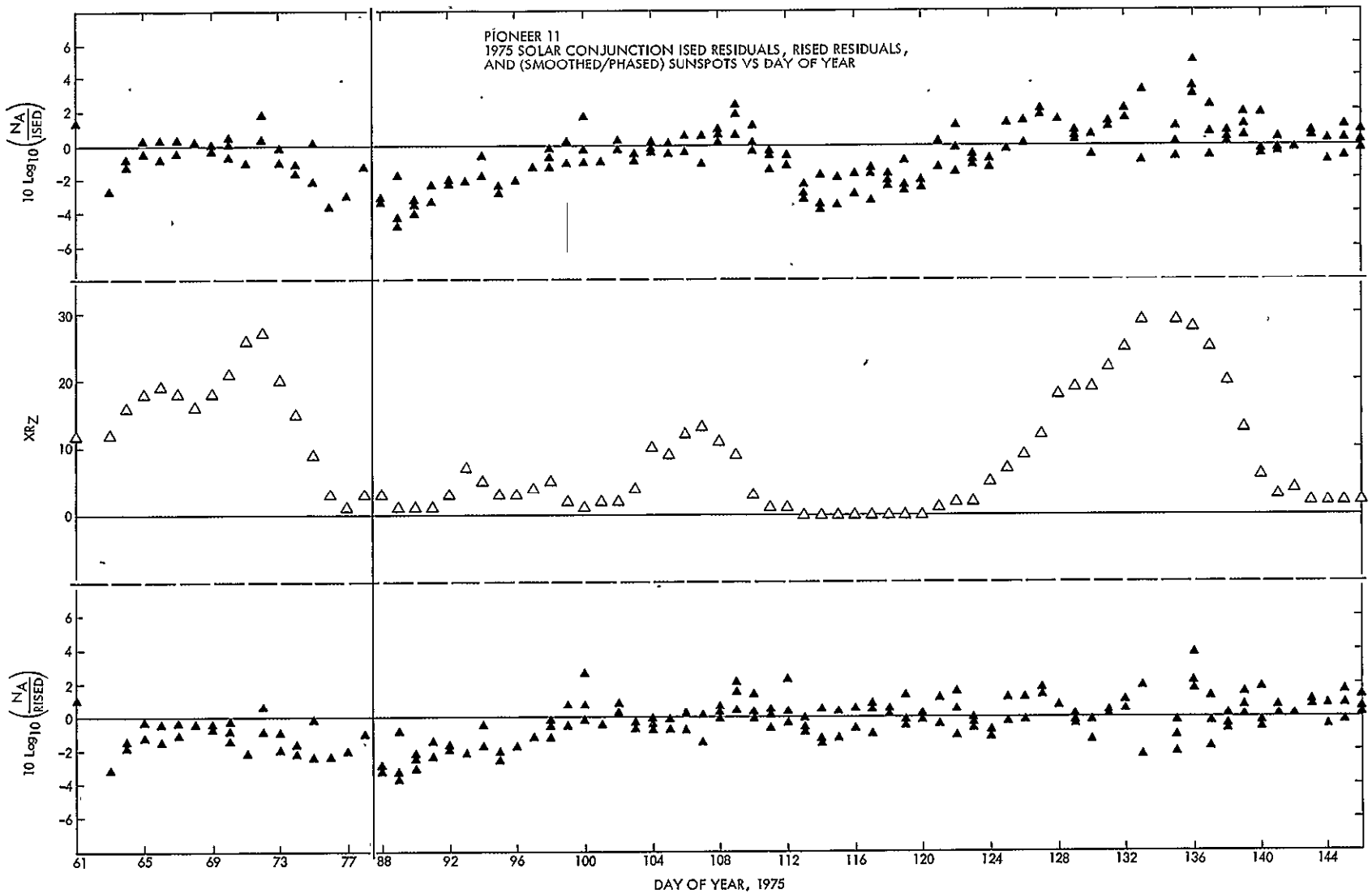

Fig. C-2. Pioneer 11 1975 solar conjunction ISED residuals, RISED residuals, and smoothed-phased sunspots versus day of year

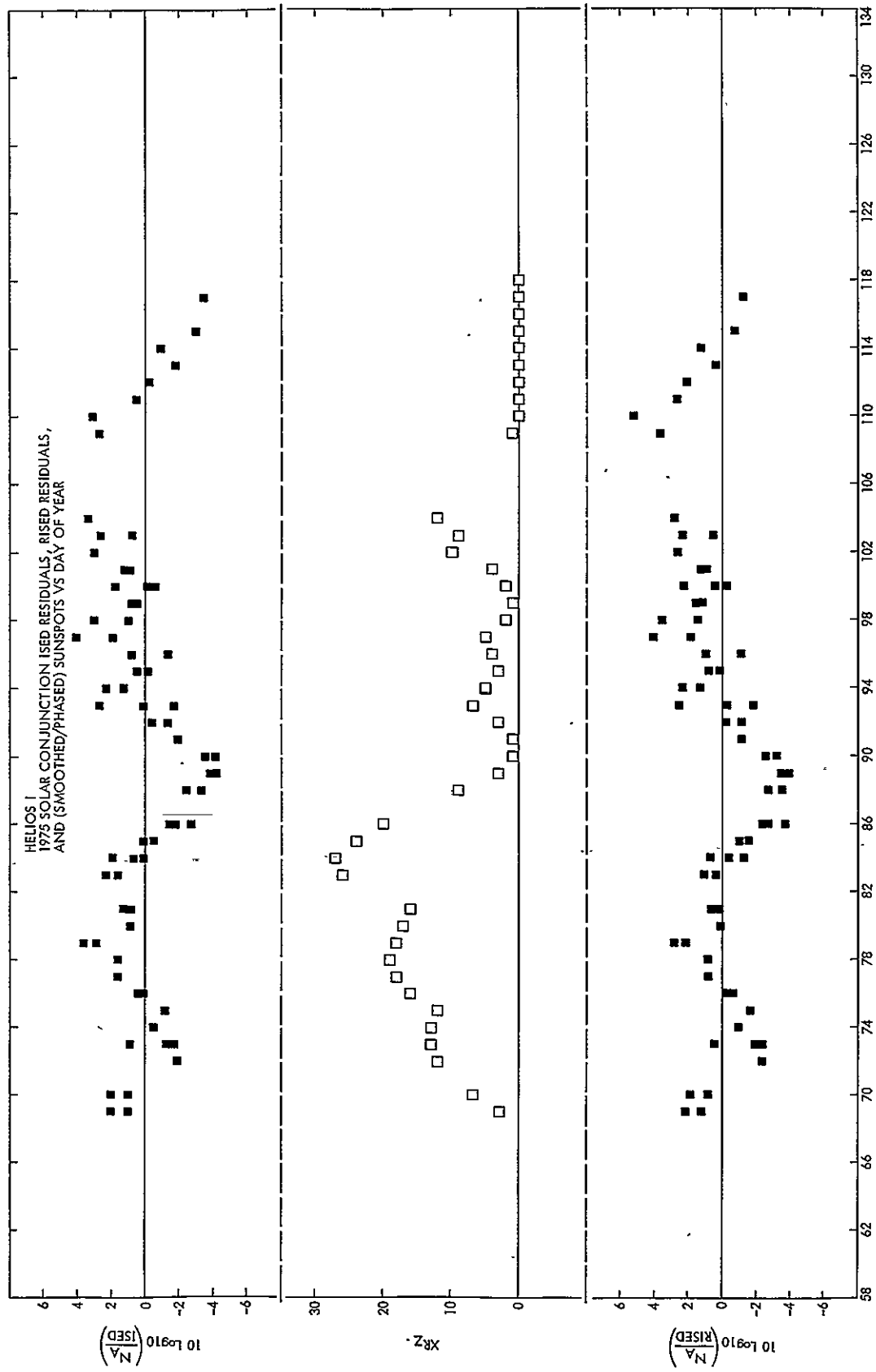

Fig. C-3. Helios 1 1975 solar conjunction ISED residuals, RISED residuals, and smoothed-phased sunspots versus day of year

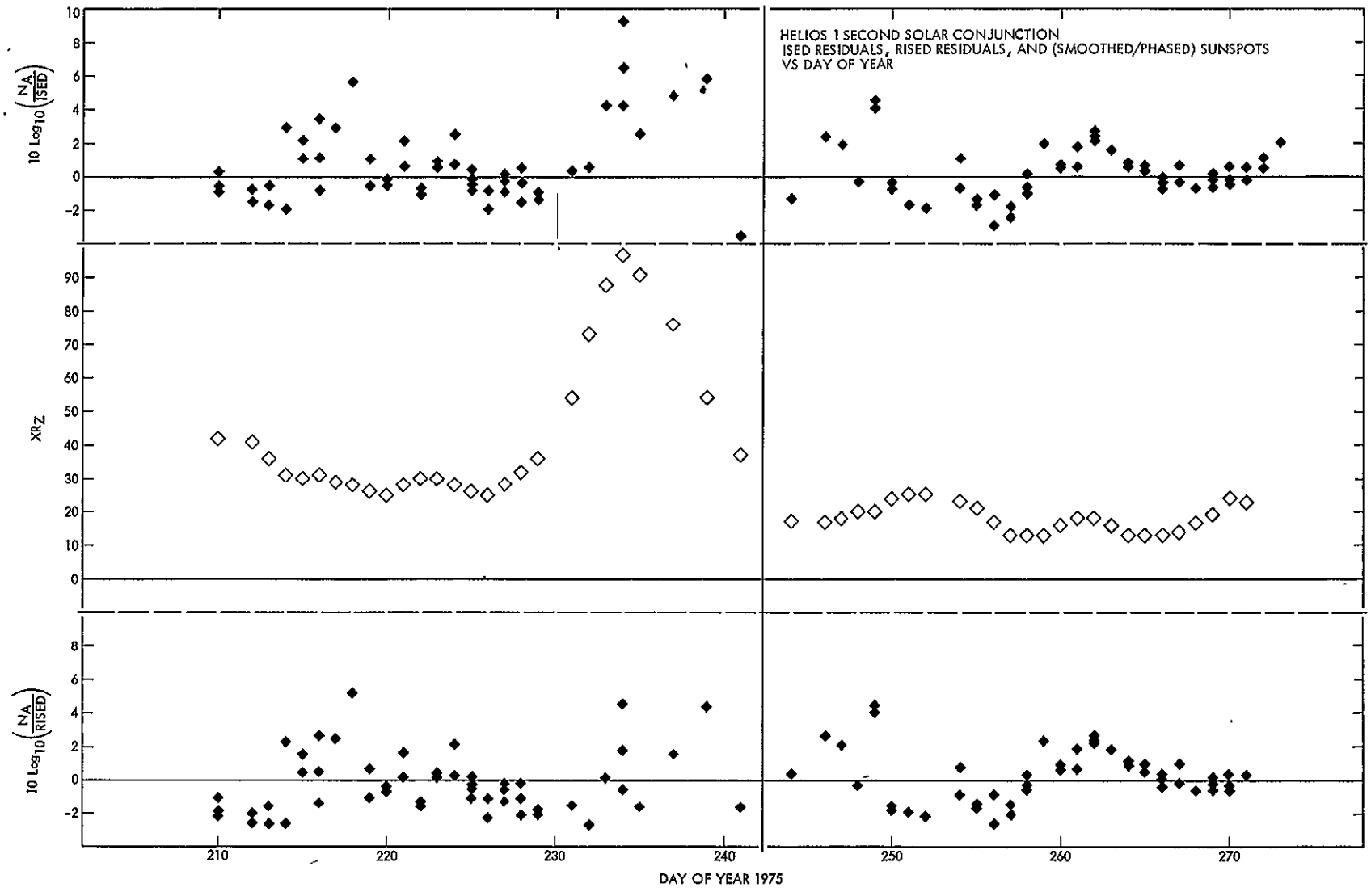

Fig. C-4. Helios 1 second solar conjunction ISED residuals, RISED residuals, and smoothed-phased sunspots versus day of year

Appendix D

Observed Noise and the RISED Model versus Day of Year

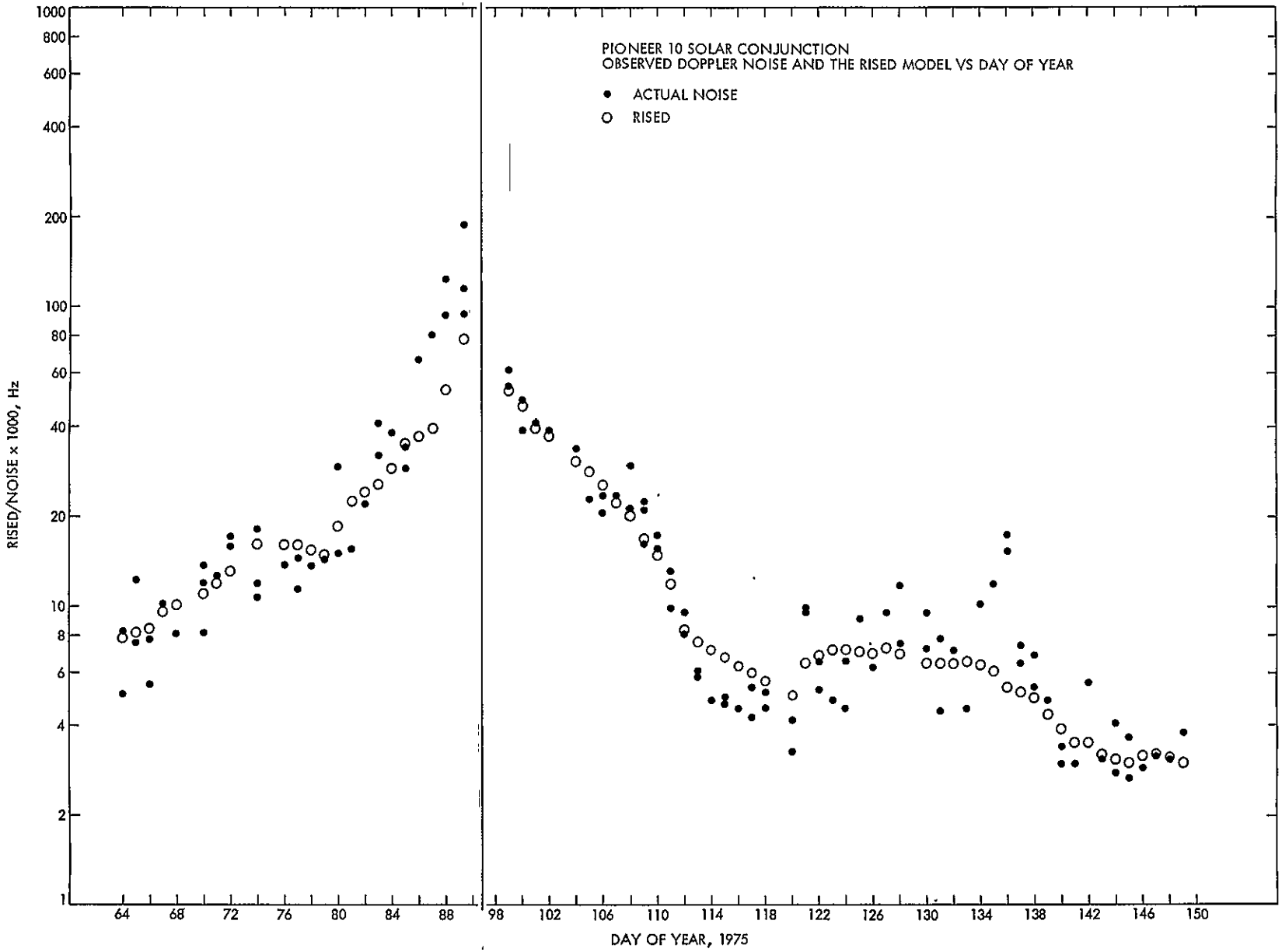

Fig. D-1. Pioneer 10 solar conjunction observed doppler noise and the RISED model versus day of year

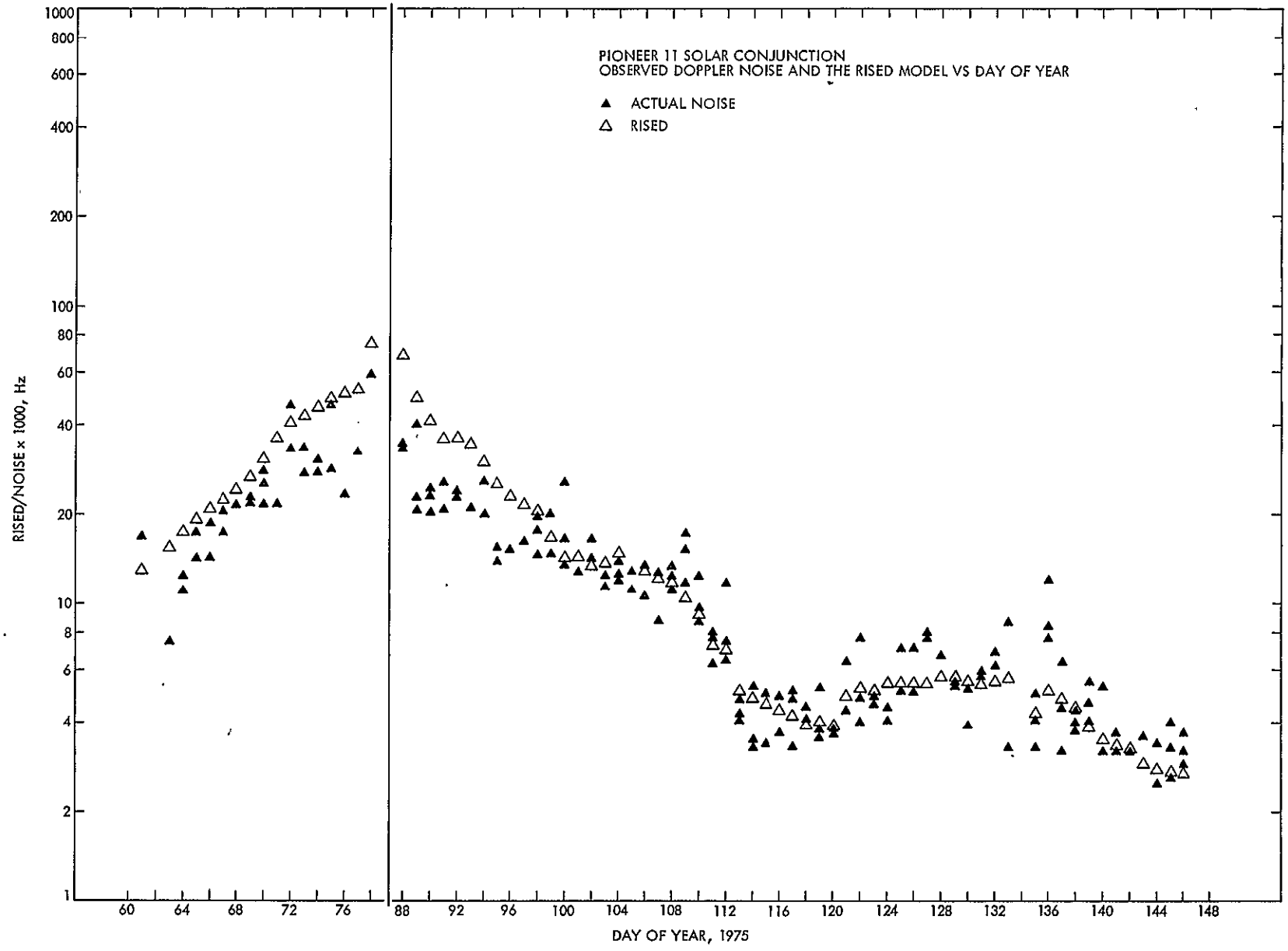

Fig. D-2. Pioneer 11 solar conjunction observed doppler noise and the RISED model versus day of year

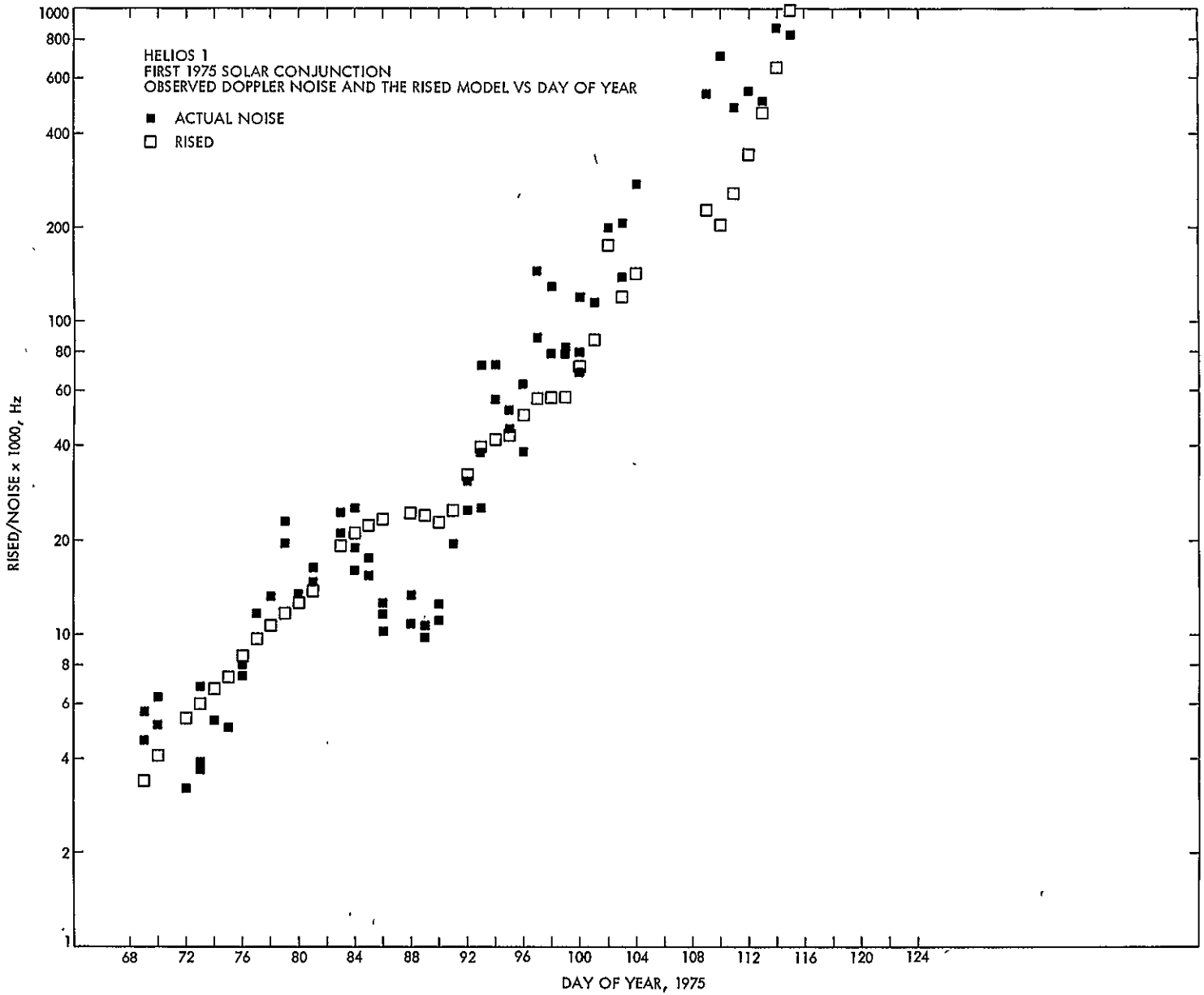

Fig. D-3. Helios 1 first 1975 solar conjunction observed doppler noise and the RISED model versus day of year

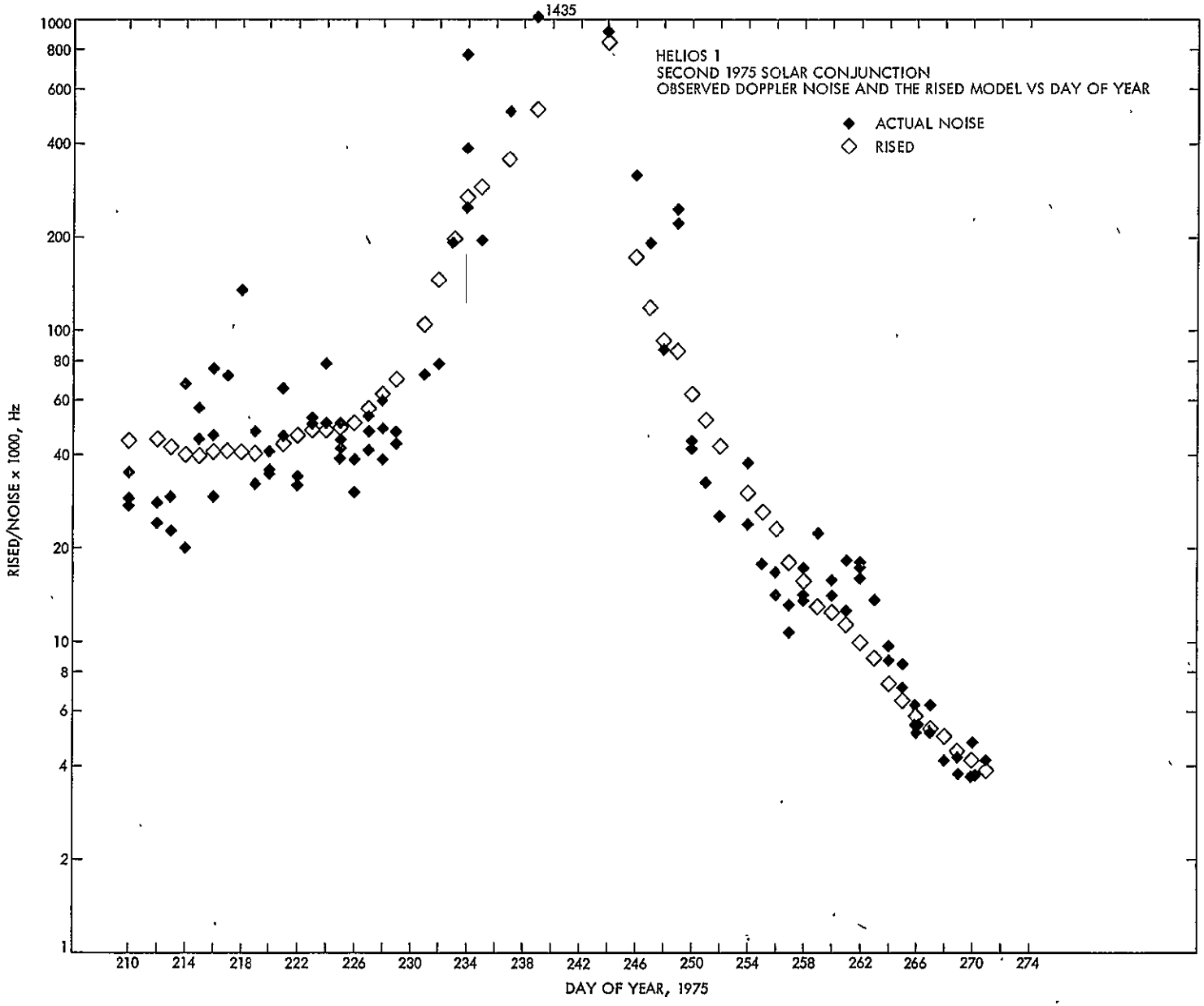

Fig. D-4. Helios 1 second 1975 solar conjunction observed doppler noise and the RISED model versus day of year

Appendix E

Observed Noise versus the RISED Model

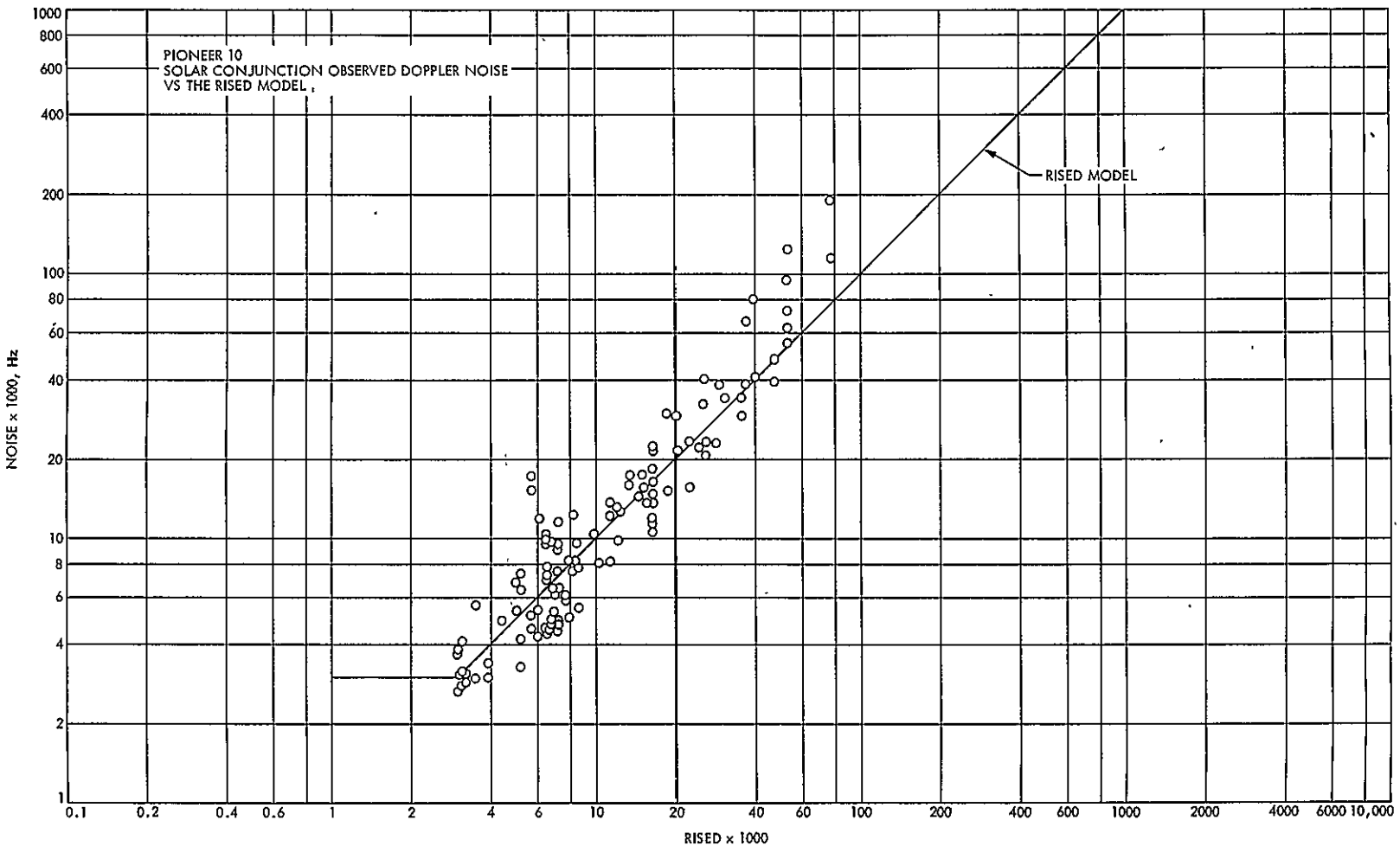

Fig. E-1. Pioneer 10 solar conjunction observed doppler noise versus the RISED model

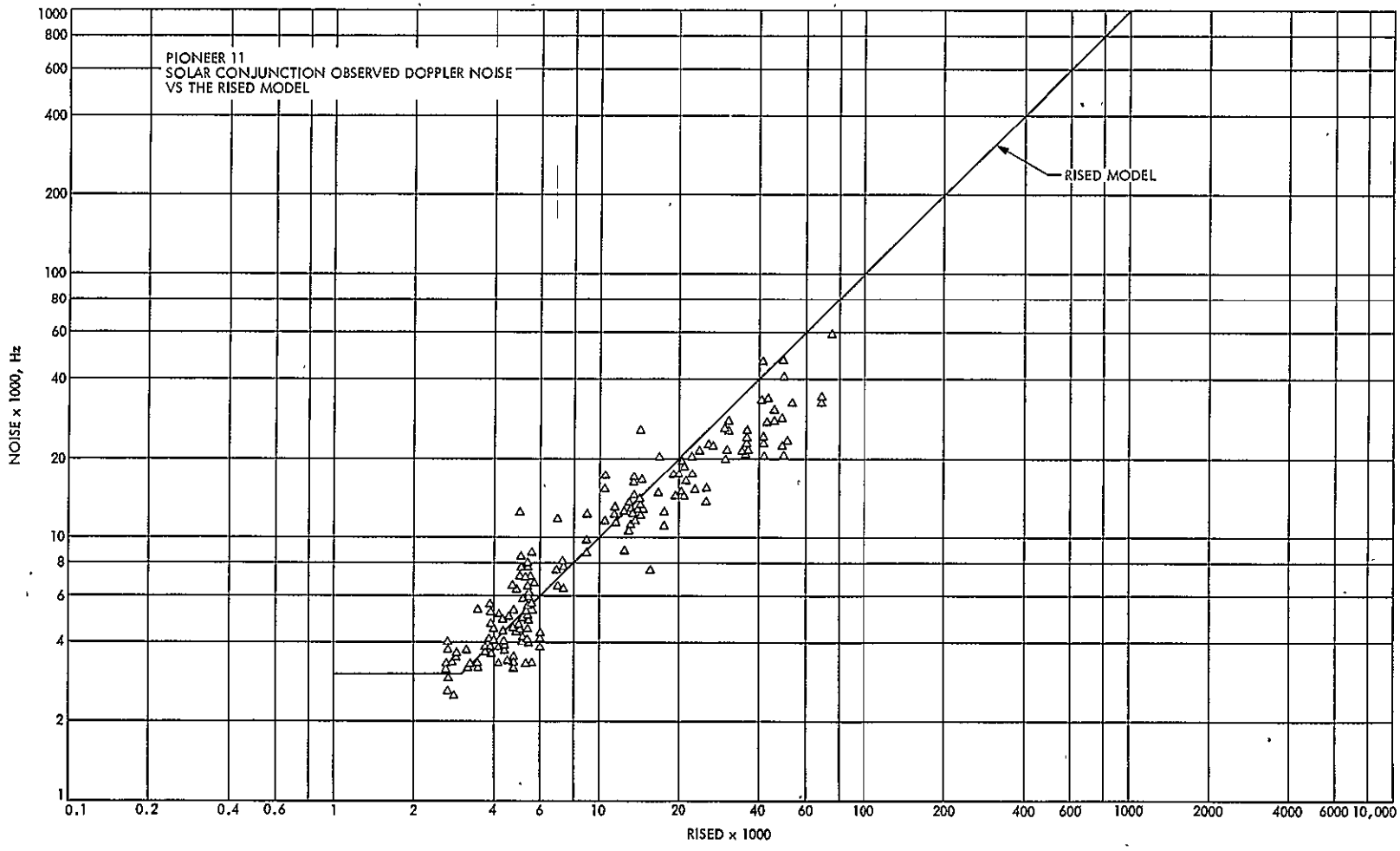

Fig. E-2. Pioneer 11 solar conjunction observed doppler noise versus the RISED model

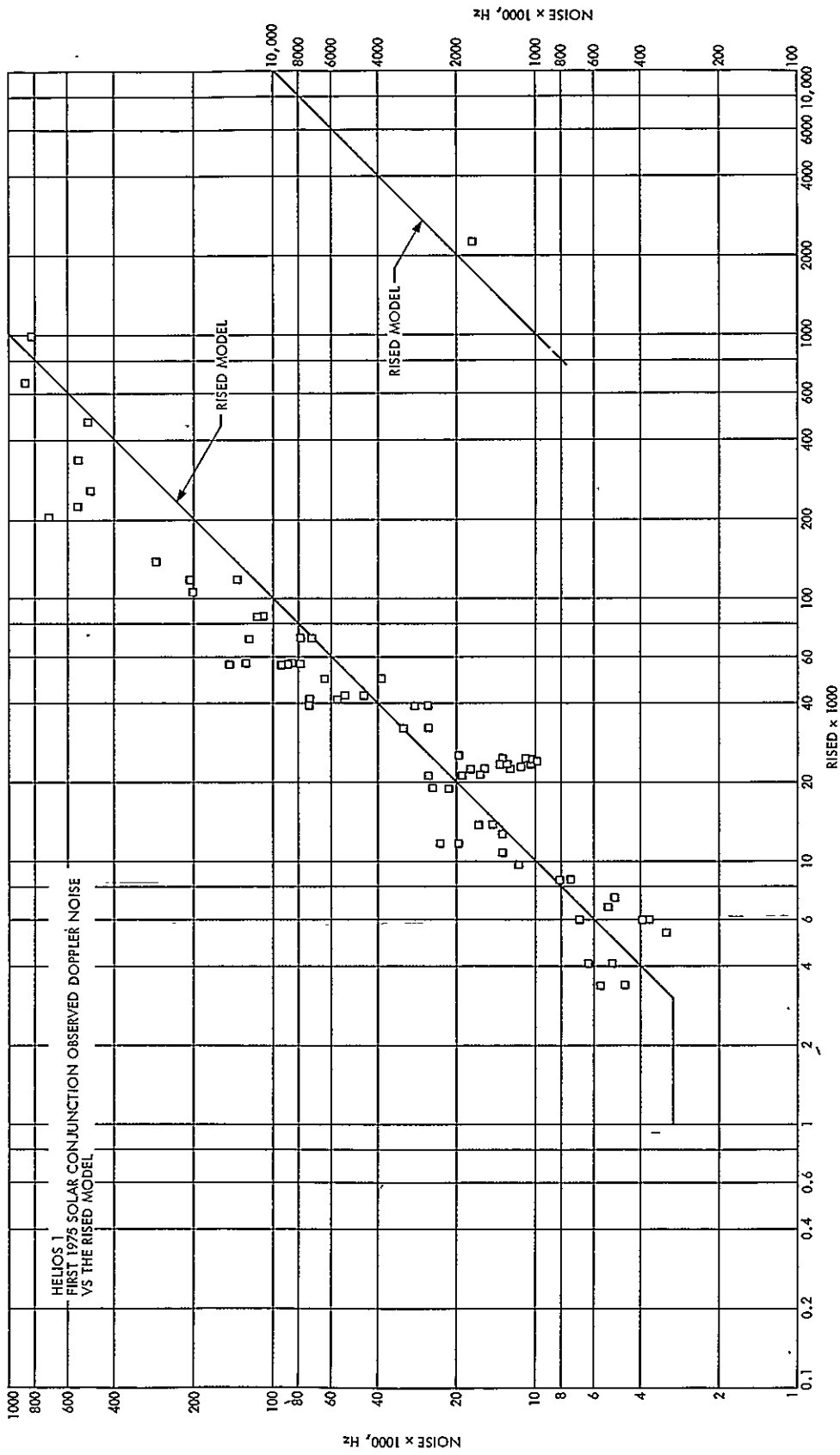

Fig. E-3. Helios 1 first 1975 solar conjunction observed doppler noise versus the RISED model

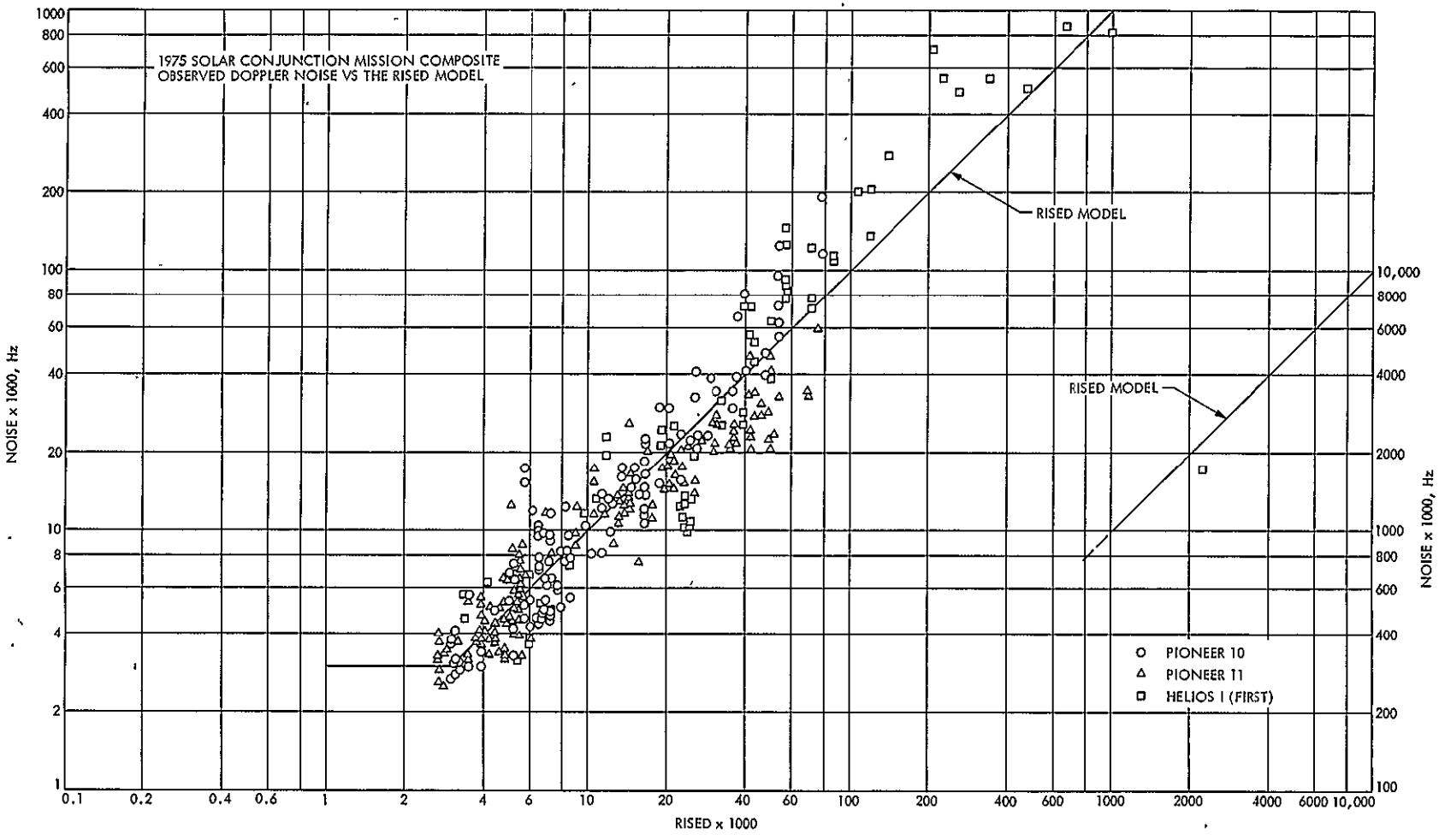

Fig. E-4. 1975 solar conjunction mission composite observed doppler noise versus the RISED model

A New Algorithm for Predicting the Apparent Polarization Angle of Linearly Polarized Spacecraft

R. S. Schlaifer
Network Operations Section

With the advent of nonecliptic spacecraft orbits and the inclusion of a NASA X-Y mounted antenna within the DSN it has become apparent that the current polarization angle prediction formulas may be insufficient for future needs. This article presents a new formulation for predicting the polarization angle which properly accommodates these new features in a concise, straightforward form.

I. Introduction

Although the Deep Space Stations (DSSs) are designed to receive a signal which is right circularly polarized, it is sometimes desirable to have the spacecraft transmit a linearly polarized signal (e.g., to study the Faraday rotation effect). While the DSS can track such spacecraft, the resultant polarization mismatch causes a loss of about one half of the available signal power. To prevent this loss of signal power, a rectangular waveguide is so constructed that when it is oriented at a forty-five degree angle to the linearly polarized input signal, the output signal is right circularly polarized with (theoretically at least) no loss of signal power. This waveguide, analogous to the "quarter wave plate" used in optics, is known as a polarizer.

To gain the full advantage of this effect, it is crucial to orient the polarizer at the proper angle with respect to the input signal. Indeed, if the error in the orientation approaches ninety degrees, the output will be left circularly polarized causing a loss of virtually all of the available signal power! It is, therefore, important to accurately predict the required polarizer setting as measured with respect to the microwave feed at each DSS. This is currently done by the polarization angle prediction program using the method developed by Stelzreid in Ref. 1.

At the time the current method was developed, only azimuth-elevation (az-el) and hour angle-declination (HA-dec) antenna mounts were used within the DSN. Furthermore, all of the spacecraft that the DSN commonly

tracked had orbits that were virtually coincident with the ecliptic. With the advent of nonecliptic spacecraft trajectories and the inclusion of a NASA X-Y mounted antenna within the DSN, it became apparent that a new method for predicting the polarization angle was needed.

II. Derivation of the New Formulation

At this point it is useful to introduce a new term: the antenna horizon. This is the great circle on the celestial sphere that lies in the X-Y plane of the local Cartesian coordinate frame. The local coordinate frame is carefully chosen, according to the type of antenna mount in use, as follows:

(1) *Az-el mount.* For an az-el mount, the standard coordinate frame is chosen. In this frame, the Z-axis passes through the zenith; the Y-axis is perpendicular to the Z-axis and intersects the local meridian circle. Finally, the X-axis is perpendicular to both the Y and Z axes and satisfies the right-hand rule.

(2) *HA-Dec mount.* To develop the coordinate frame for a HA-dec mount, the frame for an az-el mount is constructed and then rotated about the X-axis so as to cause the Z-axis to pass through the North Celestial Pole.

(3) *NASA X-Y mount.* To develop the frame for the NASA X-Y mount, once again the frame for an az-el mount is constructed. This is then continually rotated about the X-axis so that the spacecraft always lies in the X-Y plane of the coordinate frame (i.e., the Z component of the station-spacecraft vector is always zero in this frame).

Now consider the (antenna position dependent) great circle that is perpendicular to the antenna horizon and contains the point at which the antenna is pointing. As the antenna tracks a moving object on the celestial sphere, this circle moves with the antenna and maintains a constant orientation with respect to the microwave feed. This circle is the reference against which the polarizer angle is measured; a polarizer set to convert a signal that is linearly polarized parallel to the plane containing this circle is said to be set at zero degrees.

Referring to Fig. 1, A is the reference circle at some moment in time; B is the great circle perpendicular to the spacecraft's orbit and passing through its position on the celestial sphere. If the signal is polarized perpendicular to the orbit (as is usually the case), the polarization angle measured at the station is the angle ρ at which the circles A and B intersect.

By inspection of Fig. 1,

$$\rho = \pi/2 - \tau$$

and from the cosine law for spherical triangles

$$\begin{aligned}\tau &= \cos^{-1}(-\cos\phi\cos\pi/2 + \sin\phi\sin\pi/2\cos\widehat{QR}) \\ &= \cos^{-1}(\sin\phi\cos\widehat{QR}) \\ &= \cos^{-1}(\sin(\pi-\phi)\cos\widehat{QR}) \\ &= \cos^{-1}(\sin\xi\cos\widehat{QR})\end{aligned}$$

Defining

$$\beta = \widehat{Q0'} \quad \text{and}$$
$$\sigma = \widehat{0'R}$$

gives

$$\widehat{QR} = \beta + \sigma$$

and

$$\tau = \cos^{-1}(\sin\xi\cos(\beta+\sigma)).$$

Since 0′ is the point where the X-axis intersects the equator,

$$\sigma = \begin{cases} \pi/2 - \text{HA}, & \text{if HA/Dec mount} \\ 3\pi/2 - \text{Az}, & \text{if Az/El mount} \\ \pi/2 + \text{Y}, & \text{If NASA X-Y mount} \end{cases}$$

From the sine law

$$\beta = \sin^{-1}(\sin\widehat{00'}\sin\iota/\sin\xi)$$

and by the cosine law

$$\xi = \cos^{-1}(-\cos\iota\cos\phi' + \sin\iota\sin\phi'\cos 00')$$

where

$$\phi' = \begin{cases} \text{zero} & \text{if HA/Dec mount} \\ \text{station colatitude} & \text{if Az/El mount} \\ \text{X-station latitude} & \text{if NASA X-Y mount} \end{cases}$$

By inspection

$$\widehat{00'} = \text{Sidereal Time (S.T.)} - \Omega - \pi/2$$

where Ω is the right ascension of the orbit's ascending node on the equator.

Then, finally,

$$\xi = \cos^{-1}(-\cos\iota\cos\phi' + \sin\iota\sin\phi'\sin(\text{S.T.} - \Omega))$$

$$\beta = \sin^{-1}(-\cos(\text{S.T.} - \Omega)\sin\iota/\sin\xi)$$

and

$$\rho = \sin^{-1}(\sin\xi\cos(\beta + \sigma))$$

with ϕ' and σ found from Table 1.

For spacecraft whose orbits are coincident with the ecliptic,

$$\Omega = 0 \quad \text{and}$$

$$\iota = \epsilon$$

where ϵ is the obliquity of the ecliptic.

The above formulas then become

$$\xi = \cos^{-1}(-\cos\epsilon\cos\phi' + \sin\epsilon\sin\phi'\sin\text{S.T.})$$

$$\beta = \sin^{-1}(-\cos\text{S.T.}\sin\epsilon/\sin\xi)$$

$$\rho = \sin^{-1}(\sin\xi\cos(\beta + \sigma)).$$

It should be noted that although Ω is not one of the standard orbital parameters, it is easily computed.

Referring to Fig. 2,

$$\Omega = \sin^{-1}(\sin\iota_e\sin\Omega_e/\sin(\pi - \iota))$$

$$= \sin^{-1}(\sin\iota_e\sin\Omega_e/\sin\iota)$$

and

$$\iota = \cos^{-1}(\cos\iota_e\cos\epsilon - \sin\iota_e\sin\epsilon\cos\Omega_e)$$

where

Ω_e is the longitude of the ascending node

ι_e is the inclination of the orbit to the ecliptic.

III. Conclusion

By comparing this result with the method currently in use (Ref. 1), it can be seen that the new formulation is functionally simpler. Furthermore, it will accommodate nonecliptic spacecraft and the new (to the DSN) NASA X-Y mount Finally, since the formulas used are the same for all DSN antenna mounts, the development of a well-structured computer program for predicting the polarization angle will be facilitated.

Reference

1. Stelzreid, C. T., and Abreu, A., "Received Signal Polarization of the Pioneer VI Spacecraft During the 1968 Superior Conjunction," Space Programs Summary 37-59, Vol. II, Jet Propulsion Laboratory, Pasadena, Calif., Sept. 30, 1969.

Table 1. The σ and ϕ' for DSN antenna mounts

Mount type	σ	ϕ'
HA/Dec	$\pi/2 - \mathrm{HA}$	0
Az/El	$3\pi/2 - \mathrm{Az}$	Station colatitude
NASA X-Y	$\pi/2 + \mathrm{Y}$	X — station latitude

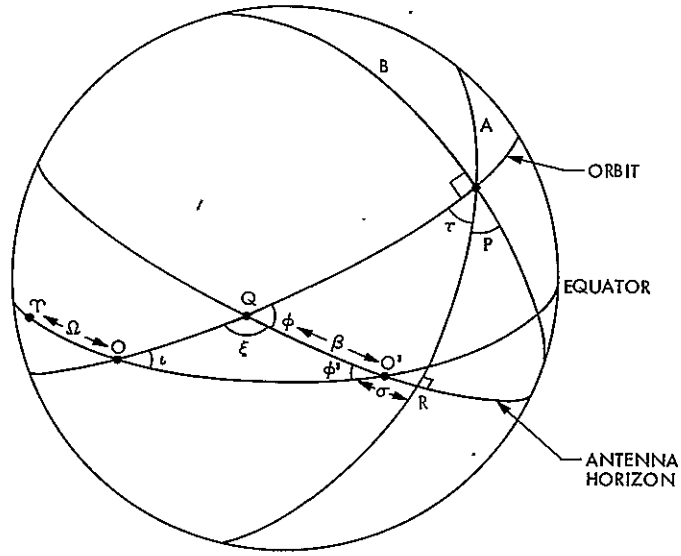

Fig. 1. Relation of polarization angle to antenna horizon and spacecraft orbit

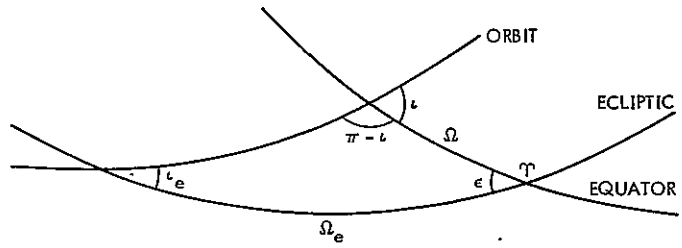

Fig. 2. Ecliptic and equatorial intersections with spacecraft orbit

DSN Diplexer, Noise Burst Testing

R. B. Kolbly
R. F. Systems Development Section

This article describes the testing of a new design high power S-band diplexer, the megawatt Cassegrain diplexer (MCD), to be used for DSN operations. The tests described were performed at 100 kW at the Venus Deep Space Station (DSS 13) Transmitter Test Area. At 100 kW or less no degradation of receive performance was detected.

I. Introduction

A diplexer is a passive microwave network that allows simultaneous transmission and reception of microwave signals. To communicate with distant spacecraft, it is necessary to utilize high transmitter power and low noise receivers. A DSN station can use up to 400 kW of continuous-wave transmitter power with receiver temperatures as low as 10 K (0.15 dB noise figure). To operate under these conditions without introducing additional system noise, a high-power diplexer must be designed for minimum voltage gradient to prevent arcing, corona discharge, and other nonlinear phenomena. The testing was performed under controlled conditions to detect any excess noise generated within the diplexer.

II. Test Configuration

The diplexer was installed in an existing DSN feedcone, the S-band Megawatt Transmit (SMT), to provide a horn as a low noise termination for the diplexer. The rest of the configuration duplicates the operating system of a DSN high-power station. A receive band reject filter, the megawatt transmitter filter (MTF) is installed between the transmitter and diplexer to reject broadband beam noise from the klystron amplifier. The receive output port of the diplexer is connected to a traveling wave maser and noise monitoring rack. A waveguide switch in the maser input allows for calibration of the maser by means of comparison with an ambient load. Figure 1 is a block diagram of the test configuration. Figures 2 through 6 show overall views of the test area.

III. Test Result

When the system was operated under high power into the water load, the voltage standing wave ratio (VSWR) was excessive (return loss of less than 20 dB). Investigation of the various components and waveguide interconnects failed to reveal any one defective component, so it was surmised that the individual reflection coefficient vectors

were phased so that they added. Figure 7 shows the VSWR of various components and sections of the system as measured with a WR-430 waveguide slotted line and a WR-430 restive load (VSWR < 1.01). To correct the problem, the E dimension of a short section of waveguide was adjusted to provide an acceptable match to the transmitter. Although it would have been possible to broad-band with this matching technique, this cone will be completely refurbished before reinstallation, and it was felt that it would not justify the time required.

The diplexer was operated at both high VSWR (f = 2110 MHz) and low VSWR (f = 2117 MHz) at 100 kW CW for four hours at each frequency. The system temperature was approximately 28 K and the recorder sensitivity was approximately 2.7 K/major division. At various times during the four-hour runs, the diplexer and other waveguide parts were examined for any heating. Also, the diplexer, waveguide, and feed were pounded with a rubber mallet to determine if there were any mechanical instabilities in the system.

IV. Results

Figure 8 is a portion of the diplexer test chart. At no time during either the high- or low-VSWR runs was any excess noise detected in the system. The slow drift of the chart to the left is caused by the zero drift of the power meter used as a noise detector. The pounding with a mallet was undetectable in the noise spectra, either on the chart recorder or the spectrum analyzer. Also, no detectable temperature rise due to RF heating was noted.

V. Conclusion

Within the constraints of relatively low-power testing (100 kW instead of the 400 kW designed operating level), no faults were found in this diplexer under RF power conditions. It is recommended that this unit be tested at 400 kW CW RF for a period of not less than four hours when a suitable power klystron becomes available. The complete testing of this diplexer, including set-up calibration, debugging and tear down of equipment for these tests, utilized 165 JPL and 320 contractor manhours.

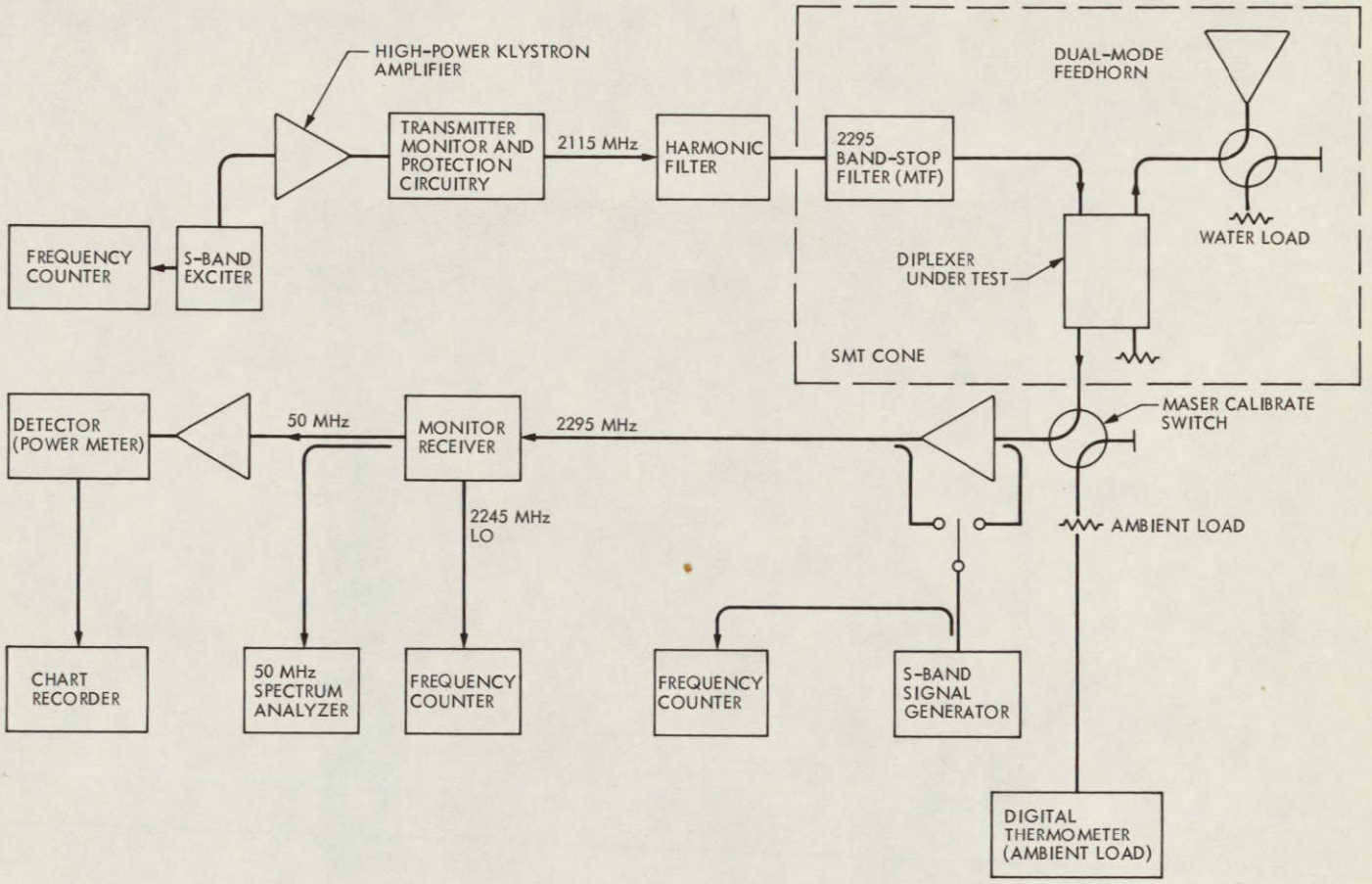

Fig. 1. Equipment configuration-diplexer test

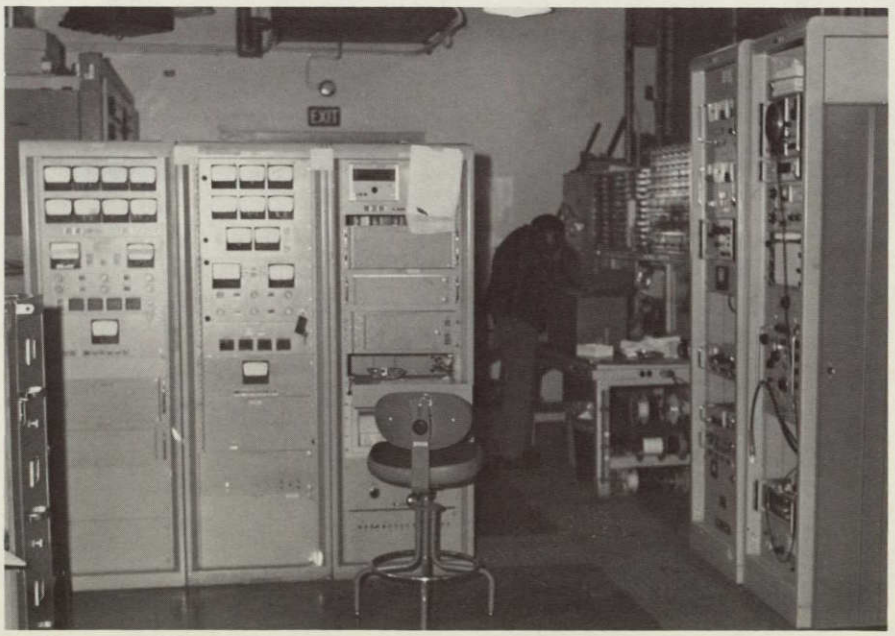

Fig. 2. Instrumentation and control racks

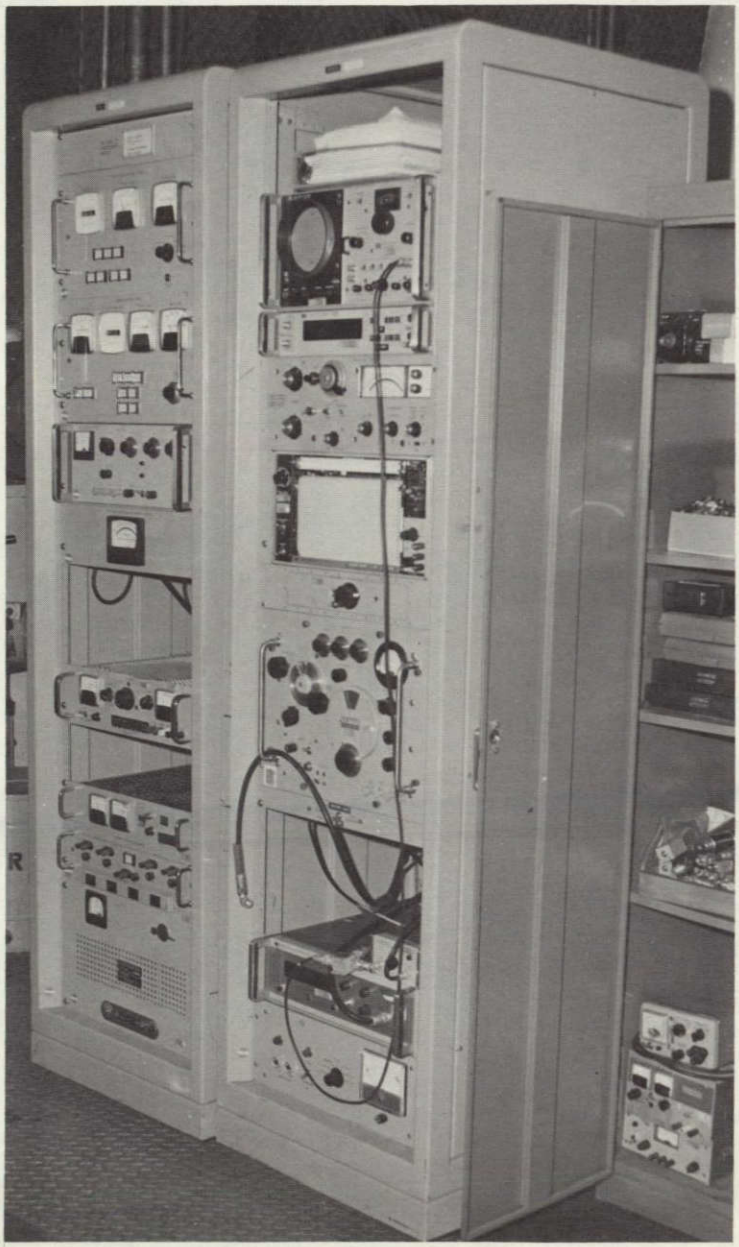

Fig. 3. Maser control and instrumentation

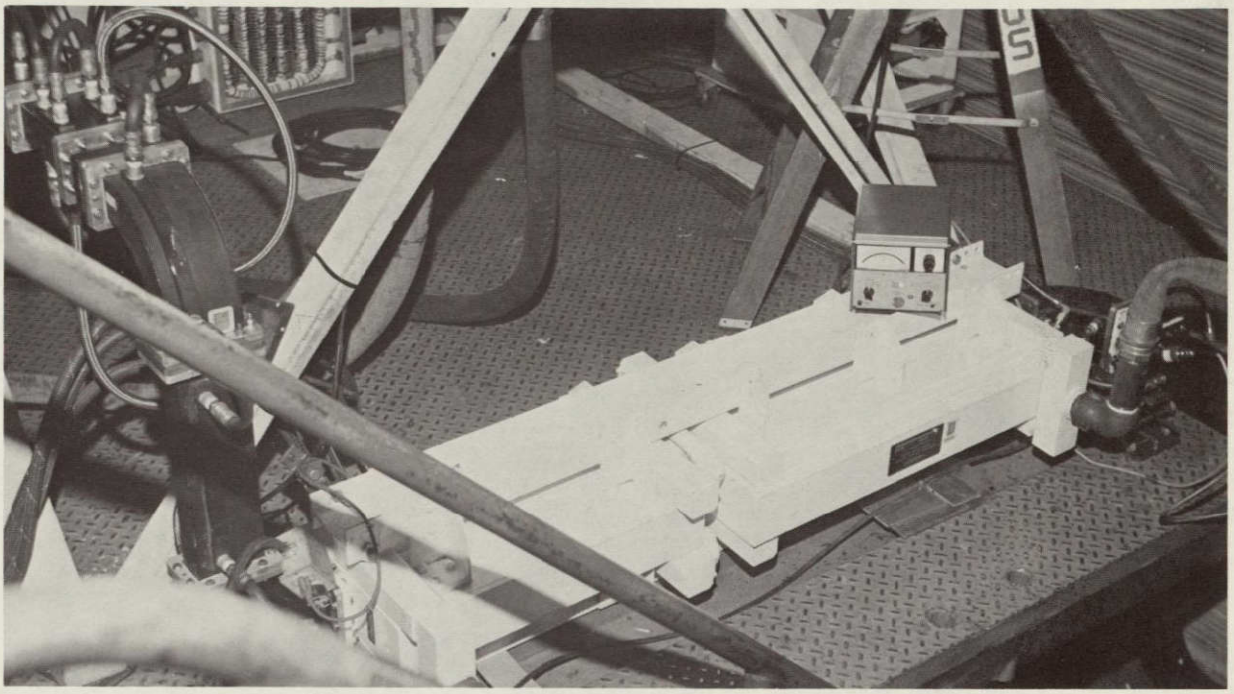

Fig. 4. Harmonic filter and input power monitor

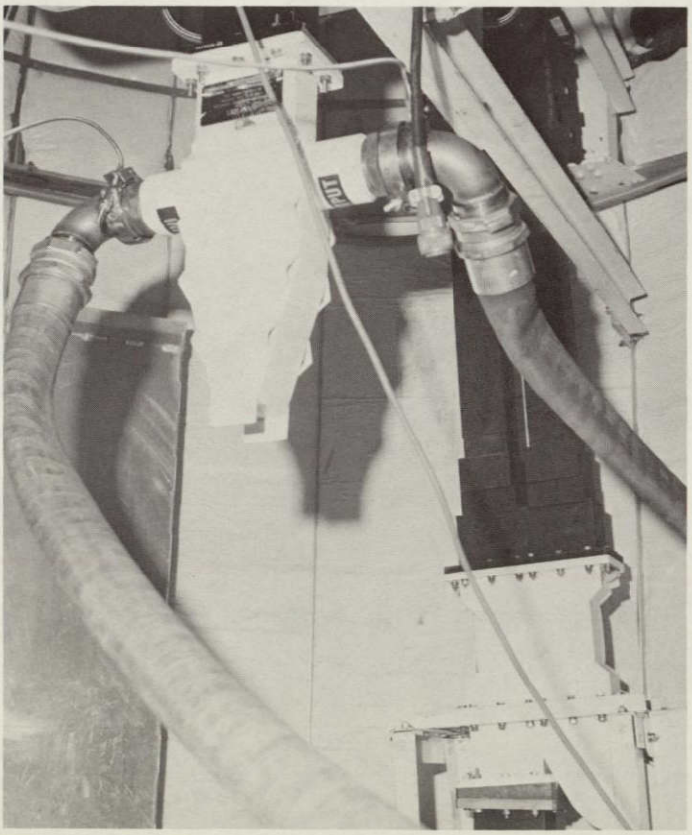

Fig. 5. Water load and diplexer installation

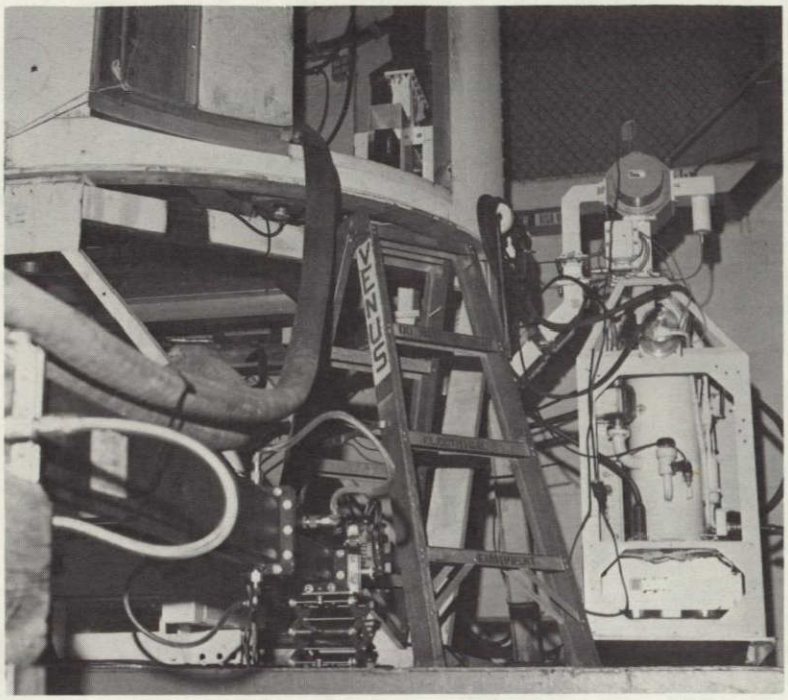

Fig. 6. Maser and diplexer installation

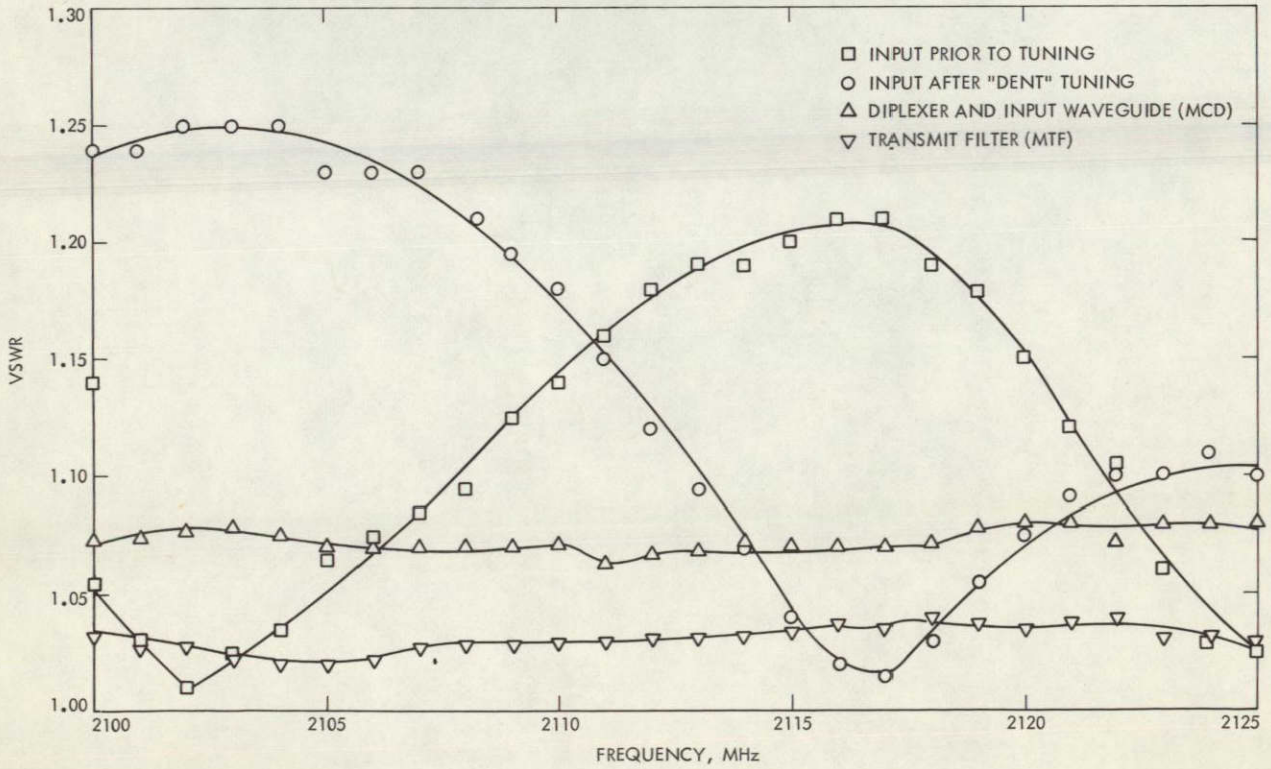

Fig. 7. VSWR data

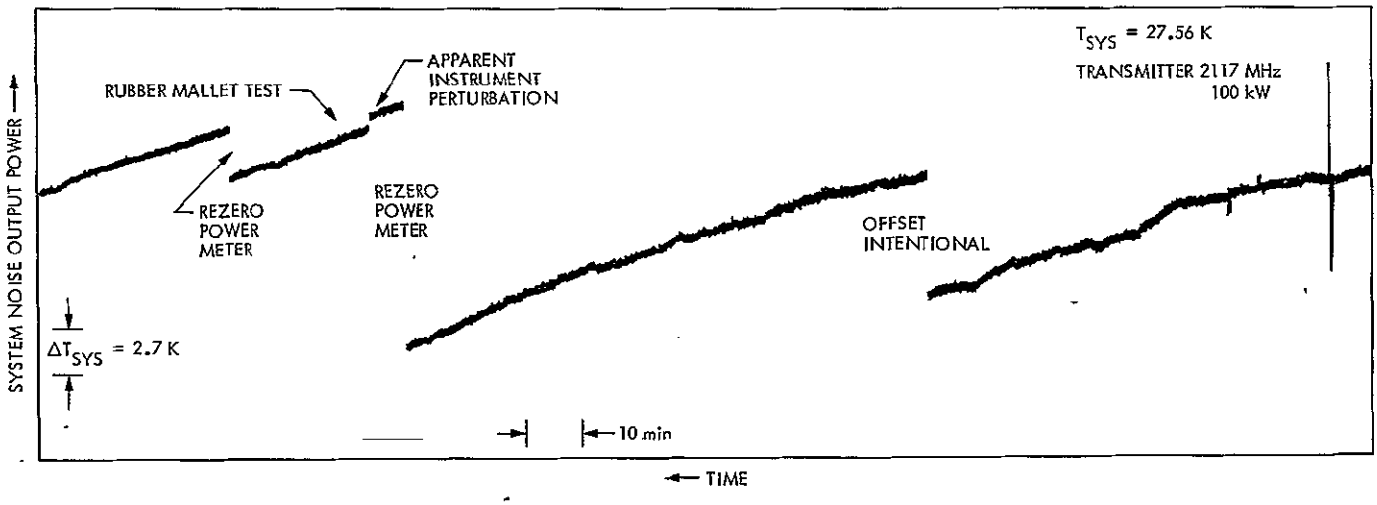

Fig. 8. Diplex test system temperature chart

DSN Research and Technology Support

E. B. Jackson
RF Systems Development Section

The activities of the Venus Deep Space Station (DSS 13) and the Microwave Test Facility (MTF) during the period Feb. 16 through April 18, 1976 are discussed and progress noted.

Continuing testing and refinement of the remote-controlled, unattended automated pulsar observing station is noted, along with routine pulsar observations of 22 pulsars. Radar observations of a geo-stationary satellite are discussed. Current status of the 400-kW X-band radar is reported along with routine automatic testing of the stability-reliability of the DSS 13 maser-receiver noise adding radiometer combination. A failure in the Faraday Rotation Receiving System is noted along with discussion in some detail of the activities of the High Power Transmitter Maintenance Facility. Continuation of receiver phase stability testing, specifically the effects of temperature on coaxial cables, is discussed and results reported

A demonstration at full power of the microwave power transmission facility is noted and routine support of the Planetary Radio Astronomy experiment is discussed. Transmission of master clock synchronization signals to overseas DSN stations is also reported.

The activities of the Development Support Group, in operating the Venus Deep Space Station (DSS 13) and the Microwave Test Facility (MTF) during the period Feb. 16 through April 18, 1976, supported various programs as discussed below.

I. Station Automation

In support of RTOP 70 "Network Monitor, Control and Operations Technology," DSS 13 will be the prototype to demonstrate an unattended remotely operated station.

Including automated tracking, 26-3/4 hours of station support were provided. Automated tracking, directed from the on-site master control computer, was performed during a 6-1/2 hour period during which data were collected from Pulsars 0031 − 07, 0329 + 54, 0355 + 54, and 1929 + 10. Except for operator input to the master control computer, directing which target was to be tracked, no operator intervention was necessary. The antenna movement, receiver tuning, and data collection are performed automatically under the control of the three computers. Katherine Moyd and Stanley Brokl, Section 331, assisted by Conrad Foster, Section 335, and supported by station personnel have been performing this testing.

II. Pulsar Observations

In support of the Radio Science Experiment "Pulsar Rotation Constancy" (OSS-188-41-51-09), DSS 13 provided 88 hours of observations during which the emissions from the pulsars listed below were recorded. These data, recorded at 2388 MHz, left-circular polarization (LCP), are used to determine precise pulse-to-pulse spacing, changes in this spacing, pulse shape, and pulse power content of the signals emitted by these pulsars.

The following pulsars were observed at DSS 13, Feb. 16 through April 18, 1976:

0031−07	0823+26	1706−16	2021+51
0329+54	0833−45	1749−28	2045−16
0355+54	1133+16	1818−04	2111+46
0525+21	1237+25	1911−04	2218+47
0629−28	1604−00	1929+10	
0736−40	1642−03	1933+16	

III. Radar Observations, Satellite

With the Mars Deep Space Station (DSS 14) transmitting and DSS 13 receiving, reflected signal radar observations are being made of a geostationary satellite. Using the DSS 14 64-m antenna, the satellite is illuminated with the 400-kW S-band transmitter at a nominal frequency of 2388 MHz, with reception of the reflected signal being accomplished on alternate round-trip light-times by DSS 13, using a programmed oscillator-controlled receiver and a 26-m antenna. Two stations are necessary because the round-trip light-time (RTLT) is so short (approximately 242 ms) that waveguide switching is impractical. The transmitting station switches frequency approximately 2 MHz every RTLT and the receiving station can receive the reflected signal every other RTLT. Although the apparent radar cross section is small, reflected signals have been detected from the satellite. A total of 17-1/4 hours of tracking have been conducted.

IV. X-Band Radar

Operational power available has continued to be increased, until 400 kW was made available early in the reporting period. In addition to providing support to increase available power, and operational support at DSS 14 during tracking, work has also continued on documentation and instruction manuals, including operations instructions. The 5th klystron, VA-949J, has now been received and a full complement of klystrons is now available for use as necessary.

V. Maser-Receiver-NAR Reliability-Stability Testing

Reliability and stability testing of the DSS 13 total receiving system is conducted automatically during nonoperational and nonmanned station periods. The 26-m antenna is prepositioned to a fixed azimuth and elevation and the noise adding radiometer (NAR) automatically records total receiving system temperature as a function of time. A radio brightness sky map is generated by Earth's rotation sweeping the fixed antenna across the sky as an additional data output from this testing. During this reporting period, the antenna was positioned at 360 deg azimuth and progressively positioned from 51.5 to 50.8 deg elevation and 491-3/4 hours of testing were automatically performed. This testing is done at 2295 MHz using right circular polarization (RCP) on the 26-m antenna.

VI. Faraday Rotation Experiment

This experiment, which collects ionospheric data with which to correct received range and doppler data from spacecraft, consists of two complete receiving systems, recording onto punched paper tape. Due to heavy rains, one of the systems failed when water entered the antenna-mounted preamplifier. The receiver was repaired by Section 333 personnel, returned to DSS 13, and has now been reinstalled.

VII. Deep-Space Network High-Power Transmitter Maintenance Facility (DSN HPTMF)

The DSN HPTMF, located at DSS 13 and at MTF, continued to support the 10, 20, 100 and 400-kW transmitters used in the DSN, with particular emphasis on the 100 and 400-kW transmitters and the 10-kW klystrons.

Klystron 4KM70SI, Serial Number F7-1, was tested to verify its ability to develop 10-kW output RF power. Additionally, bandpass curves and confirmation of the manufacturer's test data were obtained. The klystron was then shipped to DSS 62 in Spain for installation as necessary.

An X-3060 klystron, returned from DSS 63 in Spain, was tested and reported thermal drift in output power was confirmed. Consultation with the manufacturer (Varian Associates) is underway about possible on-site corrective measures.

The kit to effect installation of a 100-kW klystron into DSS 14 was completed and utilized after the failure (partially shorted filament) of the X-3075 klystron used in the DSN transmitter. Also for DSS 14, the second dual ignitron kit was tested for 12 hours at 60 kV to insure operability. Both dual ignitron kits have been modified to utilize the armored fiber optics that reduce the possibility of fiber breakage as a result of improper handling.

As a result of a recommendation by Varian Associates, four socket tanks for X-3070 and X-3075 klystrons have been modified to power the filaments with alternating current rather than direct current, which has been used in the past. Prior to this modification being implemented, a high-resolution spectrum analysis of the output RF carrier was performed to ascertain if use of alternating current would phase modulate the carrier. Using a variable frequency power supply, the socket tank was operated on 350 Hz to separate any generated modulation from 400-Hz modulation possibly present from HV power supply ripple. A spectrum analysis confirmed the presence of both 350 and 400 Hz sidebands. However, the amplitude was quite low, the 400 Hz HV power supply ripple modulation being 55 dB below the 100-kW carrier and the 350-Hz filament modulation being 63 dB below the 100 kW carrier. Both levels were undetectable in ordinary operation.

Following up on the 400-Hz sidebands observed to be due to DSS 13 HV power supply ripple, a high-resolution spectrum analysis was also performed on the dc output from this power supply. Operating at an output voltage of 20 kV, and using a 1,000::1 high-voltage probe, the spectrum shown in Fig. 1 was obtained. The strongest ripple frequency component, 400 Hz, represents approximately 0.1% of the dc output voltage of 20 kV. Harmonics of 400 Hz are clearly seen at higher frequencies, although the amplitude falls off rapidly above 5 kHz. Further testing is underway.

VIII. Diplexer Testing, High Power

A DSN diplexer, fabricated by a new technique, was tested at an operating power of 100 kW to verify its freedom from noise bursting effects. This test, and the results, are described in detail elsewhere in this issue by Richard B. Kolbly.

IX. Receiver Phase Stability Testing

An investigation into the phase stability characteristics of coaxial cable is continuing (Ref. 1). A test cable of 30-m length has been carefully wound into a coil 38 cm in diameter by taking unused cable directly from the manufacturer's shipping reel. After forming into a coil, connectors were attached using the manufacturer's dimensions and instructions. Using 2272 MHz, derived from a stable source, as an excitation frequency, continuous recording of electrical length was accomplished while the cable temperature was cycled from 0° to 50°C in a temperature chamber. Typical data records are shown in Figs. 2 and 3. The manufacturer suggests that, for maximum phase stability, coaxial cable should be cycled over the planned range of temperature usage several times before measurement or usage. Data taken during this series of measurements confirm the validity of this recommendation. Where possible, all-semiflexible coaxial cables intended for usages where phase stability is important, should be cycled over the maximum temperature extremes expected, a minimum of six times, allowing for temperature stabilization at each extreme of temperature.

Using an excitation frequency of 100 MHz, electrical length measurements were also made on an installed semiflexible coaxial cable loop at DSS 14, using ambient temperature to effect cable temperature changes. However, much of this cable installation is in the tunnel between Control Building and Antenna, and little overall temperature change takes place. Over a very limited temperature range in the vicinity of 0°C, the phase stability of the chosen cable loop is 0.42 degrees of phase/degree Celsius temperature change, at 100 MHz.

X. Microwave Power Transmission

Using radiated powers up to 300 kW at 2388 MHz, the 26-m antenna illuminated the collimation tower mounted rectenna in a demonstration of capability. The observing group consisted of William Bayley, Mahlon Easterling, and Robert MacMillin of JPL and John Wilford of the New York Times. Recovered dc power of approximately 30 kW was obtained from the rectenna, mounted 1.6 km away from the transmitting antenna.

XI. Planetary Radio Astronomy

In support of the radio science experiment "Planetary Radio Astronomy" (OSS 196-41-73-01), DSS 13 measures and records the radiation received (at 2295 MHz) from the planet Jupiter and various standard radio calibration sources. These measurements use the 26-m antenna, the DSS 13 receiving system, and the Noise Adding Radiometer (NAR). During this period 66-1/2 hours of observations were made, from Feb. 16 through April 18, 1976, measuring the radiation from Jupiter and the following calibration sources:

3C17	3C138	NRAO 530
3C45	3C147	PKS 0237-23
3C48	3C348	PKS 2134
3C123	3C353	

XII. Clock Synchronization System

Failure of a generator field excitation power supply forced postponement of a scheduled transmission to DSS 42 in Australia. Operation was otherwise uneventful. A total of ten transmissions were made with DSN scheduling, six to DSS 42-43 in Australia and four to DSS 61-63 in Spain.

Reference

1. Buchanan, H. R., and Price, A. L., "Temperature Effects on Transmission Line Phase and Group Delay," in *The Deep Space Network Progress Report 42-32*, pp. 296–300, Jet Propulsion Laboratory, Pasadena, Calif., April 15, 1976.

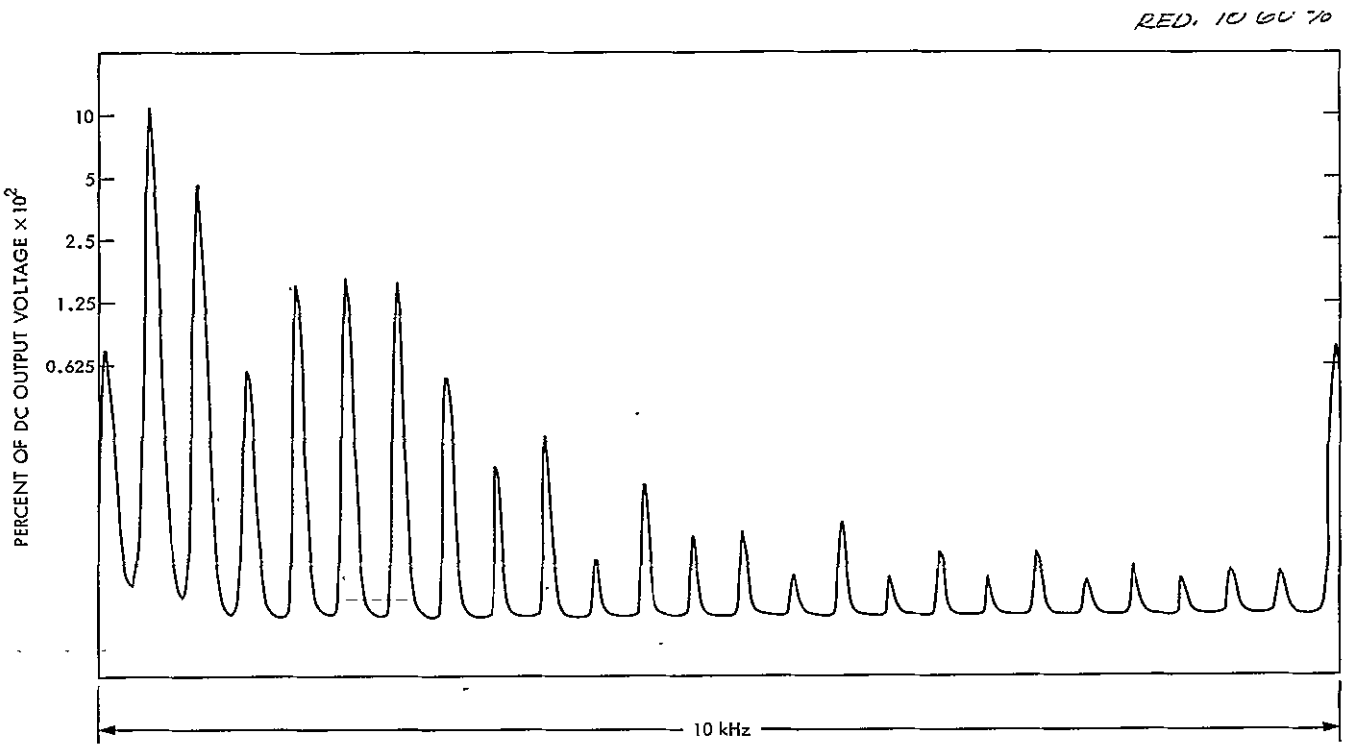

Fig. 1. DSS 13 HV DC power supply ripple voltage spectrum analysis 20 kV DC output voltage

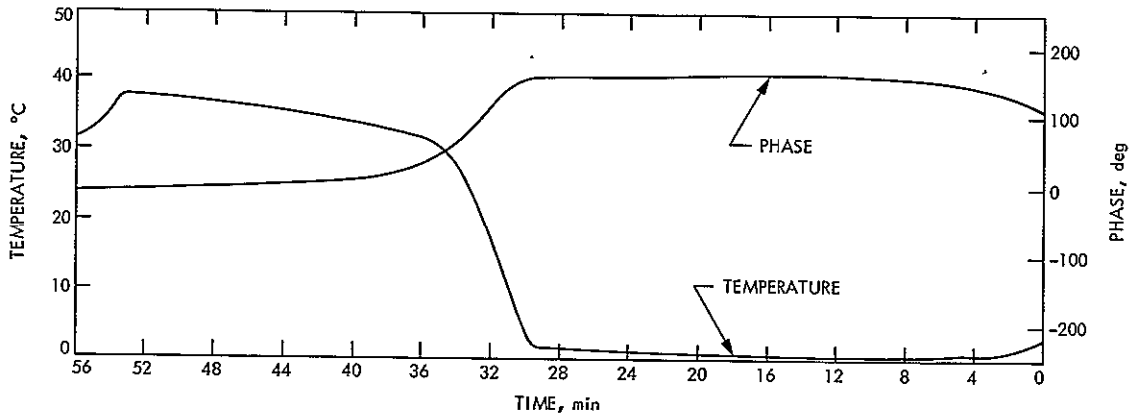

Fig. 2. 30-m test cable, differential electrical length first cycle in temperature chamber

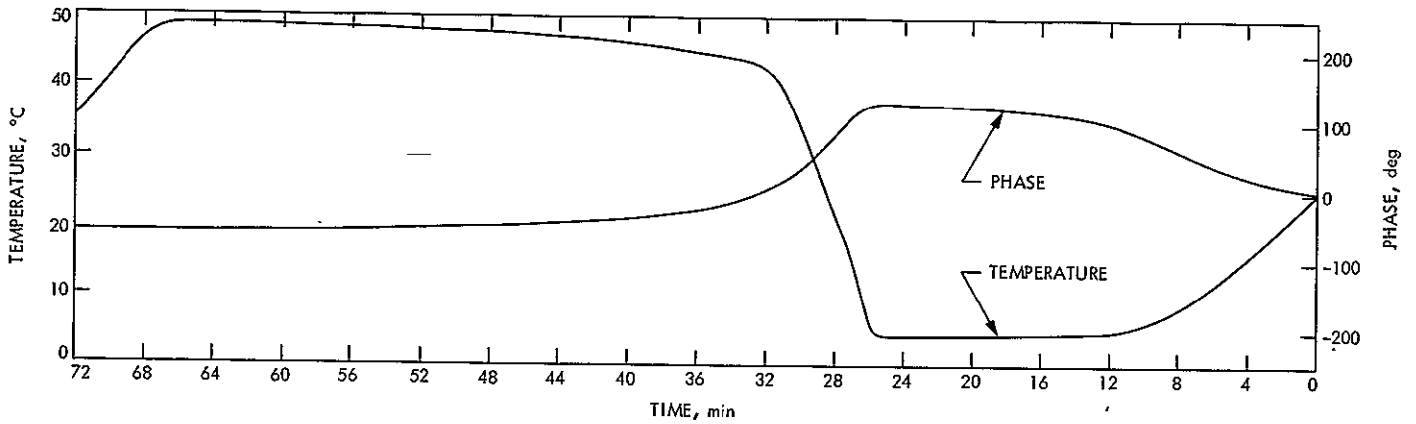

Fig. 3. 30-m test cable, differential electrical length fifth cycle in temperature chamber